

Design, Characterization and Validation of Integrated Bioelectronics for
Cellular Studies:
From Inkjet-Printed Sensors to Organic Actuators

by

Dahiana Mojena Medina

A dissertation submitted in partial fulfillment of the requirements
for the degree of Doctor of Philosophy in

Electrical Engineering, Electronics and Automation

Universidad Carlos III de Madrid

Advisors:

Pablo Acedo Gallardo
José Luis Jorcano Noval

Tutor:

Pablo Acedo Gallardo

January 2021

This thesis is distributed under license “Creative Commons Attribution – Non Commercial – Non Derivatives”.

 **creative
commons**



A mis padres y hermanas.

A Ángel.

Recuerda lo que te trajo hasta aquí.

Lucía Benavente

Acknowledgments/ Agradecimientos

Distancia de seguridad, mascarillas y pandemia son las palabras más escuchadas mientras se ha escrito esta tesis. Ni siquiera el final ha podido librar al proceso de parecer una perfecta distopía: Madrid cubierta bajo la nieve. Pero supongo que cuando una se siente agradecida se ha de pronunciar, ya sea en medio de una pandemia o una nevada histórica. Se ha de pronunciar de manera irreprimible a favor de esos días cotidianos, porque no existirán siempre. Esos días de fijarse un objetivo y no alcanzarlo; de guardar y crear copias de seguridad y no encontrarlas; de sentir que vuela el tiempo, con un vaso de café caliente entre las manos. Pero para no comenzar a hablar del qué o el cómo o el por qué o el para qué, voy a tomarme un tiempo para decir “quiénes”—y agradecer.

Este trabajo ha sido posible gracias a mi director de tesis Pablo Acedo. Pablo ha sabido encontrar el justo equilibrio entre proporcionar dirección y permitirme suficiente libertad para encontrar y desarrollar mi propia curiosidad investigadora. Ha sabido en que momentos aumentar la exigencia y cuando brindar el apoyo para seguir adelante. Su ayuda ha sido clave en este proceso de formación personal y profesional desarrollando en mí competencia y confianza, y por todo ello me siento muy agradecida.

A mi codirector José Luis Jorcano, por las detenidas, minuciosas y ostensibles observaciones; se va despacio cuando se va lejos. Sin duda, el resultado de este trabajo no habría sido ni de lejos el mismo sin todas esas oportunas (y tan procuradas) discusiones.

A los compañeros que he conocido a lo largo del doctorado y con los que he compartido muchos momentos dentro y fuera del bar (perdón de la universidad y el laboratorio): Aldo, Antonio, Alberto, Dragos, David, Frederik, Farid, Leonardo, Miguel, Marlon, Marcos, Karen, Jorge, Julio, Dani, Pedro y Guille. Óscar y Borja por sus interminables discusiones; Jaime porque ahora cuando no entiendo lo que ha dicho, ya sé lo que ha dicho. Mónica y Alba, por ser las mejores amigas y compañeras de viajes; gracias por hacerme sentir que puedo contar con vosotras en todo momento.

A Cristina, Guadalupe, Luis, Marina, Miguel y Rosario porque el trabajo en el laboratorio y soportar esos altos y bajos que aparecen en una investigación con la periodicidad de un ciclo biológico, no hubiera resultado tan divertido sin vosotros. A Leticia y Angélica por sacarme de tantos apuros en el laboratorio. Y en especial a Nuria, por el apoyo y el ánimo que me ha dado no solo durante si no también después de haber estado trabajando juntas. (Espero que llegues a leer todo hasta aquí).

I would also like to thank Prof. Ha-Duong Ngo for giving me the opportunity of working at Fraunhofer Institute IZM Berlin and to make my stay there so nice and productive. I have been fortunate to find excellent colleagues in Berlin. Thanks to Manu, Robin, Thang, Marie, Matthäus, Pete and Oliver for supporting my days at IZM (and for opening the door

for me whenever I need). Thank you to Prof. Raghied and Dr. Bei for their constructive criticism of my work and unsolicited yet helpful advice that guide my efforts in Berlin to a good end. And to Hu for the small talks and the understanding of all my complains and worries. A very special thanks to Moritz for his support and help inside and outside the lab; his mood is contagious and I am grateful to have had him as my closest collaborator. I have caught on that “German’ stereotypes” might be just conventional wisdom. To Alex for the endless discussions of so wide range of topics and for listening to when I needed to bounce my ideas off someone.

Agradezco además la financiación recibida desde el Ministerio de Educación, Cultura y Deporte para la realización de esta tesis doctoral a través del programa Formación de Profesorado Universitario.

Sin lugar a duda, a mi familia por siempre apoyarme incondicionalmente. A mi tía Mimita (creo que te será difícil imaginar por esos días allá en Santiago, cuando me veías comenzando los estudios en la universidad, que llegaría a este momento); en especial, a mi tía Anis y a Yanet por su insaciable cariño. A mis abuelos, Aba y Papita, nunca tendré palabras para agradecerles todo lo que han hecho y hacen por la familia. El corazón se me expande de luz y gratitud solo con escribir estas líneas. A mi abuelo Papita, por la sorpresa de pedirme que escribiera una versión de este documento para él (en castellano y sin tecnicismo) para poder conocer lo que hago. A veces me pregunto cuánto sería capaz de hacer si me vistiera con la mitad de su energía, curiosidad y perseverancia. Agradezco a mi abuela Mamá Dulce porque sé que desde algún lugar me protege y disfruta mis logros.

A mis padres, por guardarme sitio; a mis hermanas, por hacerme espacio. Gracias por el amor y la alegría que nos damos a pesar de la distancia y el apoyo en todos los sentidos que recibimos mutuamente a fin de alcanzar las metas (personales y como familia). En especial a mi madre por toda la ayuda durante esta etapa final de escritura sin la cual este proceso no hubiera sido el mismo. Simplemente estaré siempre agradecida por ser la familia que somos.

A Ángel, por la escucha atenta y el consejo oportuno. Por confiar en mí y animarme a seguir a pesar de los tropiezos. Por recordarme ante los “y si” los “y si no” y que algunos sueños no tienen plan B. Por saber desde cómo hacerme reír hasta cómo poner los puntos sobre las íes. Dicen que todos tenemos un ángel que nos ama y cuida: gracias por hacerme sentir que tengo dos.

Published and submitted content

Paper 1.

D. Mojena-Medina, M. Hubl, M. Bäuscher, J. Jorcano, H-D. Ngo and P. Acedo, “*Real-time impedance monitoring of epithelial cultures with inkjet-printed flexible interdigitated-electrode sensors*” *Sensors*, 2020, 20(19), 5711; <https://doi.org/10.3390/s20195711>

This item has been wholly included in this thesis in Chapter III and Chapter IV. The material from this source included in this thesis is not singled out with typographic means and references.

Paper 2.

D. Mojena-Medina, M. Martínez, M. de la Fuente, J. Posada, G. García, J. Jorcano, and P. Acedo, “*Design, Implementation and Validation of a Piezoelectric Device to Study the Effects of Dynamic Mechanical Stimulation on Cell Proliferation, Migration and Morphology*” *Sensors* 2020, 20, 7 <https://doi.org/10.3390/s20072155>

This item has been wholly included in this thesis in Chapter III and Chapter V. The material from this source included in this thesis is not singled out with typographic means and references.

OTHER RESEARCH MERITS

D. Mojena-Medina, R. Quevedo de Cea, N. López-Ruiz, J.L. Jorcano and P. Acedo “Detection of Cell Attachment on Flexible Printed Interdigitated Electrodes by means of Impedance Spectroscopy” EMBC2019-41st Annual International Conference of the IEEE Engineering in Medicine & Biology Society, Berlin, Germany.

D. Mojena-Medina, C. López, N. López-Ruiz, J.L. Jorcano and P. Acedo, “Optical Real-Time Oxygen Monitoring in 2D Tissues” OSA2019-Optical Sensor and Sensing Congress, San José, USA.

D. Mojena-Medina, M. Martínez, M. de la Fuente, J. Posada, G. García, J.L. Jorcano and P. Acedo, “Effects of mechanically active substrates on morphology, migration and proliferation of epithelial cells” IBE2019-Annual Conference Institute of Biological Engineering, St. Louis, USA.

D. Mojena-Medina, R. Quevedo de Cea, N. Lopez-Ruiz, J.L. Jorcano and P. Acedo, “Impedance monitoring in HaCaT cell cultures by means of interdigitated electrodes” BioEI2019-6th International Winterschool on Bioelectronics, Kirchberg, Austria.

Abstract

Advances in bioinspired and biomimetic electronics have enabled coupling engineering devices to biological systems with unprecedented integration levels. Major efforts, however, have been devoted to interface malleable electronic devices externally to the organs and tissues. A promising alternative is embedding electronics into living tissues/organs or, turning the concept inside out, loading electronic devices with soft living matters which may accomplish remote monitoring and control of tissue's functions from within. This endeavor may unleash the ability to engineer "living electronics" for regenerative medicine and biomedical applications. In this context, it remains a challenge to insert electronic devices efficiently with living cells in a way that there are minimal adverse reactions in the biological host while the electronics maintaining the engineered functionalities. In addition, investigating in real-time and with minimal invasion the long-term responses of biological systems that are brought in contact with such bioelectronic devices is desirable.

In this work we introduce the development (design, fabrication and characterization) and validation of **sensors** and **actuators** mechanically soft and compliant to cells able to properly operate embedded into a cell culture environment, specifically of a cell line of human epithelial keratinocytes. For the development of the **sensors** we propose moving

from conventional microtechnology approaches to techniques compatible with bioprinting in a way to support the eventual fabrication of tissues and electronic sensors in a single hybrid platform simultaneously. For the **actuators** we explore the use of electroactive, organic, printing-compatible polymers to induce cellular responses as a drug-free alternative to the classic chemical route in a way to gain eventual control of biological behaviors electronically. In particular, the presented work introduces inkjet-printed interdigitated electrodes to monitor label-freely and non-invasively cellular migration, proliferation and cell-sensor adhesions of epidermal cells (HaCaT cells) using impedance spectroscopy and the effects of (dynamic) mechanical stimulation on proliferation, migration and morphology of keratinocytes by varying the magnitude, frequency and duration of mechanical stimuli exploiting the developed biocompatible actuator.

The results of this thesis contribute to the envision of three-dimensional laboratory-growth tissues with built-in electronics, paving exciting avenues towards the idea of living smart cyborg-skin substitutes.

Resumen

En los últimos años los avances en el desarrollo de dispositivos electrónicos diseñados imitando las propiedades de sistemas vivos han logrado acoplar sistemas electrónicos y órganos/tejidos biológicos con un nivel de integración sin precedentes. Convencionalmente, la forma en que estos sistemas bioelectrónicos son integrados con órganos o tejidos ha sido a través del contacto superficial entre ambos sistemas, es decir acoplando la electrónica externamente al tejido. Lamentablemente estas aproximaciones no contemplan escenarios donde ha habido una pérdida o daño del tejido con el cual interactuar, como es el caso de daños en la piel debido a quemaduras, úlceras u otras lesiones genéticas o producidas. Una alternativa prometedora para ingeniería de tejidos y medicina regenerativa, y en particular para implantes de piel, es embeber la electrónica dentro del tejido, o presentado de otra manera, cargar el sistema electrónico con células vivas y tejidos fabricados por ingeniería de tejidos como parte innata del propio dispositivo. Este concepto permitiría no solo una monitorización remota y un control basado en señalizaciones eléctricas (sin químicos) de tejidos biológicos fabricados mediante técnicas de bioingeniería desde dentro del propio tejido, sino también la fabricación de una “electrónica viva”, biológica y eléctricamente funcional. En este contexto, es un desafío insertar de manera eficiente dispositivos electrónicos con células vivas sin desencadenar reacciones adversas en el sistema biológico receptor ni en el sistema electrónico diseñado. Además, es deseable monitorizar en tiempo real y de manera mínimamente invasiva las respuestas de dichos sistemas biológicos que se han añadido a tales dispositivos bioelectrónicos.

En este trabajo presentamos el desarrollo (diseño, fabricación y caracterización) y validación de **sensores** y **actuadores** mecánicamente suaves y compatibles con células capaces de funcionar correctamente dentro de un entorno de cultivo celular, específicamente de una línea celular de células epiteliales humanas. Para el desarrollo de los sensores hemos propuesto utilizar técnicas compatibles con la bioimpresión, alejándonos de la micro fabricación tradicionalmente usada para la manufactura de sensores electrónicos, con el objetivo a largo plazo de promover la fabricación de los tejidos y los sensores electrónicos simultáneamente en un mismo sistema de impresión híbrido. Para el desarrollo de los actuadores hemos explorado el uso de polímeros electroactivos y compatibles con impresión y hemos investigado el efecto de estímulos mecánicos dinámicos en respuestas celulares con el objetivo a largo plazo de autoinducir comportamientos biológicos controlados de forma electrónica. En concreto, este trabajo presenta sensores basados en electrodos interdigitados impresos por inyección de tinta para monitorear la migración celular, proliferación y adhesiones célula-sustrato de una línea celular de células epiteliales humanas (HaCaT) en tiempo real y de manera no invasiva mediante espectroscopía de impedancia. Por otro lado, este trabajo presenta actuadores biocompatibles basados en el polímero piezoeléctrico fluoruro de poli vinilideno y ha investigado los efectos de estimular mecánicamente células epiteliales en relación con la proliferación, migración y morfología celular mediante variaciones dinámicas de la magnitud, frecuencia y duración de estímulos mecánicos explotando el actuador biocompatible propuesto.

Ambos sistemas presentados como resultado de esta tesis doctoral contribuyen al desarrollo de tejidos 3D con electrónica incorporada, promoviendo una investigación hacia la fabricación de sustitutos equivalentes de piel mitad orgánica mitad electrónica como tejidos funcionales biónicos inteligentes.

List of Contents

AGRADECIMIENTOS/ACKNOWLEDGMENTS	VII
PUBLISHED AND SUBMITTED CONTENT	XI
OTHER MERITS	XII
ABSTRACT	XIII
RESUMEN	XV
CHAPTER I. DISSERTATION SUMMARY	1
1.1. Motivation of the work	3
1.2. Interfacing electronic devices with biological tissues	7
1.3. Understanding the skin tissue	15
1.4. Objectives of the thesis	18
1.5. Structure of the dissertation	20
1.6. Thesis framework	24
CHAPTER II. FLEXIBLE AND STRETCHABLE ELECTRONICS	25
2.1. Background	27
2.2. From early flexible electronics to breathable sensors by structure-based approaches	29
2.3. Material-based routes. From early plastic electronics to self- healing materials	42
2.4. Overview of manufacturing technologies for flexible and stretchable electronics	54
2.5. Inkjet printing technology	62
2.5.1. Inkjet printers and printheads	64

2.5.2. Substrates and inks for inkjet printing	66
2.5.2.1. Substrates and substrate-based strategies for inkjet printing	67
2.5.2.2. Inks and inks requirements for inkjet printing	69
2.5.3. Processes for inkjet printing.	72
2.5.4. Inkjet printing in the development of flexible electronics and systems.	77
2.6. Conclusions and outlook	81
CHAPTER III. MATERIALS AND METHODS.	85
3.1. Introduction	87
3.2. Cell biology.	88
3.2.1. Cell line, media and transfection	89
3.2.2. Alamar Blue assay.	91
3.2.2.1. Alamar Blue as an indicator of cytotoxicity and proliferation	95
3.2.3. Live/Dead Kit Assay	96
3.2.4. Cell fixation for immunofluorescence	97
3.2.5. Antibodies and Reagents	97
3.2.6. Coating of actuators, sensors, and bottom dishes	98
3.2.7. Cell fixation for morphology observation.	98
3.2.8. Cell treatment for impedance-based detection of chemicals	99
3.2.9. Migration assay using a PDMS stencil.	99
3.2.10. Migration assay using Scratch assay.	100
3.3. Microscopy, image processing and analysis.	101
3.3.1. Microscopy equipment and Profilometry	101
3.3.2. Scanning electron microscopy	102
3.3.3. Biological Image processing	103
3.3.3.1. Live/Dead assay.	103
3.3.3.2. Cell migration and analysis	103
3.3.3.3. Cell migration in the scratch assay	104
3.3.3.4. Size of the Nucleus	105
3.3.4. Statistical analysis.	105
3.4. PDMS curing.	107

3.5. Design and fabrication of the sensors (Chapter IV)	107
3.5.1. Inkjet printing of interdigitated sensors	107
3.5.2. Materials for inkjet printing the sensors	110
3.5.3. Assembly of IDE-based devices	110
3.5.4. Protocol for impedance spectroscopy and data processing	111
3.6. Design and fabrication of the actuating system (Chapter V)	113
3.6.1. Materials for fabricating the experimental stage	113
3.6.2. Materials of the driver	115
CHAPTER IV. DEVELOPMENT OF PRINTED FLEXIBLE SENSORS FOR CELLULAR STUDIES	117
4.1. Introduction and motivation	119
4.2. From biological impedance measurements to cell-substrate impedance spectroscopy	121
4.2.1. Theoretical models and impedance representation	126
4.3. Fundamental concepts of impedimetric biosensors based on coplanar interdigitated electrodes	128
4.4. Design and fabrication of the inkjet-printed sensors for cellular studies	134
4.5. Description of the measurement system	140
4.6. Characterization of the inkjet-printed sensors	142
4.6.1. Sensors morphological and electrical characterization	142
4.6.2. Cytocompatibility characterization of the printed sensors	148
4.7. Demonstration of the use of the developed inkjet-printed sensors for non-invasively monitoring of cell cultures	151
4.7.1. Validation of the developed sensors for cellular studies: Impedimetric sensing of cell proliferation	152
4.7.2. Validation of the developed sensors for cellular studies: Detection of cell-sensor adhesions in epithelial cell culture using inkjet-printed sensors	159
4.7.3. Validation of the developed sensors for cellular studies: Preliminary use of inkjet-printed sensors integrated into cell cultures to monitor cell migration	165

4.8. Discussion of the results	170
CHAPTER V. DEVELOPMENT OF A NOVEL ACTUATING SYSTEM FOR CELLULAR STUDIES	177
5.1. Introduction and motivation	179
5.2. How force regulates cell function: tissue, cellular and molecular outlooks.	182
5.3. Techniques to study and influence on the cellular mechanical responses	187
5.4. Description of the piezoelectric actuating device for cellular studies	189
5.4.1. Description of the piezoelectric device and associated setup	189
5.4.2. Physics behind the piezoelectric actuation for dynamic cellular studies.	194
5.5. Characterization of the piezoelectric actuating device	198
5.6. Estimation of the applied forces into the cells generated by the actuating device.	201
5.7. Preliminary studies of the effects of dynamic mechanical stimulation on cell proliferation, migration and morphology	203
5.7.1. First observation: Low-frequency mechanical stimulation enhances HaCaT cell proliferation	205
5.7.2. Second observation: Dynamic mechanical stimulation of low frequency enhances the cell migration rate in HaCaT cells.	213
5.7.3. Third observation: Effect of dynamic mechanical stimulation on the morphology of cells	218
5.8. Discussion.	224
CHAPTER VI. GENERAL CONCLUSIONS AND FUTURE WORK	229
6.1. Conclusions.	231
6.2. Future directions.	237
CHAPTER VII. BIBLIOGRAPHY	i

CHAPTER VIII. APPENDIX	xxiii
APPENDIX I. Materials List for the fabrication of the sensors	xxv
APPENDIX II. Materials List for the fabrication of the actuators.	xxvi
APPENDIX III. Board Circuit Schematic for the driver of the actuator device	xxviii
APPENDIX IV. Flow chart in the assembly of the experimental stage of the actuator devices.	xxix
APPENDIX V. Experimental setup for the analysis of fluid streaming within the actuating device.	xxx
APPENDIX VI. Additional scanning electron microscopy images of cell cultures seeded on the actuators	xxxi
APPENDIX VII. Fitting values of the electrical circuit model for detachment experiments	xxxii
APPENDIX VIII. Materials List for the cell biology experiments and Solutions	xxxiv

List of Tables

Table 1. Typical substrates for inkjet-printed electronics and their physical properties. Reference from K. Suganuma, 2014. ¹⁹²	68
Table 2. Values of the molar coefficients in the oxidation and reduction of the Alamar Blue.	94
Table 3. Three methods used for cell impedance-based measurements.	126
Table 4. Parameters and values of the PVDF for the calculation of the fundamental frequency.	197
Table 5. Summary of the experimental conditions for the piezoelectric actuating device to stimulate cell cultures of HaCaT epithelial cell line.	204
Table 6. Summary of the results using plot regression with the values obtained from the processed images in the cell migration experiments.	216

List of Figures

- Figure 1.** Concept of living-like bioelectronics as bionic skin substitutes. 6
- Figure 2.** Flexible and stretchable electronics interrogate, wrap, and conform around complex tissues on and into the human body. a) A photograph of an array of intrinsically stretchable transistors conformally adhered to a human palm. The array enables sensing the position of a synthetic ladybug by a multiplexing measurement and a matched map of the on-current magnitudes of the resistive tactile sensors. b) An epidermal microfluidic sensor mounted on a human forearm. The device collects and stores sweat during exercise to monitor different biomarkers based on colorimetric measurements. A wireless interface enables data transfer to a smartphone that captures and analyses data. c) Optical images of a wearable sweat-analysis patch with a transdermal drug-delivery module. The system adheres to the skin and resembles most of the skin's properties, allowing a compliance interface even under deformation. d) Multifunctional electronic-skin (e-skin) fabricated with naturally derived ingredients that enable a soft and stable, but fully biodegradable hydrogel-based system. The on-skin-worn electronic patch measures temperature, humidity, and strain and integrates a reusable electronic module to record, analyze, and transmit the data wirelessly. e) Silicon-based flexible device of serpentine filaments wrapping around a Langendorff-perfused rabbit heart. Different functional elements are highlighted inside the picture. f) Novel material-based device of an intrinsically stretchable electrode array conforming to the surface of the superior right ventricle of a rabbit heart *via* surface tension. The system enables *in vivo* electrophysiological mapping of atrial fibrillation. g) Biodegradable strain and pressure sensors implanted subcutaneously on the back of a Sprague-Dawley rat for long-term monitoring of tendon-healing. The devices were able to operate stably over 2-3 weeks *in vivo* after implantation. h) Freely moving mouse with an implanted bioresorbable spectrometer for the continuous monitoring of brain oxygenation, temperature, and neural activity. The device is injectable and is fabricated using materials that naturally undergo clearance from the body after its operational lifetime. i) A wireless closed-loop system implanted between epidermal skin and muscle in the abdominal cavity of a mouse. The miniaturized bio-optoelectronics implant exploits inorganic light-emitting diodes to opto-activate light-sensitive proteins (opsins) in the bladder together with a sensing system based on strain gauge to monitor the organ function (i.e., bladder filling/voiding). Note. Reproduced from (a) Wang, Bao, *et al.*, 2018; (b) Koh, Rogers, *et al.*, 2016; (c) Lee, Kim, *et al.*, 2017; (d) Baumgartner, Kaltenbrunner, *et al.*, 2020; (e) Xu, Rogers, *et al.*, 2014; (f) Liu, Bao *et al.*, 2020; (g) Boutry, Bao, *et al.*, 2018; (h) Bai, Rogers, *et al.*, 2019; (i) Mickle, Rogers, *et al.*, 2019. 9
- Figure 3.** Tissue-like electronics. a) Macro-porous mesh electronic scaffolds with silicon-

nanowire field-effect transistors and platinum electrodes integrated into cardiac tissue of cardiomyocytes. b) Mesh device with gold electrodes for sensing of tissue electrical activity, and electrically stimulate the cells and tissue (right). The device incorporates electroactive polymer to release drugs and small molecules that may promote tissue growth. The electronics are integrated within a scaffold of electrospun nanofibers of SU-8 that support tissue cultures. In the left plot is observed an image of the hybrid cardiac patch. c) 3D free-standing electronics as a scaffold for tissue cultures (right) and the electronics embedded into extracellular matrix-based hydrogels for culturing cardiomyocytes. Note. Images reproduced from (a) Dai, Lieber, *et al.*, 2016; (b) Feiner, Dvir, *et al.*, 2016; (c) Wang, Rogers, *et al.*, 2020. 12

Figure 4. Sketch of the skin tissue describing its structural layers and the signals and parameters accessible from the skin. Note: image modified from Liu, Salvatore *et al.*, 2017. 16

Figure 5. Graphical overview of this dissertation. Chapter 2 reviews the basics concepts that endow electronics flexible and malleable. Chapter 3 describes the materials and methods used for developing both the sensing and actuating systems, and for their characterization. Chapter 4 demonstrates a sensing system embedded into a monolayer of epithelial cell layer to monitor cell-substrate impedance as an indicator of cellular states. Chapter 5 demonstrates an actuating system embedded into cultured epithelial cell to influence cellular outcomes by (dynamic) mechanical stimulations. 23

Figure 6. Progress in flexible electronics. a) Thin-film transistor (TFT) of hydrogenated amorphous silicon was fabricated on top of stainless-steel foils with thickness from 3 μm to 20 μm . A 25- μm -thick TFT wrapped around a pencil.⁷⁷ b) Extreme bending flexibility of a polymer-based photovoltaic device on 1.4- μm -thick poly(ethylene terephthalate) foils, wrapped around a human hair with a radius of 35 μm without impairing its functionality, this is, a specific power of 23 W/g.⁵⁸ c) Birth of imperceptible electronics by fabricating 12 \times 12 active-matrix array (8 \times 8 cm) with resistive tactile sensors on ultrathin (1 μm) plastic foils (poly(ethylene naphthalene), PEN), with extremely lightness of 3 g/m² allowing them to float to the grown more slowly than a feather⁵⁶, crumple like a paper, and d) conform to human skin. 30

Figure 7. Bending of a film-on-foil structure into a radius R. The externally applied bending causes mechanical strain in the film ϵ in each axis resulting in a matrix of values. The film on top of the substrate has a thickness h_f while the underneath material h_s 31

Figure 8. Stretch-compatible ultra-flexible electronics. a) Illustration of the process to laminate an imperceptible electronic foil (3- μm thick) on a pre-stretched elastomer (3M VHB) by picking and placing. When the prestrain in the elastomer is relaxed, the electronic foil forms out-of-plane wrinkles enabling subsequent tensile strains without impairing the functionalities in the device. b) Picture sequence of a one-step pick-and-place transfer, and the formation of folds in an organic field-effect transistor when the elastomer is relaxed. Source and drain were fabricated with gold while aluminum serves as the gate electrode; a hybrid aluminum oxide and phosphonic acid self-assembled monolayer as gate dielectric, and DNTP (dinaphto[2,3-b:2',3'-f] thieno[3,2-b] thiophene) as an organic semiconductor. Note a) and b) modified from reference ⁵⁶. 35

Figure 9. Strategies in flexible and stretchable electronics. a) Difference between elastic moduli of conventional electronic materials and soft matters found in our body. Most typical materials used are highlighted ranging from elastomers, polymers for substrates

- to liquid metals, conductors, and semiconductors for active layers. Note: sketch modified from reference⁶⁴. b) Wavy/wrinkly design of an array of gallium arsenide nanoribbons (left) in wavy shapes bonded to a PDMS membrane pre-strained to 50 %, where the bond occurs only at the positions of the troughs by chemically patterning the PDMS substrate with UV light,⁹⁵ and (right) AFM image of silicon membrane (100-nm thickness) bonded to a piece of rubber (PDMS pre-strained to 3.8 %) allowing a biaxial strain.⁹⁸ c) Island-bridge concept for stretchable electronics, where functional components usually reside on the islands and interconnect form the bridge. The island consists of CMOS inverter transistors interconnected by non-coplanar serpentine structures.⁹⁹ d) Two examples of Origami/Kirigami-inspired design that renders stretchability by adding cuts at selected locations. The strategy has mostly been exploited for stretchable batteries, but a Kirigami-based multifunctional patch has recently been demonstrated.¹⁰⁰ In the image, the microscale patterns were fabricated with graphene oxide/PVA nanocomposites, allowing strains up to 370 % at a device level.¹⁰¹ 38
- Figure 10.** Epidermal electronics. a) Multifunctional electronics with physical properties resembled human epidermis. The system was mounted on a water-soluble polymer sheet of polyvinyl alcohol and conformally attached to the skin via van der Waals interactions alone, analogous to a temporary transfer tattoo. Thin narrow interconnected lines in forms of filamentary serpentine (FS), and ultrathin active devices that adopt similar FS layouts were found as effective parameter designs to achieve the extreme mechanical properties of the system b) FS pattern for a silicon solar cell. c) Optical micrograph of silicon RF diode for the wireless capabilities in an island-bridge structure. d) Epidermal electronics are mechanically invisible for the user in undeformed (right), compressed (center), and stretched (left) forms without any variation in their functionalities and imposing negligible mechanical loading. Note: a-d from reference ⁴⁹. 40
- Figure 11.** Breathable electronics. a) Sketch of the gold nanomesh electronics laminated directly onto the skin. The gold is evaporated onto electrospun nanofibers of polyvinyl alcohol (PVA). When PVA meshes laminated onto the skin are sprayed with water, the substrate dissolves, and nanomesh conductors adhere directly to the skin. b) A picture of a nanomesh conductor laminated to a fingertip (left) and a magnification of the image (right, scale bar 1 mm), showing a high level of adherence and conformability to the irregular surface of the skin. A micrograph by scanning electron microscopy (SEM) of a nanomesh conductor attached to a silicone skin replica (down, scale bar 5 μm). Note: a,b modified from ⁵⁷. 41
- Figure 12.** Material-based strategies for flexible and stretchable electronics. a) In the deterministic composites, thin films or complex geometries of otherwise stiff materials render stretchability from an initial length L to an $L+\Delta L$, by out-of-plane motions or by channeling strain into the interconnects. b) In the random composites, electronic fillers (nanoscale materials, and/or conjugated polymers) form a mesh-like network structure atop or into an elastomer backbone, and the percolation pathways for the electric charge is the key that underpins flexibility. c) Intrinsically stretchable materials do not in principle require of strain relief by substrates or topographies, but their molecular structures accommodate strain. 45
- Figure 13.** Random compositing for flexible and stretchable electronics. An electronic filler and an elastomer matrix form the elastic composite, in which the percolation networks of the electronic fillers enable electrons to move through networked pathways when the

composite is stretched. A variety of nanomaterials including zero dimension (0D),^{146,147} one dimension (1D),^{141,148} and two dimension (2D)^{149,150} forms, and conjugated polymers have been used as electronic fillers for random compositing. Elastomers often comprise the bulk support because they are soft (i.e., Young's moduli < 10 MPa) and easy to process. The electrical properties of material composites strongly depend on the type of electronic filler, while mechanical properties (e.g., Young's moduli) are mainly determined by the elastomer backbone. Note: figure modified from reference ¹³⁴. 49

Figure 14. Example of e-skin electronic systems based on intrinsically stretchable materials. a) Self-cleanable, transparent ionic sensors attached to the fingers. They were wired connected to a controlled board, and by a binary code, real-time communication was demonstrated. "DREAM" was typed using a combination of finger touches.¹⁵⁵ b) Molecular design of the seal-healable elastomer (top), and schematic representation of a stretched polymer with broken weak bonds (down left), notched film (down the middle), and self-healed film (down right).¹⁵⁶ c) Electronic skin consisting of stretchable modules of ECG, strain sensors, and LEC-type displays. The electrodes/interconnections of the system are composed of hybrid conducting fillers of AgNW/CNT embedded in the self-healing polymer matrix.¹⁵⁷ Note: Images modified from a) ref. 155; b) ref. 156; c) ref. 157. 53

Figure 15. Manufacturing techniques and processes in the lamination approach for flexible/stretchable electronics. a) Components are prefabricated using conventional microfabrication techniques in a wafer substrate. b) The structures or the devices are laminated into the target substrate using different methods such as transfer printing. 56

Figure 16. Different manufacturing techniques used in the integration approach for flexible and stretchable electronics. 59

Figure 17. Inkjet printing technology state-of-the-art in research. Inkjet printing technology is at its very early stage of development compared with the rest of additive manufacturing techniques. Source: Scopus database. A search carried out on June 2, 2020. 63

Figure 18. Categories of inkjet printers. a) Schematic of a continuous inkjet printer (CIJ). CIJ produces a continuous stream of liquid drops, ejected through a small nozzle. To direct and position the drops, further potential is applied in deflector plates. Unwanted drops are deflected by the electric field to a gutter and for most applications in material science and electronics this recycling is wasted. b) Schematic diagram of a drop-on-demand (DOD) inkjet printer. In DOD, drops are ejected by a pressure pulse in a fluid-filled cavity. This pressure pulse can be generated (b.1) by a bubble generated by a heater or (b.2) by a mechanical actuator. Note: figure modified from ¹⁸². 64

Figure 19. Piezoelectric inkjet printing. Detailed schematic of the structure and function of a piezoelectric single nozzle printhead. The pressure generation, propagation, and reflection upon a voltage application are described in a waveform file from a computer. 66

Figure 20. Schematic of the basis of an inkjet printing process. Pre-processing prepares the printing process and includes the digital design, and treatment of substrate and/or inks(1). The printing process (2) implies the ink deposition and the post-processing steps. (3) Final printed pattern or device. 72

Figure 21. Schematic of a) printer, b) ink, and c) substrate and particularities of each one. 74

Figure 22. Coffee ring effect. a) The process of drop drying after deposition leading to a coffee ring effect due to an excess of solute at the edges of the ink-jetted drop during

solvent evaporation. b) The coffee ring can be minimized by different methods, such as using a co-solvent mixture in the ink formulations or by controlling the temperature of the substrate. When using a co-solvent system, the solvent with a high boiling point evaporates at the outer edge, resulting in a surface tension gradient that leads a Marangoni flow to carry the solute inward to the center of the droplet.	75
Figure 23. The sequence of post-processing in a metal nanoparticle-based ink. In the drying, the solvent is evaporated using low temperatures or room temperature. The sintering can be done by different techniques such as UV, microwave, plasma treatment, to apply external energy that enhances the functionalities of the ink.	76
Figure 24. Utilization of technology in the fabrication of devices for flexible electronics. The color bars show where silicon-based technology (blue) and printed electronics (orange) are exploited.. . . .	77
Figure 25. Graphical summary of chapter II based on the description of the electronic skin reported in ¹⁰⁸	82
Figure 26. a) Histological slide of skin tissue and b) HaCaT cell line cultured <i>in vitro</i> . HaCaT is a cell line from human adult skin keratinocytes propagated under low Ca ²⁺ conditions and elevated temperature which were released from full-thickness dermo-epidermal skin. Note: a) adapted from Lai-Cheong and McGrath, 2017. ²²⁸	88
Figure 27. Flowchart of the Alamar Blue protocol used in this thesis.	93
Figure 28. Schematic representation of the cell migration protocol using a PDMS stencil.. . . .	100
Figure 29. Schematic depicting the scratch protocol to study cell migration.	101
Figure 30. a) Sketch of the printed sensors (Chapter IV) with dimensions and b)-e) manufacturing process for the inkjet printing coplanar capacitors. Materials and details of the process are summarized within the figure.. . . .	108
Figure 31. Dimensions and schematic of the experimental stage based on polymeric piezoelectric actuator (Chapter V). a) Top view with the description of the different materials used in the manufacturing of the biocompatible actuator-based device. b) Schematic representation with a lateral view of the actuator-based device, (i) the piezoelectric film remains in the bottom of the Petri dish with a chamber made of PDMS, (ii) and (iii) show a representation of a cell culture with basal medium seeded on the collagen-coated piezoelectric film under (ii) static condition (0 voltage in the electronics stage) and (iii) dynamic condition. AC: alternating current.. . . .	114
Figure 32. a) Simulation of the dispersion of tissues first measured by Schwan. The dispersions occur due to the loss of certain polarization modes in biological tissues: α -dispersion arises from the tangential flow of ions across the cell surfaces, β -dispersion comes up due to the accumulation of charges at the cell membranes and γ -dispersion is related to the dipolar movements of molecules, mainly water. b) The simplified electrical model of cells under an electric field. The model is named single-shell model. c) Schematic of the differences in low- and high-frequency signal traveling through healthy and damaged tissue. Note: a) adapted from Nasir and Al Ahmad, 2020; ²⁵⁵ b) adapted from Grimmes <i>et al.</i> ²⁵⁰	123
Figure 33. Two graphical representation of the impedance spectrum of an RC electrical circuit. a) In the Complex plane plot, also called Argand diagram or much more common Nyquist plot, the imaginary part of the impedance is represented versus the real part. b) In the Bode plot the magnitude ($\log Z $) and phase (ν) are represented versus de frequency. Note: a) and b) adapted from M. Sluyters-Rehbach, 1994.	128

Figure 34. Interdigitated electrodes. a) Penetration of the electric field in a parallel plate capacitor and interdigitated capacitors. b) Structure of interdigitated electrodes most often used, and the parameters used to describe the geometry: the number of fingers (n), the length of the digits (L), the width (W), and the spacing between electrodes (S).	131
Figure 35. Sensing mechanism of interdigitated sensors based on the impedimetric transducer. Upon the presence of cells, the electric field in the plane above the interdigitated electrodes is disrupted leading to electrical changes that can be detected in the impedance measured between the negative and positive terminal of the device.. . . .	132
Figure 36. Novel approaches to improve printing resolutions for inkjet-printed interdigitated electrodes. a) Exploring new geometrical structures in inkjet-printed capacitors to achieve higher capacitances per area. b) Using a sandwiched non-conductive layer of parylene C deposited by metal vapor deposition between two conductive combs printed by inkjet printing allowed to reduce the gap of the printed electrodes with no short-circuit the printed lines. Note: images modified from a) Rivadeneyra <i>et. al.</i> , 2014 and b) Molina-López <i>et al.</i> , 2013.	133
Figure 37. Drop watcher image of ejected droplets from the inkjet printhead.	137
Figure 38. Study of the adhesion between consecutive layers of the SU-8 to passivate the silver-nanoparticle electrode. An electrode of 1mm×11 mm was printed on a PET substrate and a SU-8 pattern was patterned on top in a sequence of 1L, 2L and 3L displacing the origin of the printhead 1 mm in the X-axis. Different interfaces (AgNP-substrate; AgNP-1LxSU8; 1LxSU8-2LxSU8; 2xSU8-3xSU8) were observed under microscope and using a profilometer. Oxygen plasma treatment was used after printing 1LxSU-8 to improve the wettability between two consecutive layers of SU-8 but it was observed that the exposed AgNP-based electrodes were oxidized after several days. Well-defined passivation could be obtained with 3L of SU8, resulting in the final number of layers selected for the passivation.	138
Figure 39. Optical pictures of the flexible interdigitated electrodes of silver-nanoparticles with a passivation of the SU8 on flexible PET foil manufactured by inkjet printing.. . . .	139
Figure 40. a) Assembly and packaging of the IDEs-based devices to perform impedance spectroscopy measurements of cultured cells. Inkjet-printed sensors were custom packaged and bonded as a substrate for cell cultures on Petri dishes. b) Representation of the experimental system. The system consists of the IDEs-based chamber, an impedance analyzer, a microscope with an integrated bioreactor, and a PC to acquire images and the impedance signals in real-time.	141
Figure 41. Morphological characterization of the manufactured inkjet-printed interdigitated electrodes with a passivation on top using optical microscopy and an optical profilometer. a) Optical micrography of the inkjet-printed sensors (scale bar 100 μm). b) Surface profilometry of two continuous inkjet-printed electrodes revealing a thickness of a 0.6 μm for bare Ag electrodes. c) Morphological profile of two continuous fingers in the interdigitated electrodes passivated with three layers of SU8 revealing a thickness of 4 μm	144
Figure 42. Morphological characterization of the interdigitated electrodes manufactured by inkjet printing using Scanning Electron Microscopy. a) SEM micrography of the inkjet-printed sensor surface in a top view (scale bar 200 μm). b) Transversal view of the inkjet-printed sensors (scale bar 50 μm) revealing a thickness of 38 μm in the printed layers	

- on top of the substrate. c) and d) Effect of UV curing on the outermost layer of the SU-8 showed an increase in the smoothness of the outmost layer. UV treated samples showed a smoother surface (d) compared with non-treated samples (c). 145
- Figure 43.** Electrical characterization of the inkjet-printed sensors by impedance spectroscopy. Sensors were characterized before (pristine) and after being functionalized with collagen, and after performing *in vitro* cultures of HaCaT cells. The measurements were performed at 37 °C, 5 % CO₂, and 2 mL of culture medium. The left plot shows the magnitude of the impedance (a) and the plot on the right shows the phase angle (b). 147
- Figure 44.** Cytocompatibility characterization of the inkjet-printed sensors and the sensor-based unit to perform the impedance spectroscopy. a) Live/Dead assay on the HaCaT cell line after 3 days of culture. Distribution of live and dead cells of a total of 60 images of areas around different electrode sites on the IDEs. The error bars represent the observed standard deviations. b) Fluorescence image of the surface of two consecutive fingers of the electrodes (scale bar 100µm). Living cells can be seen in green while red spots identify dead cells. Due to the non-transparency of the conductive lines (AgNP), stained cells can be observed only on the gaps between the interdigitated electrodes as the sample was illuminated from below. 149
- Figure 45.** Cytocompatibility characterization using SEM. (Top left) An SEM top view of the inkjet-printed sensors covered by a confluent monolayer of HaCaT cells (scale bar 1mm). (Top right) A zoom-in on the electrodes confirmed that when stained cells are observed using the Live/Dead assay on the gaps they were also present over the opaque electrodes (scale bar 100 µm). (Bottom) The image (scale bar 20 µm) demonstrates the adherence of the cells to the surface of the sensors. 150
- Figure 46.** Monitoring of cell proliferation through the temporal variation of the impedance. a) Micrography of the samples with different initial cell densities of 12 000 cells/cm²; 35 000 cells/cm², 75 000 cells/cm² and 130 000 cells/cm² on collagen-coated IDE-based devices. The green-fluorescent HaCaT-GFP cells were observed only over the gaps of the interdigitated electrodes since the opacity of the conductive electrodes makes it unable to observe the samples over the complete surface of the sensors. b) Monitoring of the cell index values versus time in hours associated with HaCaT-GFP cell adhesion and proliferation over 96 h. Differences in the cell index value were obtained for different initial cell densities. For an initial density of 75 000 cells/cm² the maximum in the cell index value is attained at 72 h which suggests that the cell culture reached confluence. At low initial cell density (12 000 cells/cm²) changes in the impedance are almost inappreciable over the experimental period. The maximum value in the cell index for each sample is obtained at different time points, which was associated with differences in the time for cultures initially seeded with different densities to reach their confluence. In other words, the time to reach the maxim value in the cell index is inversely proportional to the cell density initially seeded. 154
- Figure 47.** Cell index versus initial cell density at 5 h obtained using the samples initial seeded with 35 000, 75 000 and 130 000 cells/cm²(error bar represents the standard deviation, n=3). Samples with initial cell densities of 12 000 cells/cm² were not included since the value remained almost constant even after 69 h which was interpreted to be under the sensitivity limit of the device. 156
- Figure 48.** Study of the influence of the electrical isolating properties of the cellular membranes on the impedance changes. a) Cell index values versus time in minutes

during 25 minutes after adding Triton X100 at the endpoint of the proliferation assay (the moment when the cell index value measured was around 1.4 units in culture medium). Triton X100 is a non-ionic detergent that physically disrupts the cellular membranes of the culture. b) Micrography of one cell culture of HaCaT-GFP at 23 min after adding Triton X100 to 0.1 %. The changes in the impedance correlated with the disruption of the cellular membrane since the detergent did not detach the cells from the surface of the sensors. 158

Figure 49. Equivalent circuit model for the sensors and sensing process to study cell detachment. a) Equivalent electrical circuit to fit the experimental data resulting from a non-faradic analysis of the system cells/sensor. The effects of the different electrolytes were modeled using resistances, this is, R_c for the culture medium and R_s for the metabolic results. Cells' electrical response was modeled using a CPE and the geometrical capacitance of the interdigitated sensors as a capacitor C_g . b) Schematic modeling of the physical interaction between the cell and the surface of the sensors. The current flows are associated with the capacitive behavior of the IDEs and must pass through the culture medium. When the cells cover the sensor the impedance increases. 161

Figure 50. Nyquist plot to monitor cell-sensor adhesions over 80h. a) Real part and imaginary part of the impedance are plotted at each time point of the experiment. At time 15h the adherent cells (negatively charged) yield a surface impedance greater than the impedance at time 80h. b) Example of the fitting of the experimental data using the electrical circuit model proposed. 163

Figure 51. Analysis of the cell-sensor adhesions using microscopy observation and impedance-based monitoring. a) Nyquist plot and cellular images at time 23 h b) and time 80 h. It is observed that in some areas of the sensors at time 23 h the number of cells attached to the surface is more than at time 80 h. Consequently, the diameter of the semicircle lying in the Z' axis, associated with the value of R_s , reduces. (scale bar in the images 100 μm) 165

Figure 52. Monitoring of cell migration by time-lapse microscopy. a) Examples of the time-lapse of the cell monolayer migrating over the IDE-based devices and control (Petri dish). b) Mean-edge displacement of a monolayer of cell cultures in the experimental groups versus time in minutes during the time-lapse observation. The velocity in the cell migration resulted in 0.35 $\mu\text{m}/\text{min}$ in controls and 0.3 $\mu\text{m}/\text{min}$ in the IDEs-based groups calculated from $v = \frac{\Delta \text{Displacement}}{\Delta \text{Time}}$ as explained in 3.3.3.2. 167

Figure 53. Monitoring of cell migration by impedance spectroscopy. a) Relation between the mean edge displacement determined by image processing and the cell index by impedance-based analysis versus time in minutes. b) Cell index units versus the recovery degree of the wound showing a linear correlation ($R^2 = 0.89$). 168

Figure 54. Skin receptors and transducing process. Schematic of the types and location of the mechanoreceptors in the skin tissue: slow adapting receptors, SA-I and SA-II; fast adapting receptors, FA-I and FA-II. SA-I complex is in the basal layer (SB, stratum basalis) of the epidermis, appears in clusters of cells and responds with high-resolution to static forces which may help in the spatial images of tactile stimuli. FA-I afferents are localized in the dermal papillae (SS, stratum spinosum) and their responses detect movement across the skin. SA-II endings are localized deep in the dermis and have been associated with slow thresholds responses when skin stretches. FA-II corpuscles are located in the dermis and they detect high-frequency vibrations. The ensemble output

- generated by the mechanoreceptors inputs the neural system which ultimately interprets and processes the information and generates a translation. SC, stratum corneum; SG, stratum granulosum; SS, stratum spinosum; SB, stratum basalis. Figure adapted from Abraria and Ginty, 2013.³⁴⁴ 183
- Figure 55.** Cell mechanoreceptors and transduction process. A representation of how a local force applied externally to the cells (from the extracellular matrix, ECM) travels to the nucleus. A force is applied to integrins through the ECM which is concentrated at the focal adhesions. The channel that connects the integrins to the cytoskeleton of the cell is through proteins embedded in the plasma membrane that end up in Talin. The filamentous F-actin is bundled by α -actinin and tensed by myosin ii generating a prestress. In the cytoskeleton F-actins and microtubules (MTs) are connected through actin-crosslinking factor 7 (ACF7) while F-actins and intermediate filaments (IFs) are connected through plectin. Plectin also connects IFs to MTs and IFs connect to the outer nuclear membrane through Nesprin 3, and in turn, to SUN1 and SUN2 on the nuclear envelope. Nesprin 1 and nesprin 2 connect F-actin to the inner nuclear membrane protein SUN1. The SUN proteins on the nuclear envelope connect to Lamina A in the nuclear scaffold, which could connect through matrix attachment regions (MARs) to chromatin and DNA. Nuclear actin, myosin, and titin might help to regulate nuclear prestress. Thus, the force channeled into the nuclear scaffold might affect gene activation within milliseconds due to the stress wave propagation. By contrast, a growth factor in the plasma membrane takes seconds to alter nuclear functions by chemical cascades of signaling mediated by chemical diffusion or motor-based translocation. LINC, linker of nucleus and cytoskeleton; rRNA, ribosomal RNA. Figure adapted from Wang et al., 2009.³⁴⁶ 185
- Figure 56.** A nano topography technique for mechanical stimulation of cells in a static fashion. a) Microfabricated pots to be used as cellular substrate. b) An individual cell lying on a micro dimensional array of nanopillars. c) Cell monolayer spread on the nanopillars. (C inset) Magnification of the area delimited by the black square. Adapted from du Roure et al., PNAS, 2005.³⁶² 188
- Figure 57.** Schematic representation of the actuating system to perform dynamic stimulation on cell cultures. 190
- Figure 58.** a) Custom-made piezoelectric actuating device to dynamically stimulate cell cultures. b) Manipulation of a biocompatible actuator device integrated into a cell culture of an epithelial cell line inside a biosecurity cabin. The stage is compatible to perform experiments in the standard conditions of a tissue engineering laboratory. c) Samples to perform the cellular studies. Controls were fabricated lacking the piezoelectric material using a Petri dish a cellular substrate with a ring of PDMS. Controls material were static devices fabricated identically than the dynamic samples, but not electrical energy was applied. Dynamic samples were electrically stimulated to transmit mechanical stimulation to the cell cultures. 192
- Figure 59.** Schematic representation of the actuating system to mechanically stimulate cell cultures. The system consists of an experimental stage (actuating device), a custom electronic stage to configure the electrical parameters to input the piezoelectric actuator, and an incubator to keep physiological conditions in the cell culture. The system allows real-time modification of the dynamic mechanical stimulation of cells. 193
- Figure 60.** Interferometric system for the characterization of the polymeric piezoelectric-based device to cyclically oscillate the cellular substrate. a) Vibrometer using a common

path fiber optical topology (CPT). b) Actual layout for the experimental characterization of the piezoelectric actuating device using the CPT vibrometer. 199

Figure 61. a) Linear relation of the piezoelectric mechanical displacement to an increasing input voltage at frequencies of 100 Hz, 300 Hz and 1 kHz. b) Dynamic mechanical deformation of the PDVF-based device vs. the applied frequency. Very small differences between the response of collagen-coated devices and uncoated devices are observed. 200

Figure 62. Cytocompatibility results for a total of $n = 28$ control cultures (CC) and $n = 25$ static control samples (SC). No statistical significance was detected in the experimental group compared with the control cultures and thus it can be stated that the designed and fabricated actuating devices are biocompatible. 206

Figure 63. Proliferation assay (AlamarBlue (AB)) performed using a monolayer of HaCaT keratinocyte cells stimulated continuously with a frequency of 1 Hz for 8 days. The curve represents the values of the calculated absorbance (percent reduced) of the AB dye in the control cultures (CC), static controls (SC) and dynamic samples (FR). Statistical analysis showed highly significant differences ($p < 0.001$) in the experimental samples stimulated at 1 Hz compared with both controls (i.e., static devices and control cultures) at day 6 and 8. Note that day 0 represent 24 h after seeding the cells. 207

Figure 64. Proliferation assay performed on a monolayer of HaCaT keratinocyte cells stimulated continuously with a frequency of 1 Hz for 8 days using AlamarBlue (AB). The curve represents the values of the fluorescence of the AB dye in the control culture (CC), static control (SC), and dynamic (FR) samples. Statistical analysis showed that the samples stimulated at 1 Hz were metabolically more active compared with both controls (i.e., static controls and control cultures) since day 1. Note that day 0 represent 24 h after seeding cells. 208

Figure 65. Visual inspection of the cell cultures of HaCaT keratinocytes cells expressing green fluorescent protein (GFP) in their nucleus using a fluorescence microscope at day 1 and day 5 during the proliferation assay. A) Photomicrograph of one control culture (CC) sample at day 1. B) Photomicrograph of one CC sample at day 5. C) Optical image of one static control (SC) at day 1. D) Fluorescence image of one SC without mechanical stimulation at day 5. E) Stimulated sample at 1-Hz frequency at day 1. F) Photomicrograph of one sample continuously stimulated with 1 Hz at day 5. (Scale bar: 100 μm). 209

Figure 66. Proliferation assay of a monolayer of HaCaT cells stimulated continuously with a frequency of 80 Hz for 6 days using AlamarBlue (AB). The curves represent the values of the absorbances of the AB dye in the control (black line), static (green line), and dynamic (pink line) samples. 210

Figure 67. Proliferation assay of a monolayer of HaCaT keratinocytes cells stimulated continuously with a frequency of 80 Hz for 6 days using AlamarBlue (AB). The bars represent the values of the fluorescence of the AB dye in the control (black bars), static (green bars), and dynamic (pink bars) samples. Note that day 0 represent 24 h after seeding cells. 211

Figure 68. Visual inspection of the cell cultures of HaCaT keratinocytes cells expressing green fluorescent protein (GFP) in their nucleus was observed using a fluorescence microscope at day 1 and day 5 in the proliferation assay for the 80 Hz excitation frequency. A) Photomicrograph of one control culture (CC) sample at day 1. B) Photomicrograph of one CC sample taken at day 5. C) Image of one static control (SC) at day 1. D) Image of one SC

- device at day 5. E) Stimulated sample at 80-Hz frequency at day 1. F) Photomicrograph of one sample continuously stimulated with 80 Hz at day 5. (Scale bar: 100 μm)... 212
- Figure 69.** Wound healing progression in control cultures and static controls. The upper figure shows cell migration of cells in control-culture (CC) samples while the one in the bottom the cell migration of cells in static-control (SC) samples (i.e., cell seeded on static devices but without stimulation). The scratch is completely closed at 27.9 h in CC samples while it takes 28.8 h in SC samples. Total of samples: $n = 9$ CC, $n = 9$ SC in three experiments. 214
- Figure 70.** Wound closure progression in dynamic samples stimulated with 1 Hz (upper figure) and 80 Hz (lower figure). The scratch is completely closed after 24 h in 1-Hz samples and after 30 h in 80-Hz samples. Total of samples: $n = 9$ for 1Hz, $n = 9$ for 80Hz in three repetitions. The blue dashed lines in the curves show the confidence interval and the brackets the error bars which cannot be shown when the size is shorter than the size of the symbol (i.e., triangle for 1 Hz and circle for 80 Hz). 215
- Figure 71.** Fluorescence micrographs of the scratch progression in a control (C) and experimental groups seeded on the actuator-based device stimulated at 1 Hz and 80 Hz at different time points. Qualitatively, cell migration in the samples dynamically stimulated at 1 Hz shows a faster rate of the scratch closure. 217
- Figure 72.** SEM images of control and experimental group samples. Differences in the area and projections in the dynamically excited samples compared to the static controls are observed. Non-significant differences are observed between samples of the control group, i.e., images A and B, at $t = 48$ h. However, cellular morphology is different between control group and the 1 Hz excited samples (image C) and 80Hz excited samples (image D). In the image C (1Hz) the cells show cytoplasmic projections and a more condensed nucleus at 48 h. On the other hand, the morphology of cells stimulated with 80Hz was rounded at 48 h. Length scale: 20 μm 219
- Figure 73.** Immunostaining assay for the study of the effect of the dynamic mechanical stimulation on the cellular morphology. Merged images of f-actin stained with phalloidin Alexa Fluor® (red) and nuclei stained with DAPI (blue) at 48 h of treatment of dynamic mechanical stimulation. A) Control-culture samples seeded on Petri dishes. B) Static control of cells grown on the actuating device under static conditions (no excitation). C) 1-Hz excitation group. D) 80-Hz excitation group. 221
- Figure 74.** Nucleus' sizes normalized to control-culture samples at 48 h obtained through the processing of the DAPI images. (Number of nuclei, $n > 300$). 222

List of Acronyms and Abbreviations

The following acronyms and abbreviations are used throughout this dissertation. The acronyms and abbreviations are not always defined to avoid interruption of the text. If the meaning of a term is not obvious to the reader, it will be found in this list.

OD	Zero-Dimensional	DMEM	Dulbecco's Modified Eagle Medium
1D	One-Dimensional	DMSO	Dimethyl Sulfoxide
2D	Two-Dimensional	DOD	Drop-on-demand
3D	Three-Dimensional	E.g.	Exempli gratia
AB	Alamar Blue	ECG	Electrocardiogram
AgNW	Silver Nanowires	ECIS	Cell-Substrate Impedance Sensing
ANOVA	Analysis of Variance	ECM	Extracellular Matrix
BSA	Bovine Serum Albumin	EIS	Electric Impedance Spectroscopy
CCD	Charge-coupled Device	EMG	Electromyogram
CIJ	Continuous Inkjet Printing	Et al.	Et alia
CNT	Carbon Nanotubes	Etc.	Etcetera
CMOS	Complementary Metal-Oxide Semiconductor	FBS	Fetal Bovine Serum
CPE	Constant Phase Element	GFP	Green Florescence Protein
DAPI	4',6-Diamidino-2-Phenylindole Dihydrochloride	HaCaT	Spontaneously Transformed Human Epithelial Cell Line
DC	Direct Current		

I.e.	Id est	SBS	Styrene-Butadiene-Styrene
IDE	Interdigitated Electrodes	SiNW	Silicon Nanowires
IFC	Impedance Flow Cytometry	SWNT	Single-Walled Carbon Nanotubes
LED	Light-emitting Diode	RFID	Radio-frequency Identification
MEA	Metal Multielectrode Array	Tg	Glass-transition Temperature
NP	Nanoparticle		
OOC	Organ-on-a-chip		
P3HT	Poly(3-Hexylthiophene)		
PANI	Polyaniline		
PBS	Phosphate Buffer Serum		
PDMS	Poly (Dimethyl) Siloxane		
PEDOT: PSS	Poly(3,4-Ethylenedioxythiophene)-Poly(Styrene Sulfonate)		
PEN	Polyethylene Naphthalate		
PET	Polyethylene Terephthalate		
PI	Polymide		
PL	Parylene		
PMMA	Poly(methyl Methacrylate)		
PU	Polyurethane		
PVA	Polyvinil Alcohol		
PVDF	Polynvinylidene Difluoride		
SEM	Scanning Electron Microscopy		



■ I. DISSERTATION
SUMMARY

*Para ver las cosas de cerca
conviene alejarse un poco.*

Miki Naranja

CHAPTER I. Dissertation Summary

1.1. MOTIVATION OF THE WORK

Skin loss and damage caused by severe burns, chronic ulcers, surgeries, and other genetic/acquired skin disorders require rapid and proactive medical treatments. As the skin is our primary protective barrier to the surrounding, severe-skin injuries can be a major source of infection and may lead to multiple complications including osteomyelitis, edema, and sepsis, often associated with mortality. Annually, the incidence of acute-skin trauma that requires medical treatment is estimated to 6 million patients worldwide with at least 1 % leading to death.¹

One of the essential steps in preventing mortality and morbidity in patients suffering from some of these skin injuries relies on an early excision of the wound's site followed by proper coverage. To cover and thus repair such acute or chronic wounds several clinical approaches have been explored, being methods based upon synthetic-skin substitutes with biological but not living components one of the most extensively used. As many of these synthetic-skin substitutes are commercially available, they

are often a preferred choice for the clinical treatment of such injuries to restore the epidermal barrier function and control water losses.² Unfortunately, in scenarios where there is a deep-partial or full-thickness skin loss these methods lack efficacy, leaving skin grafting as the recommend, preferred, and often exclusive surgical intervention.³ Among all types of skin grafting, the autologous graft (a split-thickness of the patient's skin transplanted from a non-damaged area into the damaged region) remains the current gold standard since it avoids patient's immune rejection. Regrettably, for skin injuries involving an extended surface area, own-patient donor sites from which to harvest an autograft are limited. These limitations have led researchers to explore new approaches for skin replacement based on cellular therapies and tissue engineering.¹

As a result, significant progress in the development of sophisticated dermo-epidermal substitutes has been achieved by tissue engineering techniques. Compared with passive dressing (synthetic-skin substitutes), tissue engineering-based therapies have demonstrated to improve clinical and functional outcomes in burn patients⁴ and are compatible with rapid three-dimensional (3D) biofabrication,⁵ including the possibility of *in situ* real-time bioprinting.⁶ However, one of the main issues remaining in the field is the ability to monitor such engineered skin substitutes either during their fabrication or once they have been transplanted. Current clinical practice for assessing both the fabrication and eventual transplant of such laboratory-growth skin grafts relies on professional surveillance and immunohistochemical testing. Unfortunately, these assessed methods not only involve both subjective judgments and examinations for short periods which may jeopardize patients' physiological states,⁷ but they also led to samples' destruction. To overcome these major burdens a wound-healing technology

in form of smart bandages has appeared as a promising alternative. In this technology, different types of (bio)sensors are integrated into a synthetic bandage to monitor the injury while keeping the wound bed or implant sealed.⁷⁻⁹ Although those systems are optimized to operate in the unique environment of wounds (*id est* (i.e.) deformable, soft, wet, and warm) and provide data for wound assessment,⁹ they are incapable of serving as natural components to viably replace the skin loss, this is, they cannot fulfill simultaneously the twofold function of biologically regenerating and electrically monitoring of the damaged tissues.

To tackle this inability of treating such damaged skin tissues actively, some approaches have incorporated drug-delivery systems into the wound care dressing. Drug delivery technologies incorporated in most of those existing dressings, however, are passive, which means that the profile or permeation rate of these drugs released into the tissue is pre-designed and cannot be controlled externally.¹⁰ As the physiological understanding of both the clinical heterogeneity of wounds and dynamical changes of the status of wounds advances, clinicians have been increasingly demanding the possibility to vary the release quantities and kinetics of such drugs on the fly.¹¹ The utilization of anti-inflammatory drugs, antibacterial compounds, or antibiotics at improper times and doses can hinder healing processes and can lead to the development of antibiotic resistance.¹² Fortunately, some smart bandages have incorporated on-demand drug delivery systems to precisely control the temporal and spatial profile of the administered drug in response to external stimuli.^{13,14} However, these active drug delivery systems not only are limited to a few examples, but they also are expensive, with inherently drug side-effects, and often deliver therapeutics only to superficial layers of the skin where the dermal dressings are placed.

Incorporating dermo-epidermal skin equivalents as part of electronic devices or, the other way around, integrating bionic devices (sensors and actuators) as non-biological components within laboratory-growth skin substitutes would encompass the multiple functions of 1) biologically regenerating the lost tissue and restoring the organotypic functions, 2) electrically monitoring the status of the implant from within and 3) drug-free stimulating the engineered tissue when needed. This groundbreaking innovation for the treatment of wounds and skin losses would unleash the accomplishment of what we introduce as *living smart bionic skin substitutes* (Figure 1).

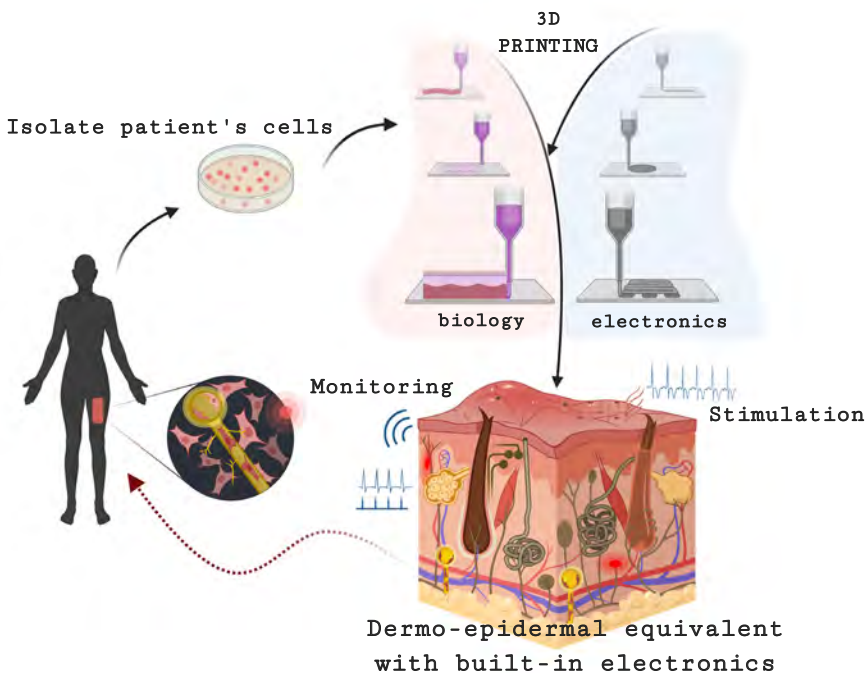


Figure 1. Concept of living-like bioelectronics as bionic skin substitutes.

The integration of the electronic devices into an engineered skin substitute for the assessment of skin grafting would thus merge concepts from tissue engineering for regenerative medicine and bioelectronic technology. To fabricate such cyborg organotypic skin tissues, a deviation from electronic fabrication methods to pattern devices and integrate living components in a single, programmable, hybrid platform with a palette of functional inks is necessary. Additionally, the technology should be adaptable to moderate-volume production, compatible with personalized medicine (i.e., for using patient-specific cells, biomaterial and wound-covering needs) and economical.

This envisioned technology to bring engineered dermo-epidermal substitutes with built-in electronics to research is not yet available. In recent years, however, unprecedented progress has been achieved in the endeavor of interfacing electronics with soft and complex biological tissues, which has opened the path towards embedding electronics into skin substitutes. We briefly introduce some of these works in the next section.

1.2. INTERFACING ELECTRONIC DEVICES WITH BIOLOGICAL TISSUES

Bioelectronics involves the union of electronic devices with biological systems (from single cells to complex tissues) with the aim to monitor or modulate biological outcomes or both.¹⁵ Two examples of bioelectronic devices that interface with biological systems are patch-clamp technology,¹⁶ which has been long used to understand the mechanisms of the electrical activity of neural cells, and metal multielectrode arrays (MEAs),¹⁷ which have been used to record electrophysiological signals from

isolated cells, tissues and organs without impairing them. Other bioelectronic systems that have been shown to record and deliver signals from within cells are, for example, those based on electrodes with three-dimensional complex morphologies¹⁸ such as mushroom¹⁹ and silicon nanowires (SiNW) field-effect transistors (FET).²⁰ Although these works have been increasingly closing the gap between tissue-electronics interactions, helping in the understanding of many cellular behaviors, they have conventionally relied on standard silicon-based electronics which have lacked in the contemplation of the physical and mechanical mismatch between rigid electronics and the fragile target tissues.

Cells and tissues are several orders of magnitude softer than the standard electronic materials and typical substrates and we must be aware that cells respond to the mechanical properties of the surfaces they interface.²¹ By contrast, most of the bioelectronic devices have been traditionally stiff and static while the natural mechanical compliance of biology calls for softer interfaces. Novel strategies have thus been devised to overcome this mechanical mismatch, allowing not only a proper electronic communication with and within tissues, but also a harmless and intimate interface (Figure 2).

One of these approaches has borrowed materials from the classical microelectronic technology and has endowed electronics malleable by using novel geometries either in the substrate used or in the electrodes themselves. Another alternative has involved the manufacturing of electronic devices with new engineered stretchable materials that render them soft and elastic. Exploiting either of those two general approaches, advanced electronic systems have been engineered to interface conformally to the human body. The skin, as an obstructed organ, has become a perfect platform to test and laminate such systems for applications such as health care monitoring, medical rehabilitation programs, and biological studies.

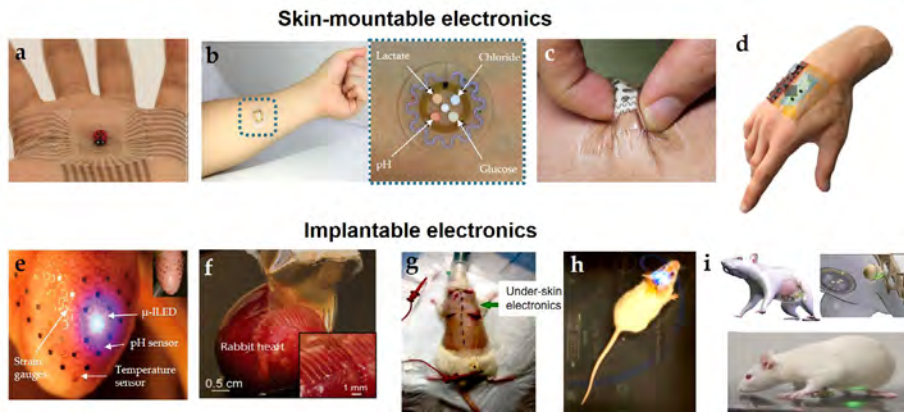


Figure 2. Flexible and stretchable electronics interrogate, wrap, and conform around complex tissues on and into the human body. a) A photograph of an array of intrinsically stretchable transistors conformally adhered to a human palm. The array enables sensing the position of a synthetic ladybug by a multiplexing measurement and a matched map of the on-current magnitudes of the resistive tactile sensors. b) An epidermal microfluidic sensor mounted on a human forearm. The device collects and stores sweat during exercise to monitor different biomarkers based on colorimetric measurements. A wireless interface enables data transfer to a smartphone that captures and analyses data. c) Optical images of a wearable sweat-analysis patch with a transdermal drug-delivery module. The system adheres to the skin and resembles most of the skin's properties, allowing a compliance interface even under deformation. d) Multifunctional electronic-skin (e-skin) fabricated with naturally derived ingredients that enable a soft and stable, but fully biodegradable hydrogel-based system. The on-skin-worn electronic patch measures temperature, humidity, and strain and integrates a reusable electronic module to record, analyze, and transmit the data wirelessly. e) Silicon-based flexible device of serpentine filaments wrapping around a Langendorff-perfused rabbit heart. Different functional elements are highlighted inside the picture. f) Novel material-based device of an intrinsically stretchable electrode array conforming to the surface of the superior right ventricle of a rabbit heart *via* surface tension. The system enables *in vivo* electrophysiological mapping of atrial fibrillation. g) Biodegradable strain and pressure sensors implanted subcutaneously on the back of a Sprague-Dawley rat for long-term monitoring of tendon-healing. The devices were able to operate stably over 2–3 weeks *in vivo* after implantation. h) Freely moving mouse with an implanted bioresorbable spectrometer for the continuous monitoring of brain oxygenation, temperature, and neural activity. The device is injectable and is fabricated using materials that naturally undergo clearance from the body after its operational lifetime. i) A wireless closed-loop system implanted between epidermal skin and muscle in the abdominal cavity of a mouse. The miniaturized bio-optoelectronics implant exploits inorganic light-emitting diodes to opto-activate light-sensitive proteins (opsins) in the bladder together with a sensing system based on strain gauge to monitor the organ function (i.e., bladder filling/voiding). Note. Reproduced from (a) Wang, Bao, *et al.*, 2018; (b) Koh, Rogers, *et al.*, 2016; (c) Lee, Kim, *et al.*, 2017; (d) Baumgartner, Kaltenbrunner, *et al.*, 2020; (e) Xu, Rogers, *et al.*, 2014; (f) Liu, Bao *et al.*, 2020; (g) Boutry, Bao, *et al.*, 2018; (h) Bai, Rogers, *et al.*, 2019; (i) Mickle, Rogers, *et al.*, 2019.

For example, using novel intrinsically stretchable materials, Bao and co-workers have reported the development of a skin-like, stretchable, polymer-based transistor array with a high-density and performance, able to adhere and conform to the skin²² (Figure 2a). Alternatively, Rogers' research group has reported the integration of diverse electronic components based on silicon and conventional microelectronic materials in diverse applications such as sweat monitoring²³ (Figure 2b). Combining both strategies, Kim and co-workers have fabricated a sweat-based monitoring device with a transdermal drug-delivery module²⁴ (Figure 2c), whereas Kaltenbrunner and co-workers have recently introduced an edible electronic system with resilient yet entirely degradable gelatin-based hydrogels²⁵ (Figure 2d). These new classes of electronic devices laminated externally to the skin are often referred to as electronic skin, epidermal electronics, or electronic tattoos. Although advances in these new form factor of electronics have overcome the main issues of the mechanical mismatch between tissues and electronics, two distinguished characteristics remain in those systems: They have required the existence of the organ meant to interface (i.e., skin) and they have been tested onto healthy skin tissues externally, as a second layer.

As an alternative to on-skin-worn electronics, various types of flexible and stretchable electronic sensors and systems have been fabricated to withstand the topographical constraints of the organs into the body. Beneath the skin, these implantable electronics have allowed interfaces to soft and complex tissues' surfaces such as blood vessel lumen,²⁶ cardiac epicardia,²⁷⁻²⁹ brain parenchyma,^{30,31} and sciatic nerve³² without interfering the organ's functions (Figure 2e-i). For example, Boutry, Bao *et alia* (et al.) reported under-skin, implantable, pressure and strain sensors made entirely of biodegradable materials to monitor the mechanical forces on ten-

dons for orthopedic applications³³ (Figure 2g). They fabricated the sensors with a biodegradable metal (magnesium Mg) and established biodegradable polymers and tested them *in vivo* with immobilized mice (Figure 2g). Using freely moving mice, Rogers and co-workers showed a bioresorbable photonic device made of conventional electronic materials (*exempli gratia* (e.g.) monocrystalline silicon and silicon oxide SiO₂) for the spectroscopic characterization of physiological processes³⁴ (Figure 2h) and optogenetic modulation³⁵ (Figure 2i). These examples demonstrate the significant advances that have been achieved in soft bioelectronics interfacing organs on and into the body, this is, on the skin and under the skin.

Yet when such bionic devices are implanted into the body two major issues remain. First, even the softest and most compliant electronic device is recognized as foreign to the tissues, which causes an inflammatory response that often walls off the device in a scar capsule of cells.^{36,37} In other words, such electronic systems are tolerated by the body rather than seamlessly integrated. Second, human tissues uninterruptedly undergo micro-motions due to respiratory pressure, blood flow, or tissue healing, which may create an unstable contact between electronics and the interfaced tissue, affecting the electronic measurements. In other words, such electronic devices are microscopically decoupled from their anchoring tissue.

To overcome these limitations, a new paradigm for bioelectronics has evolved —tissue-like bioelectronics— in which the electronics are laden with cells to improve the integration of the implant while allowing a proper electronics interrogation of the tissue's functions from within. Lieber's group pioneered this hybrid approach in the development of a cardiac-patch tissue.³⁸ They integrated a sensory system based on silicon nanowires field-effect transistors (SiNW FET) within different biomaterials

such as electrospun fiber mat and hydrogels for seeding cardiomyocytes. They showed the ability to monitor the electrical activity of the cardiac cultured tissue from within as well as to monitor the pH. In a similar approach, an electronic network of either gold³⁹ or platinum⁴⁰ electrodes was integrated into a porous biomaterial not only to monitor but also to control the direction of the electrical signal through the engineered cardiac tissues spatiotemporally (Figure 3a,b). By depositing biomolecules onto electroactive polymer-based electrodes,³⁹ it was possible to release drugs to the tissue from within in a highly controlled fashion.

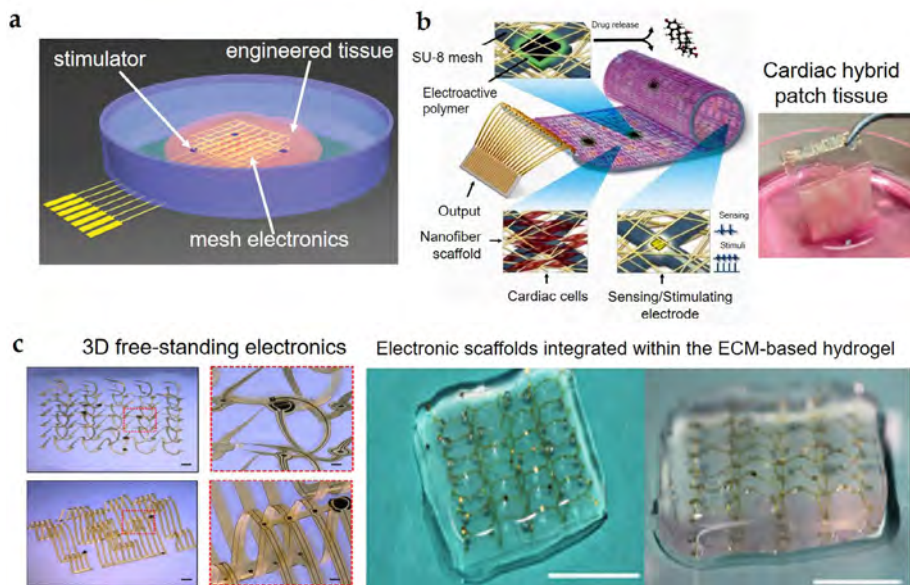


Figure 3. Tissue-like electronics. a) Macro-porous mesh electronic scaffolds with silicon-nanowire field-effect transistors and platinum electrodes integrated into cardiac tissue of cardiomyocytes. b) Mesh device with gold electrodes for sensing of tissue electrical activity, and electrically stimulate the cells and tissue (right). The device incorporates electroactive polymer to release drugs and small molecules that may promote tissue growth. The electronics are integrated within a scaffold of electrospun nanofibers of SU-8 that support tissue cultures. In the left plot is observed an image of the hybrid cardiac patch. c) 3D free-standing electronics as a scaffold for tissue cultures (right) and the electronics embedded into extracellular matrix-based hydrogels for culturing cardiomyocytes. Note. Images reproduced from (a) Dai, Lieber, *et al.*, 2016; (b) Feiner, Dvir, *et al.*, 2016; (c) Wang, Rogers, *et al.*, 2020.

In this hybrid-tissue direction, two groups have recently gone a step forward using biodegradable dielectric materials for the substrate of the device (serving as scaffolds for culturing cells): Lee, Someya, *et al.* using electrospun fibers of the synthetic polymer polyvinyl alcohol,⁴¹ and Feiner, Dvir, *et al.* using fibers of the natural protein albumin.⁴² In both examples, the electrodes were evaporated onto the electrospun nanofibers through a shadow mask, creating the electronic-based scaffolds for culturing cardiomyocytes. The researchers showed the possibility to record extracellular potentials, stimulate the cells electrically, and release anti-inflammatory drugs.

In this scenario, the precise control of the 3D distribution of the electronic devices into the tissue requires a different type of fabrication. Wang, Dvir, Rogers, *et al.* have introduced a device with a pre-designed 3D complex architecture embedded into a thermoresponsive extracellular matrix-based hydrogel prepared from a decellularized omentum for culturing cardiomyocytes (Figure 3c).⁴³ The strategy for the fabrication of the electronic device is based on bonding the electrodes in specific regions to a pre-stretched elastomer that leads to a 3D engineered structure in the electrodes once the elastomer is released. Cells were mixed inside the hydrogel and seeded onto the porous electronic structure that served as a substrate. Due to the nature of the hydrogel that solidified at physiological temperatures of 37 °C, this strategy allowed the formation of a functional hybrid engineered cardiac tissue. Using this 3D electronic device, it was possible to electrically stimulate the tissue, record electrophysiological potentials, and release drugs from within the engineered cardiac tissue controlling both the distribution and functionality of the electronics.

The manufacture of soft, living, completely implantable bioelectronic systems has not been demonstrated yet. Nonetheless, the design rules and strategies enumerated above are allowing the research community to engineer hybrid tissues and electronic implants with unprecedented biological integration and electronic capabilities. Some of these systems can be even syringe-injected into the tissues, allowing a minimally invasive approach for implantable electronics.⁴⁴⁻⁴⁶ However, some limitations remain for these bioelectronic technologies to be used in pioneering living bionic skin substitutes. First, biology —from nanometer proteins to macroscopic organs/tissues— is temperature sensitive and three-dimensional which renders the electronic manufacturing technology exploited for fabricating most of those devices incompatible with current bio-fabrication techniques. Second, the concept of drug release is not always sufficient to induce cellular responses once they are liberated. It is known the ability of cells to respond to mechanical stimuli and self-induce reactions⁴⁷ yet it has been sidelined and therefore less studied as an alternative to the conventional chemical treatment. Finally, most of the solutions for interfacing electronics with biological systems presume the existence of the organ or tissue, which regrettably, do not contemplate the scenario of skin loss. These remained issues motivate the study in this thesis of alternative approaches in the fabrication, methodology and application of sensor/actuator devices to cellular tissues to pave the way towards the envisioned concept of living bionic skin substitutes.

To envisage a bioengineered organotypic skin with built-in electronics, a detailed understanding of skin architecture is first required. In the next section, we shall see an overview of the structure and main functions of the skin tissue.

1.3. UNDERSTANDING THE SKIN TISSUE

All surfaces of our body (internal and external) are clad in cellular layers named epithelia. Epithelia are classified as simple epithelium when it contains a single cellular layer and as stratified epithelium when it comprises multiple layers of cells. Different superimposed layers of these epithelial tissues shape what is often said to be the largest organ in the human body: the skin.

Skin is physically the end of an organism and the beginning of the remaining, external world. Stripped from such a barrier, living beings can no longer survive. The most important role of the skin is therefore to create an obstacle for the world outside the biological system. Internally, the skin shelters organs; externally, it protects the whole organism against the environment. Hermetically sealed, life would be impossible because an organism develops in continuous, two-directional communication with its surroundings. So, the barrier which protects, must also allow the exchange of stimuli of different nature such as chemical, thermal, and mechanical. Thus, skin plays a key role in several biological functions such as thermal regulation, prevention of fluid loss, and metabolism. These features also render skin an ideal surface for an unobstructed gate to important biological metrics, serving as a diagnostic platform for health care monitoring (Figure 4).

Macroscopically, skin encompasses a surface area of ~170-200 cm² and accounts for about 16 % of the total body weight.⁴⁸ Although it appears smooth and continuous, the outermost layer of the skin exhibits wrinkles and shallow/deep grooves with feature sizes of 15-100 μm in amplitude

and 40-1000 μm in width.⁴⁹ These apparently unimportant creases and pits that mark polygons in the tissue are essential for permitting the skin to stretch. They also may concentrate forces onto the skin's mechanoreceptors and provide more contact area for sensory perception.⁵⁰ Skin houses other constituents such as hairs and nails and contains invisible outlets of the sweat glands. Skin shows a linear elastic response to stress until 15 %, non-linear behavior until 30 %, and irreversible effects beyond.⁵¹ These interesting biomechanical properties of the skin are due to its viscoelasticity. The first lineal response is primarily due to the alignment of the elastin fibers in the dermis and the reorientation that suffer collagen fibers upon applied mechanical stress. Once the collagen fibers reach their maximum length, the force required to deform the tissue must be increased, explaining such a non-linear behavior. The skin responds to a deformation time-dependently,⁵² which is observed in its hyperplastic response (i.e., the stress required to maintain the skin at a certain length decrease over time).

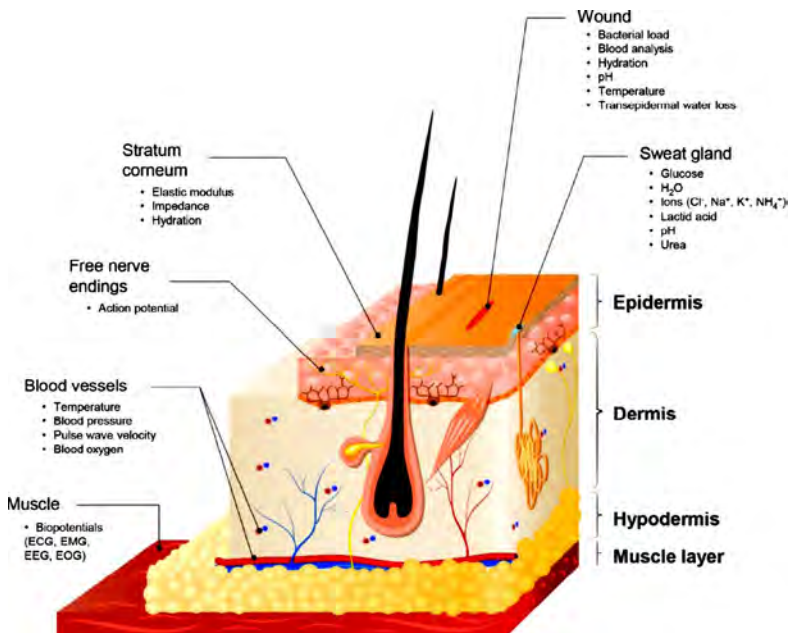


Figure 4. Sketch of the skin tissue describing its structural layers and the signals and parameters accessible from the skin. Note: image modified from Liu, Salvatore *et al.*, 2017.

Microscopically, the complex structure of the skin is divided into three anatomical and functional layers: a superficial epidermis, a middle dermis, and a deeper hypodermis (Figure 4). The interfollicular epidermis is the outermost stratified squamous epithelium (flattened cells of stratified epithelium) in contact with the environment. The thickness of the epidermis ranges from 0.05 mm (on eyelids) to 1.55 mm (on palmoplantar regions). The major cell that comprises the epidermis is the keratinocyte (90-95 %) and the other 5 % includes melanocytes, Langerhans cells, and Merkel cells. These different types of cells overlap in a well-defined manner, conformingly four sublayers named (from deep to superficial) stratum basale, stratum spinosum, stratum granulosum, and stratum corneum. The homeostasis of the epidermis relies upon the continuous shedding of dead cells and replacement by newly differentiated cells every 28 days.⁴⁸ The dermis is a tough and resilient layer, supporting the thinner epidermis. It is bounded externally by the epidermis and internally by dermal adipose tissue. Depending on the body site, dermal thickness varies between 0.3 and 3.0 mm. It comprises a dense matrix of specialized structures and the most abundant cells are fibroblasts, which synthesize collagen and elastin fibers. Finally, the hypodermis is mainly composed of adipocytes and connects the skin to subjacent organs.

In conclusion, the skin is soft yet tough, it retains yet exchanges. This intrinsic balance of biomechanical properties and functions endows skin with its unique features. In turn, it has challenged the use of traditional rigid and bulky electronics and imposed several limitations for skin-mountable or implantable electronic devices.

1.4. OBJECTIVES OF THE THESIS

To pave the way for engineering a far-reaching yet ambitious living bionic dermo-epidermal substitutes with advanced, non-biological (i.e. sensing and actuating) functionalities, this thesis deals with the integration of sensors and actuators into a simple model of skin tissue based on a single layer of a cell line of keratinocytes for real-time monitoring/configuration of the electronic measurement and actuation.

Combining different sensors and actuators with engineered tissues to create organ-on-a-chip (OOC) systems has shown to be a valuable platform to mimic organs for biological studies and rapid pharmacological testing.⁵³ However, OOC devices cannot be transplanted into the body: implantable applications require free-standing electronic devices able to in real-time monitor and actuate. Thus, to achieve the vision described above the sensors/actuators need to be engineered allowing their future integration with laboratory-growth skin equivalent.

To pursue these goals, first, we propose moving from conventional microtechnology for the manufacturing of the sensors in a way to support the eventual fabrication of sensorized living tissues concomitantly, using techniques compatible with bioprinting. Second, we explore the use of electro-active actuators to induce cellular responses as an alternative to the classic chemical treatment, enabling future control over tissue's function and behavior electronically. The proposed actuators and sensors must be flexible, thin, and biocompatible; electronic performance must be fulfilled over a long period of time;

cell monolayer of keratinocytes must be retained viable and biologically functional, and the system needs to be easy-to-use and cost-effective. Considering such requirements for these two research lines, the objectives of this thesis are:

- **To develop a sensing system to monitor an epithelial cell culture in real-time by using additive manufacturing techniques.** The achievement of this objective includes the following sub-goals:

- To develop flexible sensors by inkjet-printing technology using polymeric (biocompatible) substrates.
- To characterize the morphological, electrical, and biocompatible properties of the developed inkjet-printed sensors to assess their feasibility to monitor cell cultures.
- To integrate inkjet-printed sensors into a monolayer of epithelial cells and develop an electronic platform to perform real-time long-term cellular experiments.
- To validate the proposed sensing system in the measurements of some cellular processes that are relevant to organotypic skin cultures using a simpler biological model.

- **To develop an actuating system to stimulate dynamically an epithelial cell culture by using organic piezoelectric materials.** The pursuit of this goal addresses the following sub-objectives:

- To fabricate biocompatible ultrathin organic-based actuator devices using polymeric piezoelectric materials.

- To characterize the electromechanical and biocompatible properties of the developed actuator devices to assess their feasibility to dynamically stimulate cell cultures.
- To integrate biocompatible ultrathin actuators into a monolayer of epithelial cells and develop an electronic platform that allows performing long-term cellular experiments and configuring the electroactive actuator embedded in the cell culture in real-time.
- To study the effects of the dynamical stimulation on cellular responses in some processes relevant to organotypic skin cultures using a simpler biological model by testing the organic actuator.

1.5. STRUCTURE OF THE DISSERTATION

This thesis describes the integration of sensors and actuators into an epithelial cell culture for paving the way towards achieving bionic skin substitutes. The subsequent chapters present methodology, design criteria, fabrication, characterization, and validation of the proposed systems based on biocompatible flexible sensors/actuators. The remained sections are thus organized with the following structure.

CHAPTER II Flexible and stretchable electronics reviews the basics concepts of flexible and stretchable electronics throughout its most relevant developments and applications. First, strategies and design rules to endow electronics flexible and stretchable are presented. Then, manufacturing techniques for developing flexible electronic systems are reviewed to introduce the novel additive manufacturing technique of inkjet printing. This chapter concludes with the limitations that underline the work carried out in this thesis.

CHAPTER III Materials and Methods describes materials and methods to develop and characterize both sensing and actuating systems, as well as protocols and assays used to evaluate the two proposed systems in biological scenarios using a monolayer of cells.

CHAPTER IV Development of printed flexible sensors for cellular studies demonstrates the fabrication and characterization of flexible sensors by inkjet printing and their integration into a two-dimensional epithelial cell culture. It investigates the use of impedance spectroscopy to monitor non-invasively and in real-time cellular proliferation, migration, and cell-sensor adhesions. Impedance spectroscopy has been explored for decades to characterize biological cells and tissues, but the use of flexible printed sensors for cell-substrate impedance sensing has been less studied. The system presented in this chapter: a) supports the low-cost inkjet printing technology as an emerging yet competitive fabrication technique for compelling and high-technological applications and b) demonstrates that impedance measured across flexible ink-jetted sensors detects in real-time cellular behaviors relevant to organotypic skin cultures. The integration of the sensors into the cell cultures

also represents an initial step towards engineered-skin substitutes with smart embedded sensors.

CHAPTER V Development of a novel actuating system for cellular studies demonstrates the fabrication and characterization of a novel electromechanical device based on an organic, printing compatible, piezoelectric polymer of polyvinylidene difluoride (PVDF), and their integration into a two-dimensional epithelial cell culture. The effects of stimulating dynamically the cell cultures are investigated entailing cellular proliferation, migration, and morphology. The system presented in this chapter: a) supports the research of the cellular mechanotransduction, b) stimulates cells *via* dynamic variations of the cellular substrate, and c) allows the study of whether such external-regulated stimulations are of significance for cellular behaviors relevant to organotypic skin cultures and eventually, regenerative medicine. The system also represents an initial step towards engineered-skin substitutes with smart embedded actuators.

Finally, **CHAPTER VI General conclusions and future work** summarizes the key contributions of this research that steer the conclusions of the dissertation and suggests future directions to continue studies drawn from this work.

A graphical overview of the remained chapters of this thesis is provided in Figure 5.

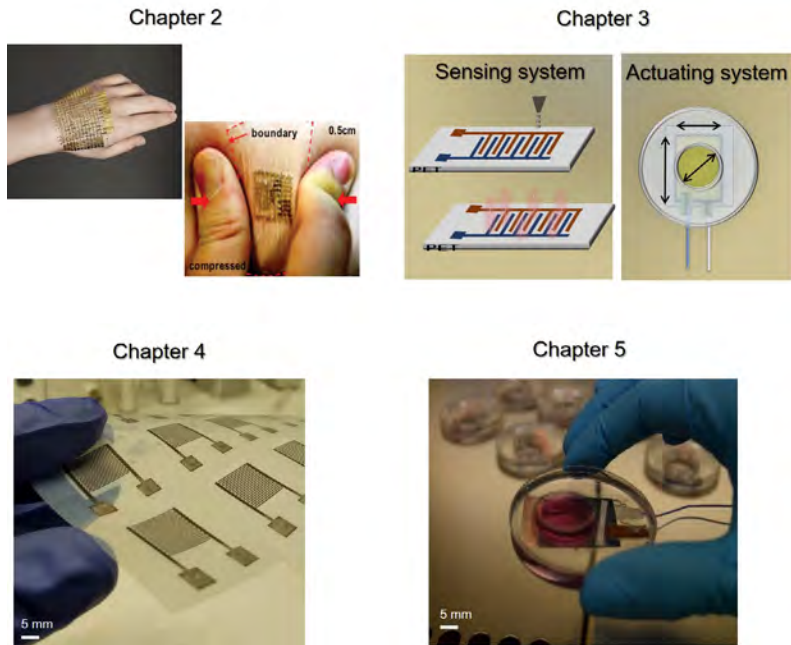
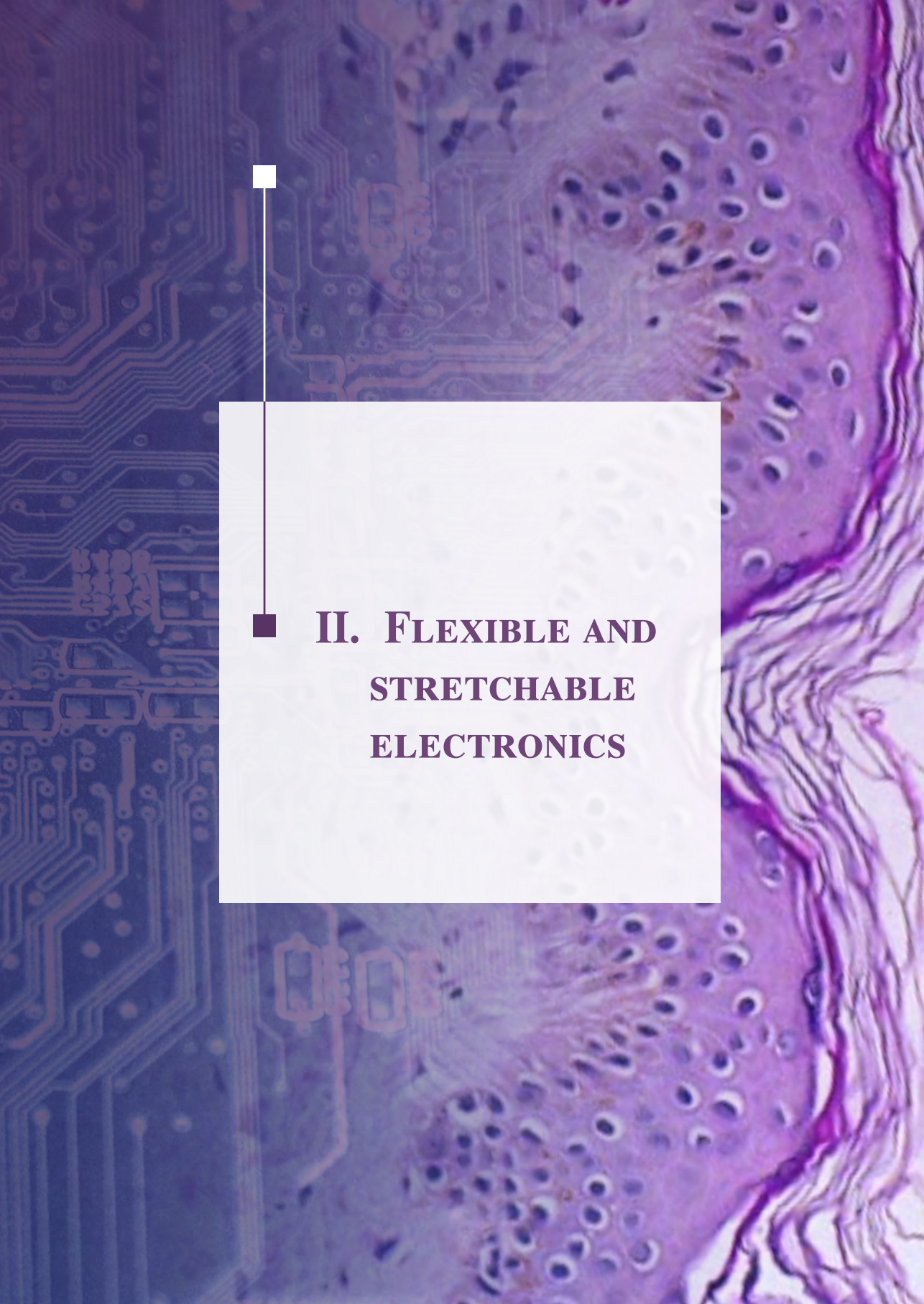


Figure 5. Graphical overview of this dissertation. Chapter 2 reviews the basic concepts that endow electronics flexible and malleable. Chapter 3 describes the materials and methods used for developing both the sensing and actuating systems, and for their characterization. Chapter 4 demonstrates a sensing system embedded into a monolayer of epithelial cell layer to monitor cell-substrate impedance as an indicator of cellular states. Chapter 5 demonstrates an actuating system embedded into cultured epithelial cells to influence cellular outcomes by (dynamic) mechanical stimulations.

1.6. THESIS FRAMEWORK

The main works presented in this thesis have been conducted in the facilities of the Universidad Carlos III de Madrid with support from the program Formación del Profesorado Universitario FPU015/06208 granted by Spanish Ministry of Education, Culture and Sports. Some of the work has been also developed in the facilities of the Fraunhofer-Institut für Zuverlässigkeit und Mikrointegration (IZM) and University of Applied Sciences (HTW) in Berlin, under the supervision of Prof. Dr. Ing. H-D. Ngo during a research visit funded by the Mobility Fellows Program by the Spanish Ministry of Education, Culture, and Sports.

This work has been developed in the framework of the projects BIOPIELTEC-CM (P2018/BAA-4480), funded by Comunidad de Madrid, and PARAQUA (TEC2017-86271-R) funded by Ministerio de Ciencia e Innovación.



■ II. FLEXIBLE AND STRETCHABLE ELECTRONICS

Creo firmemente en la flexibilidad.

Miki Naranja

CHAPTER II. Flexible and stretchable electronics

2.1. BACKGROUND

Softness, lightness and flexibility may dominate the future metrics of a new generation of electronic devices. Roughly twenty years ago an unconventional vision of electronics unleashed some tentative approaches of flexible circuits fabricated on bendable sheets of plastic.^{54,55} Unprecedented progress has since then been attained to turn electronics not only from stiff and bright to flexible and elastic, but also into imperceptible,⁵⁶ epidermal⁴⁹ and breathable.⁵⁷ Such ultralightweight⁵⁸ and extreme mechanical properties have allowed for a wide range of applications spanning from environmental harvesting⁵⁹ to biomedical systems, from food quality monitoring⁶⁰ to implants.^{61,62}

Being able to seamlessly integrate and mechanically match electronics with the human body and living tissues is still under development, yet an active scientific activity worldwide has brought malleable forms of wearable electronic interfaces mainly in two ways: on-skin sensors and systems for healthcare monitoring, and electronic skins (e-skin) for soft robots and virtual reality.

Strategies to yield circuits the ability to be stretched, twisted and deformed in complex shapes include two —conceptually different— general routes:^{63,64} 1) devising new structural designs using conventional materials and 2) developing new materials in conventional layouts. Two simple yet key engineering points underline within the first route.^{65,66} First, aggressively scaling the thickness of an object enables flexibility by decreasing the flexural rigidity (i.e., the resistance of a material to bending) to the third power, which was predicted in the Euler-Bernoulli beam theory. Thus, in concept, nearly all kind of materials (even hard and brittle silicon) sufficiently thin can achieve a flexible mechanical behavior. Second, placing the active layer of the circuit at the neutral mechanical plane —in the out-of-plane location upon strain— reduces the bending-induced strain, in other words, by positioning the active electronics away from the surface of the substrate (where the bending strains are largest) to deeper regions within the substrate (where mechanical strains are reduced).

Research has also sought compelling solutions for on-skin sensors and e-skins by developing new intrinsically stretchable materials^{67,68} that range from nanomaterials to elastic-conductive composites. Not missing a single feature of living organisms, efforts have further engineered self-healing materials^{69,70} that will soon allow, with additional properties like biodegradability,^{71,72} the development of very sophisticated, technically challenging, bio-inspired electronic systems that can closely behave like their archetype.

In this chapter, we shall see these two mentioned strategies of flexible and stretchable electronics throughout the description of its most relevant development and applications. First, we review the strategies based on structural designs (section 2.2), next, we give an overview of those material-based routes (section 2.3). Later, we describe the manufacturing techniques for developing

flexible and stretchable devices and systems (section 2.4) to eventually introduce the state-of-the-art of the novel additive manufacturing technique of inkjet printing (section 2.5). Research is just beginning to explore ways to utilize such developed techniques and electronic devices in biomedical applications and thus, before closing (section 2.6), this chapter concludes with an outlook and future challenges of these bioelectronic systems within this context.

2.2. FROM EARLY FLEXIBLE ELECTRONICS TO BREATHABLE SENSORS BY STRUCTURE-BASED APPROACHES

Conventional materials devised in novel geometries have yielded electronics the ability to be flexible and elastic. The malleability does not rely on whether the material is soft or elastic, brittle or tough, inorganic or organic, but mostly on the geometry and structure of the device, on its weight and dimensions. This section 2.2 reviews the main mechanical principles that have become key points for the design of flexible circuits and how researchers have harnessed this knowledge to fabricate many of the current skin-imperceptible electronic systems.

Flexible electronics were born out of scientific curiosity, but their widespread use was not immediately anticipated. The concept of thin-film field-effect transistors, firstly introduced as early as 1962,⁷³ forms the basis —and, perhaps, the primary building blocks— of the modern flexible electronics. As the apex of space exploration grew out in the political climate in the mid-1960s, technical requirements of solar cells with

improved power-to-weight ratios were launched into the scientific community. Light and flexible solar panels⁷⁴ were surprisingly well fabricated by then, meeting such practical specifications, but setbacks and oblivion throve,⁷⁵ and it was just before turning the millennium when milestone contributions^{76,77} would show transistors on steel foil, with thickness raging down to 3 μm , able to bend around a pencil (Figure 6a). Since then, bending radii of electronic circuits have been further reduced reaching, for example, an impressive radius of curvature of 35 μm (the size of a human hair) for the photovoltaic organic solar cell⁵⁸ with the highest ratio of power to mass (23 W/g) to date, without device failure (Figure 6b).

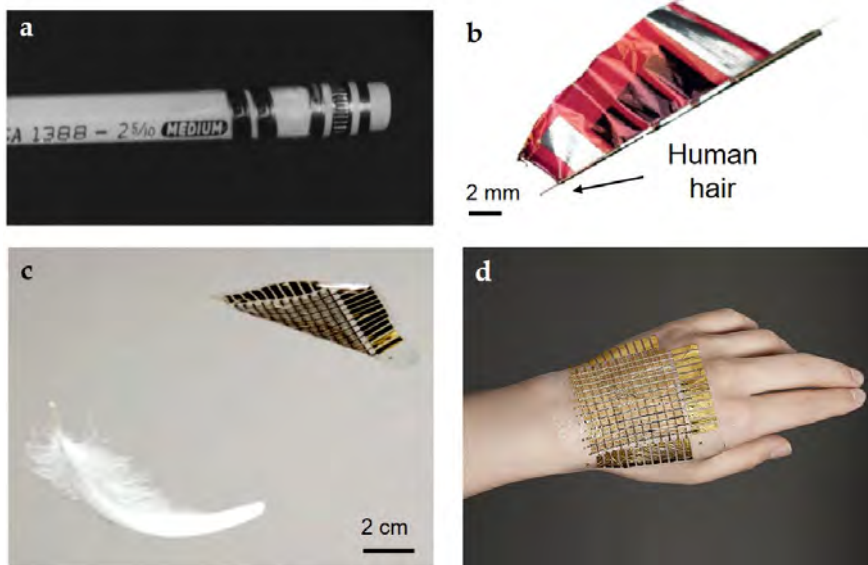


Figure 6. Progress in flexible electronics. a) Thin-film transistor (TFT) of hydrogenated amorphous silicon was fabricated on top of stainless-steel foils with thickness from 3 μm to 20 μm . A 25- μm -thick TFT wrapped around a pencil.⁷⁷ b) Extreme bending flexibility of a polymer-based photovoltaic device on 1.4- μm -thick poly(ethylene terephthalate) foils, wrapped around a human hair with a radius of 35 μm without impairing its functionality, this is, a specific power of 23 W/g.⁵⁸ c) Birth of imperceptible electronics by fabricating 12 \times 12 active-matrix array (8 \times 8 cm) with resistive tactile sensors on ultrathin (1 μm) plastic foils (poly(ethylene naphthalene), PEN), with extremely lightness of 3 g/m² allowing them to float to the grown more slowly than a feather⁵⁶, crumple like a paper, and d) conform to human skin.

Mechanical strain (i.e., a unitless parameter to describe physical deformation) occurs when a device is deformed or bent, causing not only modification in the dimension and shape of the device, but also altering its electrical performance. As a straightforward example, capacitance expressed as $C = \kappa A / d$ changes when either area A or thickness d vary, assuming the dielectric permittivity κ as a constant. Many other electrical properties of electronic materials are sensitive to stress (e.g., mobility of electrons within a semiconductor, etcetera (etc.)). Then, how can such electronic devices withstand extreme mechanical flexibility while their functional properties are unaffected by the straining process? Two factors mainly account for the feasibility of such devices. To appreciate the first factor, let us start with equation (1) which reveals the mechanical compliance relation of two materials one deposited on top of the other. (see Figure 7)

$$\frac{\epsilon_s}{\epsilon_f} = \frac{E_f h_f}{E_s h_s} \quad (1)$$

where ϵ , h , and E are the strain, thickness, and Young's modulus of the active film (f) and the substrate (s) respectively.

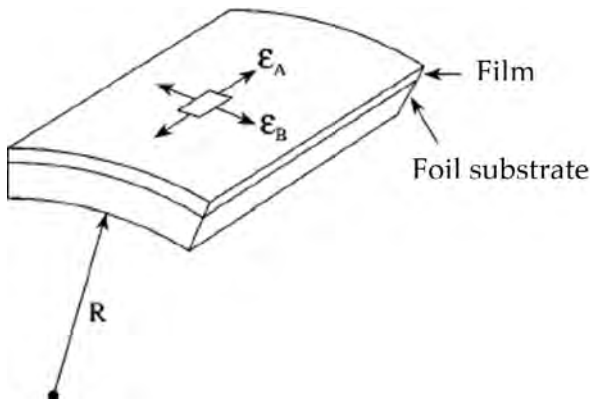


Figure 7. Bending of a film-on-foil structure into a radius R . The externally applied bending causes mechanical strain in the film ϵ in each axis resulting in a matrix of values. The film on top of the substrate has a thickness h_f while the underneath material h_s .

From the relation in equation (1) the mechanical stress in the active electronic layer ϵ_f directly loads from the Young's modulus-thickness product $E_s \cdot h_s$ of the substrate.^{76,77} Should the $E_s \cdot h_s$ product be low, the strain in the active electronic layer ϵ_f will be effectively offloaded from the bottom substrate. Clearly, the only way to lower the $E_s \cdot h_s$ product without altering the bulk properties of the substrate material itself, this is, without changing to a more compliant material with a lower Young's modulus E , is reducing its thickness. With this, the strain in the active electronics layer is reduced and therefore not only mechanical but also electrical degradation due to stress is minimized. The thickness of the substrate in the development of flexible electronics plays a key role in withstanding the minimum allowable bendability.

The second factor comes from the radius of curvature. According to the Euler-Bernoulli beam theory for a bending process of a sheet film, a strain is maximum on the film surface and no strain is present at the mechanical neutral plane, that is, at the exact center of the structure (in the bending direction). The peak value of the strain (imposed on the apex of the surface) can be approximated by the equation $\epsilon_{max} = h/2r$ (*) under certain assumptions,^{78,79} where h and r are the thickness of the film and the radius of curvature, respectively. Moreover, whether the sheet film is analyzed as a thin plate (i.e., when deflection experienced is larger than the thickness),⁸⁰ flexural rigidity D can be described as $D = \bar{E}h^3$ (**), where \bar{E} is the plane-strain modulus of the film given by $\bar{E} = E/(1-\nu^2)$ (here ν is the Poisson's ratio and E the elastic modulus) and h the thickness. From either of those analytical approaches, we can extract a cubic dependence of flexural rigidity on the thickness (**), and a linear relation of the thickness with bending radius (*). Reducing both the total thickness of the device and positioning it at the neutral strain plane the effect of

mechanical stress is diminished and the overall mechanical tolerance before failing is enhanced.

Manufacturing such functional devices challenges many fabrication issues⁶⁵ and may require complex mechanical models,⁸¹ simulations,⁸² and detailed mathematical analysis^{83,84} other than the basic ones given above, yet the general concepts are indeed stacked simple. This is how *imperceptible electronics* were born out: employing ultrathin plastic films as a substrate when scientists were squeezing the question of “how thin can electronics go?”. In 2012, Kaltensbrunner, Someya, *et al.* fabricated tactile sensors⁵⁶ with a total thickness of 2–3 μm , a weigh of 3 g/m^2 , and a bending radius down to 5 μm marking the birth of a whole new world for soft electronics (see Figure 6c,d).

Flexible displays, flexible large-area electronics and electronic textiles are just a few examples of applications that remain out of reach of wafer-based electronics and directly benefit from imperceptible electronics. Yet to mimic our moist, dynamical and stretchable biology, electronics not only must be able to bend but also to stretch to accomplish a complete conformability and compliance with our natural features. For instance, mammalian skin can elastically undergo strains up to ~15–30 %⁴⁹ and ~100 % at joints,^{85,86} exchange gases, nourish and maintain a moisture level, self-heal, and even self-clean (the outermost cell layer of epidermis shed from stratum corneum when they reach the surface over about 28 days).⁸⁷ To bring electronics a step closer to our soft, movable biology, an extended, a complementary form of electronics was required and research turned towards what has become known as *stretchable electronics*.

When circuits are made on plastic films (flexible electronics), the deformation they can experience is permanent (i.e., within the linear plastic curve of the plastic foil that serves as substrate). When they are made on elastomeric substrates, the deformation can go beyond within a reversible elastic behavior offering superior mechanical compliance. Once, Lacour, Wagner *et al.* fabricated elastic electrical conductors evaporating thin films of gold (100-nm thickness) onto pre-stretched elastomeric membranes of poly(dimethyl) siloxane (PDMS) (1-mm thickness).⁸⁸ A spontaneous wrinkling structure whose amplitudes were parallel to the substrate was induced in the gold films when the pre-strain in the membrane was released. Such stretchable wrinkling gold wirings exhibited good electrical performance (negligible variation in the resistance conductivity under an applied strain) and low mechanical fatigue simultaneously. Since this work, the buckling and wave formation of thin films driven by a pre-strained substrate not only has been considered as the born of stretchable electronics, but it also has been adopted as one of the main approaches to endow electronics with high levels of stretchability. Technical examples ranging from individual devices (e.g., transistors) to integrated systems (e.g., bio-inspired eye cameras)⁸⁹ have been developed by using such a wavy pattern-based strategy. When this buckling approach makes use of imperceptible electronics (i.e., ultra-flexible electronics laminated onto a pre-stretched elastomer) (Figure 8a,b), advanced devices and electronic systems with attractive mechanical attributes and high operating functionalities have been achieved⁹⁰⁻⁹²

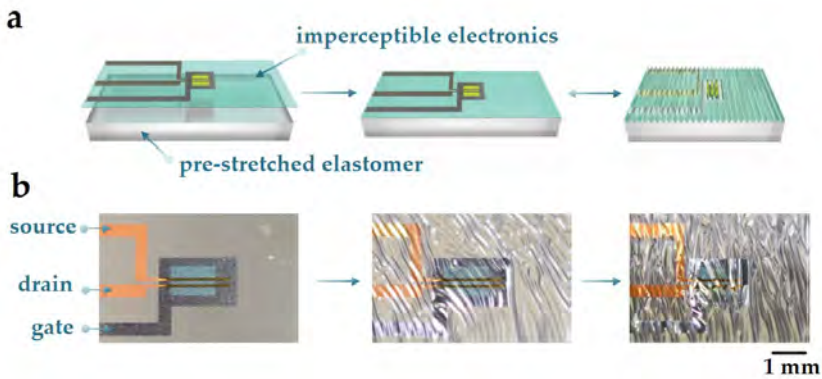


Figure 8. Stretch-compatible ultra-flexible electronics. a) Illustration of the process to laminate an imperceptible electronic foil (3- μm thick) on a pre-stretched elastomer (3M VHB) by picking and placing. When the prestrain in the elastomer is relaxed, the electronic foil forms out-of-plane wrinkles enabling subsequent tensile strains without impairing the functionalities in the device. b) Picture sequence of a one-step pick-and-place transfer, and the formation of folds in an organic field-effect transistor when the elastomer is relaxed. Source and drain were fabricated with gold while aluminum serves as the gate electrode; a hybrid aluminum oxide and phosphonic acid self-assembled monolayer as gate dielectric, and DNTT (dinaphto[2,3-b:2',3'-f] thieno[3,2-b] thiophene) as an organic semiconductor. Note a) and b) modified from reference ⁵⁶.

Such wrinkling patterns are abundantly found in nature by the same principle: an out-of-plane motion of thin layers to accommodate strain experienced in the plane. For instance, “waves” of our skin can be revealed due to a delicate ultrathin film (epidermis) on top of a soft thicker substrate (dermis). In electronics, the buckling formations can be mathematically analyzed by a sinusoidal profile of an out-of-plane displacement. When the energy of the total strain is minimized (i.e., the simplest possible scenario), buckled structures can be described by the wavelength (λ_0) and amplitude (A_0) of such a deformation (equations in (2)).

$$\lambda_0 = \frac{\pi h_f}{\sqrt{\epsilon_c}} = 2\pi h_f \left(\frac{\bar{E}_f}{3\bar{E}_s} \right)^{1/3}, \quad A_0 = h_f \sqrt{\frac{\epsilon_{pre}}{\epsilon_c} - 1} \quad (2)$$

where the subscripts f and s refer to the film and the substrate, respectively; \bar{E} is the plane-strain modulus $\bar{E} = E/(1-\nu^2)$, with ν denoting the Poisson's ratio and E the elastic modulus; h denotes the thickness; $\epsilon_c = (3\bar{E}_s/\bar{E}_f)^{2/3}/4$ is the critical strain to trigger the buckling; and ϵ_{pre} is the pre-strain.

Although the detailed physics for analyzing wrinkling patterns in electronic devices may be non-trivial,⁸² resulting response in the buckled structure resembles those of an accordion bellows under an applied strain.⁹³

From the relations expressed in (2), the following conclusions can be extracted. In stretchable electronics thickness remains as a critical parameter—the wavelength and amplitude of the wavy formation can be controlled by the thickness (lineal relation)— and amplitude depends lineally on the prestrain. Unfortunately, experimental observations of silicon ribbons on elastomeric substrates showed that large prestrain (i.e., $\epsilon_{pre} > 5\%$) in rubbers conducted to a nonlinear behavior in the wavelength and amplitude of the wrinkling, leading to a low fracture level.⁸² Besides this, and unlike bonding isolated ribbons or conductive connectors, achieving interconnections or other elements to obtain a complete electronic system directly bonded on an elastic substrate is prohibitively difficult when inorganic materials are used.⁹⁴ Alternative configurations⁹⁵ using non-bonded regions between the nanoribbons and the substrate and more accurate analytical models⁹⁶ of the wavy structures have yielded devices experience considerable strain (e.g., 100%)⁹⁵ with materials that are intrinsically brittle and exhibit much lower fracture limits.

One major challenge when dealing with electronics-human tissue interfaces arises from the mechanical mismatch between the Young modulus of conventional electronic materials and those found in our body (see Figure 9a). Main representative structure-based strategies that have tackled the issue to integrate hard (e.g., 1000 GPa for graphene) and soft (e.g., 200 Pa for brain tissue) materials in the development of *flexible* and *stretchable* electronic devices are provided in Figure 9b-d. They are named wavy/wrinkled design (introduced above) (Figure 9b), island-bridge design (Figure 9c), and Origami/Kirigami-inspired design (Figure 9d). A key strategy here has involved the optimization of new and complex geometries by using conventional materials. This path may branch out further into two main categories depending on the materials used, this is, i) organics⁹⁷ or ii) inorganics,⁹⁴ each of which holds their own merits and disadvantages regarding the manufacturing processes (e.g., organic carbon is compatible with large-area electronic fabrication, but shows poor electronic properties) and electrical performances (e.g., inorganic crystalline silicon exhibits well-established high electronic performance, yet allows modest modification to conventional fabrication techniques).

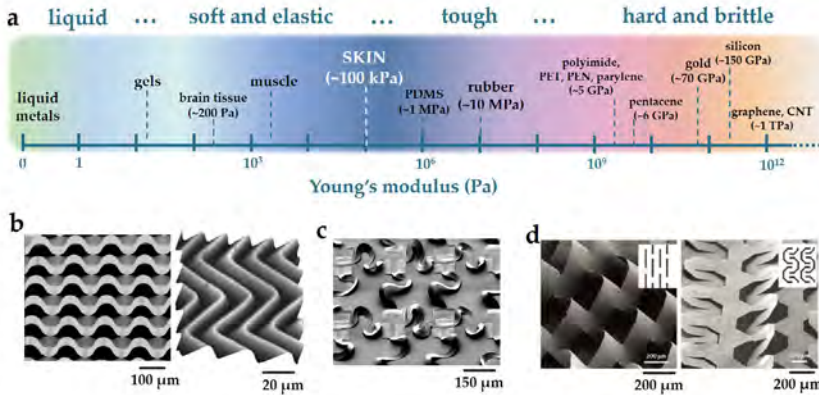


Figure 9. Strategies in flexible and stretchable electronics. a) Difference between elastic moduli of conventional electronic materials and soft matters found in our body. Most typical materials used are highlighted ranging from elastomers, polymers for substrates to liquid metals, conductors, and semiconductors for active layers. Note: sketch modified from reference⁶⁴. b) Wavy/wrinkly design of an array of gallium arsenide nanoribbons (left) in wavy shapes bonded to a PDMS membrane pre-stretched to 50 %, where the bond occurs only at the positions of the troughs by chemically patterning the PDMS substrate with UV light,⁹⁵ and (right) AFM image of silicon membrane (100-nm thickness) bonded to a piece of rubber (PDMS pre-stretched to 3.8 %) allowing a biaxial strain.⁹⁸ c) Island-bridge concept for stretchable electronics, where functional components usually reside on the islands and interconnect form the bridge. The island consists of CMOS inverter transistors interconnected by non-coplanar serpentine structures.⁹⁹ d) Two examples of Origami/Kirigami-inspired design that renders stretchability by adding cuts at selected locations. The strategy has mostly been exploited for stretchable batteries, but a Kirigami-based multifunctional patch has recently been demonstrated.¹⁰⁰ In the image, the microscale patterns were fabricated with graphene oxide/PVA nanocomposites, allowing strains up to 370 % at a device level.¹⁰¹

Not all stretchable, structure-based strategies exploit the out-of-plane motion (examples shown in Figure 9b-d are all out-of-planes). Building in-plane stretchable circuits significantly increases the range of stretchability in electronic devices.¹⁰² Coiled- and leaf-arm springs,¹⁰³ fractal-inspired designs,¹⁰⁴ and S-shaped structures are some examples of geometries that involve in-plane motions (with a rotation similar to that of scissors) to accommodate strains in electronic devices and systems. Among in-plane geometries, a serpentine structure is one of the most effective used at both an individual device and an integrated system level.^{26,105} A

reference strategy among structure-based implementations has been to place the circuit devices on platforms (islands), pattern high-performance nanomembranes into in-plane stretchable geometries with fractal-inspired layouts (e.g., filamentary serpentine) as bridges to interconnect the islands (to absorb strain by local bending and twisting), and then transfer the integrated system to ultrathin elastomeric substrates.¹⁰⁵⁻¹⁰⁸

Rather than being drawn from the trend of Moore's Law¹⁰⁹ and shrinking critical dimensions of functional elements to ever increase the number of transistors, the emerging field of flexible, stretchable electronics has leveraged a much different direction. It has sparked new electronic systems and ways to integrate them into our lives. Indeed, only ten years ago Kim, Rogers, *et al.* introduced an electronic system⁴⁹ with a thickness of $\sim 30 \mu\text{m}$, a reversible elastic response $>30\%$, and an effective modulus of $\sim 150 \text{ kPa}$ in a gas-permeable elastomeric sheet as a new class of biotic/abiotic interface. The system exploited ultrathin layouts, neutral mechanical plane configurations, and filamentary serpentine nanoribbons of silicon and gallium arsenide (i.e., established inorganic electronic materials with higher Young's modulus than the interfacing tissue). Such an electronic system not only was intentionally engineered to resemble the main, and unique, properties of our skin, but also was named after such an organ. It was sharply defined as *epidermal electronics* (Figure 10a-d).

Epidermal electronics has since made unstoppable, great strides. Not only has it enabled a paradigm shift in electronics, but also has fostered innovation in biomonitoring and health care applications. Only in the medical arena, skin-interfaced electronic systems monitor wound healing,⁹ temperature,^{86,106} blood oxygenation,^{91,110} and all types of electrophysiological signals in standard clinical care (e.g., heartbeat rate, respiration rate, ECG,¹⁰⁵

EMG,¹¹¹ etc.). Besides accurate measurements quite equivalent to those of the existing tethered rigid sensors, such systems offer extra features such as non-invasiveness, wireless operation, and comfort; all features that beyond being desirable in certain applications such as point-of-care or fitness tracking, may turn out invaluable in others such as neonatal and pediatric critical care,¹¹² or in a pandemic outbreak (e.g., the recent Covid-19) with wireless mechano-acoustic sensing epidermal systems.¹¹³

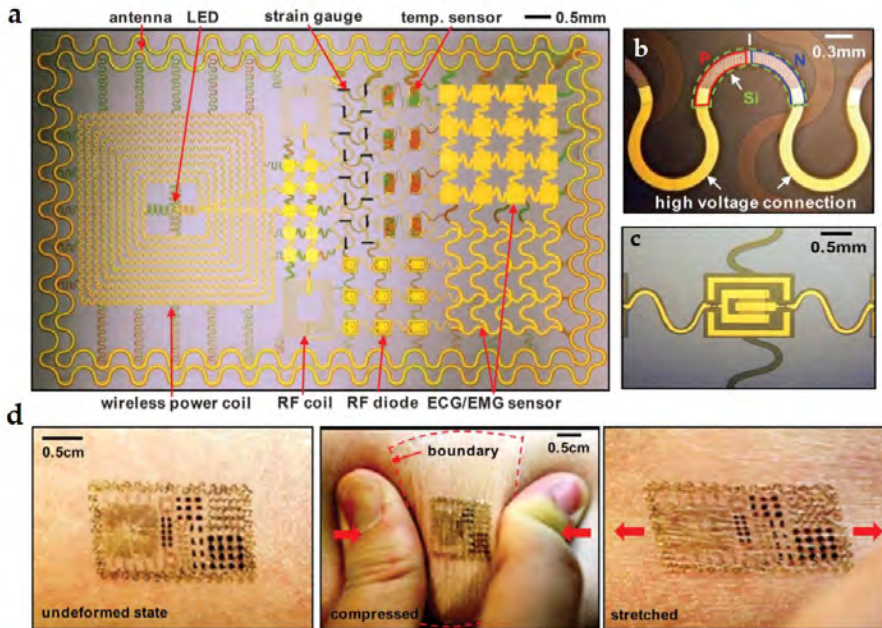


Figure 10. Epidermal electronics. a) Multifunctional electronics with physical properties resembled human epidermis. The system was mounted on a water-soluble polymer sheet of polyvinyl alcohol and conformally attached to the skin via van der Waals interactions alone, analogous to a temporary transfer tattoo. Thin narrow interconnected lines in forms of filamentary serpentine (FS), and ultrathin active devices that adopt similar FS layouts were found as effective parameter designs to achieve the extreme mechanical properties of the system b) FS pattern for a silicon solar cell. c) Optical micrograph of silicon RF diode for the wireless capabilities in an island-bridge structure. d) Epidermal electronics are mechanically invisible for the user in undeformed (right), compressed (center), and stretched (left) forms without any variation in their functionalities and imposing negligible mechanical loading. Note: a-d from reference ⁴⁹.

Engaged in extreme functionalities, research has steadily pursued new forms of electronics for on-skin sensors. Another example is substrate-free electronics,⁵⁷ enabling not only adhesion to the skin but also sweat secretion (Figure 11a,b). Nanomesh conductors were fabricated with a sparsely overlapping spaghetti-like structure on a sacrificial substrate of polyvinyl alcohol for EMG recording. They were also coupled to temperature and pressure sensors systems demonstrating their electrical and mechanical performances while facilitating skin breathing. To be called up to its capabilities this new form of electronics was named *breathable electronics*.

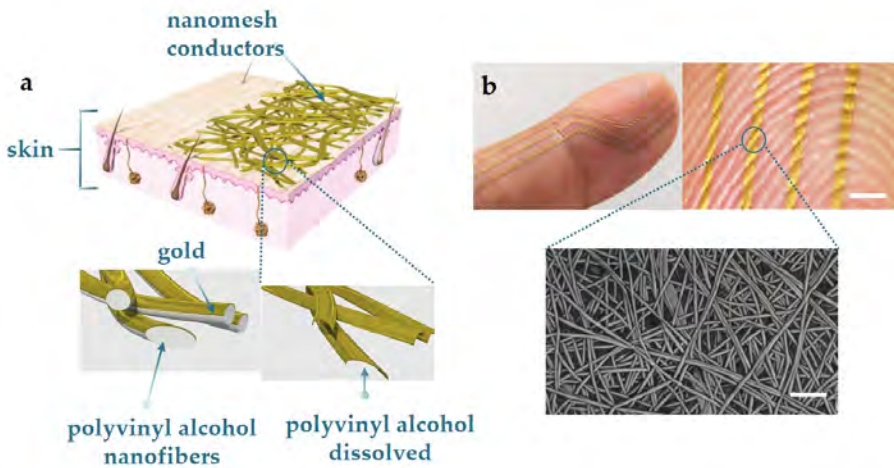


Figure 11. Breathable electronics. a) Sketch of the gold nanomesh electronics laminated directly onto the skin. The gold is evaporated onto electrospun nanofibers of polyvinyl alcohol (PVA). When PVA meshes laminated onto the skin are sprayed with water, the substrate dissolves, and nanomesh conductors adhere directly to the skin. b) A picture of a nanomesh conductor laminated to a fingertip (left) and a magnification of the image (right, scale bar 1 mm), showing a high level of adherence and conformability to the irregular surface of the skin. A micrograph by scanning electron microscopy (SEM) of a nanomesh conductor attached to a silicone skin replica (down, scale bar 5 μm). Note: a,b modified from ⁵⁷.

During the last decade, high technological applications in flexible, stretchable, imperceptible, epidermal, and breathable electronics have arisen at a breath-taking speed. The subject has been reviewed elsewhere^{67,114-119} and the interested reader is referenced to these sources for further information in which examples of applications ranging from soft robots to implant electronics are comprehensively described. Besides those reviews, it is very relevant the handbook¹²⁰ edited by the leading experts, Rogers, Ghaffari, and Kim in 2016 that provides a big-picture perspective of the field, and the special issue recently published by *Advanced Materials*¹²¹ on “Flexible hybrid electronics” in March 2020. The special issue, with a total of 27 reviews, brings excellent contributions from experts in the topic and showcases fresh advances in this rapidly growing, explorative field.

2.3. MATERIAL-BASED ROUTES. FROM EARLY PLASTIC ELECTRONICS TO SELF-HEALING MATERIALS

Devising novel materials to be patterned in conventional layouts have endowed scientists with the ability to fabricate electronic devices intrinsically soft. Contrary to what we saw in section 2.2, in this strategy the malleability does rely on the properties of the material, on its softness and elasticity. This section 2.3 is about another strategy that has not been concealed from the eyes of researchers to fabricate many of the current skin-imperceptible electronic systems.

Advances in two major scientific fields in the 20th century —plastics and electronics— touched virtually every aspect of modern life. Whilst synthetic polymers (saturated polymers) could —and still— be found in larger quantities than any other class of materials at the industrial scale, it was only with the advent of hybrid technology in the form of conjugated polymers (i.e., conducting polymers)¹²² when polymer science drew the attention of electronics. Conducting polymers uniquely combined antagonist properties not observed in other materials, this is, electronic performance and mechanical compliance, the best of “both worlds”.¹²³

Conducting polymers —for which Heeger, Shirakawa, and MacDiarmid were awarded with the Nobel Prize in Chemistry in 2000— have the add-on ability to be doped over the full range from insulator to metal.¹²² In conjugated molecules, the chemical bonding results in one unpaired electron per carbon atom (the π electron). Such π bonding leads to electron delocalization which is fundamentally important for efficient charge mobility within a semiconductor. The number and the kind of atoms within the chemical unit (i.e., chain symmetry) can be altered (doped) to reduce, for example, intermolecular hydrogen bonds that may interrupt electron delocalization. Improving electrons delocalization allows free movements of the carrier along the backbone of the polymer which may mean enhanced conductivity. As a result, properties in conjugated polymers are related to features of the chemistry and/or physics at a molecular level. Because of this versatile capacity scientists are given the opportunity, and the challenge, to design a variety of novel semiconducting materials. This versatility inevitably unfurled the burgeoning field of *plastic electronics*.

Early work in the field focused on improving electronic figures of merit (e.g., charge-carrier mobility) which was seized for instance in light-emitting diodes.¹²⁴ Consequently, important mechanical aspects were left behind. As interest in plastic electronics —or perhaps in plastic in the literal sense of “deformable”— began in earnest, researchers started to improve and understand the mechanical properties of such organic materials paving the way for new leading-edge areas of research. For bio-applications, for instance, it may be permissible to sacrifice performance metrics for the sake of mechanical compliance.

The terms organic and polymer electronics are synonymous with plastic and flexible electronics though descriptors in the former mask the mechanical properties emphasized by the latter. However, neither all organic-electronic materials exhibit flexible and elastic behavior, nor the carbon framework common to both organic electronics and biological macromolecules implies an easy and seamless integration between those two components. Organic materials can be hard (e.g., Young’s modulus of ~ 1 TPa) and brittle (e.g., fail at 1–3 % strain), they exhibit charge mobility, stability, and purification far lower, and poorer, than conventional inorganic counterparts (electron mobilities in the range of dozens of $\text{cm}^2 \text{V}^{-1} \text{s}^{-1}$ in the former versus hundred $\text{cm}^2 \text{V}^{-1} \text{s}^{-1}$ in the latter),¹²⁵ and, on top of that, substantial work is also required to overcome the mismatch between organic-based devices and biological tissues.⁹⁷ However an attractive, and unique, aspect remains —the opportunity to reimagine not the electronics but the materials of the individual device components by synthesizing, assembling, and patterning new materials, or tuning existing ones: the compelling opportunity to fabricate flexible electronic devices in which materials are flexible themselves.¹²⁶

Three main categories summarize the material-based approaches for making electronics deformable from an initial length (Figure 12a-c): fabricating deterministic geometries of otherwise stiff materials to render malleable behavior (Figure 12a), synthesizing random composites with both an electronic filler and an elastomer backbone matrix (Figure 12b), and, perhaps overlapped with the aforementioned category, designing new intrinsically stretchable materials by modifying the chemical structure (Figure 12c), which has been nicknamed as “molecularly” stretchable materials.¹²⁷

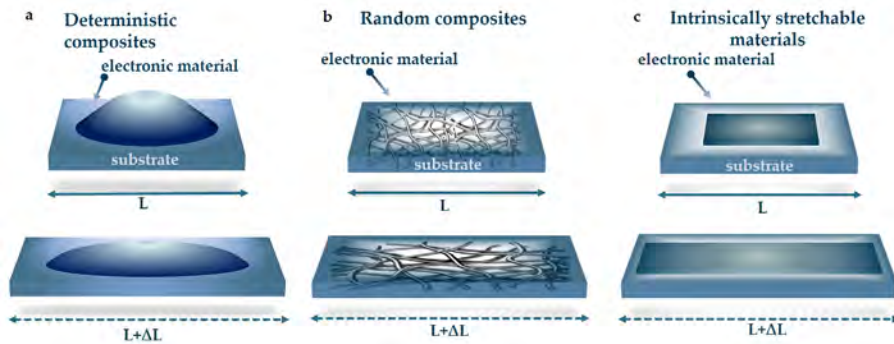


Figure 12. Material-based strategies for flexible and stretchable electronics. a) In the deterministic composites, thin films or complex geometries of otherwise stiff materials render stretchability from an initial length L to an $L+\Delta L$, by out-of-plane motions or by channeling strain into the interconnects. b) In the random composites, electronic fillers (nanoscale materials, and/or conjugated polymers) form a mesh-like network structure atop or into an elastomer backbone, and the percolation pathways for the electric charge is the key that underpins flexibility. c) Intrinsically stretchable materials do not in principle require of strain relief by substrates or topographies, but their molecular structures accommodate strain.

In deterministic compositing active materials are patterned into geometries (e.g., wavy structures, serpentine meshes, Kirigami designs, etc.) to impart flexibility/stretchability by out-of-plane motions or by channeling strain into the interconnects. We have introduced this approach in

section 2.2 from a structure-based point of view, thus here only a mere mention of the materials (substrate and electronic materials) mostly used in their fabrication is given.

In deterministic compositing the following substrate materials are the most commonly exploited: poly(dimethyl) siloxane (PDMS), polyurethane (PU), polyimide (PI), polyethylene naphthalate (PEN), polyethylene terephthalate (PET), polyvinyl alcohol (PVA), polyaniline (PANI) and parylene (PL). All these materials are classified as *polymers* though they can be divided into three sub-categories depending on their physical properties: i) thermosets, ii) thermoplastics, and iii) elastomers. Their properties have been summarized elsewhere¹²⁰ and they can also be used to encapsulate circuits¹²⁸ to protect them from mechanical and chemical agents. With this encapsulation the active layers of the circuits are placed in the mechanical neutral plane, serving therefore not only as an encapsulation, but also as a strategy to minimize the stress as we saw in section 2.2. The main forms in which these substrate materials have been exploited include continuous forms as membranes or foils (depending on whether it is an elastomer or a thermoset/thermoplastic, respectively) and open fishnet forms.¹²⁹ Recent applications of skin-mountable electronics have used hydrogels^{25,130,131} as substrates to more closely mimic the target living tissue. Using hydrogels facilitates advanced applications like drug delivery by diffusing drugs throughout the same gel matrix.

For the electrically active materials, *inorganic* components such as silicon (Si), gallium arsenide (GaAs), germanium (Ge), indium tin oxide (ITO), zinc oxide (ZnO), and platinum (Pt), among others, or *organic* components can be used. Inorganic materials represent the foundation for all conventional electronic devices. They exhibit, so far, unmatched

performance and superior capabilities (e.g., highest field-effect mobilities, and better resolution in the fabrication processes) in all types of applications including wearable and implantable electronic devices. Main concerns in the use of inorganic materials, however, follow from delamination issues, limitations in the combination between material choices, and fabrication strategies (i.e., the glass-transition temperature (T_g) of most flexible substrate materials are unsuited with high temperatures needed in certain fabrication steps), and the incompatibility, in many instances, with large-area electronics fabrication (e.g., roll-to-roll printing).¹³² On the other hand, examples of organic components for flexible electronics are carbon, pentacene, polyacetylene, poly(3-hexylthiophene) (P3HT), among others. Among the attractive characteristics of using organics include ease of processing (e.g., organics are compatible with solution-based printing), facile tunability of optical (e.g., transparency), electronic, and mechanical features, programable degradation (biodegradability), and capacity of self-repair.¹³³

In the second method, **random compositing** (Figure 12b), nano-scale materials, and/or conjugated polymers (electronic fillers) form a mesh-like network on top or into an elastic support (elastomer backbone matrix).¹³⁴ The key factor that underpins flexibility and stretchability is the percolation pathways for the electric charge in the electronic fillers provided by alternative (*random*) deformable pathways in the elastomer matrix.¹³⁵⁻¹³⁷ In other words, as the bulk structure is deformed, the strain is accommodated by the elastic matrix and electrons can move through the network of the electronic filler as long as the composite structures retain an uninterrupted pathway. Whereas the electrical properties of material composites depend on the type of electronic fillers, the mechanical properties (e.g., Young's moduli) are mainly determined by the elastomer.

Nanomaterials of diverse forms (e.g., nanoparticle, nanowire, and nanoflake) are good candidates to be used as electronic fillers because they naturally create networks with many contact junctions. Elastomers often comprise the bulk support because they are soft (i.e., Young's moduli <10 MPa) and easy to process. A variety of both electronic fillers and elastomeric matrix can be used. An overview of all of them is summarized in Figure 13.

In this random composite-based strategy remarkable progress has been achieved concerning stretchability with examples of conductors supporting strains as high as 10000 %, ¹³⁸ yet there is plenty of room for improvements in other directions such as enhancing both the electrical performance and the adhesion at soft-hard interfaces ¹³⁹ which remain the major weakness of the method. Despite this, a range of electronic devices spanning from sensors ^{135,136,140}/actuators ^{141,142} (resistive-type thermal actuators) to multifunctional integrated systems ^{143,144} has been demonstrated using random composites. Recently Park, Kim, *et al.* reported an epicardial implantable system able to conformally wrap around the endocardial surface of the ventricles of the human heart. ¹⁴⁵ The components of the system are based on a homogenous dispersion of silver nanowires and styrene-butadiene-styrene (SBS) elastomer (styrenic elastomer). In other words, they are based on a random elasto-conductive composite. The implantable device was able to record high-quality ECG and electrically stimulate *in vivo* rodent heart to restore ventricular tachycardia and heart fibrillation.

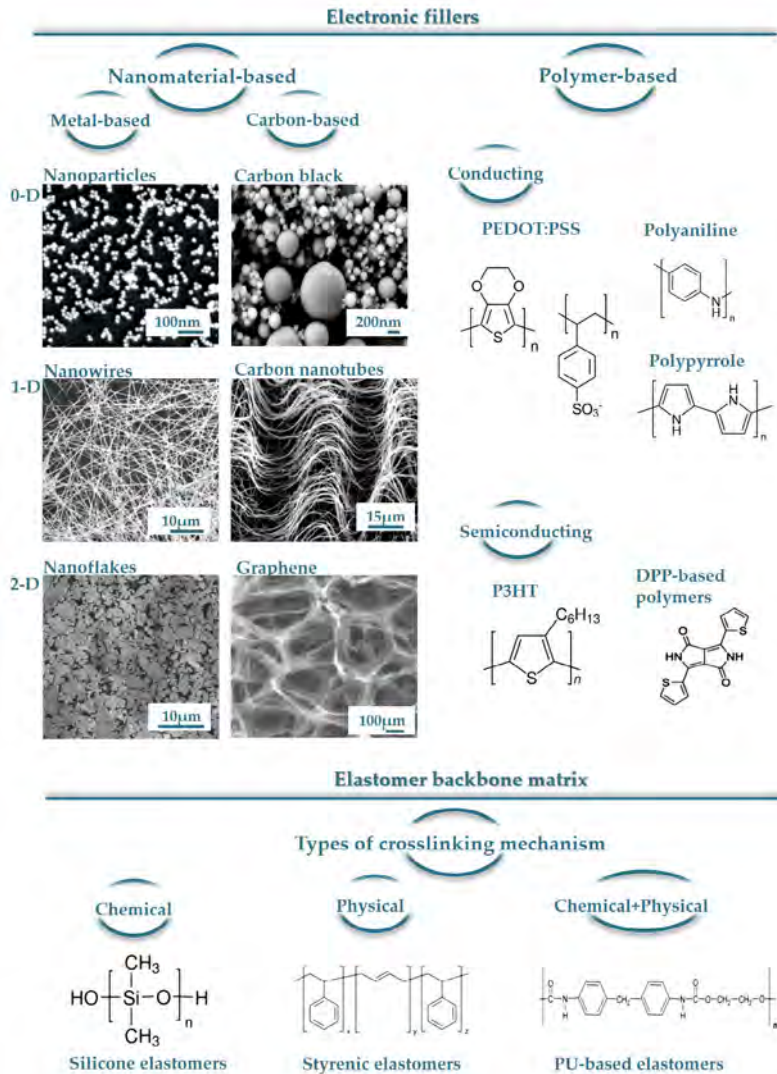
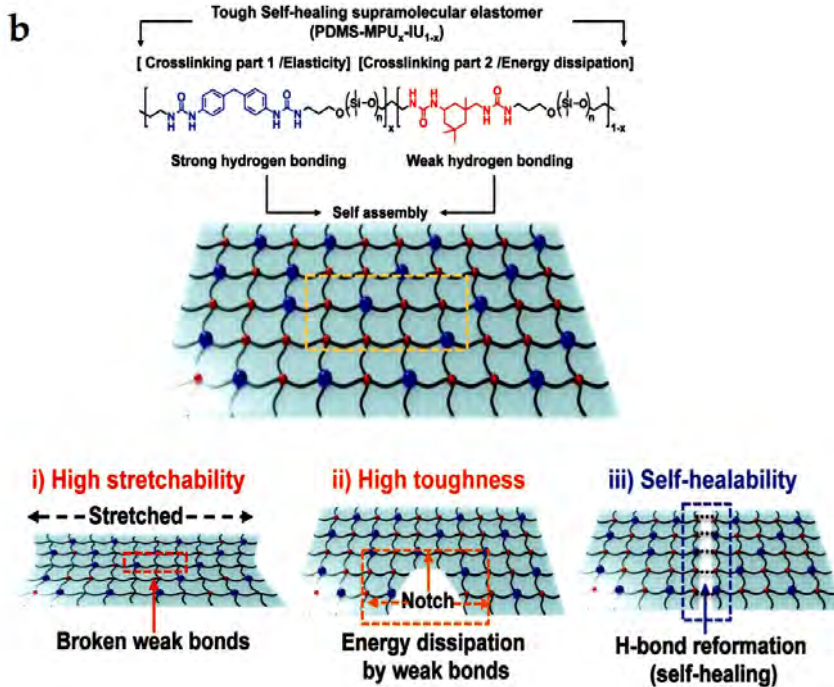
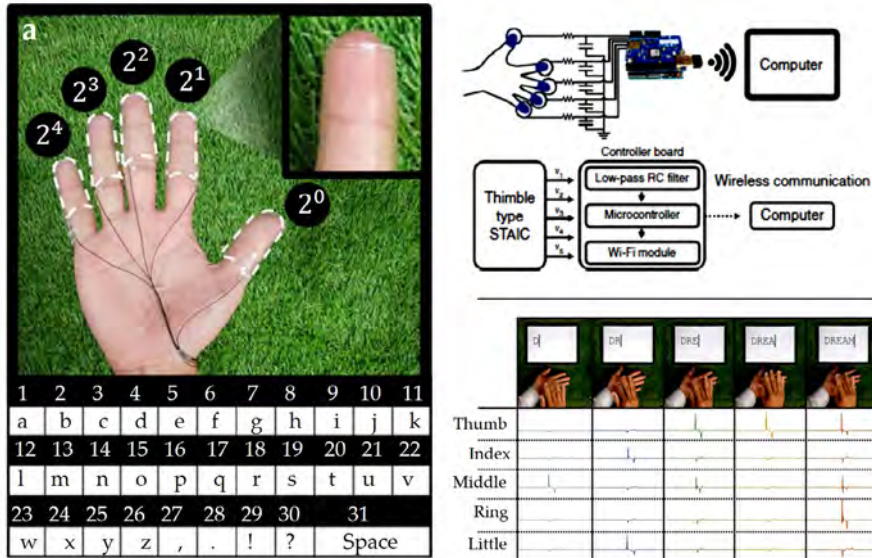


Figure 13. Random compositing for flexible and stretchable electronics. An electronic filler and an elastomer matrix form the elastic composite, in which the percolation networks of the electronic fillers enable electrons to move through networked pathways when the composite is stretched. A variety of nanomaterials including zero dimension (0D),^{146,147} one dimension (1D),^{141,148} and two dimension (2D)^{149,150} forms, and conjugated polymers have been used as electronic fillers for random compositing. Elastomers often comprise the bulk support because they are soft (i.e., Young's moduli < 10 MPa) and easy to process. The electrical properties of material composites strongly depend on the type of electronic filler, while mechanical properties (e.g., Young's moduli) are mainly determined by the elastomer backbone. Note: figure modified from reference ¹³⁴.

The complementary third approach of intrinsically^{151,152} (or “molecularly”)¹²⁷ **stretchable materials** is perhaps the one which remains in the most infant stage. The approach is based on designing, synthesizing, and using materials that —by virtue of their molecular structure— accommodate strain without disrupting effective charge-transport pathways. Using intrinsically stretchable materials simplifies patterning (compared to deterministic approach) and does not in principle require of strain relief through substrates or complex topographies. These devices mostly exploit π -conjugated molecules (i.e., conducting polymers) due to their excellent tunability (doping) and ease processability. When combined with a variety of chemical moieties, polymers develop novel molecular structures with properties that may be superior to the precursor (e.g., lower tensile moduli, higher carrier mobility, etc.). Great effort has therefore been devoted to understand which are the molecular parameters that allow mechanical compliance and electrical behavior to coexist.^{123,153}

Beside conjugated polymers, conducting hydrogels (and their composites) and liquid metals (gallium (Ga) and/or its alloys, the rest of the liquid metals are toxic or radioactive) have shown potential as intrinsically stretchable materials in flexible/stretchable electronics. Liquid metals are usually held in microfluidic channels to fabricated stretchable electrodes and have been successfully used both at device and system level, for example, in a wireless on-skin system that monitors human motion using liquid gallium indium tin (GalnSn) for all the active components (strain sensor, antenna, interconnections).¹⁵⁴ Using hydrogels, individual components such as tactile sensors or triboelectric devices as well as on-skin system¹⁵⁵ have been reported. This e-skin system, for instance, is self-cleanable, transparent, and biocompatible and it was attached to the fingers to code different alphabet letters by simple finger touches (Figure 14a).¹⁵⁵

Such a third material-based strategy advocates for designing bio-inspired materials embellished with the tissue-like properties of elasticity, degradability, and self-healing.¹³³ The latter feature —skin-inspired by definition— has recently seen some significant achievements. The self-healing mechanism can be attained by different mechanisms largely categorized regarding their healing principle in non-covalent interaction and covalent bonds.¹³³ Oh, Bao, *et al.*⁷⁰ used a non-covalent-bonding mechanism in a conjugated polymer (conductive) prepared with repeated units of DPP (3,6-di(thiophen-2-yl)-2,5-dihydropyrrolo[3,4-*c*]pyrrole-1,4-dione) by inserting a non-conjugated polymer (non-conductive) PDCA (2,6-pyridine dicarboxamide) as a dopant to make a wearable stretchable transistor. Reducing intermolecular hydrogen bonds was the primary focus in the early work using conjugated polymers,^{122,124,153} but surprisingly Oh and colleagues' strategy benefits from the opposite. By adding non-conjugated segments, conjugation inside the conductive polymers was disrupted, forming new hydrogen bonds between the adjacent polymer chains. Weak and dynamic hydrogen bonds can easily be broken and reformed in the material. When stretched, hydrogen bonds allow an energy dissipation (breaking themselves) without greatly compromising the conducting behavior in the original DPP polymer. Because dynamic hydrogen bonding easily reforms, damage in the bulk structure can be healed with the aid of healing agents (in this case using a solvent vapor).



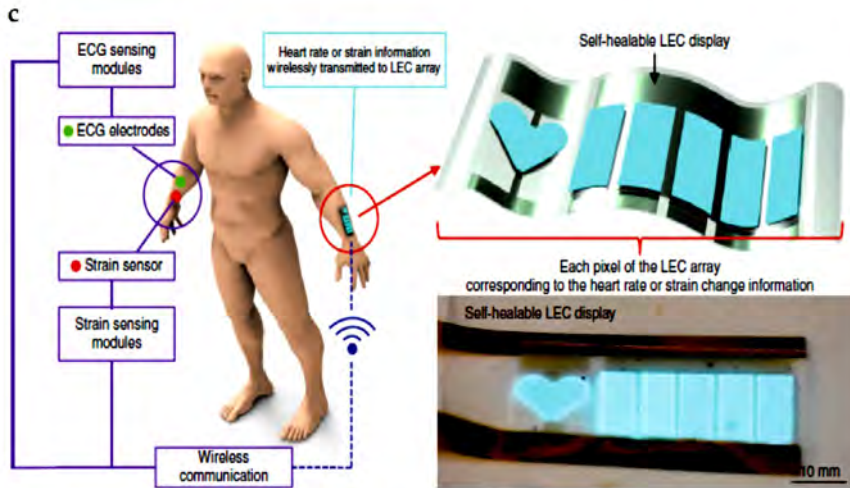


Figure 14. Example of e-skin electronic systems based on intrinsically stretchable materials. a) Self-cleanable, transparent ionic sensors attached to the fingers. They were wired connected to a controlled board, and by a binary code touches, real-time communication was demonstrated. “DREAM” was typed using a combination of finger touches.¹⁵⁵ b) Molecular design of the seal-healable elastomer (top), and schematic representation of a stretched polymer with broken weak bonds (down left), notched film (down the middle), and self-healed film (down right).¹⁵⁶ c) Electronic skin consisting of stretchable modules of ECG, strain sensors, and LEC-type displays. The electrodes/interconnections of the system are composed of hybrid conducting fillers of AgNW/CNT embedded in the self-healing polymer matrix.¹⁵⁷ Note: Images modified from a) ref. 155; b) ref. 156; c) ref. 157

Recently, the same research group has used an autonomous self-healing elastomer¹⁵⁶ (Figure 14b) with conducting nanofillers of carbon nanotubes (CNTs) and silver nanowires (AgNWs) to fabricate a multifunctional optoelectronic self-healable e-skin¹⁵⁷ (Figure 14c). The underlying principle in the self-healable material is achieved through the spontaneous formation of both strong and weak hydrogen bonds in the elastomer (Figure 14b). When electrodes fabricated with such composite were cut, their resistance increased sharply but decreased over time as the healing reaction advanced. The conducting fillers (i.e., AgNWs and CNTs) embedded in the elastomer can reconnect their lost networks while the elastomer backbone

rejoined physically even soaked in water or artificial sweat. Besides those attractive properties of self-healability at room temperature and stretchability (even after damage), the material exhibits other appealing features like a high fracture toughness ($12\,000\text{ J m}^{-2}$). This property can open many interesting applications, for example, to suture electronics on soft skin surfaces. Indeed, the elastomer in form of thin films was used to be sutured a temperature sensor on a pig's inner skin.¹⁵⁶

Progress in the domain of material-based strategies for flexible and stretchable electronics has also evinced the tremendous effort and interest drawn from the field. Thus, hybrid forms of electronics have benefited from a cross-fertilization of diverse disciplines in a variety of two-way alternative routes. A body of literature exists on the topic and several reviews exist^{127,134,158} where the interested reader can find comprehensive insight into this material-based perspective.

2.4. OVERVIEW OF MANUFACTURING TECHNOLOGIES FOR FLEXIBLE AND STRETCHABLE ELECTRONICS

Fabricating flexible and stretchable electronic devices and systems involve —broadly speaking— two, not exclusive, processes: 1) integration and 2) lamination.⁶⁴ Given the two established strategies to obtain flexible electronics (this is, stretchable structures and stretchable materials as we have seen in sections 2.2 and 2.3, respectively), it may be expected that there would be “standard

processes” or “standard manufacturing technologies” to develop such electronic devices and/or systems. Rather the opposite, developing any new unconventional forms of electronics carries with it an associated challenge of establishing equally new (likewise high-yield, low-cost, and efficient) means for their fabrication.

In the lamination processes, the components are prefabricated in a substrate that is different from the target substrate (final application).¹²⁵ The advantage of decoupling high-temperature growth and certain aspects of some processing steps (e.g., chemical harsh conditions) from the desired final substrate is a key enabler. The method facilitates the use of both conventional, well-developed, semiconductor technology and high-performance inorganic electronic materials of diverse forms (e.g., wafer-derived silicon nanomembranes, nanoribbons, and nanowires).^{125,159,160} To prefabricate the components the well-known bottom-up (i.e., a wide range of chemical synthetic approaches) and top-down (e.g., photolithography patterning and etching) techniques have been adopted.^{125,132} The fabrication process finishes with the assembling (*lamination*) of the components or the complete circuits at room temperature (ambient environment) *via* physical transfer (e.g., transfer printing technique)¹⁶¹ or other processes (e.g., fluidic self-assembly)¹⁶² from the starting or “mother” wafer onto the desired substrate such as plastics. (Figure 15a,b)

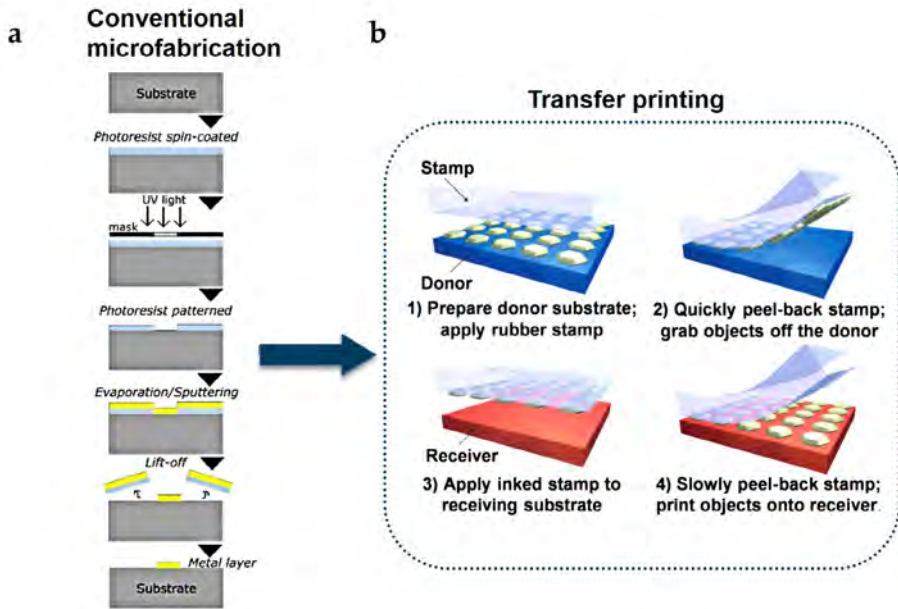


Figure 15. Manufacturing techniques and processes in the lamination approach for flexible/stretchable electronics. a) Components are prefabricated using conventional microfabrication techniques in a wafer substrate. b) The structures or the devices are laminated into the target substrate using different methods such as transfer printing.

The devices/circuits built in this fashion allow for classes of deterministic structures that exhibit high performance inherited of the mother wafer (e.g., carrier mobilities up to several hundred $\text{cm}^2 \text{V}^{-1} \text{s}^{-1}$) while endurance arbitrary curvilinear shapes.^{125,163} Mechanical fragility, and nano/micro-scale dimensions in the transferring structures, as well as the need for tight control and high throughput in the transferring process have directed considerable effort from research to make reliable assembly methods possible.¹⁶⁴

The preferable transferring method is a physical transfer-based one named *dry transfer printing* in which no jet-able but solid inks

(fragile, nano/microstructures, or fully devices) are printed in the target substrate. A generic process within the dry transfer printing relies on two stages: the inking and the printing step (Figure 15b). In the inking step a stamp (usually made of PDMS) is placed in contact with a donor substrate (usually silicon wafers) to peel off the inks. During the inking, physical or chemical bond-based methods allow selectively removing the desired structures from the wafer.¹⁵⁹ In the printing step the ink is released on top of the receiving substrates where by contact forces, coating adhesives, or modifications of the receiving surface, components are ultimately transferred. Other viable methods are based on fluidic self-assemblies in which wafer-based structures are dispersed in solvents. External forces (electrical, magnetic or mechanical) induce order in the disorganized suspensions resulting in a well-defined structure in the ultimate substrate.^{125,147,162}

Transfer printing is an effective but complex, time-consuming, and not a low-cost method. Nevertheless, since the first reported work using transfer printing¹⁶⁵ to harvest silicon nanoribbons from a silicon-on-insulator wafer, transfer printing has been adopted in countless, high-technical solutions as part of the fabrication process.^{49,105,106,108,112,113,166} For example, recently Lee, Kim, *et al.* reported a wearable/disposable sweat-based glucose epidermal system²⁴ in which some of the devices of such an integrated system were firstly fabricated on a handle, wafer-based substrate and then transfer-printed onto a skin-compliance patch made of silicone. As a rule, structure-based solutions for flexible/stretchable electronics presented in section 2.2 have mainly exploited the lamination-based approach.

On the other hand, in the **integration process** among the fabrication approaches, materials are directly deposited and patterned on the final substrate. The integration can be achieved by *subtractive printing* (i.e., deposition of materials followed by selective removal) or *additive printing*. In this sense, organic materials can be processed at temperatures compatible with those that can support most of the polymeric substrates, and nanomaterials can be dispersed into solvents and be processed using solution-based approaches. Consequently, and contrary to inorganic materials that benefit mostly from the lamination process, organic/nano-based materials well-match, and seize, the integration fabrication methods. Molding, screen printing, spray coating and dip coating are examples of *additive manufacturing* methods (integration processes) able to integrate electronic materials directly onto soft substrates (Figure 16).

Molding processes can fabricate complex patterns with decent resolutions (microscale) by a simple deposition of the material followed by the evaporation of the solvent. For example, homogenous dispersions containing AgNWs and SBS elastomer were patterned in a mesh structure by casting the solution in a photolithographed master mold.^{141,145} SBS elastomers were molded using identical molds, while the mesh conductors were then hot-pressed and sandwiched between such SBS elastomers. The created mesh-structured was able to stretch and wrap around complex three-dimensional forms such as the surface of the wrist¹⁴¹ or human organs.¹⁴⁵

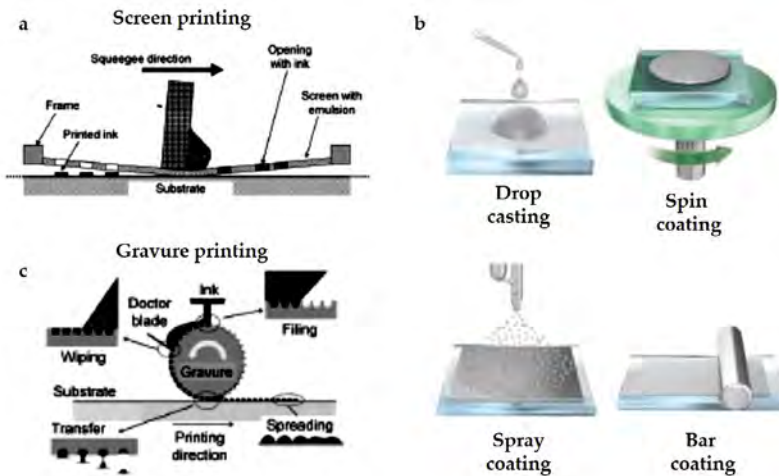


Figure 16. Different manufacturing techniques used in the integration approach for flexible and stretchable electronics.

Screen printing transfers the ink to a variety of substrates by squeezing the ink through a pattern or shadow mesh as it is shown in Figure 16a. Screen printing becomes a suitable choice when the functional materials instead of being embedded in the elastomer form a bilayer with the supporting substrate, the nature of the inks is highly viscous (500-5000 cP), and the resolution and thickness of the device can be between 50–150 μm and 5–100 μm respectively.¹⁶⁷ For example, Sekitani, Someya, *et al.* prepared a viscous paste with single-walled carbon nanotubes (SWNTs) and fluorinated copolymer rubber.¹⁶⁸ They patterned lines of 100 μm with such conductive composite on PDMS using screen printing and ultimately fabricated a stretchable organic display.

Spray coating sprays functional inks on the target substrates by using compressed air (Figure 16b). Nano-based materials such as met-

al-based nanowires and carbon nanotubes have been easily sprayed in a variety of substrates without grand restrictions but with an appropriate high-aspect-ratio in the solution. By using stencils higher resolutions ($<100\ \mu\text{m}$ width, thickness $\sim 1\ \mu\text{m}$) in the patterns can be obtained. For example, Chou *et al.* proposed the use of a parylene stencil mask on a wafer-scale PDMS as a new, spray coating-based, technique to pattern nanomaterials for wearable and flexible applications.¹⁶⁹

In the method called **dip coating**, substrates either flat or with complex geometries like three-dimensional scaffolds are dipped into a nanomaterial solution. The method is straightforward and cheap but lacks resolution and yields relatively uneven and thick coating layers. It becomes appropriate when electrodes in a variety and/or uncommon forms like sponges¹⁷⁰ are needed.

Other printing methods as **gravure** and **blade coating** and **slot die coating** have been also used to manufacture sensors and devices directly on the final flexible substrate. In gravure printing, for example, the ink gets transferred from the inlet on the gravure cylinder (Figure 16c) while a doctor blade wipes the excess ink from the cylinder. The features are engraved in the cylinder and multiple gravure cylinders can be connected in series to print multilayer films. For large-area and high-volume manufacturing gravure with a resolution of a few μm and speeds of $\sim 10\text{ms}^{-1}$ is the ultimate choice.

In *subtractive fabrication methods*, the entire substrate is coated with the active material by different methods such as vacuum deposition or sputtering. The unwanted material is later removed resulting in a considerable amount of wasted material. To pattern structures on the final

substrate, laser and/or mechanical techniques can be used to remove the unwanted material. When using a laser, an appropriate cooling strategy such as a thermal buffer layer should be applied to avoid burning of the substrate. Despite all, using lasers to heat the materials has been an effective approach to pattern either organic or inorganic materials *in situ* on plastic substrates. However, the increase in the total thickness of the device due to the required cooling layer has resulted in an undesired, but unavoidable, consequence.^{125,164}

Finally, it is important to note that manufacturing flexible and stretchable integrated systems typically include multiple steps and the use of more than one fabrication method. Those techniques described above as part of the integration approach are becoming technically appealing and worthwhile for both industry and academia. Even though the fabrication processes choice is ultimately done considering resolution, material-based requirements (e.g., solvent compatibility, range of working temperatures), and throughput in the manufacturing process, the ready scalability and the economic processing have pushed the electronic industry towards these new production methods, promoting the development of cost-effective disposable electronics.

Such low-cost printing methods capable of rapid-prototyping flexible electronics present the common feature of the additive principle of operation which has emerged into a broader concept known as *Printed Electronics*, or even more generally, additive manufacturing electronics. Application areas for printed electronics stretch beyond mountable-skin sensors and systems for healthcare (or e-skins). Flexible displays, large-area sensor arrays for environmental, industrial, and agricultural sensing, and Internet-of-things infrastructures are among examples that break away from the rigid, con-

ventional, electronics to speed into printed electronics. IDTechEx, a market research agency, forecasts printed electronics market will grow up to \$74 billion by 2030 from the current \$41.2 billion in 2020.¹⁷¹

One technique among those associated with printed electronics not mentioned previously is inkjet printing. Because this is the fabrication method selected in the framework of this thesis a special section to further describe this emerging technology follows.

2.5. INKJET PRINTING TECHNOLOGY

Inkjet printing technology is a fabrication technique based on a mask-less and non-contact process. Functional materials in liquid form are deposited onto the substrate controlled in a very accurate fashion to follow a given, pre-determined pattern. Due to its low-material consumption and wastage, convenience, and speediness, not only has inkjet printing attracted attention as an alternative, environmentally friendly, manufacturing technique, but also it has fostered the burgeoning field of flexible electronics.

This fabrication process has no physical, pre-manufactured masks, or stencils.¹⁷² Printing parameters and patterns can be changed simply by altering the code in the control files. This versatility gives a significant advantage in rapid prototyping and/or manufacturing that usually require a high level of in-line corrections with little cost impact. Non-contact process means that with inkjet printing, electrical patterns

can be fabricated on surfaces without physical contact. This non-contact enables fabrication on both substrate materials which are highly sensitive to physical contact and surfaces with uncommon topographies (e.g., three-dimensional surfaces). The impact force onto the substrate or sublayer has been demonstrated to be insignificant (see ^{173,174}).

Although inkjet printing has aroused wide attention from both industry and academia, making significant progress in devices such as light-emitting diodes,¹⁷⁵ solar cells, RFID antennas,^{176,177} and sensors,¹⁷⁸⁻¹⁸¹ inkjet printing technology lies within the foot of its S-curve of development (see Figure 17), which means new applications can be expected to appear (with an exponential impact) in the coming years. As progress in the development of ink formulations, printheads, and strategies for high-quality patterns emerges, the technology may consolidate and even prevail within the electronic manufacturing industry.

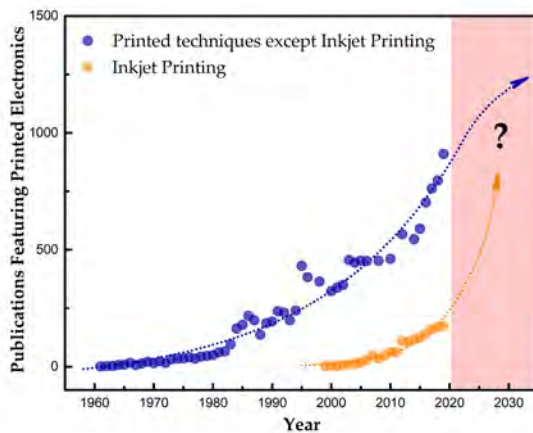


Figure 17. Inkjet printing technology state-of-the-art in research. Inkjet printing technology is at its very early stage of development compared with the rest of additive manufacturing techniques. Source: Scopus database. A search carried out on June 2, 2020.

2.5.1. Inkjet printers and printheads

The inkjet printing technology can be classified into two categories based on the mechanism of droplets generation: continuous printing and drop-on-demand (DOD) printing (Figure 18). In continuous printing —the first available inkjet technology— the ink droplets are continuously ejected at a constant frequency. The ink stream is then adapted into volume-controlled droplets by acoustic pressure waves and droplets are directed either to the substrate to form the desired pattern or back to the printhead's circulation system (Figure 18a).

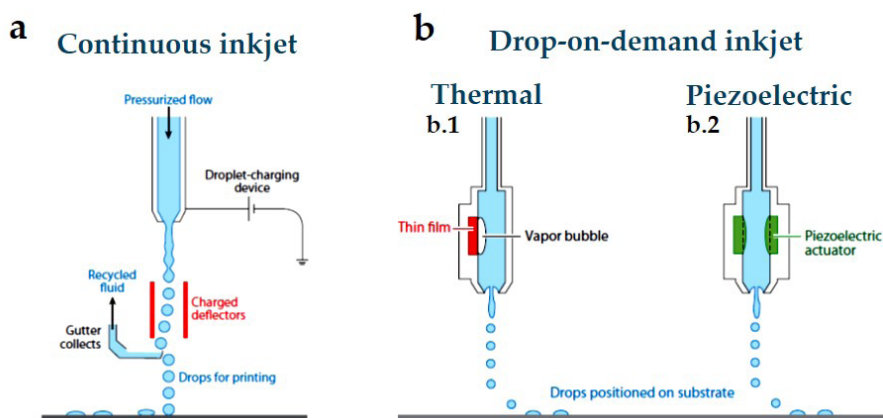


Figure 18. Categories of inkjet printers. a) Schematic of a continuous inkjet printer (CIJ). CIJ produces a continuous stream of liquid drops, ejected through a small nozzle. To direct and position the drops, further potential is applied in deflector plates. Unwanted drops are deflected by the electric field to a gutter and for most applications in material science and electronics this recycling is wasted. b) Schematic diagram of a drop-on-demand (DOD) inkjet printer. In DOD, drops are ejected by a pressure pulse in a fluid-filled cavity. This pressure pulse can be generated (b.1) by a bubble generated by a heater or (b.2) by a mechanical actuator. Note: figure modified from ¹⁸².

In DOD printing, the ink droplets are only ejected by the cartridge nozzles as needed on the desired location within the substrate. By contrast to continuous jet printing, in DOD printing all formed droplets end up on the substrate. Thus, the amount of ink used is minimum. DOD is the more commonly used of the two technologies and the resolution is strongly dependent on the drop volume ejected by the printheads. Currently, commercial inkjet printheads can deliver liquid droplets with a volume starting at 1 pL, which can create spots $>15\ \mu\text{m}$ in diameter on the substrates. To achieve patterns with higher resolutions Park, Rogers, *et al.* have reduced the nozzle diameter to 300 nm achieving resolutions of 240 nm in the printed lines.¹⁸³ However, reducing the nozzle diameter to a sub-micrometer range creates a large resisting capillarity pressure which may make droplets difficult to be ejected.

Printheads, on the other hand, can be divided into two large categories¹⁸² depending on which droplet formation technique is used (Figure 18b). The first technique (Figure 18b.1) generates bubbles to form and eject the ink drops out of their reservoir by using a heater (thermal inkjet). The second way (Figure 18b.2) uses a piezoelectric actuator to generate the pressure pulse necessary to squish the ink out (piezoelectric inkjet). Piezo element-based drop formation is the most commonly used as it is the easiest to control and the most repeatable, reliable, and compatible with most of the commercial jet-able inks.¹⁸⁴ The printhead used in the framework of this thesis is a piezoelectric-based system.

Figure 19 illustrates the basic functionality of the piezoelectric inkjet printing process. The computer controls the ink drop formation based on voltage pulses described within an input file named waveform. The waveform is responsible for the jetting through the nozzles by expanding the piezoelectric transducer according to the input signal. In Figure 19

the waveform is divided into different phases, each one containing three parameters: duration, level, and slew rate. The volume of the pumping chamber strongly relates to the applied voltage (level) while the speed of the droplets ejection mainly to the slew rate.

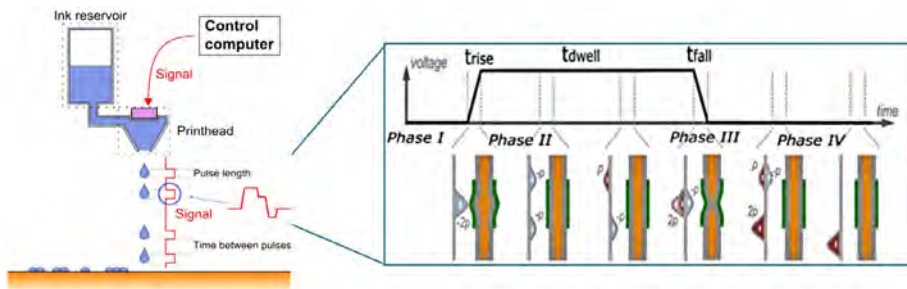


Figure 19. Piezoelectric inkjet printing. Detailed schematic of the structure and function of a piezoelectric single nozzle printhead. The pressure generation, propagation, and reflection upon a voltage application are described in a waveform file from a computer.

2.5.2. Substrates and inks for inkjet printing

Aside from the development of printers and printheads, two key points have enabled the use of inkjet printing as an electronic manufacturing technique: the development of functional inks and flexible substrates, and the strategies to make them compatible between each other. The surface free energy of the substrate and the surface tension of the inks define the wettability and adhesion between the ink and the substrates, dominating the final shape of the printing structure. Other factors such as the drying dynamics of the droplets, the coalescence of consecutive droplets (i.e., the uniformity of two droplets encountering each other), and the solute depositing behavior are also pivotal to print reliable patterns.

2.5.2.1. Substrates and substrate-based strategies for inkjet printing

As described before (section 2.2), polymers are the best candidates used in deterministic approaches for flexible electronics. For inkjet-printed electronics, among thermoset polymers, the polyethylene derivatives are the most used such as PET and PEN. They offer flexibility, low-cost solutions, and come in various thicknesses, sizes, and surface chemical properties that make them compatible with both commercial inks' formulations and commercial printers. Their surface roughness is as low as a few nm. As the biggest drawback, the relatively low glass-transition temperature (T_g) limits both many hybrid applications (i.e., electronic systems that combine printed parts with integrated circuits) if solder is used in their connections,¹⁸⁵ and the use of inks that require post-sintering at high temperatures. Kapton polyimide (PI) shows much higher T_g but, at the same time, higher surface roughness and it is opaque. Paper^{176,178,186} is also an attractive substrate when inkjet printing is used and it is the cheapest solution. Since paper is fibrous, special treatment and many layers of planarization may be required. Although with limited reports, textiles^{177,187} can be also adopted for inkjet printing and it is the primary choice for clothes-based electronics. Finally, elastomers^{188,189} and hydrogels have been recently used in inkjet printing, being PDMS by far the most overwhelmed substrates exploited for flexible on-skin electronics. Besides those flexible substrates inkjet printing also applies to rigid substrates such as glass¹⁹⁰ or 3D structures.¹⁹¹

The performance of the substrates for printed electronics using inkjet printing techniques is listed in Table 1.

Table 1. Typical substrates for inkjet-printed electronics and their physical properties. Reference from K. Suganuma, 2014.¹⁹²

Substrate	Thickness (μm)	Transparency (%)	Density (g cm^{-3})	T_g ($^{\circ}\text{C}$)	Young's Modulus (GPa)
PET	16-100	90	1.3	120	2.8
PI	12-125	–	1.4	410	2.5
PEN	12-250	87	1.4	120	3.0
Paper	20-250	–	0.6-1.0	–	0.5-3.5
PDMS	5-1500	92	0.965	125	0.57-3.7

However, some problems may appear when using inkjet techniques to print electronics on flexible substrates. For example, droplets may overspread due to a high porosity or hygroscopicity of the substrate, the range of temperatures needed in the sintering of many ink formulations (especially when using paper or textiles) may be incompatible with the substrate, or other issues may appear due to the low surface energy in the top of the substrates.¹⁹³

To overcome many of those issues, several strategies have been adopted to prepare the substrates prior to printing. Plasma ionization or chemical treatments¹⁸⁹ are among the most effective surface modifications. Pre-patterning the surface to create hydrophobic/hydrophilic structures¹⁹⁴ and thus force the ink to remain in the designed area using capillary forces have also been exploited. When printing on viscoelastic or even liquid substrates the wetting behavior of inkjet droplets is greatly different than on solid surfaces.¹⁹⁵ Song *et al.* have studied such conditions proposing two approaches to endow printability. First, they have controlled the morphology of inkjet-printed droplets on a liquid-solid composite by external

magnet field.¹⁹⁶ Second, they have used the viscoelastic properties of the substrate to wrap the droplets with the fluid, controlling either a subsequent retraction of the droplets¹⁹⁷ or a completely wrapping.¹⁹⁸ These strategies can be highly useful for printing electronics onto bioinspired/entirely biological substrates. Finally, some strategies presented in section 2.2 as a structure-based approach for flexible/stretchable electronics have been also adopted for inkjet-printing of stretchable conductors. For example, Hong *et al.* have inkjet-printed silver conductors on wavy structures of PDMS¹⁹⁹ and pre-stretched PDMS.²⁰⁰

2.5.2.2. Inks and inks requirements for inkjet printing

Ink formulations represent the key platform for printing. Inks contain the functional materials and various additives dissolved or dispersed in a liquid carrier (aqueous or organic solvent). At least three types of functional materials can be used in an ink composition: conducting, semiconducting or insulating. Additives such as surface tension modifiers, humectants, defoamers and binders enable a stable printability, a prerequisite to achieving well-generate droplets and, consequently, a reliable printed pattern.

Silver and gold nanoparticle suspensions are the most common conductor-based inks for inkjet printing. Carbon-based nanomaterials including graphene, conducting polymers-based inks such as poly(3,4-ethylene dioxythiophene)-poly(styrene sulfonate) (PEDOT: PSS)²⁰¹ and PANI, or metal oxides, have been also employed in inkjet-printed electronics. As dielectric materials, polymers such as poly(amic acid) or SU-8 are the most exploited. To fabricate fully inkjet-printed electrochemical sensors,

other ink formulations are gaining strong demand. For example, sensitive materials such as enzymes, selective coatings based on conducting polymers, antibody spots, and colorimetric reagents have been prepared for fully inkjet-printed (bio)sensors.

Inkjet printing inks must meet very specific rheological requirements. Their design and preparation are often complex with a variety of physicochemical properties. As a rule, viscosity and surface tension need to be within a margin of 1–30 cP and 25–40 mN m⁻¹, respectively. Piezoelectric inkjets usually work at ink viscosity in the range of 8–15 cP, while thermal inkjets function at viscosities below 2 cP.

Three dimensionless numbers define the behavior of the inks: the Reynolds number, the Weber number, and the Ohnesorge number (equations in (3)).

$$\text{Re} = \frac{v\rho\alpha}{\eta} ; \text{We} = \frac{v^2\rho\alpha}{\gamma} ; \text{Oh} = \frac{\sqrt{\text{We}}}{\text{Re}} = \frac{\eta}{\gamma\rho\alpha} \quad (3)$$

where v , ρ , α , η and γ represents the velocity, the drop diameter, the density, the viscosity, and the surface tension of the ink, respectively.

The first number refers to the ratio of the inertial forces to viscous forces in the fluid. The second number represents the balance between the inertial forces and the surface tension. Finally, the Ohnesorge number (Oh)—introduced by Wolfgang von Ohnesorge well-before the advent of inkjet printing technology— groups the other two numbers to relate the viscous forces to the inertial forces and surface tension. The Oh does not include the speed of the drop and therefore it is generally used to indicate

the printability of any ink formulation because it depends only on the intrinsic physical properties of the fluid and drops diameter. Whereas at high value of Oh viscous forces prevent drop ejection, lower value drops are accompanied by many satellites. Thus, the specific rheological requirements to inkjet-print stable droplets can be achieved by proper modulation of the viscosity and surface tension in the ink composition.

Besides the rheological requirements, avoiding solute clogging and blockage during the printing process is crucial. Clogging is generally induced by one of the three following reasons. First, an overlarge size of the solute which should be less than 1/10th of the diameter of the printer's printhead orifice. Second, the solvent evaporation in an orifice. This is avoided using inks with a high boiling point to keep the solvent volatility sufficiently low. Finally, poor dispersion of the ink (i.e. agglomeration and sedimentation). This issue could be further solved by treating the functional material of the ink with a polymer coating, by adding a surfactant, or by introducing solvents.

Such strict requirements and issues in inkjet-printing inks, and the fact that commercial inks are scarce, expensive, and have a very limited life, have attracted considered research interest in the design of new inks composition. Substantial work reported to date using inkjet printing technology has involved the in-house development of one or several of the used inks. This has already borne fruits in exploring annealing-free or low-temperature annealing process for the ink formulations which opens potential applications not only for flexible electronics. Magdassi *et al.*, for instance, presented an annealing-free silver nanoparticle-based ink.²⁰² By adding NaCl, the conductive ink self-sinters during the drying stage spontaneously, which eliminated the need for a post-sintering process.

2.5.3. Processes for inkjet printing

A general schematic of the inkjet-printed complete process is shown in Figure 20. The process can be simplified in three steps: the pre-processing step, the inking deposition step, and the material post-processing step.

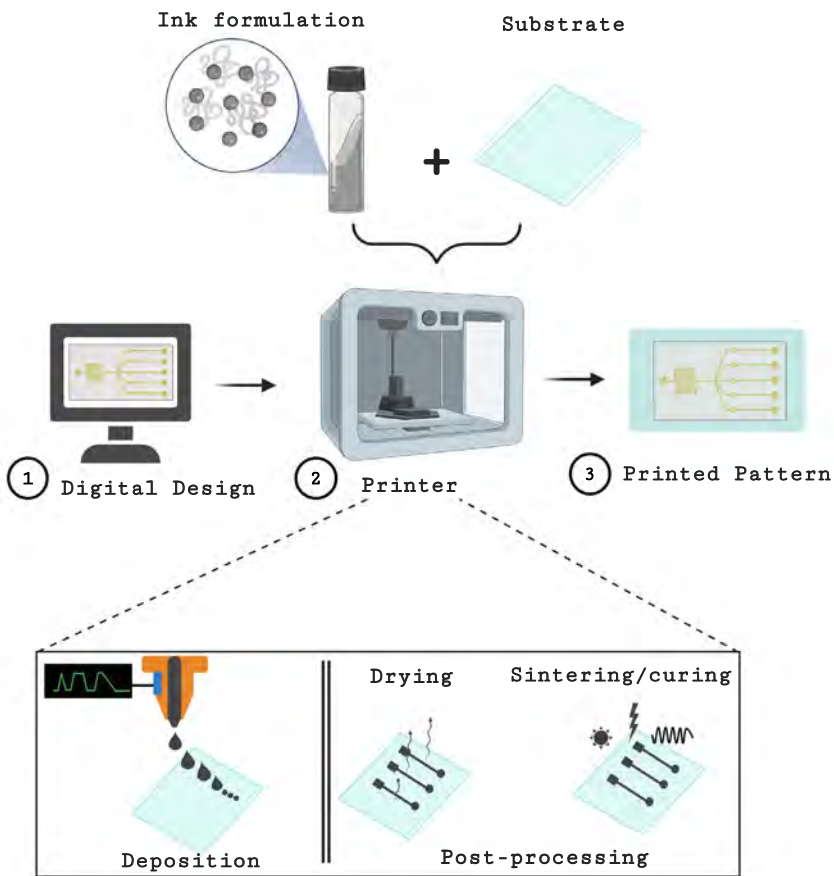


Figure 20. Schematic of the basis of an inkjet printing process. Pre-processing prepares the printing process and includes the digital design, and treatment of substrate and/or inks (1). The printing process (2) implies the ink deposition and the post-processing steps. (3) Final printed pattern or device.

Pre-processing prepares the printing process. It includes the various substrate and surface modifications described before in 2.5.2. It may also include cleaning the substrates from any contaminants and to remove dust and grease. The actual cleaning process depends on the substrate, yet the most common cleaning techniques are alcohol-based cleaning (e.g., isopropanol), UV-ozone, and corona treatment. In the pre-processing step inks can be also treated. To better suit the printing, inks can be degreased to remove air from the ink and filtered to avoid clogging the nozzles with any unwanted particles.

During **ink deposition** the functional material is deposited drop-by-drop on the substrate reproducing a digital pixel pattern. To form reliable patterns, the processes taking place before and after the ink-jetting should be carefully controlled.

To jet the inks using a waveform, the working frequency, and the distance between two consecutive drops (drop spacing) must be defined. Other important jetting parameters when using piezoelectric inkjets include ink temperature and pressure conditions on the printhead. All these configurable parameters ultimately dictate the shape, speed, and size of the ink droplet upon jetting and, therefore, the quality and reliability of the printing. Each commercial ink and printhead contain their map of configurations. The quality and accuracy of the printing are also affected by the printing height (i.e. distance between the printhead and substrate) and the printing speed. The printing speed is the relative speed by which the printhead and print plate move to each other. As inkjet is a fully digital process, placement errors introduced by the printhead height and speed can be minimized with a proper calibration and thus eliminated.

After leaving the nozzle the ink flies and hits the substrate. The droplet-surface interaction is dictated by the material parameters of both the ink (e.g., viscosity) and the substrate surface (e.g., surface tension, surface roughness, etc.). The spreading and impact forces of the drop when it reaches the substrate can be understood by a non-dimensional analysis using Reynolds, Weber, and Ohnesorge numbers. This interaction between ink and substrate strongly depends on the size of the ejected drop and the contact angle of the ink on the substrate and this, ultimately, determines the printing resolution. (Figure 21)

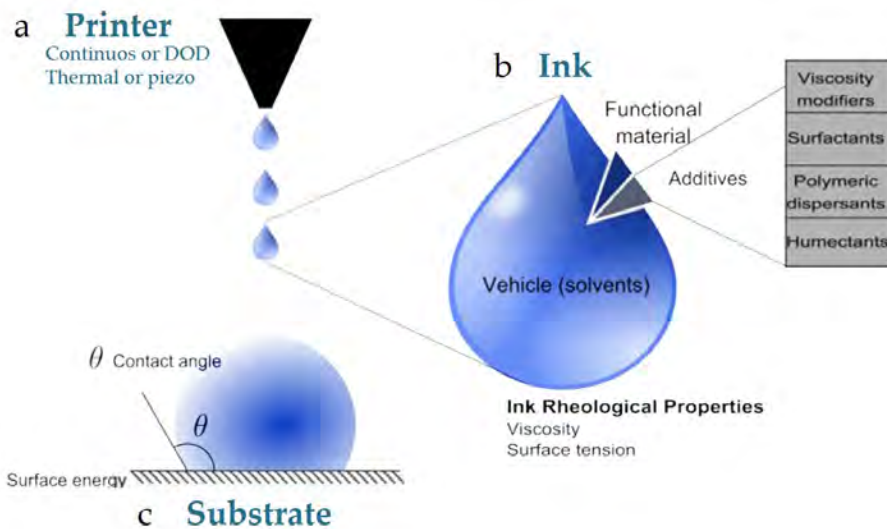


Figure 21. Schematic of a) printer, b) ink, and c) substrate and particularities of each one.

The temperatures of both the substrate and ink are also crucial. The viscosity of the inkjet inks, in many instances, is temperature dependent so it can be, therefore, regulated by heating the ink in the

printhead before jetting. To control the temperature of the substrate the print plate can be heated. This plate heating has been adopted as an effective strategy to control the spreading of the printed ink over the substrate. Heating may, however, contribute to an undesired yet often presented effect named “coffee ring effect”.

The coffee ring effect was firstly explained by Deegan *et al.* which is due to an excess of solute at the edges of the ink-jetted drop during solvent evaporation.²⁰³ Higher solvent evaporation at the outer edges of the deposited drop causes an outward material flow inside the ink to replenish the lost solvent (Figure 22). The coffee ring effect can be minimized or even eliminated using several methods such as using a co-solvent mixture²⁰⁴ with different boiling points and lower surface tension, or carefully controlling the temperature of the substrate.²⁰⁵ The coffee ring, surprisingly, has been also used as a strategy to improve resolution (5 μm -10 μm) in conductive lines of silver nanoparticles.²⁰⁶

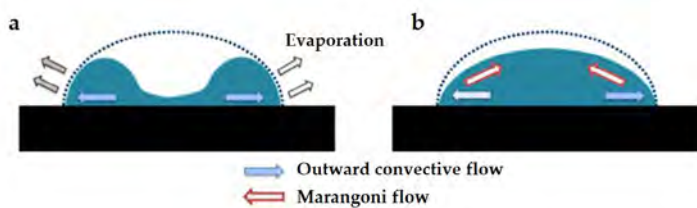


Figure 22. Coffee ring effect. a) The process of drop drying after deposition leading to a coffee ring effect due to an excess of solute at the edges of the ink-jetted drop during solvent evaporation. b) The coffee ring can be minimized by different methods, such as using a co-solvent mixture in the ink formulations or by controlling the temperature of the substrate. When using a co-solvent system, the solvent with a high boiling point evaporates at the outer edge, resulting in a surface tension gradient that leads a Marangoni flow to carry the solute inward to the center of the droplet.

To render functionality in the deposited ink layer, the post-processing step removes the solvents or other additives that form part of the original ink (beyond the functional materials). The main purpose of this step is to fuse the printed functional material into a more uniform layer and/or accelerate processes such as polymers cross-linking. Post-processing is usually achieved in two steps: the drying and the sintering/curing phases. In the drying phase, the solvent is evaporated using low temperatures (~ 100 °C or room temperature) for short times. The sintering/curing can be done by different techniques applying external energy that enhances the functionalities of the ink such as UV, microwave, or plasma treatment. Heat is the most typical technique for sintering. A sequence of the post-process of conductive nanoparticle-based ink is shown in Figure 23.

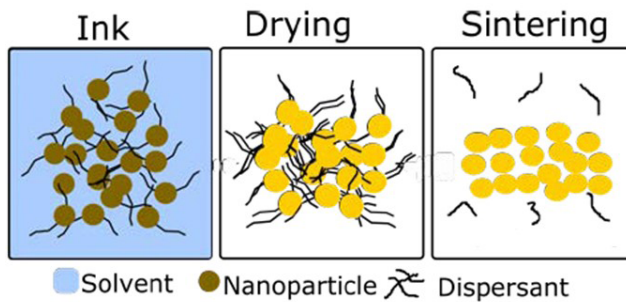


Figure 23. The sequence of post-processing in a metal nanoparticle-based ink. In the drying, the solvent is evaporated using low temperatures or room temperature. The sintering can be done by different techniques such as UV, microwave, plasma treatment, to apply external energy that enhances the functionalities of the ink.

2.5.4. Inkjet printing in the development of flexible electronics and systems

Presenting as a precise, rapid, and low-cost manufacturing approach, inkjet-printing technology has been employed for large-area and high-volume manufacturing of electronic devices and systems. The major strengths of inkjet for flexible electronic systems have been primarily exploited in the manufacturing of sensors and displays as is shown in Figure 24. Other applications include power electronics (both energy storage devices and energy conversion devices), wireless communications, and memory devices.

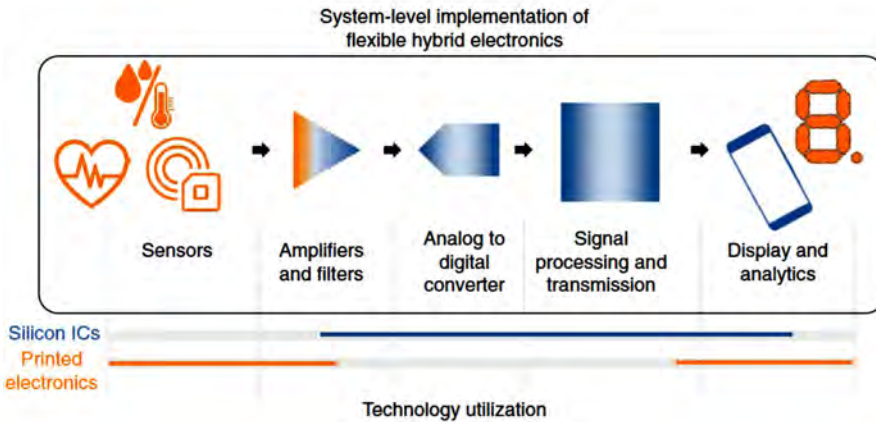


Figure 24. Utilization of technology in the fabrication of devices for flexible electronics. The color bars show where silicon-based technology (blue) and printed electronics (orange) are exploited.

Inkjet printing has been used to fabricate the main components of displays, both the front-plane (for light-emitting) and backplane (for electronic driving). Organic light-emitting diodes (LED),²⁰⁷ polymer LEDs, and quantum dot-based²⁰⁸ LEDs have also been reported. Several of such

devices were fabricated using flexible and biocompatible both substrates and inks to be used in wearable applications. As an example of a back-plane, Lee, Im, *et al.* inkjet-printed the active-matrix based on high mobility polymer transistors to drive a flexible color display.²⁰⁹

To power imperceptible biomedical systems that are worn or implanted, energy storage devices and/or energy conversion devices are a prerequisite. Using inkjet printing, supercapacitors (serving as energy storage units) either all-fully inkjet printed²¹⁰ or partially inkjet-printed²¹¹ have been reported. Photovoltaic devices, which convert the light from the sun to electrical power, have been also fabricated by inkjet printing. The deposition of different layers of such solar cells, this is, electrodes (either front²¹² or back²¹³ electrodes) or the photoactive layer²¹⁴ have been demonstrated. When interfacing electronics with the human body, other sources for energy harvesting can be exploited. Thermoelectric power generators can provide a continuous stable power associated to temperature gradients in wearable or subdermal regions (albeit the human tolerance between 2 and 5 K).¹²⁰ For example, using inkjet printing, Bes-ganz *et al.* have fabricated a thermoelectric nanogenerator that showed thermoelectricity in the 10 mV range and currents in the μA range. They used an ink composite of PEDOT: PSS/ZnO as the thermoelectric materials and Ag-ink for the interconnections.²¹⁵

With the required functionality of wireless communication in flexible electronics systems, the demand for skin-mounted antennas is increasing. Screen printing and inkjet printing have been the most common means for their fabrication.¹⁸⁵ To inkjet print antennas, different inks and substrates have been investigated such as metal-based inks, a composition of metallo-organic inks, and carbon-based inks.^{176,177} The effort for

inkjet printing flexible memory devices have also been important. Kang, Kim, *et al.* have presented an array of 256-bit organic-based memory devices on a transparent, flexible, PEN substrate by inkjet printing.²¹⁶ They investigated the effect of using a blocking dielectric layer and metal nanoparticles as a charge-storage medium which conduced them to use PMMA (for the dielectric) and nanoparticles of Au/AgNP (for the nano-floating gate). The memory device exhibited an $I_{\text{on}}/I_{\text{off}}$ ratio $\sim 10^4$ and a wide memory window of 43.5 V. The working voltages could need to be reduced for wearable applications, but the approach showed a high degree of reliability (they measured over 100 of such memories), and a promising alternative to the current inorganic-based memories that are incompatible with flexible substrates.²¹⁶

Finally, inkjet printing has found enormous opportunities in the fabrication of flexible sensors. Numerous applications ranging from biochemical sensors, photodetectors, and electromechanical sensors have been enabled by the low-cost and easy to scale approach of inkjet printing. The area of applications has, of course, not been limited to on-skin sensors and e-skins. Reviews regarding inkjet-printed tactile sensors,²¹⁷ electrochemical sensors,²¹⁸ protein deposition,²¹⁹ biochemical sensors,²²⁰ thermoelectric materials,²²¹ and wearable devices¹⁹³ exist.

Swisher, Arias, *et al.* have presented an impedance-based sensor¹⁷⁹ to early detect pressure ulcers with gold nanoparticles and thin PEN substrates (45 μm thick). The inkjet-printed sensor¹⁸⁰ comprised 31 electrodes with a minimum feature size of 62 μm . A CO_2 laser was used to cut out freestanding electrodes to allow a better conformability and contact with the skin tissue, minimizing losses in the tissue-sensor impedance interface. Ferrari *et al.* have inkjet-printed disposable, tattoo-based, electrodes

with conducting polymer (PEDOT: PSS) to monitor electrophysiology²²² and alpha waves from the occipital lobe.²²³ During the electrophysiology monitoring, the conducting tattoo enabled hair to grow, maintaining their functionalities in EMG recording for up to 27 h.²²² Inal, Baran, *et al.* have presented a glucose sensor on commercially available paper as a disposable, low-cost, approach to monitor glucose in saliva. All the components (conductive PEDOT: PSS, the biorecognition elements, dielectric, etc.) were inkjet-printed in a layer-by-layer fashion.¹⁷⁸

Inkjet printing has also been attracting interested in fabricated multielectrode arrays (MEAs) for *in vitro* monitoring of electrophysiological signals. Garma, Santoro, *et al.* have presented a plastic/printed MEA to monitor the extracellular potential of cardiac cell cultures.²⁰¹ Adly, Wolfrum, *et al.* have also shown the potential of inkjet printing in fabricating MEAs^{189,224} to record extracellular electrical potentials. Interestingly, for *in vitro* applications the use of inkjet printing is limited and thus the prevalence of silicon-based or glass-based devices for *in vitro* applications still prevails.

Inkjet printing of living cells. The vast potential of inkjet printing technology is not limited to electronics. Indeed, since scientists discovered that living cells can survive the trip through a printer, they have begun to print layers of cells with the perspective of creating artificial organs.²²⁵ With that, some feats towards the goal of printed, transplantable organs have carried their real potential to revolutionize medicine. Although the use of inkjet printing technology (both thermal and piezoelectric) for proteins and hybrid cell-containing materials has been reported, more investigation is required in the field.²²⁶ On one hand, the relatively high temperatures used in thermal inkjet-printing may influence negatively the

printing of living cells or enzymes. On the other hand, the influence of piezoelectric printing jetting parameters (e.g., applied nozzle voltage) on cell viability has not been extensively investigated. Thus, strategies for ad-hoc or in-house 3D bioprinters are an active area of research. For example, Cubo, Jorcano, *et al.* presented a 3D bioprinting platform able to print functional engineered-human skin tested as a dermis substitute *in vivo*.⁵

2.6. CONCLUSIONS AND OUTLOOK

New materials, new devices, new functionalities, and new production techniques could spark a revolution in bio-electronics. To bridge two main sides of science—biology and electronics—is critical to integrate them. Efforts have been geared towards designing electronics to mimic our biological features, but this is only the tip of the iceberg. Not only mimicking but also merging electronics into our biology could be possible in the next future, yet before the total integration between electronic and biological systems can become a reality, more multidisciplinary studies are required.

In this chapter, we have reviewed the key technological factors to render electronic devices soft and biologically compliant: materials, design strategies, and fabrication techniques. Figure 25 summarizes what the chapter outlines based on a recent report on skin-electronics.¹⁰⁸ In such an electronic system, gold and silicon were selected as the materials for the electrodes and devices [(I-Materials) in Figure 25]. Thin films (i.e., nanoribbons) of such otherwise stiff materials were patterning into

a serpentine geometry using well-developed microfabrication techniques [(II-Structural design) in Figure 25]. They were integrated by transfer printing on a more compliant substrate [(III-Fabrication) in Figure 25]. The serpentine-based electrodes stretched >20 %, very similar to the levels of stretchability reached by human skin [(IV-Soft electrodes) in Figure 25]. Sensors and actuators could be fabricated with the soft electrodes [(V-Individual devices) in Figure 25]. An integrated, electronic skin could be ultimately developed to interconnect a prosthetic, e-skin-based hand to peripheral nerve fibers of a rat model [(VI) and (VII) in Figure 25].

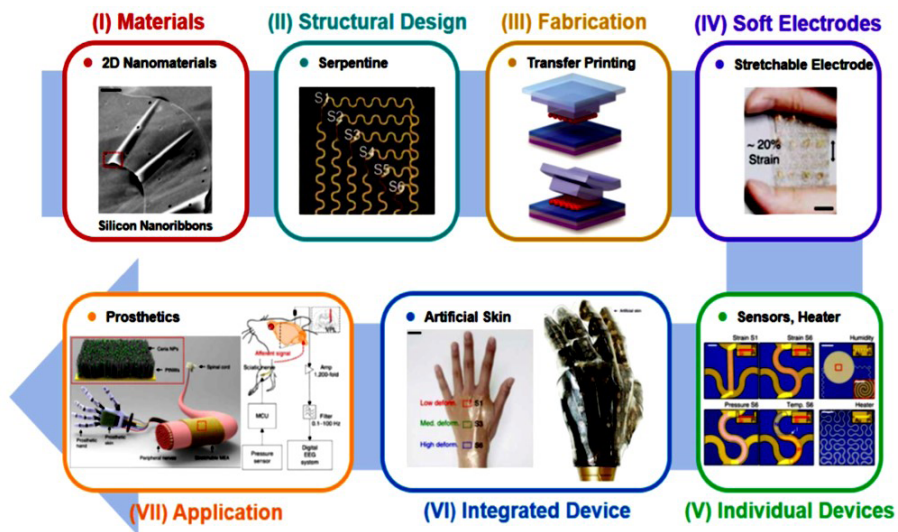


Figure 25. Graphical summary of chapter II based on the description of the electronic skin reported in ¹⁰⁸.

In the domain of flexible/stretchable electronics several strategies have succeeded and facilitated a broad range of applications. For bio-applications, the skin has inspired those designs and strategies as well as

it has attracted a substantial part of such works. Surprisingly, a wide range of applications remains in the concept of on-skin electronics where sensors and/or actuators are externally laminated into the skin. As introduced before in Chapter I, a paradigm-shift gradually emerging in soft electronics goes from skin-mountable electronics to skin with built-in electronics. Monitoring could be carried out during tissue maturation or, if implanted, from the patient's skin.

The efficient integration of electronics (sensors, actuators) into living engineered tissues requires new concepts and compatible solutions in their fabrication. Printing electronics is an attractive platform to engineer such smart skin with built-in electronics. This engineering method has strengthened prevalence as a manufacturing technique in the field of electronics and tissue engineering, independently. As discussed in this chapter, self-sintering conductive inks, sinter-free inks, and low-temperature printable inks for electronics are underway. More collaboration between materials scientists, biologics, and engineers, as well as the expected appearance of new jet-table organic materials (bio-inks- and conducting polymers), can unleash profound progress in this envisioned area.



III. MATERIALS AND METHODS

En teoría todo es práctica.

Miki Naranja

CHAPTER III. Materials and Methods

3.1. INTRODUCTION

Integrating electronics with living cells or tissues remains challenging. On one hand, the proliferation and/or maturation of cells and/or tissues cannot be interfered with by the electronics and, on the other hand, electronics must show the proper performance within the biological environment. In this Chapter III we review the materials, protocols, and assays that have been used to evaluate both devices proposed in the framework of this thesis (sensor and actuator devices that we shall see in Chapter IV and Chapter V, respectively) in such situations. Thus, this chapter covers the materials and methods used in this work that spans from cell biology (cell culture, evaluation, samples' preparation, etc.) to the required manufacturing techniques for both devices.

3.2. CELL BIOLOGY

As mentioned in Chapter I section 1.3 keratinocytes are the most abundant cell type in the skin comprising about 95 % of the epidermis. However, culturing primary human keratinocytes *in vitro* is challenging due to the limited availability of donor's samples from where to isolate the cells, the variability from donor to donor, the relatively short lifetime of the cells, and the difficulty to subculture them in multiple passages while maintaining the differentiative properties. Long-lived, immortalized cell lines may overcome these issues being the spontaneously transformed human epithelial cell line, HaCaT, one of the models most popular used since they maintain full epidermal differentiation capacity after several passages (> 140).²²⁷ HaCaT is a cell line from human adult skin keratinocytes propagated under low Ca^{2+} conditions and elevated temperature which were released from full-thickness dermo-epidermal skin²²⁷ (Figure 26).

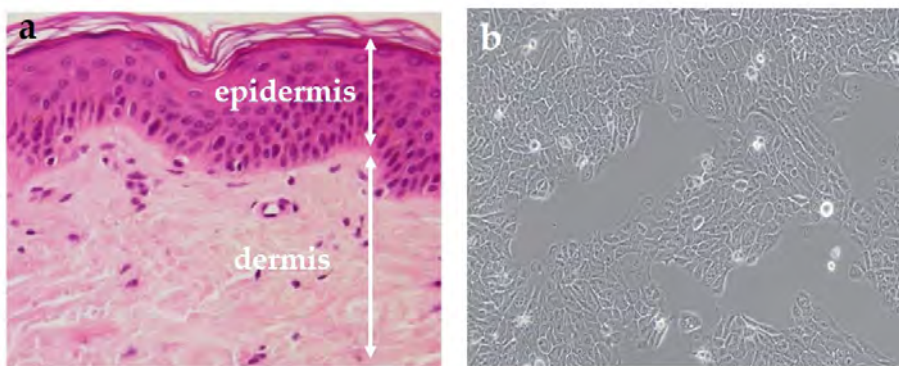


Figure 26. a) Histological slide of skin tissue and b) HaCaT cell line cultured *in vitro*. HaCaT is a cell line from human adult skin keratinocytes propagated under low Ca^{2+} conditions and elevated temperature which were released from full-thickness dermo-epidermal skin. Note: a) adapted from Lai-Cheong and McGrath, 2017.²²⁸

For this thesis, HaCaT cell line was used as the biological model to test the viability and use of the proposed devices (actuator/sensor). The preparation of the cells and culturing media is described in section 3.2.1. In addition, the different cell-based methods performed (a) to determine both the cytotoxic effects of devices on the cell culture and the proliferative activity, (b) to fluorescently label different structures in the cell and (c) to treat the surfaces of the devices are described in section 3.2.2 and 3.2.3, in section 3.2.4 and 3.2.5, and in section 3.2.6 respectively. Finally, the preparation of the cultures for investigating the cell morphology and the actual effect of cell membranes on the engineered sensing device of Chapter IV is described in section 3.2.7 and 3.2.8 respectively.

3.2.1. Cell line, media and transfection

A spontaneous aneuploid immortalized human epidermal keratinocytes cell line (HaCaT) has been used for all the biological experiments in this thesis (see ref. ²²⁷ for details of the cell line). The HaCaT cell line was provided by CIEMAT (Centro de Investigaciones Energéticas Medioambientales y Tecnológicas, Madrid, Spain). The cells were genetically modified (transfected) with Green Fluorescent Protein (GFP) in the laboratories of the Mixed Unit of Biomedical Engineering UC3M-CIEMAT, but this transfection is out of the scope of this thesis. When transfected, the HaCaT cells acquire a retroviral vector and express a green fluorescent phenotype which enhances visualization. This transfected cell line was named HaCaT-GFP.

Cells were cryopreserved at $-83\text{ }^{\circ}\text{C}$ (Unicryo DW-86L286) in freezing media containing 10 % v/v dimethyl sulfoxide (DMSO, Sigma Aldrich) in 90 % FBS (fetal bovine serum, Sigma Aldrich) in cryotubes containing 2×10^6 cells $\cdot\text{ml}^{-1}$. For passaging, HaCaT/HaCaT-GFP cells were de-frozen and cultured in polystyrene dishes P100 (100 mm diameter, 78 cm², ThermoFisher Scientific) in basal medium. Culture basal medium was prepared with Dulbecco's Modified Eagle Medium with high glucose content and sodium pyruvate (DMEM, Invitrogen Gibco) supplemented with 10 % v/v FBS (Fetal Bovine Serum, Thermo Scientific HyClone) and 2 % v/v antibiotic/antimycotic solution (10^5 U $\cdot\text{ml}^{-1}$, 10^4 $\mu\text{g}\cdot\text{ml}^{-1}$, respectively, Thermo Scientific HyClone). When required, culture media without phenol red were prepared identically, except that in this case, DMEM (no phenol red, Invitrogen Gibco) was transparent. Cells were cultured at $37\text{ }^{\circ}\text{C}$, 38 % humidity, 5 % CO₂, 95 % air in a cell incubator (Shel Lab CO₂ Serie; Sheldon Mfg. Inc). The culture medium was changed every 2-3 days.

When 80 % confluence (condition assessed by microscopy and experimentally) was reached, cells were sub-cultured. The medium was removed through aspiration, samples were rinsed with PBS (Phosphate buffer serum), and trypsinized with 1 mL of trypsin (0.25 % EDTA) for 10 min at $37\text{ }^{\circ}\text{C}/5\text{ }^{\circ}\text{CO}_2$. The detachment of cells from the bottom of the plate was confirmed by microscopy observation. Once checked, 5 mL of culture medium was immediately added to the Petri dish to inhibit trypsin action. To remove clumps and resuspend the cells, the solution was pipetted up and down several times and transferred to a 15 mL conical centrifuge tube (Corning™ Falcon Tubes, ThermoFisher) to be centrifugated at 1000 revolution per minute (rpm) for 7 minutes with a balance of the same volume (Centrifugator, OrtoAlresa, Spain). The resultant supernatant (i.e., 5 mL of culture medium plus 1 mL of trypsin) was poured off and a fresh

medium was added at the deposited cell remaining at the bottom of the tubes. The new solution was resuspended to perform cell counting.

To perform cell counting, a sample of 10 μL was used by the hemocytometer-based method. To improve the statistics of cell count, the sample was transferred at least to two independent slots in the Neubauer's chamber.

Cellular cultures were always manipulated inside biosecurity cabins (Telstar, Bio IIA/G) at the Biomedical Engineering Laboratories at Carlos III University (Molecular Biology and Cell Biology laboratories). The laboratory is rigged with Class II Biological Safety equipment and all personal must follow the biosafety regulations according to the specifications in the current guideline.²²⁹ There are no ethical issues to be discussed in this thesis since the cellular components used do not directly come from any patient as well as confidentiality procedures are not specifically needed.

3.2.2. Alamar Blue assay

AlamarBlue® is a commercial assay (BUF012A, Bio-Rad AbD Serotec Ltd.: Hercules, CA, USA) used as an indicator of cell metabolic activity and viability based on the dye indicator resazurin. Viable cells reduce resazurin to resorufin (fluorescence emission of different wavelength), which serve as a fluorometric/colorimetric indicator of the number of viable cells. This reduction is caused by increased activity of the enzyme lactate dehydrogenase during proliferation.²³⁰ An increase of fluorescence/absorbance in the Alamar blue (AB) reaction over time

has been used as an indicator of proliferation.²³⁰ AB has been demonstrated to be minimally toxic to cells and provides a stable, distinct signal.²³¹ This non-toxicity allows the same cell sample to be followed for the duration of an experiment.

The AB assay is explained in detail in references number ²³¹ and ²³². In our case, the AB reactive medium was prepared with a dilution of 1: 10 of AB's rezasurin and phenol-red-free medium, respectively. The resulting solution was mixed and sterilized by filtration (Acrodisc® syringe, VWR and filters with average pore size 0.20 μm, ThermoFisher). The culture medium in cell cultures was substituted with AB reactive medium. The protocol used in this thesis for the different experiments described in Chapter V and Chapter IV was as follows.

To diminish the influence of phenol-red in the measurement, the basal culture medium was eliminated and samples were washed with PBS twice. Subsequently, 2 mL of the AB reactive media was added to each sample and incubated for 4 h. After reacting, the AB supernatant medium in the samples for every group (i.e., experimental group and control) was removed and placed into 96-well plates (in samples of 200 μL to improve statistic and reduce instrumental errors) for absorbance analysis (using a microplate reader ELISA, Clariostar, BMG Labtech, Ortenberg, Germany). For the negative control, 2.5 mL of AB reactive medium was added to sterile flasks without cells. All these procedures were carried out in dark conditions. A flow chart of the protocol is summarized in Figure 27.

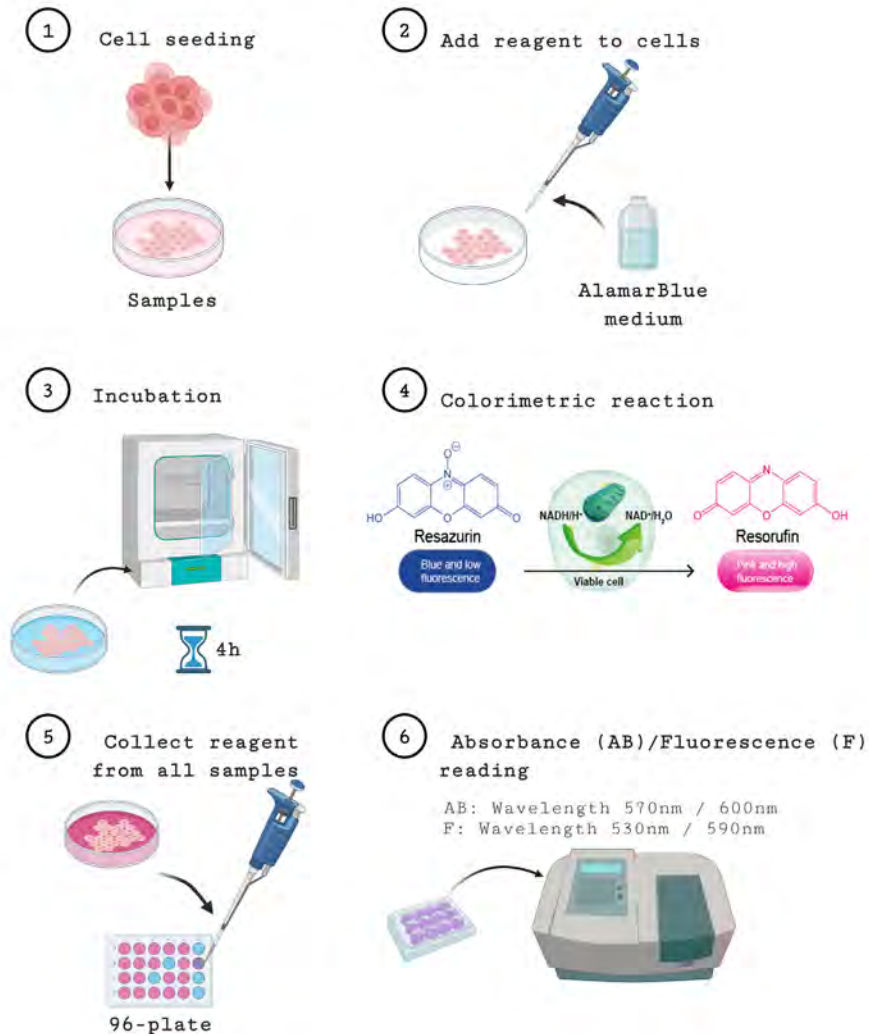


Figure 27. Flowchart of the Alamar Blue protocol used in this thesis.

The absorbance was measured at 570 nm and 600 nm, corresponding to the reduced and oxidized excitation wavelengths respectively. The absorbance reduction percentage (PR%) was calculated by applying the formula (4):

$$PR(\%) = \frac{(\epsilon_{ox})\lambda_2 \cdot A\lambda_1 - (\epsilon_{ox})\lambda_1 \cdot A\lambda_2}{(\epsilon_{red})\lambda_1 \cdot A'\lambda_2 - (\epsilon_{red})\lambda_2 \cdot A'\lambda_1} \quad (4)$$

where ϵ_{ox} and ϵ_{red} are the molar extinction coefficients of the oxidation and reduction forms of AB, respectively, A is the measured absorbance of the samples, A' is the absorbance of the negative control, λ_1 is the wavelength of 570 nm, and λ_2 the wavelength of 600 nm.

The values needed to solve equation (4) in the AB used in this thesis are listed below in Table 2.

Table 2. Values of the molar coefficients in the oxidation and reduction of the Alamar Blue.

Wavelength	ϵ_{ox}	ϵ_{red}
570 nm	155.677	80.586
600 nm	14.652	117.216

The procedure described above was carried out at different times during the experiments. Day 0 always coincided with 24 h after cell seeding. The percentage reduction (PR%) was normalized using the average value obtained for the control devices on the last day of the experiment prior to statistical analysis.

Data of the redox reaction in the AB assay can be also collected using fluorescent-based instrumentation. When attempting to detect very small changes in reduced resazurin, fluorescent measurements have shown to produce greater sensitivity.²³² Therefore, a fluorescent detection method was chosen as complementary to the absorbance's

one. Fluorescent measurements were made on a Synergy HTC microplate reader (ELISA, Synergy HTC, BioTek, Ortenberg, Germany), settings the excitation wavelength at 530 nm and emission wavelength at 590 nm. To determine the results in the AB assay based on fluorescent measurements, the read fluorescence values of the treated samples (i.e., cells seeded on the device of Chapter IV) were normalized to the fluorescence values of the untreated samples (i.e., controls) at each day. The resulted ratio was then analyzed using statistical methods as described in section 3.3.4.

3.2.2.1. Alamar Blue as an indicator of cytotoxicity and proliferation

For evaluating the cytotoxicity and proliferation of cells seeded on the actuator devices of Chapter V, 2×10^5 cells (2.8×10^4 cells·cm⁻²) in 2.5 mL of the supplemented basal medium were seeded. Samples named **control culture** were p60 Petri dishes (Ø 60 mm., Corning™ 430107, Fisher Scientific, Barcelona, Spain) with a mold of rings made of PDMS to confer a circular area of 30 mm in diameter. Samples named **static control** were piezoelectric devices without stimulation (described in Chapter IV). The **experimental samples** were piezoelectric-based devices (FR, described also in Chapter V), excited at different frequencies depending on the experiment. The FR devices were stimulated with a frequency equal to 1 Hz or 80 Hz during an experimental period of 6 days.

AB assay was carried out on days 0, 1, 3, 6, and 8 in all samples. After collecting the data from the AB assay on day 0, the stimulation of FR plates started, being thus the same condition for all samples at day 0 (no stimulation).

Image acquisition was also performed to visually confirm the relationship of the percentage reduction of AB reagent with proliferation instead of because of other cellular metabolic reactions.

3.2.3. Live/Dead Kit Assay

The Live/Dead kit (Invitrogen™ Molecular Probes™ LIVE/DEAD™ Viability/Cytotoxicity Kit, Fisher Scientific, Spain) is a fluorescence-based assay to assess via two-color discrimination live cells from the dead cell population simultaneously. Two fluorescence reactive (calcein-AM at emission/excitation wavelengths of 494/517 nm and Ethidium homodimer-1 at emission/excitation wavelengths of 517/617 nm) stain the cell's structure and indicate the health of the cultured cells.

After 3 days in vitro (3DIV), the cultures were stained using a solution containing 2 mL of PBS with 0.6 μ L of calcein-AM (final concentration of 2 μ M) and 2.4 μ L ethidium homodimer-1 (final concentration of 4 μ M). The culture medium was aspirated and the solution of the Live/Dead kit was added to each sample for 30 min in darkness condition.

The stained cultures were imaged using a 10x objective microscope with an appropriate filter for each fluorophore. A minimum of 30 images around different sites over the samples was taken and analyzed by using both a self-programming script in MatLab and ImageJ software. An average of the number of Live/Dead cells was reported as the cell viability of the assay.

3.2.4. Cell fixation for immunofluorescence

Direct immunofluorescent were carried out to study the morphology of cells. In direct immunofluorescence-based experiments a primary antibody has fluorescence properties being unnecessary a second antibody. Cells were rinsed with PBS twice and fixed using paraformaldehyde diluted to 4 % v/v in distilled H₂O. 2.5 mL of the fixed solution was left on samples for 20 min at room temperature. The reactive was removed and samples were washed thrice with PBS. Then, samples were permeabilized with a 0.1 % v/v Triton X-100 (Sigma Aldrich) in PBS for 15 min and non-specific epitopes were blocked with 1 % v/v BSA (Bovine serum albumin, Sigma Aldrich) in PBS for 30 min.

The antibodies were diluted in blocking solution (i.e., 1 % v/v BSA dissolved in PBS), and applied to cells for 90 min, with three washes with PBS between each antibody application.

3.2.5. Antibodies and Reagents

Actin was visualized using Toxin Phalloidin Alexa Fluor™ 488, ThermoFisher. 1.5 mL of fluorescent-phalloidin solution was added to the samples (1:1000 v/v in blocking solution) for 90 min at room temperature. Vinculin was marked using Monoclonal Anti-Vinculin-FITC antibody F7053, Sigma. 1.5 mL of a solution in a proportion 1:200 v/v antibody in blocking solution (final concentration of 1 $\mu\text{g}\cdot\text{ml}^{-1}$) was added to the cultures for 90 min in darkness condition at room temperature. To visualize cell nuclei, DAPI (4',6-Diamidino-2-phenylindole dihydrochloride) (1 $\text{mg}\cdot\text{ml}^{-1}$, Sigma

Aldrich) was diluted 1: 1000 v/v in PBS (concentration of $1 \mu\text{g}\cdot\text{ml}^{-1}$) and 1.5 mL of the solution was added to samples for 10 min at room temperature. Samples were carefully mounted onto glass slides using a mounting medium with DABCO (1,4-diazabicyclo[2.2.2]octane) (M1289, Sigma Aldrich) for microscopy visualization

3.2.6. Coating of actuators, sensors, and bottom dishes

To promote cell adhesion the surfaces of all samples (controls, sensors, and actuators) were coated with collagen Type II. The coated solution was prepared at 1:20 v/v collagen solution (Sigma Aldrich, 0.20%, Type II from Calfskin, Sigma Aldrich) in PBS. 2.5 mL of collagen solution was added to samples covering the complete surface. They were left exposed to UV radiation for 2 h inside a biosecurity cabin to promote crosslinking. The remaining solution was removed, and samples were washed with PBS twice.

3.2.7. Cell fixation for morphology observation

For topographical observation, samples were fixed with 2.5 % v/v glutaraldehyde (Sigma Aldrich) in H₂O distilled at room temperature for 1 h and later washed three times with PBS. Thereafter, samples were dehydrated for 5 min by subsequent passes of samples through 30 % ethanol (EOH), 50 % EOH, 70 % EOH, and 100 % EOH. Samples were left to air-dried inside the biosecurity cabins.

3.2.8. Cell treatment for impedance-based detection of chemicals

To investigate the effect of cell membranes in the electrical signal measured using the sensors of Chapter IV a non-ionic detergent (Triton X-100) was added to the cell cultures. Triton X-100 (Sigma Aldrich, Spain) was dissolved at 0.1 % v/v in PBS. The culture medium was removed and 2 mL of the solution containing Triton X-100 at 0.1 % was added. The impedance was continuously acquired for 23 min every 60 seconds. A range of frequency from 100Hz-1MHz was configured. At 23 minutes, images of the cells on the sensors were taken by a microscope.

3.2.9. Migration assay using a PDMS stencil

To monitor cellular migration using the sensors developed in Chapter IV, the protocol described in ²³³ was performed. In this protocol the artificial wound is created by using a stencil of PDMS avoiding cell damage at the edge of the wound. A stencil with an area of 3.57 cm² was used to generate a wound and cells were seeded on the non-exposed PDMS area at a density of 1.2×10^6 cells which ensured confluence the following day. Cells were left attached to the sensors overnight. The following day the stencil was removed which left an opening space for the cells to migrate until new cell-cell interactions are created. Images of the front edge of the boundaries created by the stencil were captured at a time interval of 6 h. A summary of the protocol is shown in Figure 28.

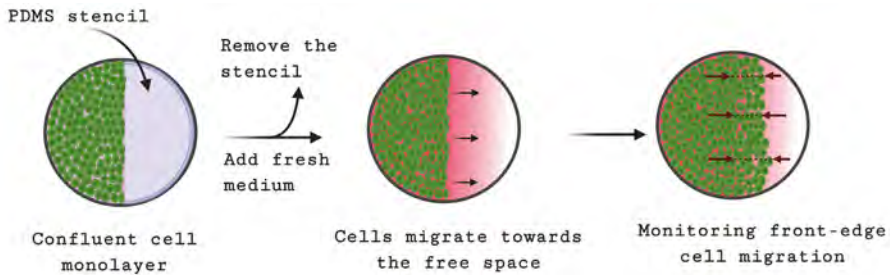


Figure 28. Schematic representation of the cell migration protocol using a PDMS stencil.

3.2.10. Migration assay using Scratch assay

To study the effect of mechanical stimulation on cellular migration using the actuators of Chapter V the biological method called scratch assay was performed. This economical protocol extensively exploited in cell biology to assess cell migration *in vitro* under a variety of experimental conditions relies on the following observation. Upon the generation of an artificial wound (a scratch) on a confluent cell monolayer by scraping the cell sheet, the edge-front of cells at the boundaries of the created gap will migrate toward the opening to close the so-called scratch until new cell-cell junctions are attained again. Having produced a scratch on monolayer cells, capturing of images at regular intervals to track the front edge of the cells can be used to determine the rate of cell migration.

The experiments were performed by seeding in the experimental samples presented in Chapter V 1.44×10^6 cells (2.03×10^7 cell/cm²) in 2.5 mL of culture medium overnight. The next day, the scratch wound

was manually generated using a p100 micropipette (LabBox, \varnothing 1.2 mm.). The culture media was eliminated, and samples were gently washed with PBS to remove cellular debris. Finally, samples were replaced with 2.5 mL fresh media to ensure the correct evolution of the cellular samples. Time 0 of the experiments are referenced to this moment. Images to monitor the state of the wound were taken at 0, 9, 24 and 30 hours after the scratch was firstly done by capturing more than four areas along the scratch. A summary of the protocol described is shown in Figure 29.

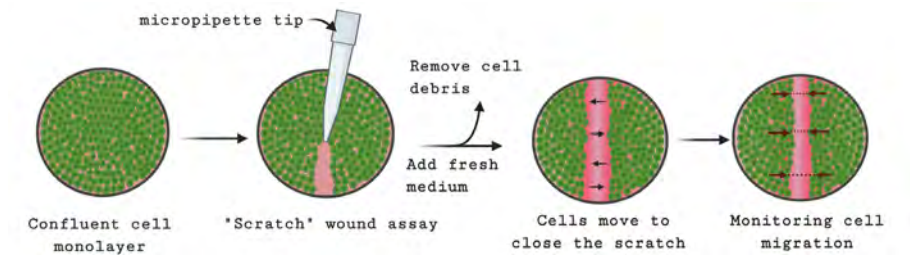


Figure 29. Schematic depicting the scratch protocol to study cell migration.

3.3. MICROSCOPY, IMAGE PROCESSING AND ANALYSIS

3.3.1. Microscopy equipment and Profilometry

To obtain the images of the cell cultures involved in the experiments of Chapter IV, a Leica DMI8 Inverted Microscope (Leica Microsystems CMS GmbH, Wetzlar, Germany) equipped with a CCD camera (Olympus DP26) and

its proprietary software LASX Navigator (Leica Microsystems) were used. The microscope is integrated with a bioreactor which maintains stable conditions of 5 % CO₂ and 37 °C suitable for cell survival during the prolonged time-lapse/impedance experiments. Both microscopies equipped the filters used for immunofluorescence experiments: specifically, they were 390/450 nm (GFP excitation/emission), 543/569 nm (TRITC excitation/emission), 350/470 nm (DAPI excitation/emission), and 494 nm/520 nm (FITC excitation/ emission).

The images of the cell cultures involved in the experiments of Chapter V were obtained (software: analySIS-getIT, Olympus®) using a fluorescence microscope (Model BX53, Olympus Inc., Japan) equipped with a CCD camera (Olympus DP26) and an Olympus U-RFL-T mercury burner.

Finally, to evaluate the morphology of the sensors presented in Chapter IV, a profilometer (Bruker DektakXT Stylus Profilometer, Germany) was used. The scanning was configured with a force in the tip of 10 m-g and a scanning time of 65 μs.

3.3.2. Scanning electron microscopy

For Scanning Electron Microscopy (SEM), samples of approximately 5 mm in diameter were mounted on standard aluminum stubs of 18 mm through a carbon double-size adhesive tape. They were treated by gold sputtering technique (Leica EM ACE200, Spain) for 90 seconds before imaging. Samples were visualized under vacuum conditions using a photodetector Philips XL-30. The scanning electron beam voltage was set at 15 kV. For cross-sectional imaging, samples were previously treated in liquid nitrogen for 30 seconds and sharply cut them.

3.3.3. Biological Image processing

All image analysis was performed using either a self-programming script in MatLab (vR2019b, MathWorks) with an Imaging Processing Toolbox or ImageJ (1.52t, NIH, USA).

3.3.3.1. *Live/Dead assay*

To quantify the number of live and dead cells, images obtained at the emission wavelength of each fluorophore (see 3.2.3), the images from each wavelength were stored and processed as separate images. To detect cell's borders and quantify the number of cells, images were transformed into binary ones and a programmed script detected the cells (by a segmentation algorithm) and quantified the resulted average of live and dead cells by applying the formula (5), which it was reported as the cell viability of the assay.

$$\text{Viability} = \frac{\text{Live cells}}{\text{Total cells}} * 100 \quad (5)$$

3.3.3.2. *Cell migration and analysis*

To determine cell velocity in the front-edge of cells equation (6) was applied.

$$v = \frac{\text{Distance}_{t_f}(\mu\text{m}) - \text{Distance}_{t_0}(\mu\text{m})}{\text{Total time (h)}} \quad (6)$$

where Distance_{t_f} is the displacement of the edge of a cell at a time point and Distance_{t_0} is the displacement at a time 0 (beginning of the experiment). Total time is the duration of the experiment.

To adjust the displacement of cells to a recovery degree of the wound the following equation (7) was applied.

$$\text{RD} = \frac{\text{Mean edge displacement}_{t_f}(\mu\text{m})}{\text{Total displacement}(\mu\text{m})} * 100 \quad (7)$$

where RD is the recovery degree of the wound in percentage, Mean edge displacement $_{t_f}$ is the displacement of the front cells at an observed time, and Total displacement the total area to be recovered by the cells over the sensors.

3.3.3.3. Cell migration in the scratch assay

To measure the width of the scratch over time, the front-edge of cells along the scratch was detected using at least four different areas photographed along such artificial wound. Widths were normalized to time 0 for each scratch.

The area reduction due to migration was determined according to equation (8):

$$\text{Migration area reduction} = \frac{A_t}{A_0} \quad (8)$$

where A_0 is the mean initial area and A_t is the mean area within the wounds' boundaries at time t .

3.3.3.4. Size of the Nucleus

To analyze the size of the nucleus DAPI images were segmented. The segmented images were fitted to an ellipse in which the length and width of the nucleus correspond to the long and short axes of the ellipse, respectively. Then, the histogram of the values of long axes was fitted to a log-normal distribution. Based on the log-normal fitting the average size of the nucleus was determined according to equation (9):

$$D_{\text{mean}} = D_0 \cdot e^{-\left(\frac{\sigma^2}{2}\right)} \quad (9)$$

where D_0 is the center of the distribution of the fitting and σ is the standard deviation in the fitting.

3.3.4. Statistical analysis

For the statistical analysis a grouped analysis two-way ANOVA was implemented by either GraphPad Prism or Origin Pro 9.0. When assays and samples and the statistical test were performed several times, adjustments of standard errors due to such repetitions were obtained through

post-Bonferroni corrections.²³⁴ Each group of samples was compared to all the others and *p*-values were examined. *P*-values higher than 0.05 were not considered as significant differences between samples and a confidence interval of 95 % was always used. Results from the statistical analysis were depicted in the figures in the form of asterisks: the higher number of symbols the higher the significance between the samples and the control values.

In the cytocompatibility and proliferation assays the reduction percentages (*y*-axis) from the absorbance-based measurements were normalized to the maximum value reached by the negative control at end days. Initial zero values do not correspond with a 0 % AB reduction at the start in all samples, but every culture had subtracted its initial reduction percentage for setting a common reference point at the origin. For the fluorescence-based data this normalization to the maximum value was not made. Instead of this, a grouped analysis two-way ANOVA was implemented directly to the fluorescence ratio (i.e., ratio of experimental samples to controls) followed by a Bonferroni post-test and a confidence interval of 95 % was applied to examine the *p*-values.

In the scratch assay the wounds' area values were normalized to the area at time 0 —the initial area of the wound— so that the area reduction at different times is expressed as a ratio of the initial area. The normalized values were analyzed with a linear regression fit with a confidence interval of 95 %.

In the nucleus size analysis, the average sizes in the experimental groups were normalized using the average value obtained for the control cultures at that specific time (i.e. at 48 h).

3.4. PDMS CURING

A base and a curing agent of the PDMS fabrication kit (Sylgard® 184, Dow Corning) was used in a proportion of 10:1 base-curing agents. The rigidity of the final elastomer depends on the base and curing agent ratio.²³⁵

Base and agent curing were weighted (analytic balance Ohaus Voyager, Ohaus, Switzerland), mixed, and stirred until a homogeneous mixture was obtained. Air bubbles at the mixture were eliminated using a vacuum chamber and the mixture was next poured onto the master mold. To enhance the curing process, molds were introduced in a preheated oven (Model 100-800, Memmert GmbH, Germany) at 70 °C for 1 h.

3.5. DESIGN AND FABRICATION OF THE SENSORS (CHAPTER IV)

In this section 3.5 the materials and methods used for the development and characterization of the sensors presented in Chapter IV as well as the methodology for their testing are described.

3.5.1. Inkjet printing of interdigitated sensors

Figure 30a shows the geometry and structure of the designed interdigitated sensor that we shall see in Chapter IV. As shown in Figure 30a both

the gap between two consecutive lines and the width of the printed lines were $300\ \mu\text{m}$. The active area of the sensors (without considering the contact pads) was $195\ \text{mm}^2$ with 22 interdigitated electrodes (IDEs) fingers of $12.7\ \text{mm}$ length each. A rectangle of $13 \times 14\ \text{mm}$ was used to passivate the active area of the sensors which resulted in a nominal area of $182\ \text{mm}^2$.

The fabrication process (based on inkjet printing) is comprised of two steps (Figure 30b,d). First a conductive ink (one single layer) was patterned and stacked on the substrate followed by the printing of a dielectric ink (three layers) on top of the previously printed conductive lines. Working (WE) and counter (CE) electrodes were formed by the conductive lines. The dielectric ink forms the passivation which became the substrate for the cell cultures.

To print the conductive lines and the passivation a drop space of $15\ \mu\text{m}$ and $20\ \mu\text{m}$, respectively, were selected. These drop spacings correspond to a printer resolution of 1693 dots per inch (dpi) and 1270 dpi, respectively.

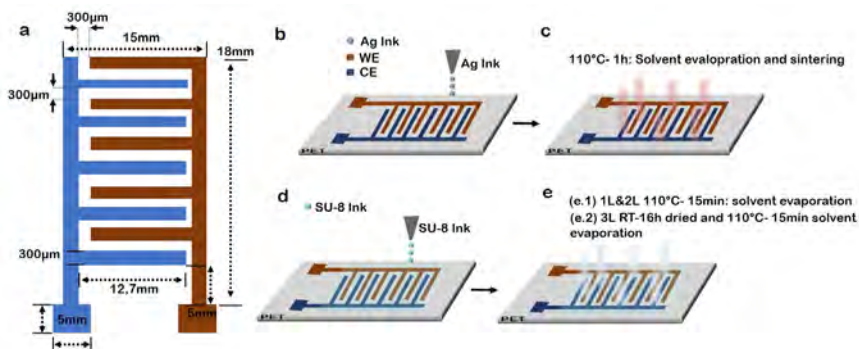


Figure 30. a) Sketch of the printed sensors (Chapter IV) with dimensions and b)-e) manufacturing process for the inkjet printing coplanar capacitors. Materials and details of the process are summarized within the figure.

The method for the printing process was as follows (Figure 30b-e). The interdigitated electrodes (Figure 30b) were firstly patterned. Then, the conductive ink was thermally dried and sintered at 110 °C for 1 h (Figure 30c). Three layers of SU-8 ink were inkjet-printed onto the IDEs lines (Figure 30d). After printing the first layer and the second layer of SU-8 the pattern was dried at 110 °C for 15 min (Figure 30e). The latest layer was dried at room temperature for 16 h and post-baked at 110 °C for 15min.

A piezoelectric inkjet Dimatix Material Printer (DMP-2800TM, Fujifilm-Dimatix, Inc., USA) was employed for manufacturing the sensors. The printer was equipped with 10 pL nominal drop volume printheads that are user fillable. The printhead had 16 nozzles, each of them with a diameter of 21.5 μm (DMC-11610).

To create the patterns to be printed, the GIMP editor program (a free downloaded image manipulator program) was used. Once designed the structure, the files were imported using the Dimatix Bitmap layout software with a subsequent scaling.

Sensors were printed using the activation of substrate vacuum. The temperature of the printhead was controlled at 28 °C for the silver ink and 40 °C for the SU-8 ink. The temperature of the bedplate was heated up to 45 °C and 31 °C for Ag ink and SU-8, respectively. The fabrication process was carried out in a standard laboratory environment in ambient conditions. Cartridges for each ink were filled with about 1 mL after filtration (Minisart® syringe filters, average pore size 0.20 μm , Sartorius GmbH, Germany).

To post-process the deposited inks, a convection oven (100-800, Memmert) in an air atmosphere was used. The annealing time should be selected considering the ink. A low annealing time could produce unstable results in the sintering process and increasing the temperature could damage the PET substrate,^{236,237} as the transition temperature (T_g) for PET is 120 °C according to the manufacturer.

3.5.2. Materials for inkjet printing the sensors

A silver-nanoparticles ink (AgNP, 796042 Ag, Sigma Aldrich (NBSIJ-MU01, with 15 % Ag, Ethylene glycol 15-25 %, ethanol 1-2 % and water 50-70) was used to fabricate the working and counter electrodes in the interdigitated sensors, the contact pads, and the feed lines. A SU-8 ink (MicroChem PriElex® SU-8, MicroChem Corp., Massachusetts, USA) was employed for the passivation of the sensors. Both inks are commercially available and show drop-on-demand inkjet specifications compatible with the printer platform. They were used as received after filtration. A polyethylene terephthalate film (PET foils, Mitsubishi Paper Mills) with a thickness of 100 μm was chosen as substrate.

3.5.3. Assembly of IDE-based devices

A silver epoxy EPO-TEK®H20E (Epoxy Technology, Inc.) was used to solder cables to the pads of the sensors. Two parts (part A and B) of the epoxy were weighted (analytic balance, Ohaus, Voyager) and mixed. Cables were soldered in the IDEs pad by curing the epoxy for 30 min at 110 °C (100-800, Memmert).

One-side adhesive Kapton® films were used to isolate the exposed welding. The IDEs were glued to the bottom of Petro dishes (Ø35 mm, ThermoFisher Scientific, Spain) by using either a biocompatible silicone grease (Dow Corning™ High-Vacuum Grease, Fisher Scientific, Spain) or a thin layer of polydimethylsiloxane (PDMS, Sylgard® 184, USA). To take out the cables from the cell culture dishes, lateral holes were pierced with a drill of 2 mm (Dremel®, 8100 Model) and externally sealed using hot silicon (glue sticks of 11 mm), avoiding any leakage of the culture medium.

3.5.4. Protocol for impedance spectroscopy and data processing

To acquire the impedance (magnitude and phase) a 25-mVp sinusoidal signal with no DC component was applied to the sensor. The impedance response was acquired at 15 points per decade from 100 Hz to 1 MHz (bandwidth) using an ISX-3 mini impedance analyzer (Sciospec Scientific Instruments GmbH, Germany) and accompanying software (Sciospec ISX3v2). The impedance analyzer can be configured using the user interface software to record the impedance spectra at configurable periods of time, allowing also real-time measurements. The setup was configured to operate in four-wire impedance measurements minimizing the main parasitic contributions that may come from both the lead and the contact resistances. An average of three repetitions for each impedance frequency point was acquired. To characterize the electrical performance of the sensors, the impedance was acquired at room temperature in 2 mL of culture medium pre-warmed at 37 °C. To perform the cellular experiments impedance was monitored under physiological conditions of 37 °C, 5 % CO₂.

Impedance data were analyzed using ZView® software from Scribner Associates to fit the data to a theoretical model (Chapter IV) and Origin Pro9 to process and plot the curves. The measured impedance was fitted to an equivalent electrical circuit to model the physical phenomena take place on the surface of the sensors. The electrical model and the physical interpretations of the processes were obtained using a non-faradic analysis of the cell-sensor interactions. To evaluate the quality of the fitting, the experimental data were compared with the mathematical fitting from the equivalent circuit. The quality of the fitting circuit was determined using chi-squared (χ^2) values representing the square of the standard deviation between the experimental data and the calculated spectrum from the fitting. For $\chi^2 < 10^{-2}$ the fitting was considered as accurate, dictating the feasibility of the equivalent circuit for representing the physical (cellular) process.

In addition to the equivalent circuit, alternative processing of the impedance data was used. To study the temporal variation of the normalized impedance, a dimensionless parameter called cell index²³⁸ was estimated (equation (10)). As the impedance data were acquired over multiple hours during the experiment, the estimation of this cell index allows to observe and quantify the tendency of the impedance at a single frequency as defined in equation (10):

$$\text{cell index (t)} = \max_{i=1, \dots, N} \frac{|Z(t, f_i)| - |Z(0, f_i)|}{|Z(t, f_i)|} \quad (10)$$

where $|Z(0, f_i)|$ is the magnitude of the impedance at the beginning of the experiment at given frequency i , and $|Z(t, f_i)|$ is the magnitude of the impedance at the same frequency but at a given time point (t) along the experiment.

3.6. DESIGN AND FABRICATION OF THE ACTUATING SYSTEM (CHAPTER V)

In this section 3.6 the materials and methods for the development of the actuator-based devices (Chapter V) are presented.

3.6.1. Materials for fabricating the experimental stage

A PVDF film (polyvinylidene fluoride, see ref ²³⁹ for details on this polymer) with a thickness of 28 μm and polarized in its transverse axis (CAT-PFS0003, TE Connectivity: Schaffhausen, Switzerland, 80 mm \times 110 mm) was used as the piezo-actuator element. A copper adhesive tape (3M TM; 1181-12, 3M: St. Paul, MI, USA) was used to connect the external cables to bias the piezo material. The original PVDF film was cut into 25 \times 35 mm pieces to fit the Petri dishes.

To passivate the conductive layer of the piezoelectric film, a single-sided adhesive polyester film (3M TM, 58 μm in thickness) was used. This passivation avoided direct electrical stimulation of the cell culture when the piezoelectric material was biased. The height of the Petri dishes was reduced to 15 mm using mechanical tools (Dremel[®] 8100 Model, Dremel[®], Racine, WI, USA) to meet the available microscopy's space for sample observation. The cables exit through holes (2 mm in diameter) on the z-axis of the Petri dish.

The dimensions and a schematic of the actuating device to culture the cells and perform the studies of mechanotransduction presented in Chapter V are shown in Figure 31. Figure 31a shows a top view of the experimental stage including the main parameters of the design. Figure 31b depicts a schematic of the lateral view of the device (i) without no cell culture nor electrical stimulation, (ii) with a cell culture seeded on the collagen-coated device under static conditions, and (iii) the cell culture under dynamic conditions.

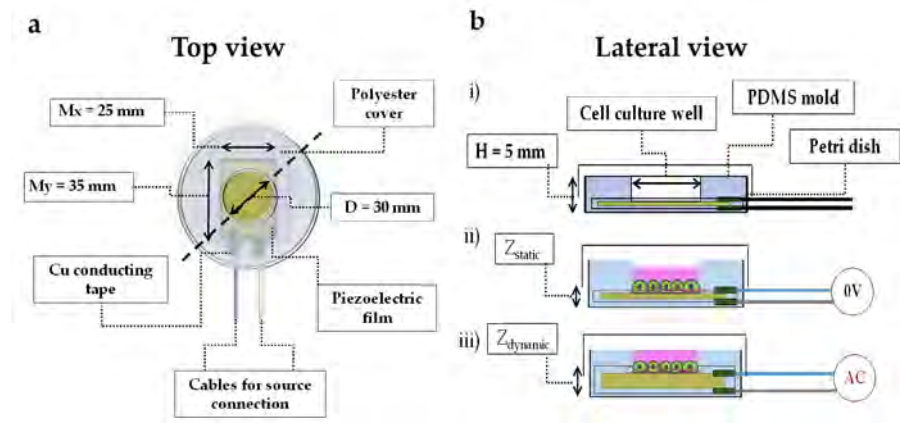
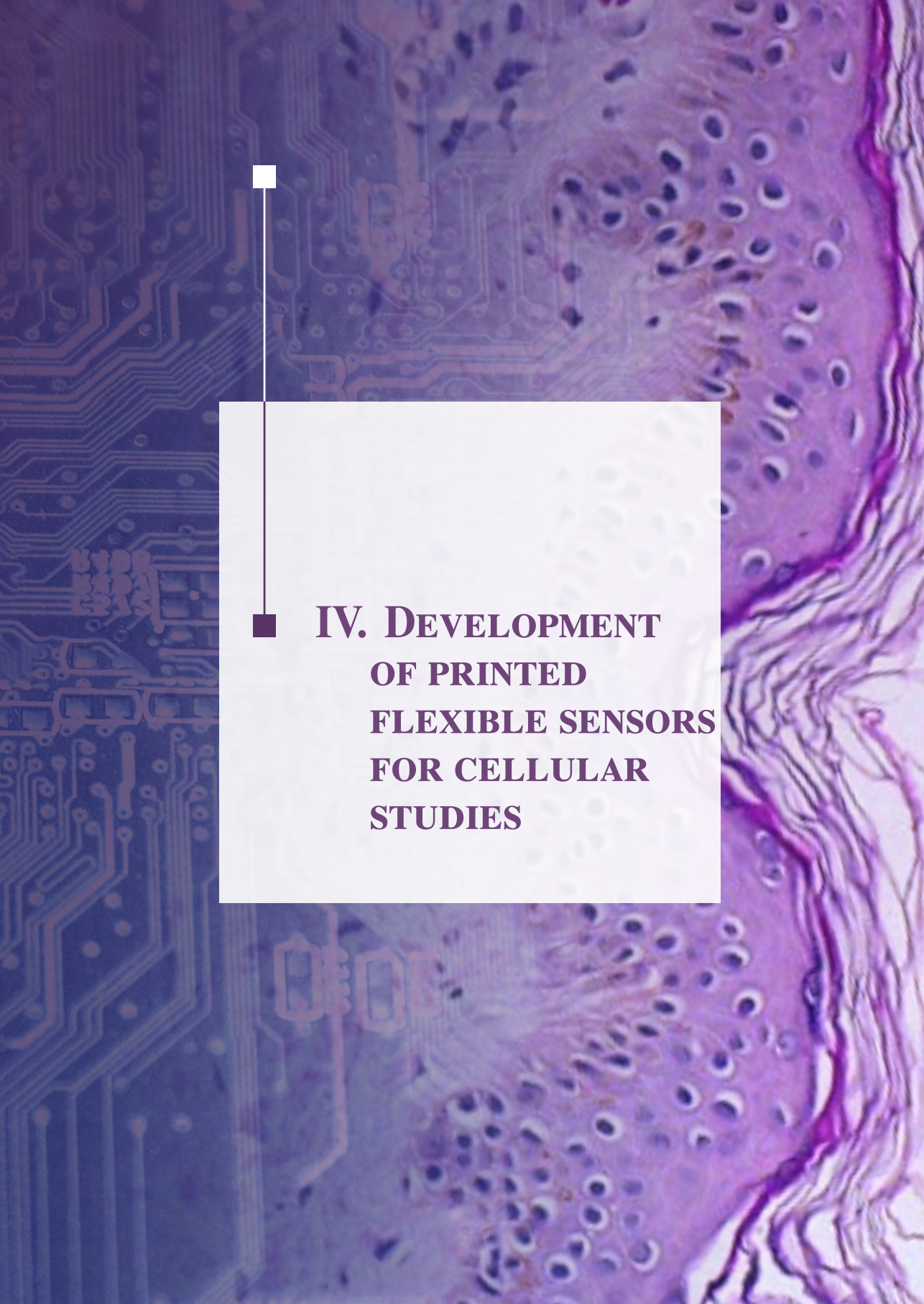


Figure 31. Dimensions and schematic of the experimental stage based on polymeric piezoelectric actuator (Chapter V). a) Top view with the description of the different materials used in the manufacturing of the biocompatible actuator-based device. b) Schematic representation with a lateral view of the actuator-based device, (i) the piezoelectric film remains in the bottom of the Petri dish with a chamber made of PDMS, (ii) and (iii) show a representation of a cell culture with basal medium seeded on the collagen-coated piezoelectric film under (ii) static condition (0 voltage in the electronics stage) and (iii) dynamic condition. AC: alternating current.

3.6.2. Materials of the driver

To amplify the voltage required at the input of the piezoelectric actuator introduced in Chapter V an electronic driver was implemented. Commercial power amplifiers (PA79, Ape Microtechnology, Tucson, AZ, USA) were configured in a bridge configuration with an overall gain of 20. A commercially available power supply (IHB200-0.12, International Power, London, UK) biases the amplifier module. Altium Designer software (Altium Limited, Chatswood, NSW, Australia) was used to implement the schematic and printed circuit board (PCB). The schematic of this driver is provided in Appendix III.



**IV. DEVELOPMENT
OF PRINTED
FLEXIBLE SENSORS
FOR CELLULAR
STUDIES**

Cuando ya no creas, crea.

Miki Naranja

CHAPTER IV. Development of printed flexible sensors for cellular studies

4.1. INTRODUCTION AND MOTIVATION

The pursuit of electronic systems that recreate the most sophisticated properties of our largest organ—the skin—has motivated many innovations in material sciences and electronic manufacturing. As discussed in Chapter II, a range of skin-like electronic systems has emerged as new classes of biotic/abiotic interfaces with some remarkable applications.^{22,25,33,240-242}

Most of those skin compliance devices are at present fabricated using standard microfabrication techniques such as wet etching, photolithography, and physical metal evaporation.^{86,107,243,244} Although these manufacturing approaches have proven valuable for fabricating electronic systems with high-level functionalities while withstanding complex and soft conformabilities with human tissues,^{49,245} they rely on expensive, technically demanding, multiple steps-based processes. These complex fabricating processes hinder rapid prototyping and customization, not to mention that they may sentence a substantive fraction of such electronic systems to remain inside the research laboratories due to their costs.

By contrast, additive manufacturing such as 3D printing enables a wide range of functional materials to be patterned and fabricated in a single manufacturing step. As we saw in Chapter II, these advantages together with low-material consumption/wastages, the possibility of printing on a variety of surfaces (including movable surfaces),²⁴⁶ and the printing accuracy achieved from reduced area to large area has drawn attention from not only electronic engineers^{178,247,248} but also tissue engineers.^{6,225} Not surprisingly, and as we have seen along through this dissertation, bioelectronic researchers are foreseeing a single platform that brings together such conventionally independent fabrications for electronic devices and living tissues. Although this sort of technology may unleash all-printed, ready-to-implant, smart organs and tissues with built-in electronics to be used as cyborg implants²⁴⁹ with augmented functionalities compared to their biological archetypes, the endeavor remains challenging.

One initial step to pave the way through the research line mentioned above require accomplishing solutions: 1) able to fabricate flexible and thin sensors using an electronic manufacturing technology that must be non-contact, mask-less, gas-free, and compatible with bioprinting; 2) able to reliable, long-lasting integrate sensors with living cells with any detrimental effect of neither the biological nor the electrical system; and 3) able to operate in real-time and non-invasively in order to monitor slow process relevant to engineered tissues.

Motivated by these crucial unmet needs and considering organotypic skin cultures as the engineered-tissue model, in this chapter we demonstrate the feasibility of integrating inkjet-printed flexible sensors into a monolayer of epithelial cultured cells to operate as impedimetric

biosensors. The proposed sensing system monitors non-invasively and in real-time relevant cellular processes that take place in tissue-engineered skin equivalents using electrochemical impedance spectroscopy. This integration represents an initial step towards engineered-skin substitutes with smart embedded sensors.

4.2. FROM BIOLOGICAL IMPEDANCE MEASUREMENTS TO CELL-SUBSTRATE IMPEDANCE SPECTROSCOPY

Electrical impedance is defined as the ratio of the voltage to the current in a direct/alternating current circuit. Any material (or medium) can impede (oppose) electric current in a combination of loss terms (resistance) and energy-storing terms (reactance). A material capable of storing electrical energy is a dielectric (from the Greek *dia*: through and *electric*: electrostatic field). A material incapable of storing energy is a conductor. Bioimpedance, as the name suggests, deals with the electrical properties of tissues. A body of literature exists on understanding, modeling, and measuring such electrical properties in human tissues; this work has been summarized previously.²⁵⁰⁻²⁵⁴

From an electrical perspective tissues may be regarded as dielectric or conductive depending on the frequency of the electrical signal passing through them. Thus, bioimpedance is measured across many frequencies to form a spectrum plot in which the different components of the biological system contribute to the total impedance measured. Schwan—one of

the founders of biomedical engineering as a discipline—described for the first time the frequency dependence of the biological impedance introducing the concept of α , β , and γ dispersions or relaxations (Figure 32a).^{253,254} These relaxations determined by the interaction of the electric field with the biological system indicate the dielectric dispersions that arise from the polarization mechanism occurring in complex biological environments under electromagnetic radiations. Likewise, this frequency dependence in bioimpedance suggests that certain disturbances of biological structures may result in detectable changes in the impedance spectrum.

The complex impedance Z of a medium can be expressed in polar form (equation (11)) or Cartesian form (equation (12)).

$$Z = |Z| e^{j\theta} \quad (11)$$

where magnitude is $|Z|$ and phase angle is θ .

$$Z = R + jX \quad (12)$$

with resistance R and reactance X .

From either of those mathematical representations, a material with a higher capacity for energy storage will exhibit a larger reactance X , and a larger phase angle, θ .

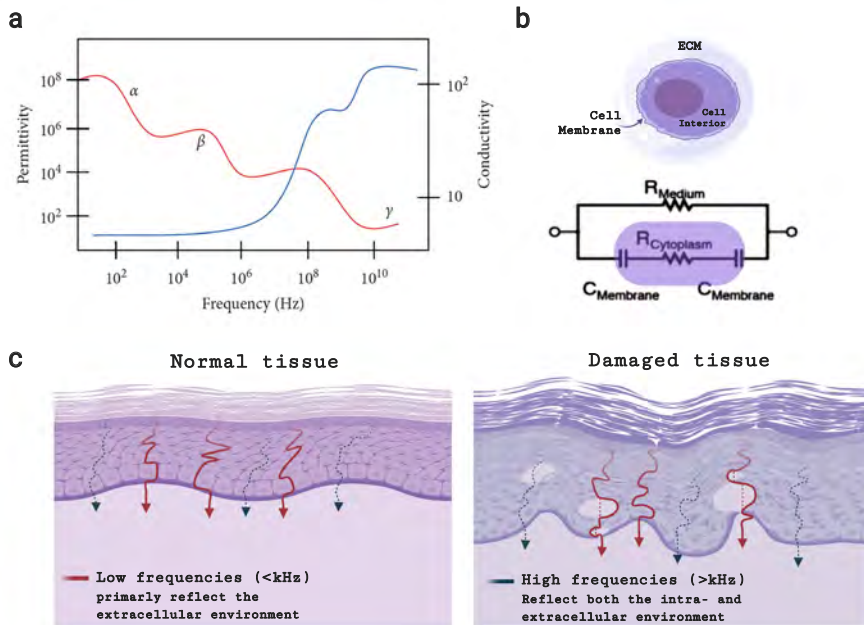


Figure 32. a) Simulation of the dispersion of tissues first measured by Schwan. The dispersions occur due to the loss of certain polarization modes in biological tissues: α -dispersion arises from the tangential flow of ions across the cell surfaces, β -dispersion comes up due to the accumulation of charges at the cell membranes and γ -dispersion is related to the dipolar movements of molecules, mainly water. b) The simplified electrical model of cells under an electric field. The model is named single-shell model. c) Schematic of the differences in low- and high-frequency signal traveling through healthy and damaged tissue. Note: a) adapted from Nasir and Al Ahmad, 2020;²⁵⁵ b) adapted from Grimmes *et al.*²⁵⁰

The study of bioimpedance and bioelectricity (i.e., the ability of tissues to generate electrical current) in the human body is not new.²⁵⁰ From an electrical perspective, the simplest model of a single cell in an aqueous medium is the single-shell model. This model represents the cells as a sphere with an ion-rich conductive center (cytoplasm) encapsulated in a relatively non-conductive barrier (cell membrane) surrounded by an ion-rich conductive medium (extracellular fluid) as shown in Figure 32b. The

ion-rich media can conduct charges (resistance) while the lipid bilayer membrane impedes charges to flow (reactance). Alterations in membrane structures (e.g., cell-membrane damage, cell death, cell shrinking, etc.) affect this “charge storage capacity” yielding current passes through the membrane and cells exhibit higher electrical conductance. Therefore, the impedance spectrum of damaged cells manifests a smaller reactance in comparison to their counterparts. In other words, damaged cells exhibit a less capacitor-like behavior and a more resistor-like response (Figure 32c).²⁵² At a tissue level similar correlations have been established between the electrical properties and the underneath biological processes.²⁵⁶ For example, impedance-based measurements of skin have shown that lower reactance and phase angle correlate to a higher risk of the presence of infection, cell loss, and pressure sores.²⁵⁷ Thus, impedance-related measurement is widely accepted as a label-free, minimally invasive, real-time, electrochemical method to assess both cell and tissue status.²⁵¹

The first impedance *in vitro* device was introduced as early as 1984 by Keese and Giaver.²⁵⁸⁻²⁶⁰ Much work has since been published using impedance-based systems to monitor cell proliferation, adhesion, and morphology, quantify biomass in suspensions, and detect bacteria.^{259,261-263} *In vivo*, impedance sensing has also been used to monitor the health of the skin tissue and to develop an imaging technique known as electrical impedance tomography.^{264,265} Other studies have shown impedance as an indicator of epidermal proliferation and granulation, hydration and infection,^{266,267} which have boosted the technique towards impedance-based devices for skin hydration monitoring and early detection of pressure ulcers.^{179,268} Nowadays, commercial systems to perform cell screening based on impedance measurements are currently available²⁶⁹ and impedance-based devices to monitor wound healing have been patented²⁷⁰ with clinical trials underway.

This evidence found in the literature led to one of the fundamental hypothesis of this thesis that motivates the work described in this chapter, this is, that impedance-based measurement may be able to monitor the physiological status of epithelial tissues using sensors embedded into the tissue. Thus, in this chapter, a flexible ink-jetted impedance device is able to detect in real-time cellular behaviors relevant to laboratory-growth skin cultures.

From the instrumentation point of view, the impedance is measured conventionally using a sensor to acquire the signal and either a lock-in amplifier (whether the measuring is acquired at a specific frequency) or an impedance analyzer (whether the impedance is measured across many frequencies) connected to a computer to collect and process the data. The acquired signal is further processed through an equivalent circuit model to simulate the physical processes behind. Three typical impedance-based techniques are derived using such technical instrumentation named Cell-substrate impedance sensing (ECIS), Impedance flow cytometry (IFC), and Electric impedance spectroscopy (EIS).

In ECIS, cells are adhered to the electrode-based substrate blocking the current flow and therefore increasing the impedance measured across the electrodes.²⁷¹ Electrodes in ECIS are often monopolar electrodes in which a small electrode is used as the working electrode (with few cells contributing to the measured impedance) and a larger electrode as the counter electrode.²⁷² In the IFC, cells pass through a flow system changing the impedance measured from the electrodes placed alongside the (micro) fluidic channel.²⁷³ Finally, EIS is perhaps the most widely used technique for cell/tissue characterization. In EIS, cells can be in suspension or adhered to the electrodes, and two electrodes or interdigitated structures

are typically used to perform the impedance measurement.^{274,275} These impedance-based techniques can be used independently or combined due to their similar principle of operation. A summary of the characteristics of the impedance-based techniques *in vitro* is summarized in Table 3. Electrical Impedance Spectroscopy using flexible inkjet-printed sensors was the measurement technique employed in the framework of this thesis.

Table 3. Three methods used for cell impedance-based measurements.

Technique	Frequency Range	Long-term monitoring
ECIS	~ 100Hz-100kHz (single frequency or sweeping)	Available
IFC	~100 Hz-10 MHz (single or several frequency points)	Not available
EIS	~10-1Hz-1MHz (single frequency or sweeping)	Available

4.2.1. Theoretical models and impedance representation

The measured impedance can be evaluated considering theoretical models that describe the studied system. For impedance-based methods these theoretical models can be mathematical equations and/or equivalent circuits that electrically behave like the physical or chemical systems to be modeled. Because tissues and cells are indeed complex systems it is not straightforward to obtain an electrical model that mimics them accurately. This difficulty is twofold. On one hand, the realism of the systems is often impossible to reproduce with ordinary, physically attainable, electrical

components such as resistors and capacitors. On the other hand, there is no univocal solution that can fit and/or describe the experimental phenomenon, with several possible circuits that can describe the electrical behavior equally well.²⁵⁰ Therefore, it is acceptable that there is not a “correct” model but it should represent selected properties of the reality that is mimicking. This entailment suggests in turn that the selected model often requires some knowledge *a priori* about the system under study.

Cells adhered to the electrodes have been modeled as capacitors,²⁷⁶ a combination of resistors and capacitors,²⁷⁷ or as constant phase elements (CPE).²⁷⁸ As it has been said, the model chosen depends on the actual interpretation of the data and it is often dictated by the measuring method or setup used. In this thesis, adhered cells to the electrodes have been modeled as CPE components.

Graphical representation of the impedance spectrum can be plotted using either a Bode plot or a Complex plane plot (Figure 33). In the Bode plot magnitude of the impedance and phase angle are plotted versus frequency. In the Complex plot, commonly known as the Nyquist plot, the real part of the impedance is plotted versus the imaginary part resulting in a diagram in which each point represents the impedance magnitude at one frequency. Thus, in the Nyquist diagram, the data is represented as a vector whose module coincides with that of the modulus of the impedance and the angle between the vector and the X-axis (i.e., Z real) coincides with the phase angle (see Figure 33a). Both of those graphical representations can be employed to monitor the changes of the impedances over frequencies obtained in an electrochemical cell or electronic device. In this thesis impedance has been mostly represented using the Nyquist diagram.

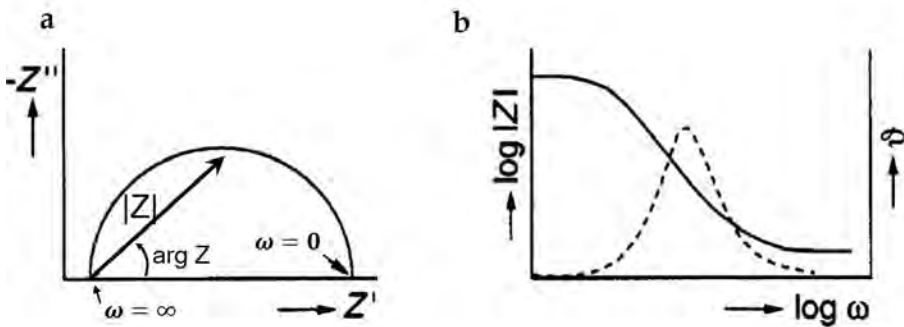


Figure 33. Two graphical representation of the impedance spectrum of an RC electrical circuit. a) In the Complex plane plot, also called Argand diagram or much more common Nyquist plot, the imaginary part of the impedance is represented versus the real part. b) In the Bode plot the magnitude ($\log |Z|$) and phase (ν) are represented versus de frequency. Note: a) and b) adapted from M. Sluyters-Rehbach, 1994.

4.3. FUNDAMENTAL CONCEPTS OF IMPEDIMETRIC BIOSENSORS BASED ON COPLANAR INTERDIGITATED ELECTRODES

Generally speaking a biosensor is an analytical device integrating a biological sensing element.²⁷⁹ Based on the transducing principle employed biosensors may be classified as optical, mechanical, electromagnetic, or electrical. Electrical biosensors rely on the measurements of voltages and/or currents and can be further subdivided depending on how this electrical measurement is made. (In other words, electrical biosensors can be classified according

to the origin of the detected signal, this is, a current, a potential or an impedance.) Amperometry-based sensors monitor the variations in the current resulting from the redox reactions of the electroactive species; potentiometric devices involve the measurement of the electrical potential difference to a reference electrode. In the first case the resulting current correlates with the concentration of the electroactive species; in the second case the potential difference (voltage) depends on the chemical activity (e.g., concentration) of the ions in the sample. These approaches are considered as DC or pseudo-DC analysis. In contrast, the working principle of impedimetric biosensors is based on comparing the electrical impedance (response) of an interface (system) in the quasi-linear steady-state applying a small sinusoidal voltage (excitation) at a given frequency and measuring the resulting current.^{280,281} In this thesis the exploited sensing mechanism has been impedimetric.

Based on the biorecognition elements (i.e. targeted receptor) biosensors can be also classified as enzymatic, antibody-based, or whole cell-based biosensors.²⁸² Artificial recognition elements such as molecularly printed polymers, aptamers, or antibodies have been also employed as a recognition element. In whole cell-based biosensors different activities such as inhibition growth, metabolic activity, or cell viability may be analyzed. The main disadvantages of using cell-based impedimetric biosensors are related to the immobilization of cells on the surfaces of the sensors and the difficulty to ensure selectivity.²⁸² However, they are extensively used due to their low-cost production and broad fields of applications. In this thesis the exploited biorecognition element has been whole cells.

Traditionally, macro-size electrodes (rods or wires) have been used for whole cell-based biosensors as the impedimetric transducer.

To miniaturize the size of the electrodes and enhance the sensitivity, microelectrodes have been adopted in combination with the traditional acquisition instrumentation. Among the different microelectrodes reported in the literature, a well-established method consists of the formation of the counter and working electrodes with the appearance of interlaced fingers, forming the so-called interdigitated electrodes (IDE). Among the advantages of using IDEs for impedance spectroscopy are the absence of an additional reference electrode to perform the measurements, the easy-miniaturization of the sensors, and the possibility of label-free (direct) detection being the sensing area directly on the surface of the sensor. For these mentioned reasons, in this thesis the structure chosen for the electrodes has been interdigitated electrodes.

Compared to parallel plate capacitors (Figure 34a) where the electric field is confined exclusively in the dielectric material located between the conductive plates, in IDE capacitors the lines of the electric field spread above the plane of the electrodes and within the underneath layer. The bottom layer of the electrodes is referred to as the substrate of the device since it also provides mechanical support. In applications such as gas sensors, the electric field interacting with the substrate could be critical for the sensing behavior. However, in applications where the substrate has a lower permittivity and lower electrical conductivity compared with the material under test (e.g., culture medium, cells), the interaction between the electric field and the substrate can be neglected.²⁸³ The most often geometry of the interdigitated electrodes is depicted in Figure 34b. The parameters used to describe these structures are the number of fingers (n), the length of the digits (L), the width (W), and the spacing between electrodes (S).

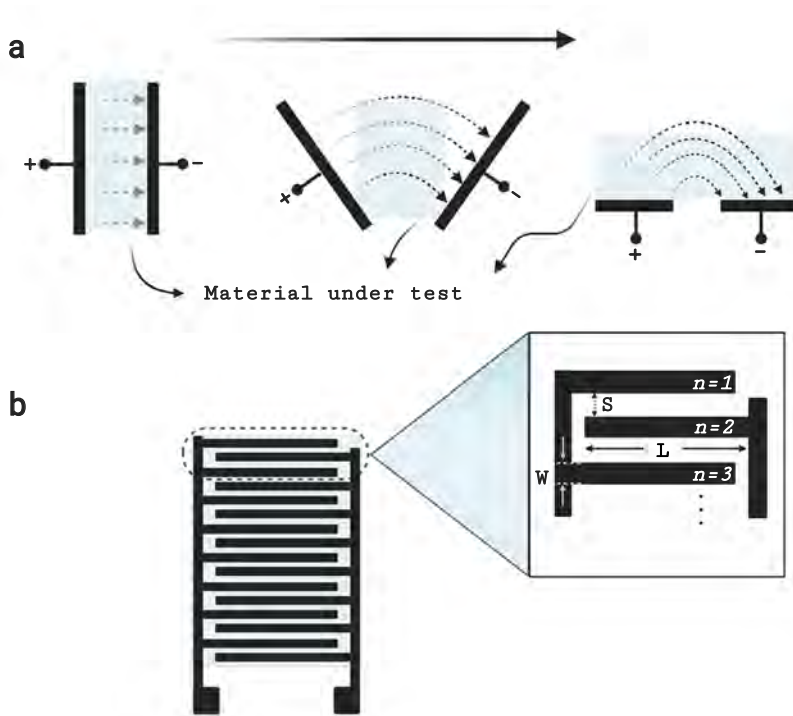


Figure 34. Interdigitated electrodes. a) Penetration of the electric field in a parallel plate capacitor and interdigitated capacitors. b) Structure of interdigitated electrodes most often used, and the parameters used to describe the geometry: the number of fingers (n), the length of the digits (L), the width (W), and the spacing between electrodes (S).

Having introduced the sensing mechanism (impedimetric), the bi-orecognition element (whole cells), and the structure of the electrodes (interdigitated electrodes) chosen in this thesis, the conceptual sensing mechanism of the sensors integrated into the cell cultures is shown in Figure 35. Upon the presence of anchor-dependent cells, the field lines in the plane above the interdigitated electrodes are disrupted, leading to changes that can be detected in the impedance measured between the negative and positive terminal of the device.

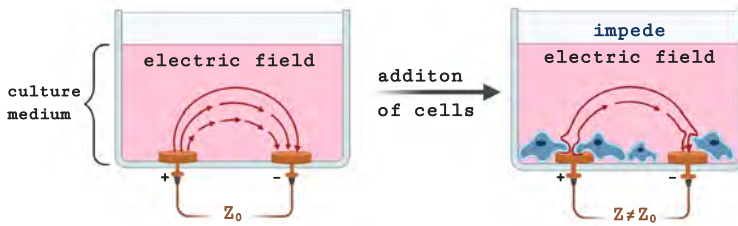


Figure 35. Sensing mechanism of interdigitated sensors based on the impedimetric transducer. Upon the presence of cells, the electric field in the plane above the interdigitated electrodes is disrupted leading to electrical changes that can be detected in the impedance measured between the negative and positive terminal of the device.

Using conformal mapping and partial capacitance methods, some studies have modeled the capacitance of the IDE sensors and have provided a mathematical framework for the effect of multiple layers deposited on the surfaces of the electrodes.²⁸⁴ However, extensive simplification of the real effects needs to be applied and, in many cases, the thickness of the electrodes is not considered. Based on this conformal mapping the penetration depth (d) of the electric field into the material under test has been approximated to $d = (W+S)/\pi$,²⁸⁵ which is almost the distance between the centers of two electrodes. However, modeling has also revealed that 80 % of the current is mostly distributed close to the surface of the electrodes, far less than the value of d .²⁸⁶ Thus, miniaturization of the electrodes allows increasing the sensitivity which has been attainable in many applications by photolithography-based fabrication. In printing processes like inkjet printing increasing the nominal value per surface area of the IDEs (i.e., reducing the finger pitch distance) is challenging due to the resolution achievable by the additive fabrication methods (e.g., a critical linewidth between 30–100 μm for inkjet printing).¹⁹²

Some strategies have increased the sensitivity of inkjet-printed IDE sensors. For example, Rivadeneyra *et al.* have proposed a novel structure

combining interdigitated and meandering electrodes to obtain an improved geometrical capacitance factor compared to the conventional interdigitated capacitor (Figure 36a).²⁸⁷ However, in this structure one damaged finger makes the sensor useless while in the traditional IDEs structures it only leads to lower sensor performance. Other interesting approaches to improve the resolution of inkjet-printed IDE structures have been proposed by Molina-López *et al.* (see Figure 36b). The authors used a sandwiched non-conductive layer of parylene C deposited by metal vapor deposition between two conductive combs printed by inkjet printing allowing a reduction in the gap of the printed electrodes with no short-circuit the printed lines.²⁸⁸ This strategy, unfortunately, suffers from an additional clean-room step. Nevertheless, optimization should always be tailored to the targeted application. In this sense, it will prevail a trade-off between the materials used, the scale of the sensors, and the fabrication method. The detailed considerations for the fabrication of the sensors proposed in this thesis are discussed in the following section.

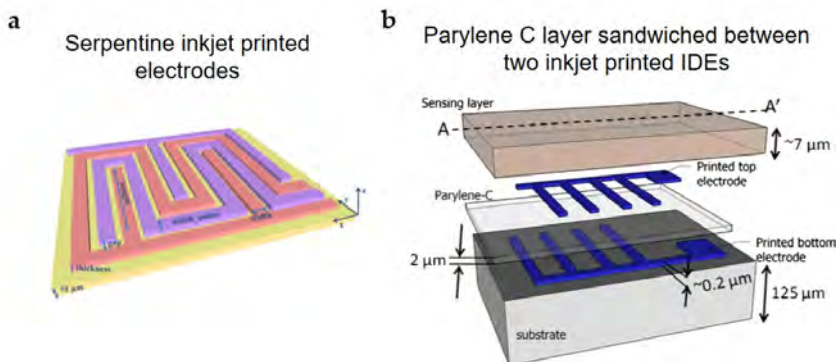


Figure 36. Novel approaches to improve printing resolutions for inkjet-printed interdigitated electrodes. a) Exploring new geometrical structures in inkjet-printed capacitors to achieve higher capacitances per area. b) Using a sandwiched non-conductive layer of parylene C deposited by metal vapor deposition between two conductive combs printed by inkjet printing allowed to reduce the gap of the printed electrodes with no short-circuit the printed lines. Note: images modified from a) Rivadeneyra *et al.*, 2014 and b) Molina-López *et al.*, 2013.

4.4. DESIGN AND FABRICATION OF THE INKJET-PRINTED SENSORS FOR CELLULAR STUDIES

In the work presented in this chapter inkjet printing technology was adopted as the manufacturing method due to its contactless and mask-less nature and its compatibility with current 3D bioprinting techniques (a major motivation for this work). Dimensions of the IDEs were carefully designed to be compatible with the dimensions of the commercial dishes used for cell cultures (see Chapter III, section 3.5). As discussed previously in section 4.3, the structure chosen for the IDEs is the most popular structure for interdigitated sensors described in the literature, albeit most of the reported IDEs in the literature have been fabricated by standard microfabrication methods resulting in devices that are stiff and non-compliant. However, one drawback of using this IDE structure fabricated with printed methods relies on its high capacitance factor which directly affects the sensitivity of the sensor. This is due to the maximum resolution achievable by additive methods compared to standard lithography methods. To improve the geometrical capacitance factor novel structures for ink-jetted sensors have been presented,^{287,288} as we already discussed in 4.3, yet they were considered not optimum for our case of sensing epithelial cell cultures. The reason behind this decision is that the complexity of those optimized structures and the multiple steps required in their fabrication make reliable patterns possible only for sensors with very reduced dimensions. Miniaturization in the size of the sensors implies a smaller area to interrogate the cultured cells, and the smaller the cultured area, the lower the number of cells available to be analyzed. Much concern during any engineering optimization should be devoted to

these application-oriented issues. For example, current dimensions of 3D organotypic skin cultures are in the order of centimeters and scaling the bio-protocol to a reduced area can be challenging as well as unsuitable. As a first approach for the target application of this thesis the problems associated with the use of flexible sensors with very reduced size would outweigh the potential advantages. Thus, materials, dimensions, and the structure for the sensors presented in this thesis were selected to render the printing process less demanding and more reliable. Nevertheless, and as it shall be discussed in section 4.8, efforts in exploring new materials and compact devices would eventually present several advantages in terms of cost, electrical performance, and local sensing, among others.

Another critical aspect of bioelectronics is that the materials used to fabricate the devices must be completely biocompatible. In the case of implantable bioelectronic devices the interaction of the materials with the living, biological, tissues must also be thoroughly characterized to avoid releasing harmful chemicals over time into the body. In this regard, printed-electronic devices deserve special consideration. First, solution-processed materials presuppose different toxic risks compared to their bulk counterparts because nanosized materials might permeate biological structures. Second, temperature-based processing could lead to an incomplete conversion from the precursors to the target final materials, resulting in intermediate chemicals and/or residuals that may change the material's properties to which the tissue is exposed. For example, while it has been shown that bulk silver reacts chemically to the body fluids and therefore its use has been questioned,²⁸⁹ the toxicity of silver nanoparticles (AgNP) has been shown to be highly time and concentration-dependent.²⁹⁰⁻²⁹² Furthermore, a recent study has shown the feasibility of deposit bio- and electronic materials in one single, additive platform^{293,294}

benefiting from the unique property of AgNP to undergo a spontaneous coalescence process (sintering) at room temperature in presence of chloride ions.^{202,295} In any case, given the complex nature of the human body's response to foreign materials, testing individual materials is insufficient to demonstrate the biocompatibility of an implanted electronic device²⁹⁶ and therefore medical devices are evaluated using a series of standards (ISO 109993).

In this framework the first (conservative) approach we followed for the fabrication of the sensors involved the use of inks with silver nanoparticles for the conductive electrodes and included a passivation layer using a SU-8 dielectric ink stacked the printed structure on a substrate of flexible polyethylene polymer (PET). Thus the (SU-8) passivation layer was the material in direct contact with the cell culture. SU-8 has been demonstrated to be biocompatible²⁹⁷ and recently it has been used in inkjet-printed microelectrode arrays for electrophysiology-based measurement of neural cultures.²⁰¹

For the fabrication of the sensors different waveforms were developed to drop-eject each ink formulation in the inkjet printheads. When multiple nozzles were activated, much care was needed to obtain similar speed and, therefore, the height of droplets in the direction perpendicular to the plate (Figure 37). This uniformity was achieved by varying the jetting voltage when it was needed.

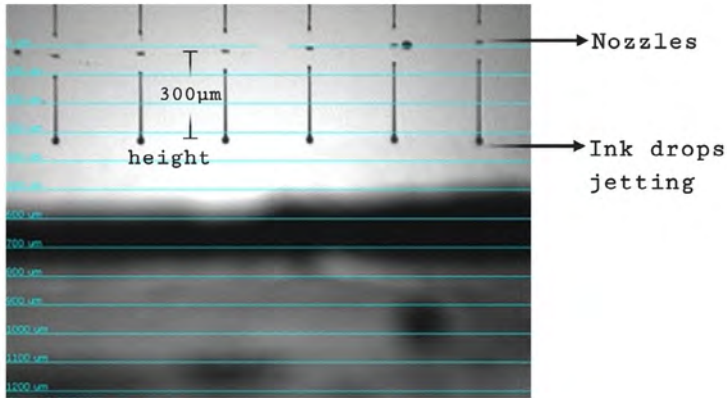


Figure 37. Drop watcher image of ejected droplets from the inkjet printhead.

An important aspect of solution-based electronics relies on the adhesion of the ink to the substrate once it dries. When the substrate is flexible, or the ink composition is deposited on top of a different ink formulation this aspect is especially critical since extra interfacial stresses and different surface energies can be generated. To evaluate the adhesion between the AgNP-based ink and the SU8 ink for the passivation of the conductive lines multiple numbers of layers using SU8 ink were tested: one (1L), two (2L) and three (3L) layers. An electrode of 1 mm × 11 mm was deposited using AgNP-based ink on a PET substrate and a SU-8 pattern was printed on top as depicted in Figure 38. This structure allowed us to study the use of different layers of SU-8 over an electrode. The printed structure was observed by a microscope and characterized with a profilometer. In the lower part of Figure 38 is shown an example of the printed test structures. After the printing of the first layer (1L) of the SU-8 on top of the conductive electrode we can observe how the non-conductive ink spreads non-uniformly on the AgNP layer and no passivation is achieved. The surface energy of the SU-8 has been determined to have a low polar part which could explain this difficult wetting of the ink on the AgNP-based layer.

The 2L was observed to almost completely covered the AgNP layer by microscope but discontinuities were detected by the profilometer in which SU-8 was observed to split up in isolated droplets. To solve this problem, and to improve the wettability control between the two layers of SU-8, the surface was treated with oxygen plasma to smooth the first printed layer of SU-8 by slightly etching it. However, it was observed that this oxygen plasma treatment tended to oxidize the exposed areas of the silver electrodes. After several tests, we observed that well-defined passivation could be obtained with a third layer (3L), resulting in the final number of layers selected for the passivation (Figure 38C) without the necessity of any surface treatment.

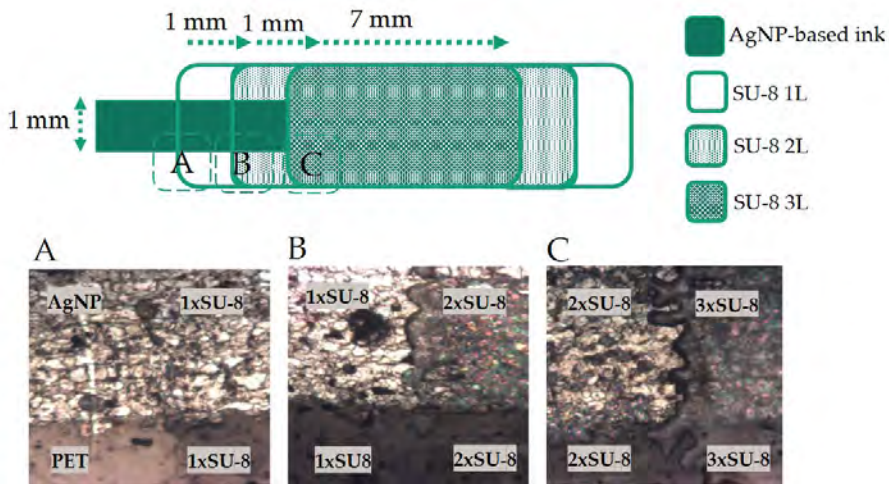


Figure 38. Study of the adhesion between consecutive layers of the SU-8 to passivate the silver-nanoparticle electrode. An electrode of 1mm×11 mm was printed on a PET substrate and a SU-8 pattern was patterned on top in a sequence of 1L, 2L and 3L displacing the origin of the printhead 1 mm in the X-axis. Different interfaces (AgNP-substrate; AgNP-1LxSU8; 1LxSU8-2LxSU8; 2xSU8-3xSU8) were observed under microscope and using a profilometer. Oxygen plasma treatment was used after printing 1LxSU-8 to improve the wettability between two consecutive layers of SU-8 but it was observed that the exposed AgNP-based electrodes were oxidized after several days. Well-defined passivation could be obtained with 3L of SU8, resulting in the final number of layers selected for the passivation.

Using the optimized printing parameters and the fabrication strategies described above, several IDEs sensors were successfully manufactured on flexible PET foil using silver-nanoparticles and passivation on top. Figure 39 depicts the printed, flexible, sensors obtained.

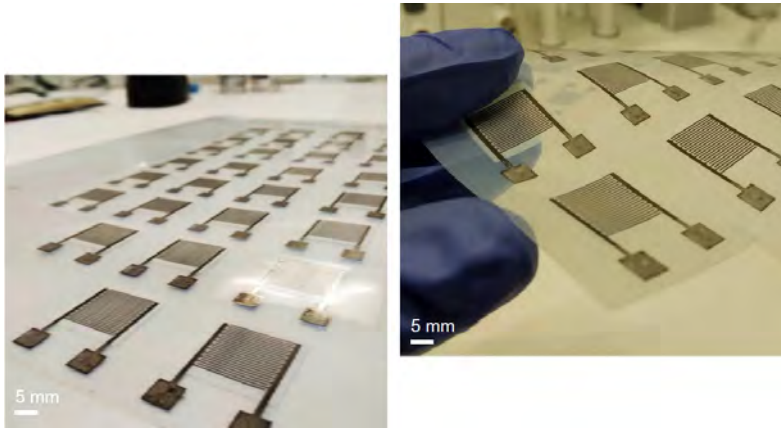


Figure 39. Optical pictures of the flexible interdigitated electrodes of silver-nanoparticles with a passivation of the SU8 on flexible PET foil manufactured by inkjet printing.

4.5. DESCRIPTION OF THE MEASUREMENT SYSTEM

The experimental system used for the sensor characterization and the different cellular studies consists of the designed inkjet-printed sensors described above, a commercial impedance analyzer to perform the impedance spectroscopy measurement of the inkjet-printed based device with the cell cultures, and a microscope with an integrated camera. The microscope is integrated with a bioreactor which allows physiological and stable conditions of 5% CO₂ and 37 °C to perform prolonged time-lapse/impedance experiments using cell cultures. A detailed description of the fabrication of both the flexible inkjet-printed sensors and the custom cell culture unit is given in Chapter III (Materials and Methods), section 3.5. The assembly process of the IDEs-based devices to perform impedance spectroscopy measurements of cultured cells is illustrated in Figure 40a while the experimental system to accomplish the real-time monitoring of 2D epithelial cell cultures in Figure 40b.

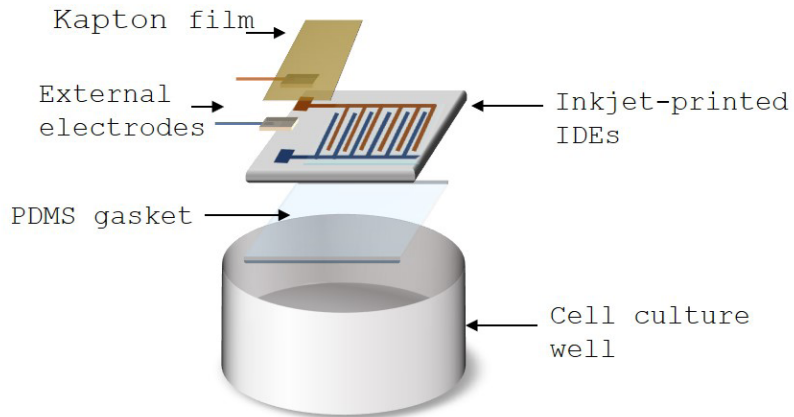
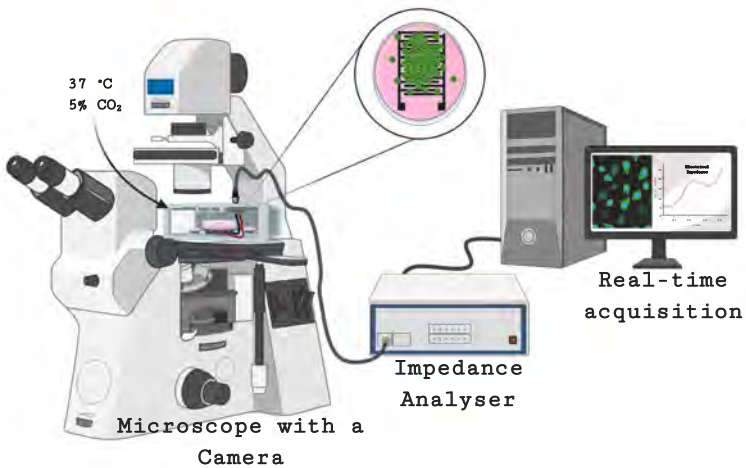
a**b**

Figure 40. a) Assembly and packaging of the IDEs-based devices to perform impedance spectroscopy measurements of cultured cells. Inkjet-printed sensors were custom packaged and bonded as a substrate for cell cultures on Petri dishes. b) Representation of the experimental system. The system consists of the IDEs-based chamber, an impedance analyzer, a microscope with an integrated bioreactor, and a PC to acquire images and the impedance signals in real-time.

4.6. CHARACTERIZATION OF THE INKJET-PRINTED SENSORS

In this section we present the characterization of the inkjet-printed sensors described in the previous section, first, to evaluate the quality of the manufacturing in terms of their morphological and electrical performance (section 4.6.1) and, second, to study any potential toxic effects associated with both the sensors and the custom IDEs-based unit to culture cells (section 4.6.2).

4.6.1. Sensors morphological and electrical characterization

As described before, the sensors were manufacturing by inkjet printing with a silver nanoparticles-based ink as a conductive element and a SU-8 ink as the passivation layer over a flexible polyethylene polymer (PET) substrate. The sensors consisted of several planar interdigitated electrodes (IDEs) and a passivation on top. For the morphological characterization of the printed sensors images of them using an optical microscope and SEM as well as the morphological profile using a profilometer were obtained. Results from this characterization show that the width of the fingers of the interdigitated sensors resulted in an average electrode size of $300 \mu\text{m} \pm 0.1 \mu\text{m}$ ($n = 66$) and the satellite drops observed had an average diameter of $20 \mu\text{m} \pm 15 \mu\text{m}$ (Figure 41a and Figure 42a).

As introduced in Chapter II, the selected parameters in the ink-jet-printing process strongly determine the features of the manufactured structures. To print the conductive lines, a drop spacing (DS) of 15 μm was adjusted which resulted in a thickness of approximately 600 nm (Figure 41b). To print the SU-8 ink, a DS of 20 μm generated a thickness of about 1 μm for one single layer. As the passivation was comprised of a total of three-layer of such SU-8 ink the total thickness resulted in about 3 μm (Figure 41c). The difference of ~ 400 nm between the thickness of a single conductive layer (600 nm) and a single non-conductive layer (~ 1 μm) may be explained with the variations in the amount of solvent and composition for each ink formulation.

Regarding the adherence of the cells to the designed devices, it has been shown that 3D topographies compared to 2D planar topographies improve cell adherence in bioelectronics which can be explained by a phenomenon named contact guidance.^{298,299} Tight adherences between the tissue and/or cells and electronics is highly desirable to record signals with a high signal to noise ratio. Thus, the obtained topographic feature that shows the appearance of microgrooves and ridges with dimensions of 300 μm and a total depth of approximately 4 μm can be considered advantageous *a priori* to promote adhesions of the epithelial cell cultures (see section 4.6.2, Figure 45).

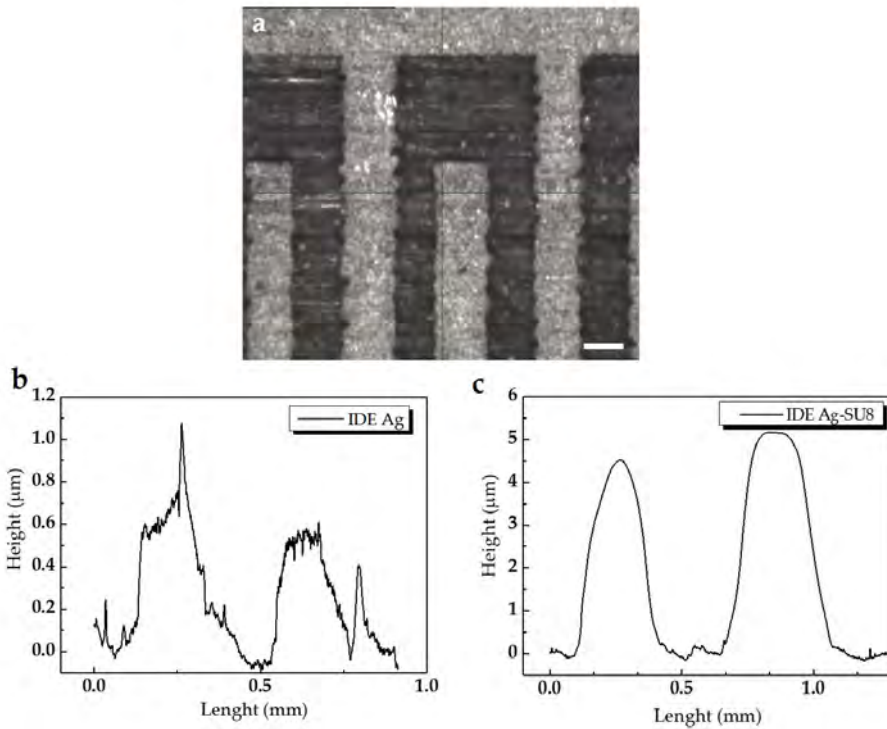


Figure 41. Morphological characterization of the manufactured inkjet-printed interdigitated electrodes with a passivation on top using optical microscopy and an optical profilometer. a) Optical micrograph of the inkjet-printed sensors (scale bar 100 μm). b) Surface profilometry of two continuous inkjet-printed electrodes revealing a thickness of a 0.6 μm for bare Ag electrodes. c) Morphological profile of two continuous fingers in the interdigitated electrodes passivated with three layers of SU8 revealing a thickness of 4 μm .

On the other hand, as discussed in Chapter II, one of the main concerns when using flexible substrates for electronic devices comes from possible delamination. Therefore, printed sensors were characterized using SEM (Figure 42) to evaluate potential delamination of the conductive printed lines from the PET substrate as well as the upper passivation and the silver electrodes. A top view of an SEM image of two consecutive fingers of IDEs onto the PET substrate is depicted in Figure

42a. The silver electrodes are continuous, crack-free, and homogenous which ensure conductivity. Inkjet-printed silver lines are smoothly and perfectly attached to the PET substrate without any visual delamination. Rather the opposite, the conductive electrodes appeared as a second layer on top of the substrate and the non-conductive layers cannot be distinguished.

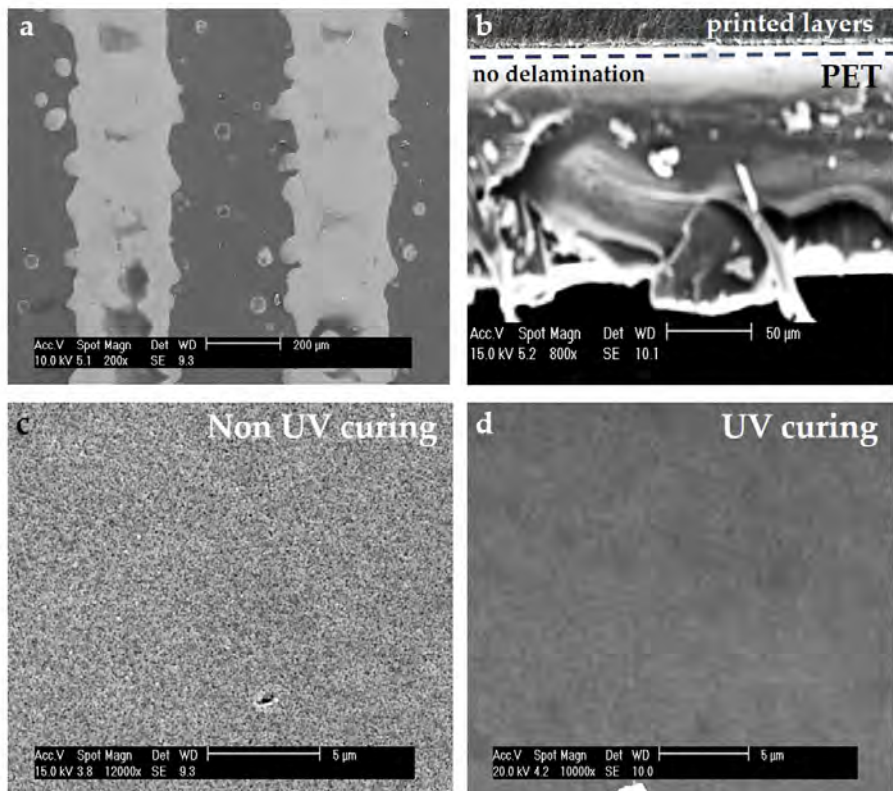


Figure 42. Morphological characterization of the interdigitated electrodes manufactured by inkjet printing using Scanning Electron Microscopy. a) SEM micrography of the inkjet-printed sensor surface in a top view (scale bar 200 μm). b) Transversal view of the inkjet-printed sensors (scale bar 50 μm) revealing a thickness of 38 μm in the printed layers on top of the substrate. c) and d) Effect of UV curing on the outermost layer of the SU-8 showed an increase in the smoothness of the outmost layer. UV treated samples showed a smoother surface (d) compared with non-treated samples (c).

To better study the interface between such three materials (substrate-conductor-insulator) a cross-section of the sensors was observed by SEM (Figure 42b). As observed in Figure 42a,b, only the PET substrate and the multiple layers on top can be observed as the silver lines together with the isolation created a compact and uniform stack. The interface between the three materials appeared continuous with a tight adhesion thus indicating that the printed materials adhere well both to the substrate and to each other.

Furthermore, since the outmost layer of the passivation layer will be directly in contact with the cells, the effect of UV curing the SU-8 ink before cell seeding was studied by SEM. Surfaces of the SU-8 ink cured with UV are smoother compared with non-cured surfaces (Figure 42c,d). This effect could be explained by the fact that UV light polymerizes SU-8 ink formulation by cross-linking. However, smooth surfaces may hinder cell adhesions (as mentioned above) and, in any case, before seeding cells the sensors would be functionalized with an extracellular component (i.e., collagen). Therefore, IDEs-based sensors used for all the cell culture experiments were not treated with this ultimate UV curing, which also reduces the pre-treatment steps.

To characterize the electrical properties of the inkjet-printed sensors, electrical impedance spectroscopy was used (Figure 43). The impedance of the electrodes was acquired in a range of 100 Hz-100 kHz, which comprises the relevant bandwidth in impedance-based cellular measurement³⁰⁰ and under identical conditions for culturing the cells (i.e., culture medium, 37 °C, 5 % CO₂). (see Chapter III, section 3.5.4)

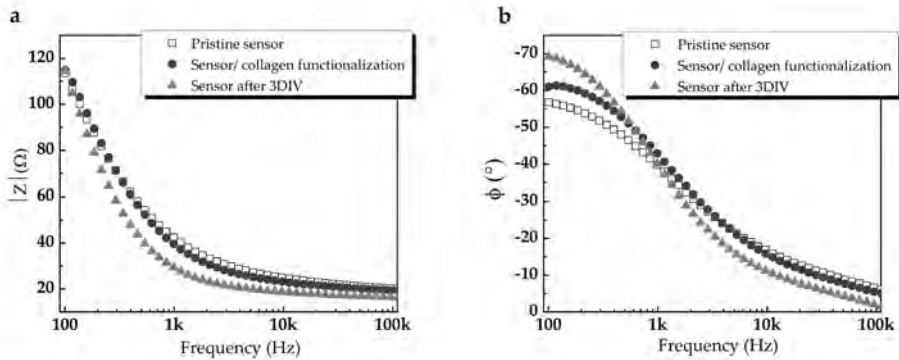


Figure 43. Electrical characterization of the inkjet-printed sensors by impedance spectroscopy. Sensors were characterized before (pristine) and after being functionalized with collagen, and after performing *in vitro* cultures of HaCaT cells. The measurements were performed at 37 °C, 5 % CO₂, and 2 mL of culture medium. The left plot shows the magnitude of the impedance (a) and the plot on the right shows the phase angle (b).

From the impedance curves, two electrical behaviors are distinguished depending on frequency. First, a capacitive-like behavior around lower frequencies until 5 kHz (phase angle = -70° at 100 Hz) and second, a resistive-like response (phase angle near to 0°) at higher frequencies. The capacitive behavior that covers most of the frequency spectrum comes from the double-layer capacitance at the electrode interface. This double layer is caused by the concentration of ions/molecules from the culture medium into the surface of the electrode when an electric field is presented. The resistive tendency at high frequencies (>20 kHz) represents the solution resistance (i.e., culture medium). As shown in Figure 43, the impedance at 100 Hz exhibited an average value of 120Ω ($n = 3$, $\sigma = 10 \Omega$) for pristine devices (i.e., before collagen functionalization and cell seeding). After functionalizing the sensors with collagen, the average impedance did not significantly change, but the phase angle varied an average of 5° at 100 Hz. This behavior could be explained by the fact that this collagen coating varied the permittivity in

the surface of the sensors, which slightly alter the capacitive response. The electrical stability of the sensors after being in contact with cell cultures was also tested by EIS. The impedance of the sensors after 3 days *in vitro* (3 DIV) with cell cultures and after following a cleaning process exhibited a small variation in the values of magnitude and phase for frequencies above 500 Hz-1 kHz. In particular, the impedance magnitude varied 10Ω ($\sigma = 0.65 \Omega$, $n = 3$) at 1 kHz while the phase angle varied $\sim 15^\circ$ ($\sigma = 7^\circ$, $n = 3$). This electrical characterization demonstrated the feasible performance of the sensor for *in vitro* monitoring of cell cultures as will be evidenced later in section 4.7.

4.6.2. Cytocompatibility characterization of the printed sensors

To study the toxicity effects on the cell cultures after 3 days *in vitro* a Live/Dead viability assay was performed. The protocol of the experiment was explained in Chapter III, section 3.2.3.

Results from the fluorescence images in the Live/Dead protocol are depicted in Figure 44a. The graph represents the percentage of living cells and dead cells in two independent experiments. Figure 44b shows the simultaneous detection of the live and dead cells: green-stained cells represent live cells while red fluorescence represents the nucleus of the population of dead cells. After processing the images, we assessed that the number of living cells was much higher than that of dead cells: an average of 96 % of the total cell population was identified as living cells and only 3 % as dead cells. The total number of images processed was $n = 60$ and the statistical analysis resulted in a $p < 0.005$.

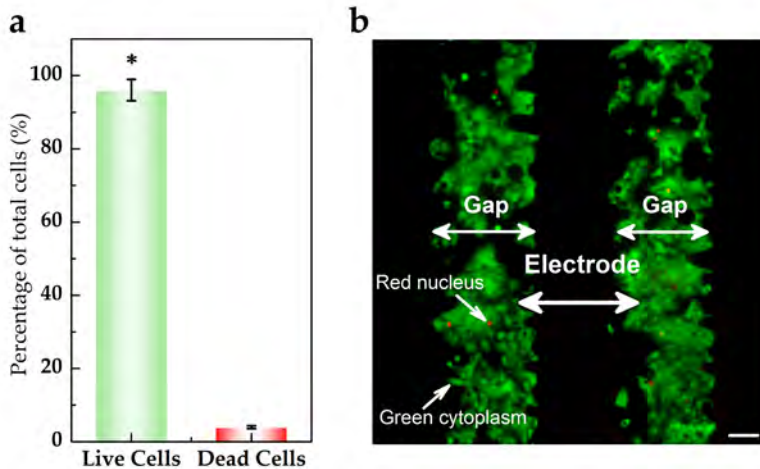


Figure 44. Cytocompatibility characterization of the inkjet-printed sensors and the sensor-based unit to perform the impedance spectroscopy. a) Live/Dead assay on the HaCaT cell line after 3 days of culture. Distribution of live and dead cells of a total of 60 images of areas around different electrode sites on the IDEs. The error bars represent the observed standard deviations. b) Fluorescence image of the surface of two consecutive fingers of the electrodes (scale bar 100 μ m). Living cells can be seen in green while red spots identify dead cells. Due to the non-transparency of the conductive lines (AgNP), stained cells can be observed only on the gaps between the interdigitated electrodes as the sample was illuminated from below.

The non-transparency of the silver lines and the fact that samples were illuminated from below made observation of the stained cells only possible on the gaps between the IDEs structures (see Figure 44b). To verify that cells were also spread over the area of the electrodes (dark zone in the Live/Dead staining images, Figure 44b) the experiments were replicated to perform an observation by SEM. A top view of the electrode area covered with a confluent cell monolayer by SEM is depicted in Figure 45. Two areas of the image at the left are shown enlarged at the right, showing a tight adherence between cell-cell and cell-substrate over the surface of sensors in general and on the opaque electrodes. Thereby, we confirmed our previous hypothesis that when cells were observed by fluorescent staining in

the gaps of the IDE-fingers, the ones on the electrodes were not seen due to electrode opacity. Besides this, the tight adhesions observed between the electronics and the cells reduce the parasitic contributions from the lack of stability in such interfaces which is essential for good and stable impedance measurement.

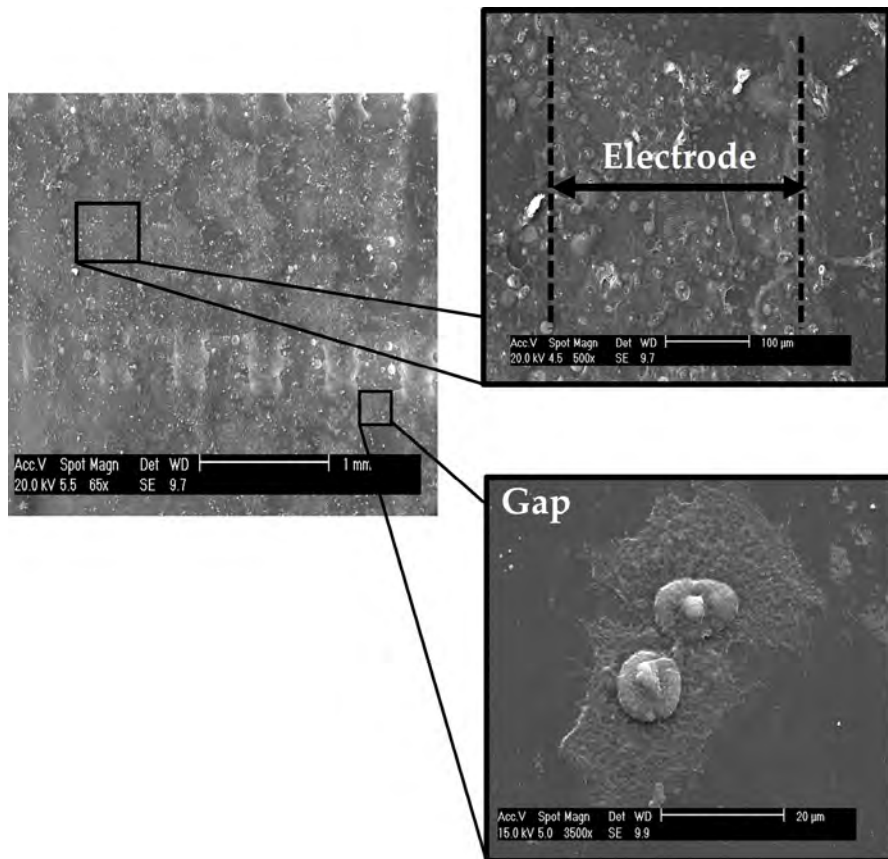


Figure 45. Cytocompatibility characterization using SEM. (Top left) An SEM top view of the inkjet-printed sensors covered by a confluent monolayer of HaCaT cells (scale bar 1mm). (Top right) A zoom-in on the electrodes confirmed that when stained cells are observed using the Live/Dead assay on the gaps they were also present over the opaque electrodes (scale bar 100 μm). (Bottom) The image (scale bar 20 μm) demonstrates the adherence of the cells to the surface of the sensors.

The results presented in this section from both the Live/Dead assay and SEM images demonstrated the cytocompatibility of the inkjet-printed sensors and the IDEs-based devices for cell cultures. In addition, this characterization confirmed that the culture of HaCaT cells is feasible for extensive periods of time and thus the system can be used for long-term monitoring of impedance spectroscopy since the sensors allow for both attachment and survival of the cells.

4.7. DEMONSTRATION OF THE USE OF THE DEVELOPED INKJET-PRINTED SENSORS FOR NON-INVASIVELY MONITORING OF CELL CULTURES

In this section we describe the integration of the inkjet-printed sensors in 2D cell cultures of a human epidermal cell line and the use of the proposed sensors in the study of biological processes of interest for laboratory-grown skin substitutes, which also provides evidence of the proper operation of the sensors under long-term exposition to cell cultures.

As described in Chapter I, the skin is composed of three structural layers: the deeper hypodermis, a thicker dermis, and the superficial epidermis. The epidermis is mainly composed of keratinocytes assembled in many layers which ultimately end up in the stratum corneum. The outermost cell layer of the stratum corneum shed from the surface in a natural cycle over 28 days.⁸⁷ When the skin is injured complex processes

are immediately activated until the skin is healed. In this wound healing process migration and proliferation of keratinocytes play a key role.³⁰¹ With this in mind we describe in this section the use of the developed sensors in highly relevant skin-related processes as are cell proliferation (section 4.7.1), cell-sensor adhesions (section 4.7.2), and migration (section 4.7.3). To that aim, a monolayer of a cell line of keratinocytes (HaCaT cells) was cultured on top of the fabricated IDE sensors, and cell-sensor interactions were monitored using electrochemical impedance spectroscopy (EIS) in a frequency range of 100Hz-1MHz which comprises the region of β biological dispersion.^{300,302} In this β dispersion region the extracellular resistance and membrane capacitance can be considered as the primary contributor to the impedance.²⁵³

4.7.1. Validation of the developed sensors for cellular studies: Impedimetric sensing of cell proliferation

The complex, frequency-dependent, impedance was measured and expressed using the dimensionless parameter **cell index**²³⁸ (as described in Chapter III, section 3.5.4) which represents the temporal variation of the normalized impedance measured by the sensors due to the presence of cells. To begin this study the interdependence of the initial cell density and the cell index values obtained with the impedance measurement was investigated by seeding different initial HaCaT-GFP densities. The initial cell densities seeded were 12 000 cells/cm²; 35 000 cells/cm², 75 000 cells/cm² and 130 000 cells/cm². The measured impedance with different initial cell densities was continuously monitored over 96 h.

Figure 46a depicts a micrography of the samples with different initial cell densities seeded at time 5 h. At this temporal point the impedance was measured and significant differences were detected between the cell index calculated at 100 Hz as shown in Figure 46b. The temporal variations of the cell index values caused by the adhesion and cell proliferation during 96 h were also monitored as depicted in Figure 46b. The representative cell index curve shown in Figure 46b was obtained at 100 Hz, however, a similar tendency was identified for the whole frequency range in which the impedance was measured. In other words, there was not a particular frequency in which changes in the impedance magnitude caused by the cells were identified as more sensitive.

After seeding, subsequent cell adhesion and proliferation induced a change in the cell index value measured. As we can see in this Figure 46, such index evolved differently for the four densities initially seeded. Changes in the cell index values for the sample with the lowest initial cell density (12 000 cells/cm²) remained almost inappreciable over the experimental period. On the other hand, samples with higher initially cell density (35 000 cell/cm², 75 000 cells/cm², and 130 000 cell/cm²) showed a clear increment in the cell index not only within the first hours but also continued constantly increasing during the experimental period. This increment was established as an indicator of the proliferation of the cultured cells with the assistance of microscopy observation.

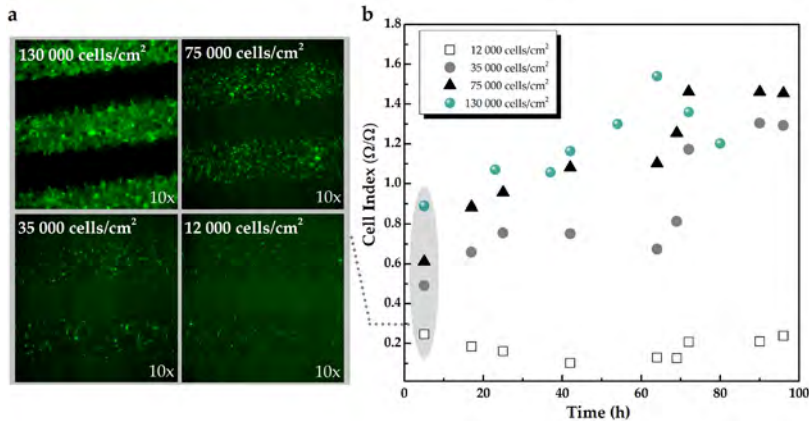


Figure 46. Monitoring of cell proliferation through the temporal variation of the impedance. a) Micrography of the samples with different initial cell densities of 12 000 cells/cm²; 35 000 cells/cm², 75 000 cells/cm² and 130 000 cells/cm² on collagen-coated IDE-based devices. The green-fluorescent HaCaT-GFP cells were observed only over the gaps of the interdigitated electrodes since the opacity of the conductive electrodes makes it unable to observe the samples over the complete surface of the sensors. b) Monitoring of the cell index values versus time in hours associated with HaCaT-GFP cell adhesion and proliferation over 96 h. Differences in the cell index value were obtained for different initial cell densities. For an initial density of 75 000 cells/cm² the maximum in the cell index value is attained at 72 h which suggests that the cell culture reached confluence. At low initial cell density (12 000 cells/cm²) changes in the impedance are almost inappreciable over the experimental period. The maximum value in the cell index for each sample is obtained at different time points, which was associated with differences in the time for cultures initially seeded with different densities to reach their confluence. In other words, the time to reach the maximum value in the cell index is inversely proportional to the cell density initially seeded.

The time at which the sample with the highest number of cells initially seeded (130 000 cells/cm²) reached the maximum cell index value (1.54 cell index units) was 60 h from seeding, while for those with 75 000 cells/cm² was 72 h (1.5 cell index units) and for those with 35 000 cells/cm² was 90 h (1.35 cell index units). This difference in the time when the maximum cell index is reached can be associated with the fact that different initial cell densities lead to a different

time for the culture to reach the plateau. In other words, the time required for a culture to reach its maximum value in the cell index (and therefore in its confluence) is inversely proportional to the cell density initially seeded. Likewise, the cell index is different in value for the different initial cell densities not only at the beginning of the experiment, but also as the experiment evolves. For example, the actual difference in the cell index value for the initial seeding of 130 000 cells/cm² from time 5 h to 24 h was 0.274 units, while for the sample with an initial cell density of 75 000 cells/cm² was 0.471 in an identical period of time. These variations in the actual differences of the cell index at different cell densities could be explained by the fact that the parameters influencing the measured signal (e.g., cell-substrate adhesion, cell-cell junctions, cellular activities) vary from one density to another.

As can be inferred from the results above, the presence of cells on the surface of the electrodes yields an increment of the impedance at the electrode-cell interface mostly due to the insulating properties of the cell membranes. However, if the number of cells is not enough to perturb the electric field on the sensor's surface, small or no changes in the impedance can be observed as is the case of the initial seeding of 12 000 cell/cm². In such situations the effect of the resistance of the culture medium prevails over the insulating effect of the cells, and the impedance measurement is not able to observe the small changes associated with cell proliferation (detection limit). Thus, for monitoring the proliferation of a population of cells using impedance the number of cells initially seeded should be first determined and characterized depending on the time of the experiment, the type of cells, and the area available for the cells to proliferate.

To advance with this study, the interrelation between the density of cells initially seeded and the measured cell index was studied. Figure 47 shows a linear correlation ($R^2=0.98$) between the cell index and the density of the cells initially seeded on the electrodes using the cell index values at 5 h. The sensitivity of the sensors was then defined by the ratio of cell index and cell density, as $S= \Delta \text{ Cell index}/\Delta \text{ cell density}$ from the slope of the lineal fit (Figure 47).

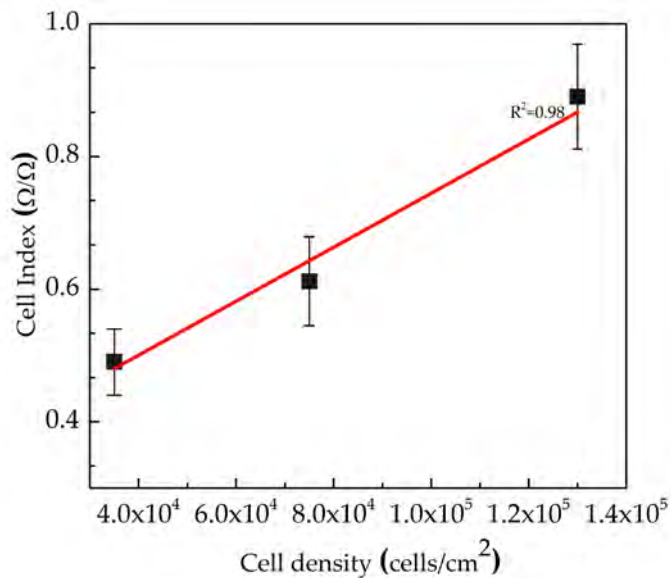


Figure 47. Cell index versus initial cell density at 5 h obtained using the samples initial seeded with 35 000, 75 000 and 130 000 cells/cm²(error bar represents the standard deviation, $n=3$). Samples with initial cell densities of 12 000 cells/cm² were not included since the value remained almost constant even after 69 h which was interpreted to be under the sensitivity limit of the device.

The sensitivity obtained for our sensors was $S = 4.07 \times 10^{-6}$ cell index/cells·cm⁻². This linear relation allows considering that the value of the cell index depends linearly on the total number of adhered

cells initially seeded on the sensors. Recently, some works have reported that impedance of conductive electrodes mirrors the numbers of cells adhered on the electrodes' surfaces with a linear correlation not only at the initial point but also as their experiment evolves.^{262,303} Based on this evidence in the literature, we infer that the linear trend estimation between the cell index and the cell density initially seeded obtained from our data at time 5 h can be associated with other periods of time, and therefore we consider that impedance-based techniques using our inkjet-printed sensors can be a feasible approach to determine cell concentrations.

To further analyze the correlation between the impedance measurements and the electrical properties of the cell membrane, Triton X-100 (a non-ionic detergent) was added at the endpoint of the proliferation assay as described in Chapter III, section 3.2.8. As impedimetric biosensors can detect changes in the cellular cultures, the electrical signal may be influenced not only by the electrical properties of the cellular membranes (their insulating properties under an electrical field) but also by variations in the medium conductivity due to wastes from the metabolic cellular activity. The addition of this non-ionic detergent allowed us to test the hypothesis that the disruption of the membranes of the cells in contact with the surface of the sensors would result in changes in the electrical monitored signal.

Results of the values in the cell index (impedance) after adding 0.1 % Triton X100 at the samples are depicted in Figure 48a. Cell index sharply decreased within the first ten minutes a total of 0.12 units. The effect of the detergent on cell membranes can be expected to insert themselves directly into the bi-lipid layer in the cellular membrane and

physically permeabilize it by a disrupting action of the polar head group on the hydrogen bonding present within the cell's lipid bilayer. Thus, the addition of detergent leads to a destruction of the compactness and integrity of the lipid membrane and, eventually, an over-permeabilization of the structure (i.e., cellular membrane). It should be noted, however, that insertion of detergent monomer into the lipid membrane at low concentrations (e.g., 0.1 % as used in our work) and in short times (i.e., lower than 30 min) does not affect cell viability (i.e., cell as a complex system).³⁰⁴

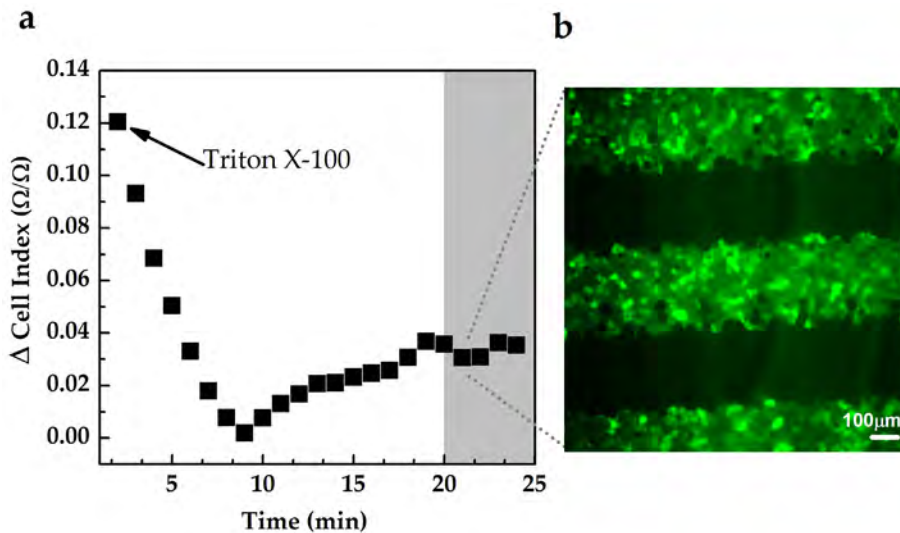


Figure 48. Study of the influence of the electrical isolating properties of the cellular membranes on the impedance changes. a) Cell index values versus time in minutes during 25 minutes after adding Triton X100 at the endpoint of the proliferation assay (the moment when the cell index value measured was around 1.4 units in culture medium). Triton X100 is a non-ionic detergent that physically disrupts the cellular membranes of the culture. b) Micrography of one cell culture of HaCaT-GFP at 23 min after adding Triton X100 to 0.1 %. The changes in the impedance correlated with the disruption of the cellular membrane since the detergent did not detach the cells from the surface of the sensors.

To assess that the change in the impedance was indeed associated with the disruption of the cell membrane and not due to the detachment of the cells or cell destruction, the treated cultures were optically observed under the microscope after 20 min of detergent addition (Figure 48b). This image demonstrated the presence of cells attached to the electrodes and therefore the variation in the cell index (i.e., in the impedance) can be attributed to the destruction of cell membranes and thus its electrical insulating function.²⁵² An increase in the cell permeability (after adding Triton X-100 to 0.1 %) altered the dielectric properties of the cell membrane due to membrane solubilization producing, in turn, a lower impediment for the electric field compared with intact cells (before adding the detergent), which we associated to that decrease in the impedance. Likewise, non-intact cell membranes lead to an increase in the exchange of ions between the medium and the cytoplasm which can cause a slight increment in the cell index value shown in the figure after the first 10 minutes. With this experiment it can be confirmed that the main contribution in the total measured impedance using the inkjet-printed sensors comes from the electrical insulating properties of the cellular membrane.

4.7.2. Validation of the developed sensors for cellular studies: Detection of cell-sensor adhesions in epithelial cell culture using inkjet-printed sensors

In this section a second type of experiments relevant for engineered-skin sensing applications, cell-sensor adhesions, are described. These experiments may be of relevance for applications where the interactions taking place at the cell-sensor interface would be of vital importance such as in implantable bioelectronics and electroceutical applications.

The cell-sensor adhesion experiments involved the seeding of a monolayer of cells with high densities on collagen-coated sensors (80 % of confluence). Then the impedance was monitored continuously over 80 h and analyzed over the whole bandwidth, this is, from 100 Hz to 1 MHz. In this case, and instead of using the cell index value used before, the data were analyzed using Nyquist plots and the obtained (frequency dependent) impedance was fitted to an equivalent electrical circuit that mimics the electrical behavior of the experimental data.

To obtain an equivalent circuit for the impedance we can focus either on faradic or non-faradic processes.³⁰⁵ In our case, the interactions between the sensors and the cells and, thus, the equivalent model, was analyzed using a non-faradic analysis in which the electrical current between the electrodes is modeled using the capacitive nature of the electrodes. In this case changes in the electrical field (measured impedance) are associated to changes in the capacitance between the interdigitated electrodes of the sensors, this is, an interface impedance. The equivalent electrical circuit selected to model the cells-sensor interfaces (and the associated impedance) is presented in Figure 49a.

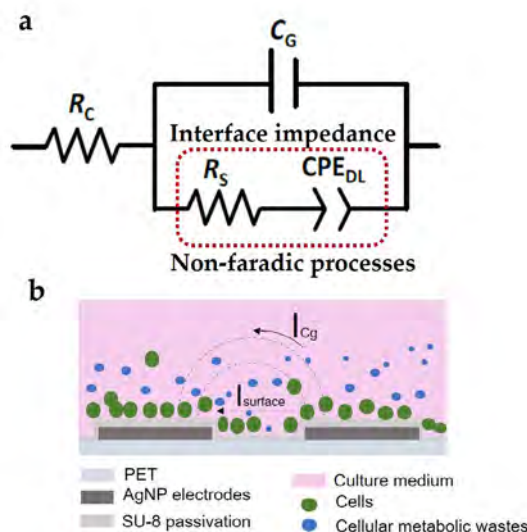


Figure 49. Equivalent circuit model for the sensors and sensing process to study cell detachment. a) Equivalent electrical circuit to fit the experimental data resulting from a non-faradic analysis of the system cells/sensor. The effects of the different electrolytes were modeled using resistances, this is, R_C for the culture medium and R_S for the metabolic results. Cells' electrical response was modeled using a CPE and the geometrical capacitance of the interdigitated sensors as a capacitor C_G . b) Schematic modeling of the physical interaction between the cell and the surface of the sensors. The current flows are associated with the capacitive behavior of the IDEs and must pass through the culture medium. When the cells cover the sensor the impedance increases.

Modeling cell-sensors interaction is challenging due to the nature of the biological components interacting. First, cell interiors contain a plethora of organelles with different electrical properties and the cell exterior is surrounded by the extracellular matrix (ECM). Second, when cells are cultured, they need to be inside a culture medium containing animal serum. Third, cell membrane comprises not only a lipidic bilayer but also ion channels that may be open or closed depending on the cell behavior and therefore may increase conductivity. Finally, the cell's adherence to the substrate is dependent on focal adhesions which are complex structures that can be viewed as conductive segments.²⁵⁹ All

these different contributions make that the best elements to model cells in a non-faradic approach are not capacitors but a constant phase element (CPE). A CPE is a reactive component in which the phase angle between the real and imaginary parts of the impedance is constant over frequency.

The physical interpretation of the equivalent circuit of Figure 49a is better understood using the schematic represented in Figure 49b. To model the capacitance between the two electrodes in a solution, a capacitor C_G was used while the culture medium was modeled as a resistor R_C . The total current must pass through the culture medium thereby R_C is inserted as a series element. This total current, in turn, can be also seen as the sum of the contributions from the geometrical capacitance of the IDEs and the non-faradic process that take place in the interface of the electrodes due to the presence of cells. Therefore, C_G is inserted in parallel with the interface impedance modeled by a CPE and a R_S that accounts for the culture medium (resistance) around the electrodes as both a product of the metabolic wastes of cells (alterations in the ionic environment) and the cell-substrate junctions (conductive segments).

Figure 50a shows the Nyquist plot of the acquired impedance in the cell-sensor adhesion experiments. As mentioned before, each point of the Nyquist plot represents the impedance measured at one frequency. The higher frequencies in the plot are located closer to the origin where the real part is smaller. The circuit model discussed above was fitted to the impedance spectra as is shown in Figure 50b.

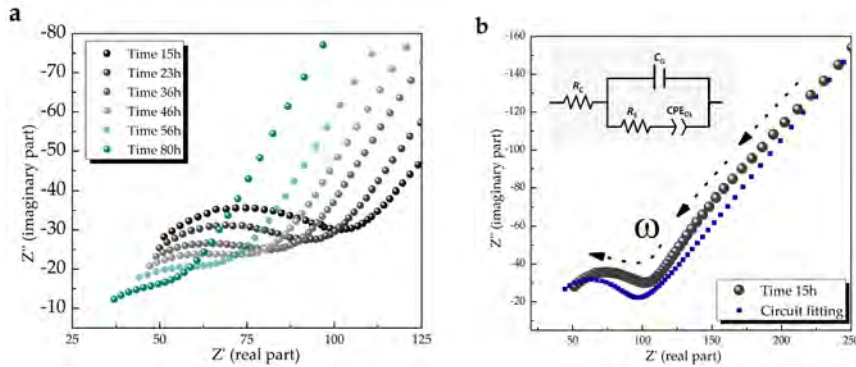


Figure 50. Nyquist plot to monitor cell-sensor adhesions over 80h. a) Real part and imaginary part of the impedance are plotted at each time point of the experiment. At time 15h the adherent cells (negatively charged) yield a surface impedance greater than the impedance at time 80h. b) Example of the fitting of the experimental data using the electrical circuit model proposed.

The plot could be divided into two main domains depending on frequency: a semicircle at high frequencies and a straight line with a certain slope at low frequencies. Using our equivalent circuit model, the R_s and C_g in parallel are responsible for the semicircular behavior at higher frequencies. This semicircle intercepts the real axis in two points: the intercept on the left-side gives the value of R_c and the intercept on the right-side accounts for R_s . As the resistivity R_c models the culture medium the value is expected to be constant (small variations at most) since the preparations and amount added to the different samples were identical. A small deviation, however, is observed along time of value $\Delta R_c = -3.13 \Omega$ which is explained by the fact that the media was not changed during the experiment and its ionic content varied slightly due to their consumption by cells.

The most important observation we can extract from this experiment is that the diameter of this semicircle reduces over time, being the most direct explanation for changes in the cell-sensor adhesions taking place on the

surface of the sensors. When cells reach a confluence density the phenomenon known as contact inhibition may lead cells to contract.³⁰⁶ This reaction manifested in high population density may produce cells to round up causing a loss in their grip on the substratum. In our model this phenomenon may be interpreted that cell-substrate interactions become weaker, leading to a lower value in the interface impedance of R_s -CPE. Another plausible explanation may be supported by the observation made by Curtis and Varde when outgrowing sheets of fibroblast on substrates with different topologies. They observed cell suspensions free from the substrate (i.e., detachment) in high population density, discussing their results with reference to the mechanism of contact inhibition.³⁰⁷ However, it has also been discussed that faced with a choice, cells outgrow on a confined space may be incapable to detach from the substrate to move across a less adhesive surface of other cells since the dorsal surfaces of cells may be less adhesive than the tissue culture substratum.³⁰⁶ In this framework our more conservative interpretation of the phenomenon being monitored is cell-sensor adhesions.

According to our model, the variation of the value of R_s is responsible for the variation of the diameter of the semicircle lying in the Z' real axis. At the beginning of the experiment (time 15 h) the higher cell-sensor adhesions yield a surface impedance greater than the impedance at time 80 h. For example, in the microscopic observation performed at time 23 h (Figure 51a) the green fluorescence over the surface of the sensors (strongly related to the number of cells attached) is bigger than at 80 h (Figure 51b). The impedance measurements were fitted to the equivalent electric circuit model and a summary of the variation of the values for the circuit elements are shown in Appendix III. $\Delta CPE(F)$ in the interface varied from 150 μF at 15 h to 0.76 μF at 80 h, while $\Delta R_s(\Omega)$ from 57 Ω at 15 h to 24 Ω at 80 h.

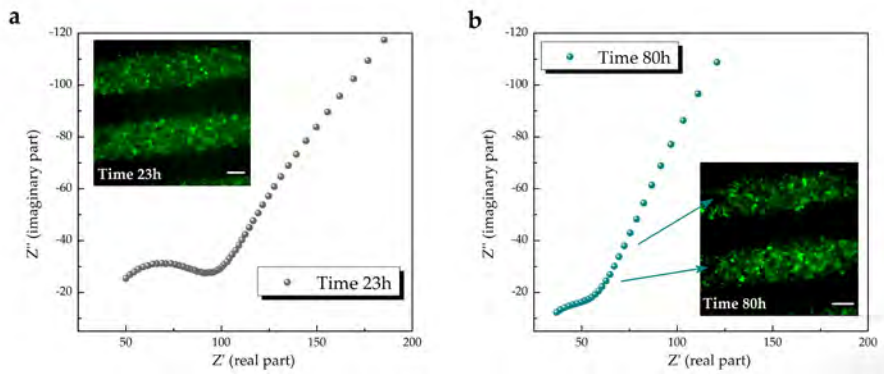


Figure 51. Analysis of the cell-sensor adhesions using microscopy observation and impedance-based monitoring. a) Nyquist plot and cellular images at time 23 h b) and time 80 h. It is observed that in some areas of the sensors at time 23 h the number of cells attached to the surface is more than at time 80 h. Consequently, the diameter of the semicircle lying in the Z' axis, associated with the value of R_s , reduces. (scale bar in the images $100\ \mu\text{m}$)

4.7.3. Validation of the developed sensors for cellular studies: Preliminary use of inkjet-printed sensors integrated into cell cultures to monitor cell migration

As mentioned before, wound healing is one of the most important processes associated with skin. For that reason, a third set of experiments were performed to study the use of the sensors developed in this important scenario. In this set of experiments a monolayer of HaCaT-GFP was seeded on collagen-coated sensors with a PDMS stencil as a barrier as was described in Chapter III, section 3.2.9. Briefly, and following the protocols from ref. ²³³, cells were seeded on the non-exposed PDMS area at a density that ensures confluence the following day. 24 h after cell seeding, PDMS was peeled off leaving free space for

cells to migrate. Compared to the standard scratch assay³⁰⁸ this method avoids cell damage at the edge of the scratch caused by the pipette and allows a simplification of the problem by analyzing only one half of the wound.³⁰⁹

The cell migration was tracked for at least 80 h by impedance spectroscopy. The acquired impedance was then processed using the cell index as described in Chapter III, section 3.5.4. Simultaneously, a time-lapse microscopy was performed to monitor the mean edge displacement in the monolayer of cells using image processing as described in Chapter III, section 3.3.3.2. Cells seeded on a petri dish were used as control groups.

Figure 52a shows an example of the migration of a monolayer of cells over the sensors and the control samples. The mean edge displacement in both the control and experimental groups was obtained by leading-edge detection using image processing. Figure 52b shows that the mean displacement of the front edge of cells for the control groups was around 1400 μm at 60 h and 1200 μm for the experimental groups (cell seeded on the IDEs sensors). Note that the actual displacement calculated is not referenced to the edge of the image but to the edge from where cells are detected at the beginning of the experiments. Likewise, a polynomial fit made on the experimental data extracted from the image-processing algorithm provided a mathematical interpolation between measured displacement to infer those Y-axis points when cells were migrating over the dark zones of the sensors.

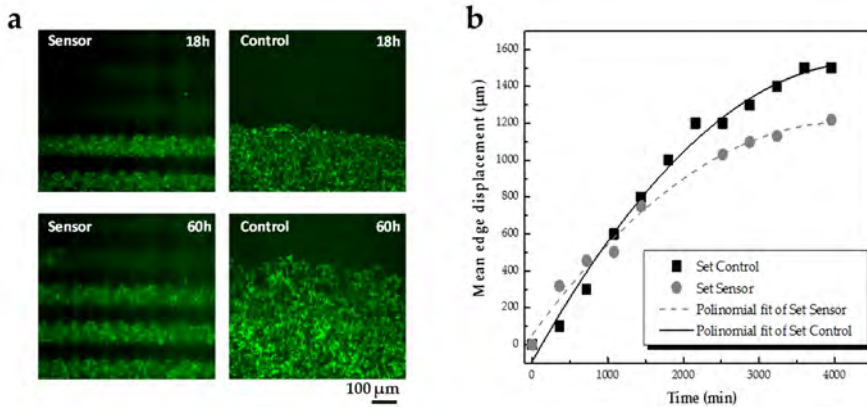


Figure 52. Monitoring of cell migration by time-lapse microscopy. a) Examples of the time-lapse of the cell monolayer migrating over the IDE-based devices and control (Petri dish). b) Mean-edge displacement of a monolayer of cell cultures in the experimental groups versus time in minutes during the time-lapse observation. The velocity in the cell migration resulted in $0.35 \mu\text{m}/\text{min}$ in controls and $0.3 \mu\text{m}/\text{min}$ in the IDEs-based groups calculated from $v = \frac{\Delta \text{Displacement}}{\Delta \text{Time}}$ as explained in 3.3.3.2.

The velocity in the cell migration resulted in $0.35 \mu\text{m}/\text{min}$ in control cultures and $0.3 \mu\text{m}/\text{min}$ in the IDEs-based cultures calculated from $v = \frac{\Delta \text{Displacement}}{\Delta \text{Time}}$ as explained in 3.3.3.2. This slight difference may be explained by two reasons. First, the flat topography in the control cultures compared with the micro-groves in the experimental groups could facilitate the migration. Second, the discontinuities presented in the fluorescence images in the experimental group due to the opacity of the conductive lines of the sensors generate blind zones, and thereby fewer points in the curve (Figure 52a). In this latter case it would be just an instrumental problem.

Taking advantage of our design that allows to combine both optical and electrical monitoring simultaneously under physiological conditions (cell cultures, 37 °C, 5 % CO₂), the impedance was also acquired every three hours during 66 h. Results from processing the impedance using the cell index adjustment and the interrelation between the optical and electrical method are shown in Figure 53a. It was observed an absolute variation in the cell index of 0.15 units after the duration of the experiment, which represents a sensitivity of $1.25 \times 10^{-4} (\Omega/\Omega) / \mu\text{m}$ using as a reference the microscopy images.

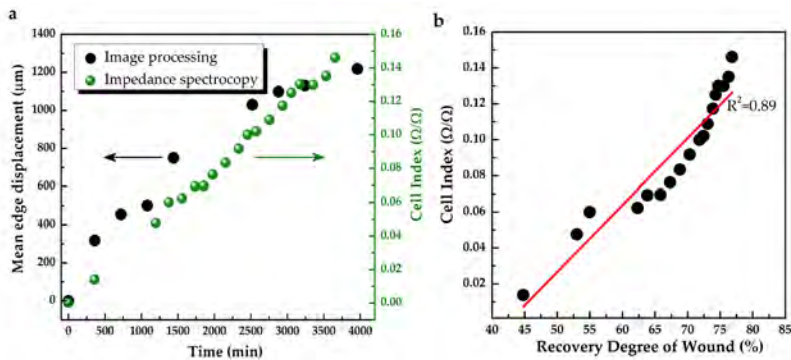


Figure 53. Monitoring of cell migration by impedance spectroscopy. a) Relation between the mean edge displacement determined by image processing and the cell index by impedance-based analysis versus time in minutes. b) Cell index units versus the recovery degree of the wound showing a linear correlation ($R^2 = 0.89$).

To gain insight into this impedance variation in response to cell migration the mean edge displacement of the monolayer of cells was used to obtain the recovery degree of the wound. This recovery degree in the simulated wound is calculated as the ratio between the total area that is free for cells to migrate and the front edge displacement (distance referred to the border of the image) at a given time point as described in

Chapter III, section 3.3.3.2. The curve is represented from 45 % of such a degree of recovery as it is the most representative data to be analyzed for the closing healing process. A linear relation ($R^2 = 0.889$) between the cell index and the recovery degree of wound was established as is depicted in the curve of Figure 53b. This continuous increment in the impedance signal from the sensors as cell migrated can be used to assess the healing degree without the need for visual observation.

It is important to note that this experiment represents a huge simplification of the extremely complex processes of wound healing. For example, cells are not only migrating but also proliferating. This proliferation increases the number of cells while changing the conductivity of the medium due to the metabolic activity of the cells themselves. Moreover, during cell migration, electrical signals are generated throughout cell-cell unions, which could lead to switching in the ion channels that are embedded in the cell membranes generating changes in the electrical signal detected. Full discrimination of the cellular process will never be completely possible with a single sensor, thereby a better understanding of the general physiology of an organotypic tissue or cell cultures is only thinkable if several sensors are simultaneously integrated. We shall see some of the potential modifications following this research line in the future-work section in Chapter IV.

4.8. DISCUSSION OF THE RESULTS

In this chapter the feasibility of integrating inkjet-printed interdigitated sensors for cell-substrate impedance monitoring of 2D epithelial cultures has been demonstrated.

The use of printed electronics and low-cost flexible substrate in the manufacturing of sensing devices for tissue engineering and bioelectronic applications have increasingly gained attraction, as we saw in Chapter II. For *in vitro* applications, the main advantage that these flexible devices have offered is they overcome the mechanical mismatch between the traditionally adopted rigid substrates (i.e., glass and silicon) and the living cells while monitoring non-invasively a variety of biomarkers and cellular processes.³¹⁰⁻³¹⁴ However, only a meager fraction of these printed devices does not need the use of additional clean-room steps or enjoy a manufacturing process compatible with current bioprinting methods. By contrast, we have fabricated our sensors by inkjet-printing technology in ambient conditions without requiring expensive clean-room facilities. Thus, both the materials selected, and the manufacturing technique allowed for low-cost fabrication and rapid prototyping of flexible interdigitated-electrodes sensors in a short time. Likewise, what is most important for our future application is that the manufacturing technique used may open the possibility of engineering a hybrid platform to print electronics and functional skin substitutes simultaneously. It still needs to be elucidated the coexistence in such a platform of bio-based inks and electronics. However, this bottleneck could be overcome if scientists in the fields of material science, biology, and engineering alike join forces.

The fabricated impedance sensors were proved as highly reproducible with low batch-to-batch variation demonstrated through the morphological, electrical, and cytocompatibility-based characterization. Such characterization allowed to determine their potential use in relevant applications as integrated sensors in cell cultures. From the morphological characterization, differences between the designed layout and the final printed results were observed. Satellite drops and certain discontinuities along the conductive lines were attributed to tunable factors during the printing process such as the non-perfect ink spreading on the surface, deficiencies in the cleaning cycles, and occasional clogging of the printing nozzles in the print-head. Thus, a previous selection of the better sensors for the cellular experiments was ensured based on the optical and electrical characterization.

The nano-topographical profile of the IDEs sensors resulted in a non-planar surface showing micro-groves with width and height of 300 μm and $\sim 4 \mu\text{m}$ respectively. Non-planar features in bioelectronics have been proved to encourage electronics-tissue adhesions by a phenomenon known as cell contact guidance.^{298,299} Such tight interfaces are a prerequisite to either electrical stimulate or record signals from the adhered cells with a high signal-to-noise ratio (SNR). For the SU-8 passivation several, yet not consecutive, layers were printed which caused the misalignment of the origin of the printing head after each printing/curing process. This misalignment is ascribable to the resolution achieved by the printer when a re-position of the origin is required which in the printer setup used in this work was 10 μm . Those deviations, however, did not hinder the feasibility of integrating and exploited the printed IDEs *in vitro* as impedimetric sensors. As described in Chapter II, many parameters can be tuned when using inkjet printing technology to achieve reliable patterns

and improve printing resolutions.¹⁸² Technical modifications in the printing system such as the use of 1 pL cartridges instead of 10 pL can be considered in the future. By varying the hydrophobicity of the substrate, and thus, the contact angle between the ink and substrate, a sub-micron resolution has been achieved on organic printed transistors,¹⁸² which can also be considered to engineer a “bio-inspired” substrate with tunable hydrophobicity while improving electronic resolutions.

From the electrical characterization of the sensors, the magnitude of the impedance of the sensors at 100 Hz resulted in 113 Ω for the pristine device. The sheet resistance of printed lines using silver nanoparticles-based ink has been reported in the literature to be 0.4 Ω/\square ,²⁴⁷ giving a theoretical value for the impedance of the fabricated sensors of 88 Ω . Thus, the experimental data resulted in the same order of magnitude compared with the theoretical value. The impedance analysis of the sensors after 3 days *in vitro* with cellular cultures resulted in a very small variation of 10 Ω at 1 kHz, which demonstrated the electrical stability of the sensors and the possibility to re-use the inkjet-printed-based devices after a proper cleaning. The cellular experiments using the IDEs devices, however, were performed always on pristine devices due to the cost-effective manufacturing technique employed. Furthermore, the effect of coating the devices with an extracellular component of cells (i.e., collagen coating) was analyzed by impedance spectroscopy. The electrical signal in the impedance magnitude with and without collagen-based coating showed no significant differences which suggested that the collagen did not influence the performance of the sensors for cell-cultures applications.

Finally, a cytocompatibility characterization to demonstrate the viability of the inkjet-printed sensors for impedance monitoring of epithelial

cell cultures was performed. This cytocompatibility characterization was carried out through both a Live/Dead Assay and SEM microscopy. The experiments demonstrated that the custom-designed, sensing device to culture the cells for the real-time cellular experiments as well as the ink-jet-printed sensors themselves were cytocompatible.

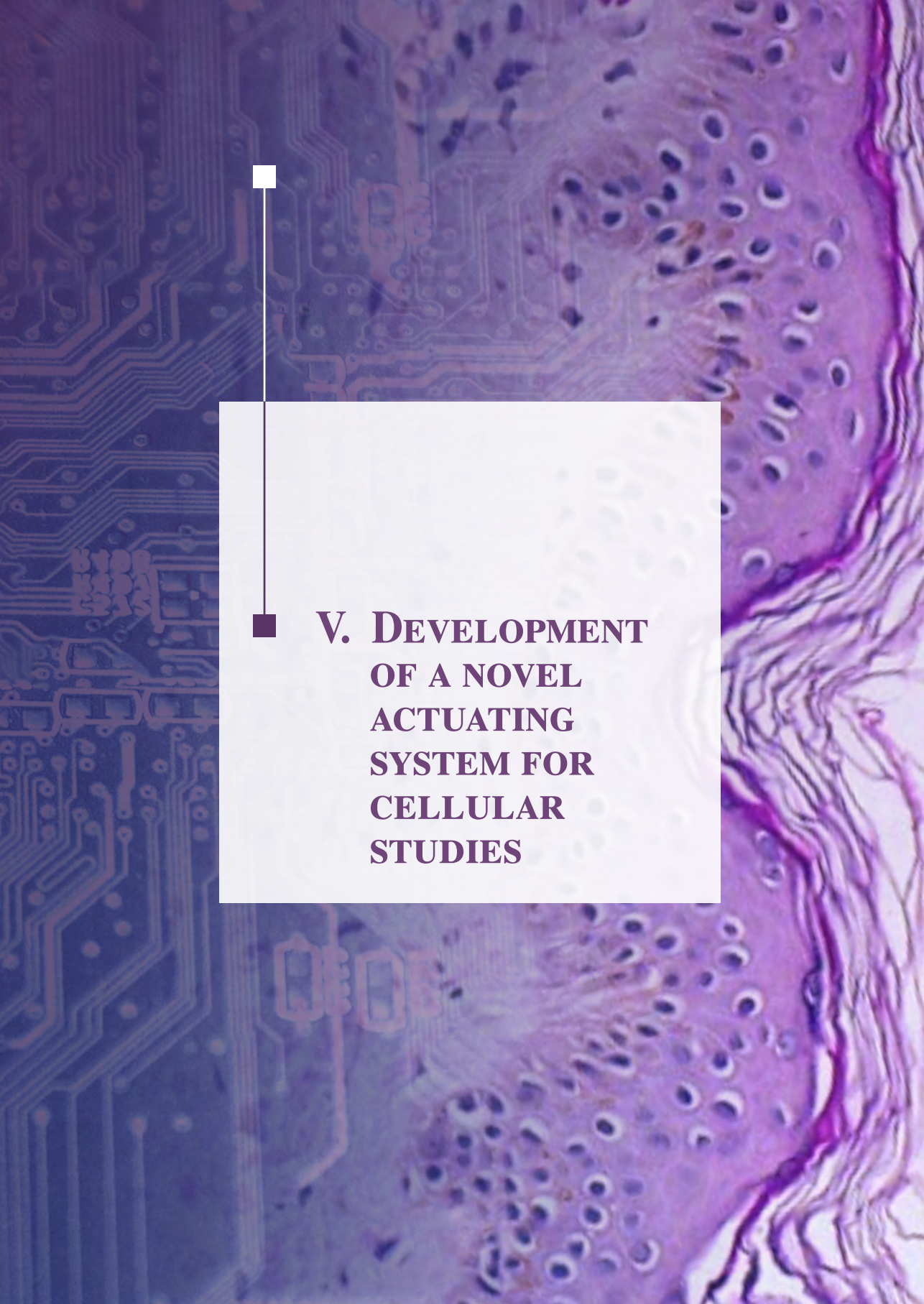
Having characterized the sensors in terms of morphology, electrical performance, and cytocompatibility, three groups of experiments were performed to use the sensors in potential engineered skin-based applications which also provided evidence of the possibility of reliable, long-term use of the sensors under cellular conditions. Those experiments were the monitoring of proliferation, cell-sensor adhesions, and migration of a cell line of keratinocytes.

The sensitivity of the impedance signal to the culture's cellular density was analyzed by seeding different initial cell densities. The relationship between the cell index value and initial cell density was supported by fluorescence microscopy. Low cell density did not generate enough changes in the signal of the sensors whereas higher densities could be monitored over 96 h. At an initial density of 12 000 cells/cm² the number of cells was still insufficient to perturb the electric field on the sensors' surfaces which resulted in non-detectable alterations in the measured impedance. Measurements under such conditions, therefore, were established as below the detection limit of the sensors in which the resistance of the culture medium prevails over the cellular impedance. The interrelation between the cell index calculation and the initial cell density was established considering the other densities (i.e., 35 000 cells/cm², 75 000 cells/cm², 130 000 cells/cm²) which resulted in a linear correlation with regression of $R^2 = 0.98$. This linearity suggested that the cell-substrate impedance mirrored the number of cells initially

seeded and demonstrated the capacity of the sensors to discriminate cell concentrations. This linear relationship between the electrical impedance and the number of cells attached to the measuring electrode is not something completely new. Indeed, it is the principle of operation behind the development of the impedance technology as an analytical tool for *in vitro* analysis of cells,^{258,271} with some examples of those devices commercially available. However, those systems are optimized to increase the sensitivity to cells' activities surrounding the working electrode, which have resulted in designs that use a very small working microelectrode and a large counter electrode. Consequently, those systems are not suitable for the monitoring of large cell aggregates. Likewise, although those impedance-based systems have been proved valuable as electrochemical systems with a special focus on characterizing single-cell dielectric properties and cell-cell junctions communication, they have not been designed considering their use for implantable applications (i.e., they are not free-standing) and their designs are still based on rigid, bulky substrates.

To increase the sensitivity of our sensors the design of the electrodes as well as the materials used can be optimized.³¹⁵ Other parameters such as the thickness of the electrodes and the passivation layer can be improved and tailored to the application.³¹⁶⁻³¹⁸ For example, fabricating IDEs with gaps in the order of the cell size³¹⁹ has been proved to enhance the sensitivity to the presence of cells (i.e., lower detection limit). Nevertheless, by using the inkjet-printed IDEs devices with gaps of 300 μm , we were able to monitor in real-time a monolayer of adherent biological cells using impedance spectroscopy within frequencies relevant to give information of the cell membrane²⁵³ (i.e., β dispersion region).

The possibility of using both the sensors and the impedance-based method for monitoring cellular behavior related to skin wound healing was also studied. The cellular processes studied were proliferation and migration of a monolayer of cells seeded on the sensors. In addition, a study of the influence of the cell membrane in the measured impedance was carried out by adding a non-ionic detergent³²⁰ at the endpoint of the proliferation assay. This study allowed to determine that the insulating properties of the membranes were the main element contributing to the IDEs measured impedance and the rapid detection in the monitored signals also confirmed the rapid response of the impedance-based method to changes in the cell structures. The experiments set-up to study cell migration showed a linear relationship between the cell index value and the progression of the wound healing (regression coefficient of $R^2 = 0.899$), taking into account that rather than a faithful representation of the complex process during wound healing, the cell migration experiment represents a simplification of such a biological scenario. Monitoring other biomarkers at the same time can give a deeper insight into the physiology of the cells or tissues, e.g., pH, dissolved O_2 , or lactate.³²¹ In addition, instead of using interdigitated-electrodes in which the measurements rely on the signal coming from the whole surface of the sensor and therefore the lumped impedance value is incapable of providing a conductivity distribution of the entire sample, monopolar microelectrodes distributed around the sensing area can be designed. Measuring the impedance between all neighboring electrodes, the magnitude and phase of the impedance can be plotted as function of the electrodes' position to provide a variation of the conductivity within the sensing area. Thus, during cell migration, the impedance of the covered-cells electrodes compared to free-cell electrodes could give a map informing not only whether cells are migrating but also their relative positions on the zone.



**V. DEVELOPMENT
OF A NOVEL
ACTUATING
SYSTEM FOR
CELLULAR
STUDIES**

*Detente en todo
y que nada
te detenga.*

Miki Naranja

CHAPTER V. Development of a novel actuating system for cellular studies

5.1. INTRODUCTION AND MOTIVATION

Cell functions are controlled through the interplay and feedback between soluble and non-soluble signals at all size scales and nature. Whereas soluble cues rely on biochemistry there are also non-soluble ones that are based on biophysics and mechanics. Biological processes, however, have been profoundly interpreted and rooted in terms of biochemical signaling. The idea that events (either physiological or pathological) are only controlled by either the biochemical environment of the cells or a signaling cascade of pure chemical nature (e.g., enzyme activity) would leave no role for mechanics in the understanding of cellular function, sidelining the myriad of mechanical forces that also influence cell-specific behaviors. Heart bump, fluid shear stress, and mechanical load in the skeletal system operate in a living organism and affect all cells of every organ. For instance, the size of blood vessels is controlled by shear stress,³²² and pressure and tensional forces cause the bone to remodel³²³ (Wolff's law).

Thanks to their complex cellular structure cells can translate mechanical stimuli into biochemical signals. This process is known as mechanotransduction.³²⁴⁻³²⁶ Mechanical parameters such as stiffness, topography, and force are informational cues by which cells sustain, detect, and interact with their environment. As such, cellular mechanically-induced responses —healing tissues, for example— are generated until a mechanical equilibrium is attained.³²⁷ Constraints in this equilibrium (caused by internal forces dictated by cell organization and/or exogenous signals transmitted *via* the cell's microenvironment) can alter multiple aspects of the tissue homeostasis which have been associated with some acquired or inborn diseases.³²⁸⁻³³⁰

The lack of instrumental techniques, devices, and protocols not only to measure but to apply changes in the cell's mechanical microenvironment to study cellular outcomes had long sidelined this physics-based approach for the understanding of living systems.³³¹ However, seminal discoveries on the mechanism of mechanoreception at a cellular level³³²⁻³³⁴ (which in turn coined the term mechanobiology)³³⁵ started turning the scientific attention towards unraveling the far-reaching implications that mechanics plays in biology. Early studies pioneered the use of classic instrumental tools such as atomic force microscopy³³⁶ and optical tweezers³³⁷ with the aim of measuring the mechanical parameters (e.g., stiffness, roughness, etc.) of cells. New methods have gradually emerged^{338,339} and the unexpected influence and crucial role that physical forces have proven to play in cellular behavior have placed mechanobiology at the forefront of biological research.

Understanding the influence of mechanics in biology opens a lot of clinical possibilities. Chemical-independent control of cellular mechanisms and/or components could have potential applications in a variety of fields ranging from drug discovery to tissue engineering. For instance, low-intensity vibration³⁴⁰ (LIV) and shock waves³⁴¹ have been used to treat pressure ulcers and chronic wounds. The use of LIV in diabetic mice enhanced both skin granulation and angiogenesis reducing the closure time of wounds in the experimental group compared with non-vibrated controls.³⁴⁰ Local mechanical therapy has also shown potential as an alternative to medicament-based treatments for pressure ulcers in a rat model³⁴² and stage-I-pressure ulcers in adult patients.³⁴³

Considering the central role that mechanobiology plays in the human body and the potential use of dynamical mechanic-based stimulation in regenerative medicine engineering, in this chapter we present a novel electromechanical device as an experimental tool to perform dynamic mechanical stimulation to cell cultures. The system a) supports the research on cellular mechanotransduction, b) stimulates cells *via* dynamic variations of the cellular substrate and c) allows the study of whether such external-regulated stimulations are of significance for regenerative medicine. The system also represents an initial step towards engineered-skin substitutes with smart embedded actuators.

5.2. HOW FORCE REGULATES CELL FUNCTION: TISSUE, CELLULAR AND MOLECULAR OUTLOOKS

Skin mediates and shapes our interaction with the physical world. Our ability to effortlessly distinguish a myriad of proprioceptive, pain, temperature and mechanical feedbacks is primary thanks to the distributed sensory receptors in human skin. Such receptors can be mainly classified into pain receptors, temperature receptors, and mechanoreceptors. This intricate network of receptors encodes information throughout signals of voltage spikes called action potentials.

Mechanical stimuli are measured by four types of mechanoreceptors (Figure 54).³⁴⁴ Each of the four types of mechanoreceptors senses forces of different scales (temporal and field sizes) which are then evoked in the receptive field of the skin. Two types of receptors respond to static pressures; they are named slow adapting receptors (SA-I and SA-II) and generate a steady signal in response to a static stimulus.³⁴⁴ Fast adapting receptors (FA-I and FA-II), on the other hand, respond to dynamic stimuli and vibrations. The location, density, and distribution of these mechanoreceptors within skin play an important effect on its sensory functions. For example, SA-I receptors are located in the basal layer of the epidermis and conform high-density clusters in areas of the skin such as the fingertips.³⁴⁴ As a consequence, they provide high-resolution responses to force indentation which is useful for discriminating shapes and texture. Hundreds of FA-II afferents distributed over large areas can detect high-frequency vibrations (up to 400 Hz)³⁴⁵ which is thought to

be mainly responsible for textile discrimination. To elicit a response, the neural system receives an input from the ensemble output generated by these mechanoreceptors, interpret and process the complex information, and generate a translation that underline touch perception (Figure 54). This recognition and interpretation of the mechanical stimuli conform the somatosensory system that serves for our reaction to signals originating outside/inside the body.

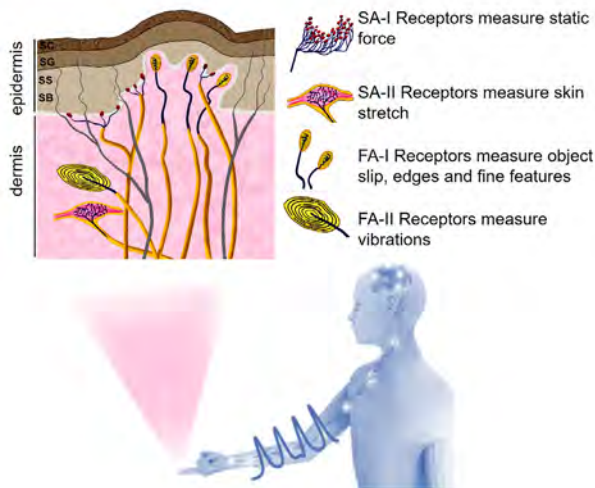


Figure 54. Skin receptors and transducing process. Schematic of the types and location of the mechanoreceptors in the skin tissue: slow adapting receptors, SA-I and SA-II; fast adapting receptors, FA-I and FA-II. SA-I complex is in the basal layer (SB, stratum basalis) of the epidermis, appears in clusters of cells and responds with high-resolution to static forces which may help in the spatial images of tactile stimuli. FA-I afferents are localized in the dermal papillae (SS, stratum spinosum) and their responses detect movement across the skin. SA-II endings are localized deep in the dermis and have been associated with slow thresholds responses when skin stretches. FA-II corpuscles are located in the dermis and they detect high-frequency vibrations. The ensemble output generated by the mechanoreceptors inputs the neural system which ultimately interprets and processes the information and generates a translation. SC, stratum corneum; SG, stratum granulosum; SS, stratum spinosum; SB, stratum basalis. Figure adapted from Abraria and Ginty, 2013.³⁴⁴

This mechanical sensing mechanism can be scaled at a cellular level as any biological function starts, after all, at the cellular scale. To detect and process forces and physical stimuli cells are equipped with structures and components that transmit such physical messages (Figure 55). The major component in the mechanotransduction signaling pathways is most likely to be molecules from the extracellular matrix (ECM). These molecules in the ECM are integrins and other proteins that join the external to the internal side of cells *via* transmembrane integrin junctions in the plasma membranes. Thus, such ECM proteins (fibronectin and cytoplasmic proteins) link integrins to the cytoskeleton of the cell. The cytoskeleton network is the main machinery for cell shape and mechanics, and it is comprised of a distinct type of functional “wires” named actin filaments, microtubules, and intermediate filaments. The three networks interplay and bundle with each other by motors, crosslinkers, and steric interactions (see Figure 55). Other complex structures bind the cytoskeletal filaments to the nuclear envelope. The nuclear envelope connects to the lamina and nuclear scaffold which binds to chromatin and DNA (deoxyribonucleic acid). This molecular connectivity yet function-specialized machinery of the cells together with the cytoplasmic viscoelasticity allows the propagation of forces from the extracellular matrix to the nucleus rapidly.³⁴⁶

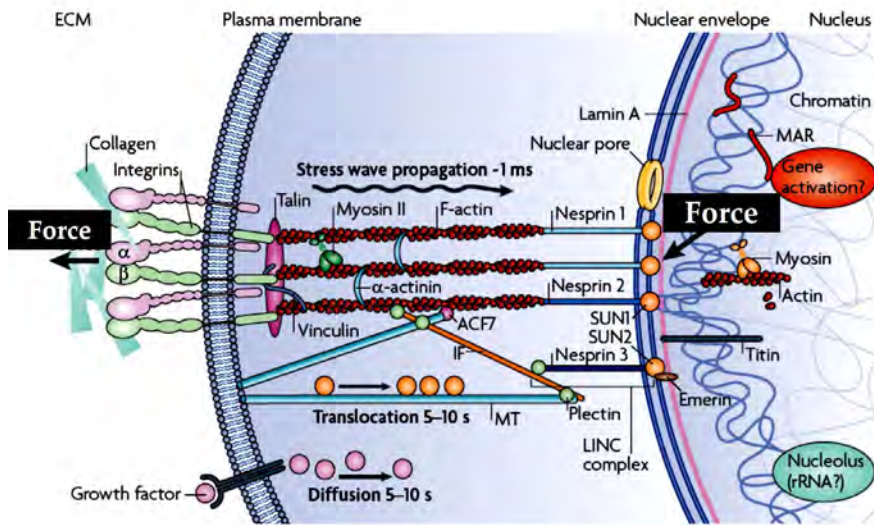


Figure 55. Cell mechanoreceptors and transduction process. A representation of how a local force applied externally to the cells (from the extracellular matrix, ECM) travels to the nucleus. A force is applied to integrins through the ECM which is concentrated at the focal adhesions. The channel that connects the integrins to the cytoskeleton of the cell is through proteins embedded in the plasma membrane that end up in Talin. The filamentous F-actin is bundled by α -actinin and tensed by myosin ii generating a prestress. In the cytoskeleton F-actins and microtubules (MTs) are connected through actin-crosslinking factor 7 (ACF7) while F-actins and intermediate filaments (IFs) are connected through plectin. Plectin also connects IFs to MTs and IFs connect to the outer nuclear membrane through Nesprin 3, and in turn, to SUN1 and SUN2 on the nuclear envelope. Nesprin 1 and nesprin 2 connect F-actin to the inner nuclear membrane protein SUN1. The SUN proteins on the nuclear envelope connect to Lamina A in the nuclear scaffold, which could connect through matrix attachment regions (MARs) to chromatin and DNA. Nuclear actin, myosin, and titin might help to regulate nuclear prestress. Thus, the force channeled into the nuclear scaffold might affect gene activation within milliseconds due to the stress wave propagation. By contrast, a growth factor in the plasma membrane takes seconds to alter nuclear functions by chemical cascades of signaling mediated by chemical diffusion or motor-based translocation. LINC, linker of nucleus and cytoskeleton; rRNA, ribosomal RNA. Figure adapted from Wang et al., 2009.³⁴⁶

Physical stimuli are thus channeled through cells to reach the nucleus which ultimately mediates the cell response. Recently Piccolo *et al.* have identified a mechanochemistry mechanism by which the presence of two molecules in the nucleus read a broad range of mechanical cues and traduce them into a cell-specific program.³⁴⁷⁻³⁴⁹ The molecules

named YAP (which stands from Yes-associated protein) and TAZ (transcriptional coactivator with a PDZ-binding motif; PDZ is a structural domain of amino-acids in signaling proteins) regulate cell differentiation and proliferation mechano-dependently. Although the identification of those nuclear relays has started to fill in the gaps in the understanding on how mechanical cues are sensed and transduced at the molecular level, the general mechanotransduction signaling pathways within cells remain enigmatic.

This gradual insight into the interaction between biology and mechanics explain the interest in developing technical instrumentation for either mechanically manipulating of cells' microenvironments or measuring mechanical properties of cells in the quest for a better understanding of 1) how mechanical forces can alter the cellular functions and 2) whether such force-regulated cellular alterations are of pathological/physiological significance. The evidence found in the literature led to the hypothesis that also the frequency of such stimulations may be relevant to vary the biological outcomes of epithelial cell cultures. However, as it is discussed in the next section 5.3, most of the techniques developed to mechanically stimulate cells rely on static modifications. As an alternative to these static-based modifications, in this chapter we present a piezoelectric-based system to study the effect of dynamic mechanical stimulation of cell cultures and demonstrate that a device based on an organic biocompatible piezoelectric influences (frequency-dependent) cellular behaviors relevant to scenarios related to organotypic skin cultures.

5.3. TECHNIQUES TO STUDY AND INFLUENCE ON THE CELLULAR MECHANICAL RESPONSES

Cell-substrate interaction-based techniques are one of the main approaches to study how the mechanical properties external to the cell influences biological outcomes.³⁵⁰ Such methods (only useful for anchorage-dependent cells) rely on mechanical modifications of the substrate, or the surface of the substrate, where cells are seeded. Nano-topography,³⁵¹ local nano-forces guided either from surfaces of cells³⁵² or from inside the cells,³⁵³ and nano-vibrations³⁵⁴⁻³⁵⁷ are among examples of such surface's modifications that have been proved to influence differentiation and growth rate in different cell type.

Cell adhesion, cell migration,³⁵⁸ and the binary decision of cells to either proliferate or die have shown to be strongly affected by the stiffness, morphology, and roughness of the cellular surfaces.³⁵⁹ Cellular reactions depend not only on those mechanical properties of the substrates but also on the type of cell under study. For instance, Huag *et al.* showed that osteoblast and fibroblast exhibited different responses under equal mechanical conditions when cells were seeded on membranes of poly(hydroxybutyric acid).³⁶⁰ On the other hand, Engler *et al.* showed that stem cells can differentiate either to osteoblast-like cells, when subjected to a stiff condition, or neural-like cells, when exposed to a soft environment.³⁶¹ These studies have demonstrated the cell-type dependent response to mechanical stimuli.

Most of such substrate-based approaches have relied on static modifications of the properties at the cell/substrate interfaces (Figure 56). Static modifications mean that mechanical conditions sensed by cells remain constant during the experiments. It is important to note here that, in many instances, the engineered surfaces used such as nano-wires³⁵¹ and nano-posts topography³⁶² patterns do not mimic any physiological situation. Besides this, some studies have focused on the study of individual cells which unfortunately, lacks similarities with the prevailing behavior of human tissue.

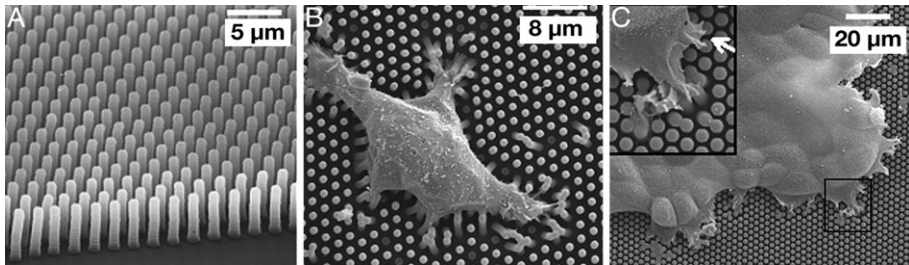


Figure 56. A nano topography technique for mechanical stimulation of cells in a static fashion. a) Microfabricated pots to be used as cellular substrate. b) An individual cell lying on a micro dimensional array of nanopillars. c) Cell monolayer spread on the nanopillars. (C inset) Magnification of the area delimited by the black square. Adapted from du Roure *et al.*, PNAS, 2005.³⁶²

In contrast to these static-based modifications of cell's substrates, recent studies have shown that dynamic mechanical stimulations yield changes in the cellular behavior.³⁶³⁻³⁶⁷ In those studies, magnitude and frequency of such mechanical stimuli influenced the cellular responses albeit the underlying biological mechanisms remain unclear.³⁶⁸

Considering the evidence of the central role of mechanobiology and the potential use of dynamical mechanics-based stimulation for regenerative medicine, an electroactive mechanical actuator to dynamically

stimulate epithelial cultures may be relevant. In this sense, the aim of the present work is to introduce a new device to perform dynamic-mechanical stimulation on cells by an organic actuator in contact with the cell culture. The actuator will act as the substrate for the cell culture and therefore the mechanical properties of the cellular substrate can be varied dynamically by cyclic, controlled, movements. Although the device is introduced as a tool to study the response of the 2D cell cultures to mechanical stimulations (i.e., mechanotransduction) by dynamic vibrations, the principle of the device is also scalable to be applied in 3D cell cultures or tissues. The materials used are biocompatible, cheap, and the design is easily replicable. Preliminary experiments on the effect of such stimuli in proliferation, migration, and morphology of epithelial cells are also presented.

5.4. DESCRIPTION OF THE PIEZOELECTRIC ACTUATING DEVICE FOR CELLULAR STUDIES

5.4.1. Description of the piezoelectric device and associated setup

The experimental set-up put together for cellular studies under time-varying mechanical stimulation consists of a lightweight, organic, biocompatible piezoelectric actuator where the cells are cultured (that we named experimental stage), a custom-made electronic driver to amplify the voltage required at the piezo-actuator input, a signal generator to

generate the voltage signal and a reading and processing stage (see Figure 57). This final stage depends on the actual experiments. For example, to study the cellular migration a reading and processing system using an optical setup together with an image processing algorithm may be needed. A detailed description of the materials and methods for the fabrication of the actuating system introduced in this chapter was already given in Chapter III, section 3.6.

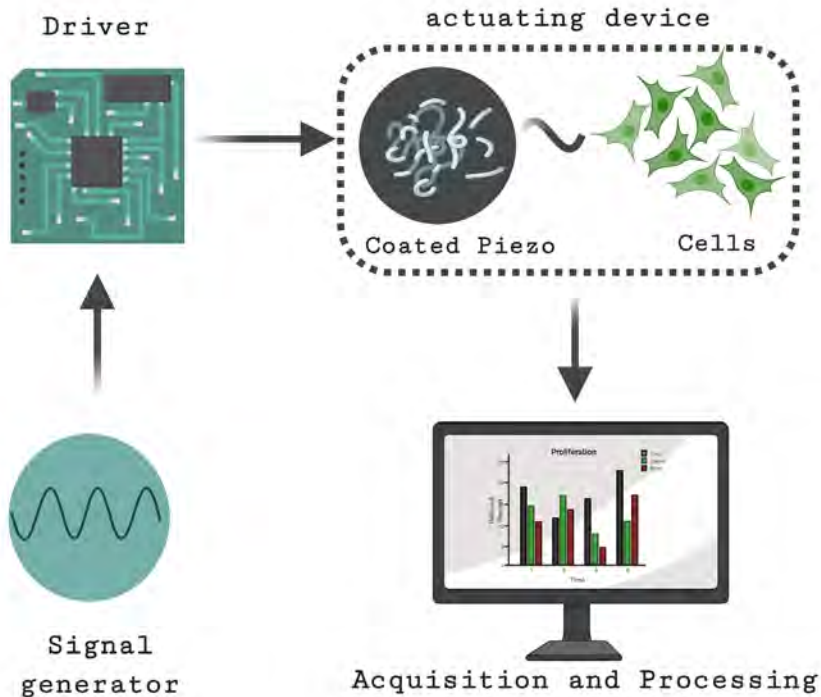


Figure 57. Schematic representation of the actuating system to perform dynamic stimulation on cell cultures.

The actuator of the experimental stage is based on an electroactive organic piezoelectric material named polyvinylidene fluoride, PVDF. PVDF has been widely used in the forms of films, membranes, or scaffolds for tissue engineering applications due to their excellent piezoelectric properties, ease of processing, and biocompatibility.³⁶⁹ However, and despite these antecedents, some challenges should be overcome when designing the experimental stage where the cells can closely interact with the piezoelectric structure, avoiding any electrical stimuli to the cells. To endow long-term viability in the cell cultures without compromising the electronic performance of the actuator, a careful design of the experimental setup was performed. First, the conductive layer of the PVDF film was electrically insulated from the cells with a non-conductive polymer. Second, a custom-made well to both culture the cells and avoid medium leakages through the external cables was fabricated with PDMS. The PVDF actuator cannot handle high temperatures and therefore the necessary biasing wires were soldered using an adhesive conductive copper film. An optical image of a piezoelectric device after fabrication is shown in Figure 58a. An image of the same experimental stage with a cell culture of an epithelial cell line inside a biosecurity cabin is shown in Figure 58b.

To study the effect of the frequency of the mechanical stimulation on cell cultures samples named control culture, static control, and dynamic experimental sample were fabricated (see Figure 58c). Control-culture samples were fabricated lacking the piezoelectric material using a Petri dish with a ring of PDMS. Static (Static Control) and dynamic setups were similar except static samples were not electrically stimulated (Figure 58c).

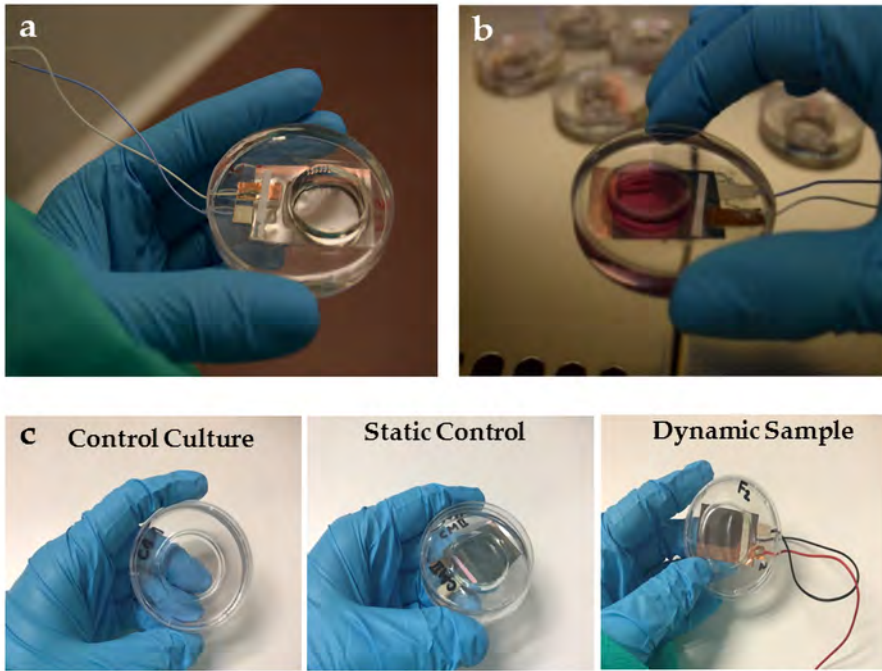


Figure 58. a) Custom-made piezoelectric actuating device to dynamically stimulate cell cultures. b) Manipulation of a biocompatible actuator device integrated into a cell culture of an epithelial cell line inside a biosecurity cabin. The stage is compatible to perform experiments in the standard conditions of a tissue engineering laboratory. c) Samples to perform the cellular studies. Controls were fabricated lacking the piezoelectric material using a Petri dish a cellular substrate with a ring of PDMS. Controls material were static devices fabricated identically than the dynamic samples, but not electrical energy was applied. Dynamic samples were electrically stimulated to transmit mechanical stimulation to the cell cultures.

Dynamic stimulation is controlled by the electronic stage, which is properly configured for each experiment depending on the mechanical conditions to be studied (see description in section 5.7). The electronic stage was attached to an incubator to ensure the physiological conditions for the long-lasting viability of the cell culture (Figure 59). The cables from the electronic stage to the experimental stage were introduced into the incubator through a lateral hole. The electronic stage

is easily configured for each experiment by setting the voltage and frequency from the signal generator to the driver.

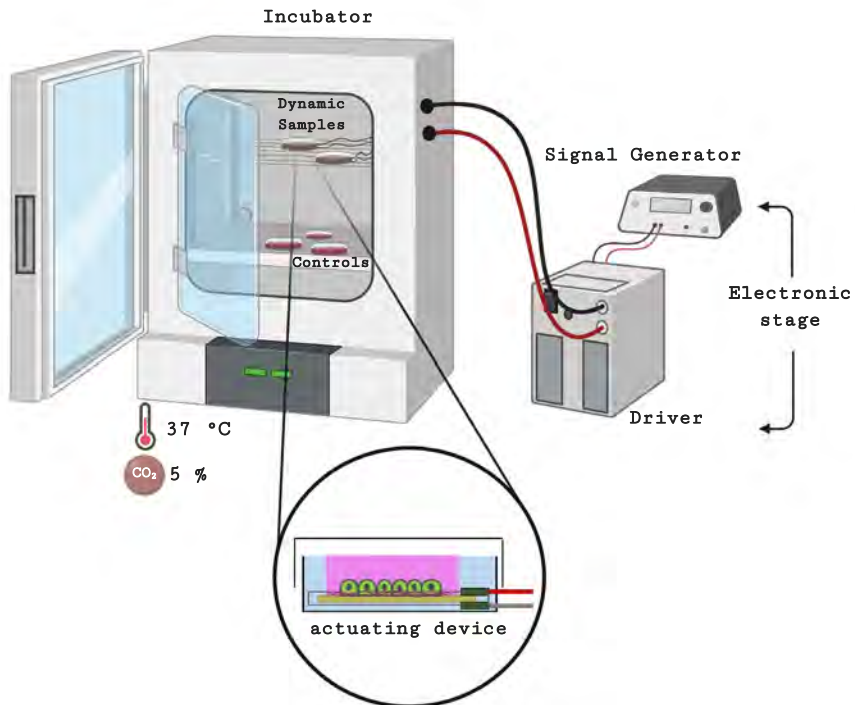


Figure 59. Schematic representation of the actuating system to mechanically stimulate cell cultures. The system consists of an experimental stage (actuating device), a custom electronic stage to configure the electrical parameters to input the piezoelectric actuator, and an incubator to keep physiological conditions in the cell culture. The system allows real-time modification of the dynamic mechanical stimulation of cells.

5.4.2. Physics behind the piezoelectric actuation for dynamic cellular studies

In the following lines we present a brief analysis of the physics behind the actuator described above for the actuating system based on PVDF. The piezoelectric properties in the synthetic PVDF stem from its atomic structure: a symmetric position of Fluor atoms and hydrogen atoms at each side of the main Carbon chain, which is only present in its crystalline β -phase. In addition, as for most polymeric piezoelectric materials, after the PDVF is synthesized, a large electric field is applied to the material to polarize the charge in a given direction. The direction of positive polarization coincides with the z-axis when a material is represented using a rectangular system. We will denote by 1, 2, and 3 the length, the width, and the thickness directions respectively. In our case, the polarized axis always coincides with axis 3. When an external electric field is applied in the poling direction (axis 3), the charges around the main Carbon chain (i.e., in the Fluor and in the hydrogen atoms) will exert a force in their respective directions leading to an elastic strain that changes the dimensions of the material. This mechanical deformation under an applied electric field is known as inverse piezoelectric effect. The equations that relates the induced strain to the applied electric field are shown in (13).

$$\begin{bmatrix} s_1 \\ \vdots \\ s_6 \end{bmatrix} = \begin{bmatrix} d_{11} & \dots & d_{31} \\ \vdots & \ddots & \vdots \\ d_{16} & \dots & d_{36} \end{bmatrix} \cdot \begin{bmatrix} E_1 \\ E_2 \\ E_3 \end{bmatrix} + \begin{bmatrix} S_{11} & \dots & S_{16} \\ \vdots & \ddots & \vdots \\ S_{61} & \dots & S_{66} \end{bmatrix} \cdot \begin{bmatrix} T_1 \\ \vdots \\ T_6 \end{bmatrix} \quad (13)$$

where s_i represents the strain vector, d_{ij} is each of the matrix elements of the piezoelectric tensor, E_i represents the electrical field, S_{ij} is the matrix of compliance (tensor), and T_i is the mechanical stress vector. The terms T_1 to T_3 are the normal mechanical stresses along axis 1, 2, and 3, and T_4 through T_6 are shear mechanical stresses.

The equation represented in (13) consists of two terms. The first term $d_{ij} \cdot E_i$ describes the strain generated by the inverse piezoelectric effect. In absence of mechanical stress, the second term is zero and the strain is related directly to the electric field by the piezoelectric coefficients' matrix in the first term. When an electrical field is applied homogeneously along axis 3, the deflection of the materials in the axis 3 can be obtained by multiplying the thickness of the piezoelectric material times the mechanical strain.

Our actuating device can be represented as a rectangular flat membrane with short edges **a**, long edges **b** and thickness **h**, whose edges are clamped by the PDMS ring (see Chapter III, section 3.6). Given these boundary conditions, the differential equation that governs the membrane displacement under uniform stress is described in equation (14).³⁷⁰

$$\frac{\delta^4 w(x,y)}{\delta x^4} + 2 \frac{\delta^2 w(x,y)}{\delta x^2 \delta y^2} + \frac{\delta^4 w(x,y)}{\delta y^4} + \frac{\rho h \omega^2}{D} w(x,y) = 0 \quad (14)$$

where $w(x,y)$ represents the normal displacement at a location (x, y) , ρ is the mass density of the material, and ω is the angular frequency of the movement.

The term represented with D in this equation (14) is the rigidity of the membrane and is related to the Young's modulus E , the Poisson's ratio ν and the thickness h according to equation (15):

$$D = \frac{Eh^3}{12(1-\nu^2)} w(x,y)=0 \quad (15)$$

From structural mechanics theory, the differential equation represented in (16) for rectangular membranes with fixed boundaries provides a second order response of the system with a first natural (resonance) frequency given by :

$$f_{00} = \frac{k_1}{2\pi} \sqrt{\frac{Dg}{wa^4}} \quad (16)$$

where k_1 is a tabulated value for various ratios of the dimensions a/b . The rest of the terms have been defined above.

Assuming that no external forces are acting on the membrane, the deflection of the piezoelectric membrane is produced by an electric field uniformly distributed over the two electrodes in the axis 3, and the uniform load w (i.e., displacement) per unit area in (16) is generated by the inverse piezoelectric effect within the elastic regime of the material. In this situation, and using the parameters enumerated in Table 4 that describe the device fabricated, we obtain for the first natural frequency of the mechanical structure a value of 148 kHz.

Table 4. Parameters and values of the PVDF for the calculation of the fundamental frequency.

Parameter	Value	Reference
Thickness	28 μm	Manufactured
Piezoelectric coefficient d_{31}	$23 \cdot 10^{-12}$ (C/m ²)/(N/m ²)	Manufactured
Piezoelectric coefficient d_{33}	$-33 \cdot 10^{-12}$ (C/m ²)/(N/m ²)	Manufactured
Young's modulus	2 to 4 (GPa) or (N/m ²)	³⁷¹
Poisson's ratio	0.326	Manufactured
Mass density	$2.10 \cdot 10^3$ (kg/m ³)	³⁷²
Short edge of the membrane	25 mm	see Chapter III Materials and Methods
Long edge of the membrane	35 mm	see Chapter III Materials and Methods
a/b	1 0.9 0.8 0.6 0.4 0.2	³⁷³
k_1	36 32.7 29.9 25.9 23.6 22.6	³⁷³

This analysis implies that all the vibrational modes of the membrane, which are integer multiples of the calculated natural frequency, will be above 148 kHz. Below this frequency, the movement of the membrane can be considered homogenous along the surface because the natural vibrational modes of the mechanical structure are not excited.³⁷³ Above this frequency, the displacement would be affected by bending processes of the membrane depending on the vibrational mode excited. In this sense, care will be taken not to excite the actuating device near or above the obtained natural frequency of the structure.

5.5. CHARACTERIZATION OF THE PIEZOELECTRIC ACTUATING DEVICE

To characterize the (dynamic) mechanical characteristics of the actuating device described above and analyzed by the theoretical model of section 5.4, an interferometric system was used. This section comprises such a characterization after the fabrication of the actuator devices and before their use as mechanical stimulators of cell cultures.

To characterize the mechanical properties of the cellular substrate (i.e., the PVDF piezoelectric actuating device) a vibrometer was used. The vibrometer was based on an interferometric system using a common optical path fiber arrangement (CPT from common path topology) previously reported in³⁷⁴ and shown in Figure 60a. The laser interferometer detected the amplitude in the perpendicular direction of the vibration of the PVDF material versus both the stimulation frequency and the amplitude of the applied voltage.

As seen in Figure 60a an optical cavity between the surface of the piezo-based device and the transceiver fiber is created in the CPT configuration. This cavity length was set at 4 cm (Figure 60b). The interferometer uses a laser diode (990 nm, Thorlabs: Newton, NJ, USA), chirped in wavelength via modulation of the bias current with a 500 kHz sinusoidal signal. The optical phase at the output of the interferometer can be written as $\Delta\phi = \frac{2\pi \cdot \Delta\nu \cdot \Delta L}{c}$; where $\Delta\phi$ is the phase change induced in the cavity by a displacement ΔL , $\Delta\nu$ is the absolute frequency shift in the laser, and c is the speed of light in air. In the CPT architecture the optical fiber acts as both the reference path (the reflection for the distal end of the fiber) and the measurement path (that also includes

the cavity) in the interferometric system. The laser light is coupled to the target using a circulator and the reflected signal is sent to a photodetector through the same circulator as seen in the schematic of Figure 60a. The phase of the signal of the photodiode is then recovered using an algorithm to obtain the two quadrature components of the signal implemented in LabVIEW (National Instruments: Austin, TX, USA) using a controlled PXI DAQ system.

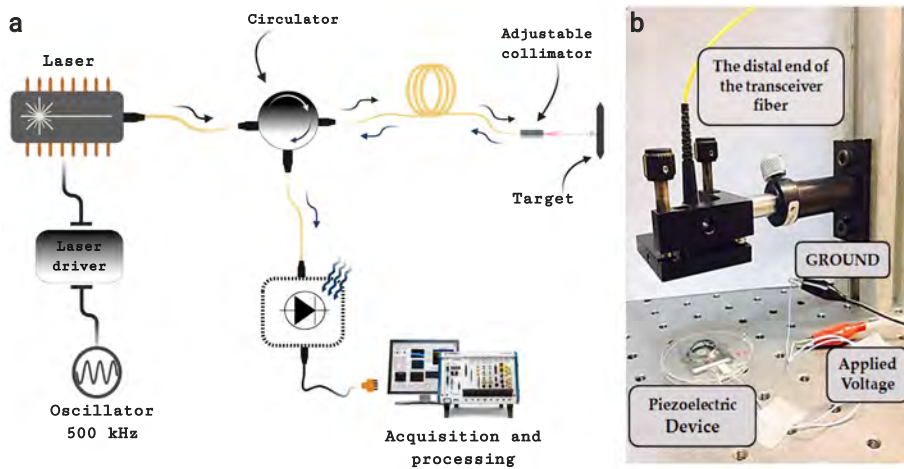


Figure 60. Interferometric system for the characterization of the polymeric piezoelectric-based device to cyclically oscillate the cellular substrate. a) Vibrometer using a common path fiber optical topology (CPT). b) Actual layout for the experimental characterization of the piezoelectric actuating device using the CPT vibrometer.

To evaluate the effect of coating the devices with an extracellular matrix component (i.e., collagen functionalization) in their mechanical response, the experimental stages (i.e., the designed piezoelectric devices) were characterized with and without such functionalization. The devices were characterized at voltages from 2 to 20 V_{RMS} and frequencies from 10 Hz to 90 Hz (well below the calculated fundamental frequency of the system).

In Figure 61 we show the mechanical characterization of the devices using the described interferometer. The two main conclusions that can be extracted are, first, that a linear response in the induced displacement was observed when the amplitude of the applied voltage was consistently increased (Figure 61a) and, second, there are very small changes in the mechanical behavior of the devices functionalized with collagen compared with those without functionalization. (Figure 61b).

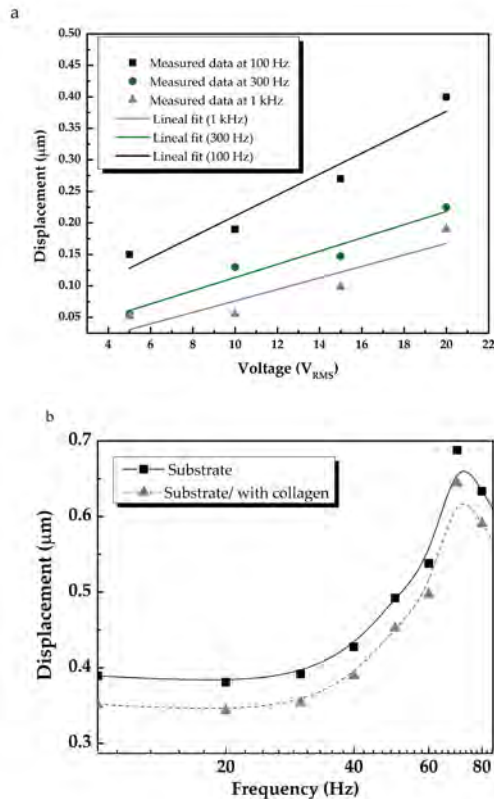


Figure 61. a) Linear relation of the piezoelectric mechanical displacement to an increasing input voltage at frequencies of 100 Hz, 300 Hz and 1 kHz. b) Dynamic mechanical deformation of the PDVF-based device vs. the applied frequency. Very small differences between the response of collagen-coated devices and uncoated devices are observed.

5.6. ESTIMATION OF THE APPLIED FORCES INTO THE CELLS GENERATED BY THE ACTUATING DEVICE

When a mechanical stimulation is applied to cells the cellular responses can be mediated by different characteristics of the applied stimulus such as the amplitude, the frequency, and the resultant acceleration, but the most relevant magnitude may be the applied force to the cells. To estimate the force exerted on the cells from the cellular substrate when a dynamical (sinusoidal) stimulus is introduced we performed the following analysis. This mathematical analysis uses the measured displacement obtained with the interferometer in section 5.5.

Considering only the forces exerted due to the peak acceleration of the sinusoidal wave, the apparent accelerative forces in the piezo-based device can be estimated by the amplitude and the angular frequency (the product of the amplitude A and the square of the angular frequency). By considering the second Newton's law (equation (17)) and knowing that the acceleration in (17) is produced by the sinusoidal displacement of the actuating system, the expression for \ddot{x} (the actual acceleration) can be obtained using the displacement (18) of the piezoelectric film.

$$F_{\text{Newton}} = m \cdot a = m_{\text{cell}} \cdot \ddot{x} \quad (17)$$

where F is the vector sum of the force, m is the mass and a the acceleration.

$$a = \ddot{x} = \frac{d^3x}{dt^2} = -A \cdot \omega^2 \cdot \sin(\omega t) \quad (18)$$

where A corresponds to the amplitude of the waveform (measured in meters) and ω refers to the frequency of the sinusoidal signal.

Returning to the characterization shown in Figure 61b, at 1 Hz a 0.4 μm displacement peak-to-peak is measured while at 80 Hz a displacement of around 0.7 μm peak-to-peak is observed. These displacements result in accelerations of around $1.2 \times 10^{-5} \text{ m}\cdot\text{s}^{-2}$ and $0.18 \text{ m}\cdot\text{s}^{-2}$, respectively. The apparent accelerations induced in the cells are then estimated to be $1.22 \times 10^{-6} \text{ g}$ and 0.02 g , respectively.

Considering the apparent acceleration calculated above and the cellular mass (using a value of density in the endothelial cells of $1.03\text{--}1.05 \text{ g}\cdot\text{cm}^{-3}$ and a mean cross-sectional area of $30 \mu\text{m} \times 30 \mu\text{m}$) the apparent forces exerted by the substrate on the cells can be obtained. At 1 Hz and 80 Hz forces were of approximately 0.04 pN and 0.8 pN, respectively.

As can be extracted from the literature, the magnitude of the forces that are known to induce different cellular processes are of the order of nano to piconewtons.³⁷⁵ In this sense, the resulting accelerative forces transmitted to the cells from the cellular substrate in its current configuration are of a similar order of magnitude. The conclusion of this analysis is that under the proposed configuration the cells will suffer from forces compatible with their viability. Had higher forces been applied by the piezoelectric device, apoptosis and/or cell detachment from the substrate could have been induced.

To ensure the non-existence of shear flow in the culture medium induced by the vibrating substrate that will invalidate the model used, we analyzed the potential presence of fluidic flows.³⁷⁶ Fluorescein Sodium (C.I. 45350, Panreac: Darmstadt, Germany) was added dropwise to devices previously filled with 2 mL of a distilled water. A blue light excitation was applied to enhance a fluorescence visualization and the tracks in the fluxes were monitored while the piezo device was operating dynamically (see Appendix V). No fluxes were observed in the process but a gradual diffusion of the dye.

5.7. PRELIMINARY STUDIES OF THE EFFECTS OF DYNAMIC MECHANICAL STIMULATION ON CELL PROLIFERATION, MIGRATION AND MORPHOLOGY

In this section, we describe the integration of the proposed actuators into 2D cell cultures of an epithelial cell line named HaCaT keratinocytes expressing a green-fluorescent protein as introduced in Chapter III, section 3.2. This integration allows 1) studying the biological responses of epithelial cells to (dynamic) mechanical stimulation and 2) demonstrating the feasibility of the long-term use of the actuator embedded into cellular conditions.

Motivated by potential organotypic skin cultures-related applications and similarly as in the case of the sensing device presented in Chapter IV, the role of the mechanical stimulation was studied associated

to three relevant cellular processes: proliferation (section 5.7.1), migration (section 5.7.2) and morphological variations (section 5.7.3) of a cell line of keratinocytes. Duration, frequency, and magnitude of the mechanical stimulation were adjusted for each set of experiments as it is described independently in each experimental section and summarized below.

The following dynamical conditions were selected for the experimental studies. One experimental group was studied at 1 Hz excitation frequency due to the fact that this is a frequency in the range of many natural physiological processes in the human body³⁷⁷ (e.g., heart rate, human sleep, blood pumping, breath). A second experimental group was analyzed at 80 Hz excitation frequency because as per the calibration curve (section 5.5) the displacement of the active substrate peaks at this frequency. The vibration was continuously applied to the different groups during the experiment. A summary of the experimental conditions is shown in Table 5 as well as the samples used in each group.

Table 5. Summary of the experimental conditions for the piezoelectric actuating device to stimulate cell cultures of HaCaT epithelial cell line.

Frequency	Cytocompatibility	Proliferation	Migration	Morphology
0 Hz	6 days	-	-	-
1 Hz	-	8 days	30 h	48 h
80 Hz	-	6 days	30 h	48 h

5.7.1. First observation: Low-frequency mechanical stimulation enhances HaCaT cell proliferation

The first biological experiment with the fabricated actuator involved their cytocompatibility validation using the AlamarBlue assay following the procedure described in Chapter III, section 3.2.2. Results of these cytocompatibility assays are depicted in Figure 62. The curve represents the normalization of the percentages in the observed reduced AlamarBlue® for a total of $n = 28$ control cultures (CC) and $n = 25$ static control samples (SC). In this figure the proliferation rate is related to the slope of each curve. In both cases the slope exhibited the typical growth-related metabolic activity of proliferating cell cultures. Statistical analysis showed no significance between the static controls (static piezoelectric devices) and the control cultures ($p < 0.005$). Considering that the cellular culture on the piezoelectric device follows a constant proliferation rate (from the slope of the line showing the reduction in the AlmarBlue) and no statistical significance was detected in the experimental group compared with the control cultures, it can be stated that the designed and fabricated actuating devices are biocompatible.

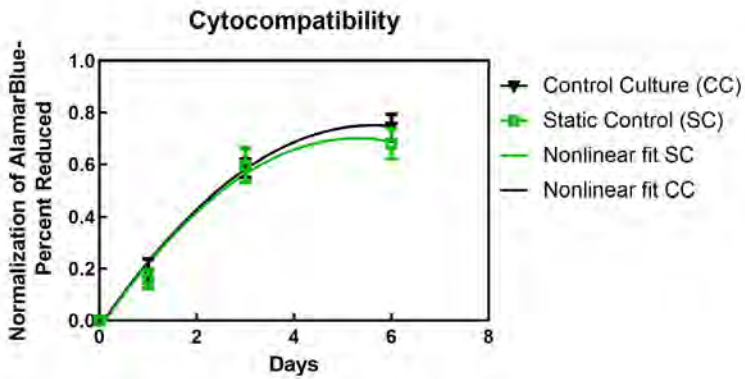


Figure 62. Cytocompatibility results for a total of $n = 28$ control cultures (CC) and $n = 25$ static control samples (SC). No statistical significance was detected in the experimental group compared with the control cultures and thus it can be stated that the designed and fabricated actuating devices are biocompatible.

The results of the experimental groups subjected to a 1 Hz vibration are detailed in Figure 63. A total of $n = 12$ control culture (CC), $n = 12$ static control (SC) and $n = 16$ dynamic samples at 1 Hz frequency (FR (1 Hz)) were tested for a total of four independent repetitions. The curve shown in this figure represents the normalization of the percentage in the absorbance measured in the AlamarBlue assay over eight days. Statistical analysis showed a significant difference ($p < 0.001$) in the experimental samples (FR (1Hz)) compared with both controls (i.e. static devices (SC) and control cultures (CC)) at days 6 and 8. The maximum value attained at day 6 in the dynamic samples was 1.58, while the mean in the absorbance value was 0.97 and 0.84 in the control and control material, respectively.

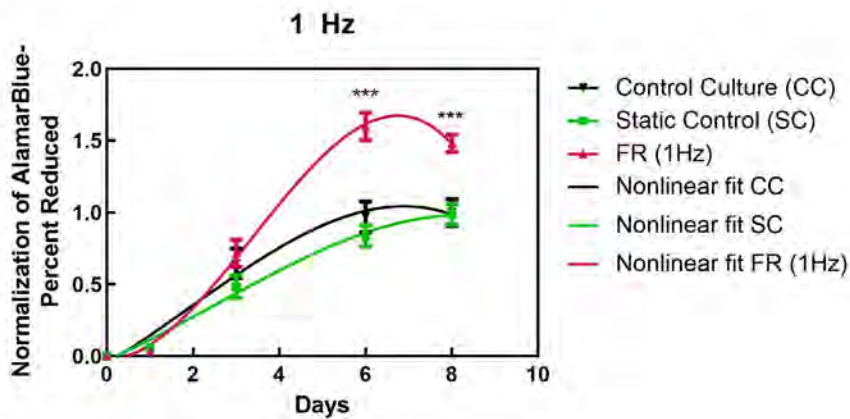


Figure 63. Proliferation assay (AlamarBlue (AB)) performed using a monolayer of HaCaT keratinocyte cells stimulated continuously with a frequency of 1 Hz for 8 days. The curve represents the values of the calculated absorbance (percent reduced) of the AB dye in the control cultures (CC), static controls (SC) and dynamic samples (FR). Statistical analysis showed highly significant differences ($p < 0.001$) in the experimental samples stimulated at 1 Hz compared with both controls (i.e., static devices and control cultures) at day 6 and 8. Note that day 0 represent 24 h after seeding the cells.

Interestingly, further analysis of the fluorescence signal (Figure 64) (processed as explained in section 3.2.2) in the reduced AlamarBlue emission wavelength showed a statistically significant difference between the experimental group and the controls since day 1. No significant differences ($p > 0.05$) were observed between the control cultures (CC) and static control (SC) samples at any day. In this sense this result seems to indicate that the FR (1Hz) stimulated samples were metabolically more active —i.e. more proliferative— a factor of 40 % at day 1, 63 % at day 3, 53 % at day 6 and 39 % at day 8. Note that when processing fluorescence-based measurements, the y-axis represents the ratio of the fluorescent signal measured in the experimental sample (static control and dynamic samples) referred to the control cultures at each day over the experiments. This normalization leads to the control's values equals

roughly one over the eight days, whereas the treated samples (i.e., static and dynamic samples) may be showing a doubling value compared with the ones obtained in the controls.

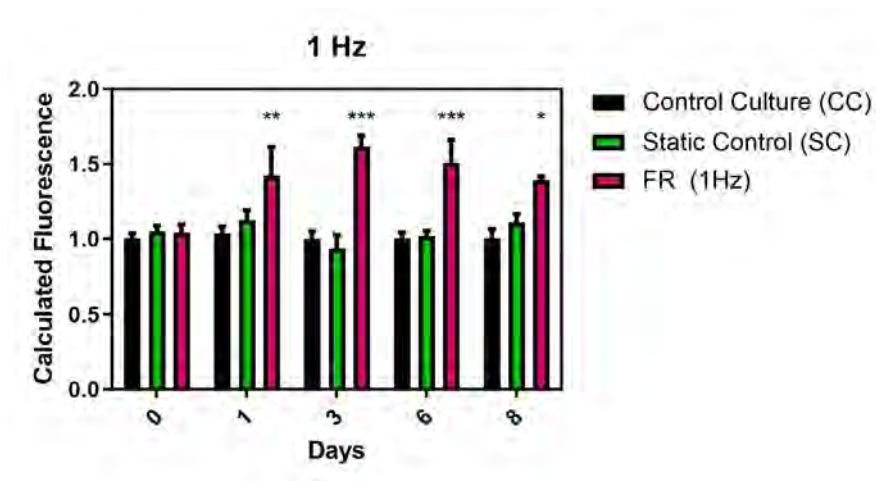


Figure 64. Proliferation assay performed on a monolayer of HaCaT keratinocyte cells stimulated continuously with a frequency of 1 Hz for 8 days using AlamarBlue (AB). The curve represents the values of the fluorescence of the AB dye in the control culture (CC), static control (SC), and dynamic (FR) samples. Statistical analysis showed that the samples stimulated at 1 Hz were metabolically more active compared with both controls (i.e., static controls and control cultures) since day 1. Note that day 0 represent 24 h after seeding cells.

Cell cultures were observed using a fluorescence microscope at day 1 (i.e., 24 h after seeding cells which correspond to the measurement of day 0 in Figure 63 and Figure 64) and day 5. Micrographs of the samples are depicted in Figure 65. Qualitatively, all samples have a similar number of cells at day 1 (Figure 65A,C,E) and a higher population of cells at day 5 demonstrating that the cell proliferation assay is evolving properly. Samples stimulated at 1 Hz present more cells compared with the control cultures and the static control samples (Figure 65B,D,F), while both the

control cultures and the static controls (CC and SC, respectively) reached similar cell numbers at day 5 (Figure 65B,D). Qualitatively, these data agree with those calculated from the fluorescence signal of the AB dye (Figure 63 and Figure 64).

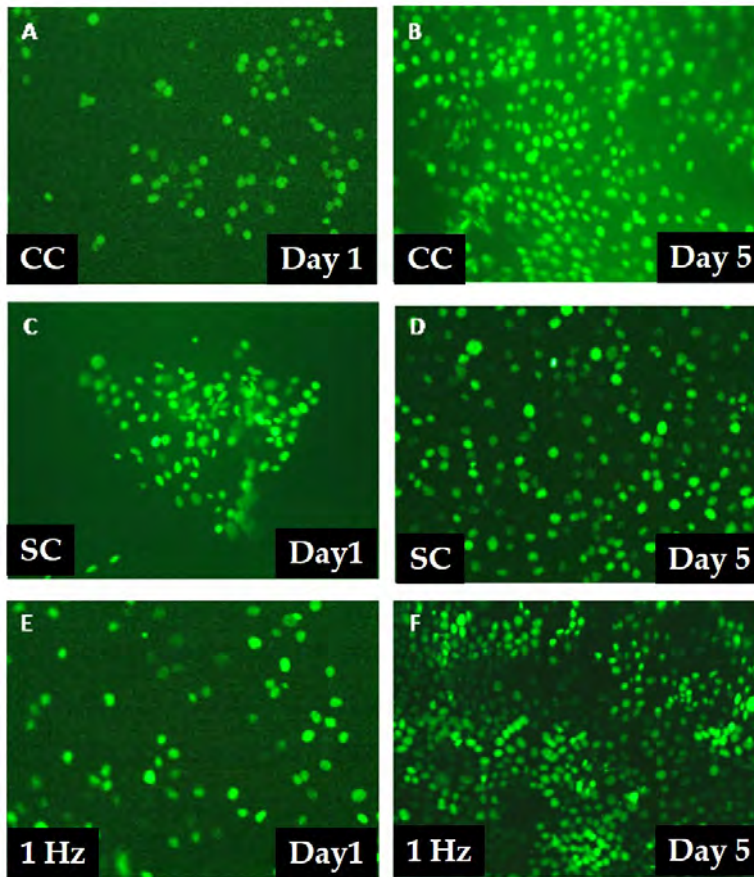


Figure 65. Visual inspection of the cell cultures of HaCaT keratinocytes cells expressing green fluorescent protein (GFP) in their nucleus using a fluorescence microscope at day 1 and day 5 during the proliferation assay. A) Photomicrograph of one control culture (CC) sample at day 1. B) Photomicrograph of one CC sample at day 5. C) Optical image of one static control (SC) at day 1. D) Fluorescence image of one SC without mechanical stimulation at day 5. E) Stimulated sample at 1-Hz frequency at day 1. F) Photomicrograph of one sample continuously stimulated with 1 Hz at day 5. (Scale bar: 100 μm).

Figure 66 shows the proliferation and metabolic-related growth in the 80 Hz excitation frequency experimental group. For a total of three experiments, $n = 9$ control culture and static control samples, and $n = 8$ dynamic samples at 80 Hz excitation frequency (FR (80Hz)) were analyzed. The statistical analysis showed significant difference between the dynamically excited samples and controls at day 3 and at day 6 ($p < 0.01$). No significance ($p > 0.05$) was detected between the control cultures (CC) and static controls (SC). Contrary to the previous case, the FR (80Hz) samples were metabolically less active —i.e., less proliferative— with a difference of 34 % at day 3, and 27 % at day 6.

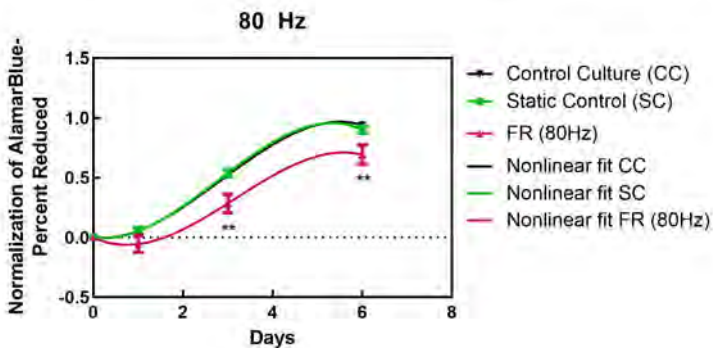


Figure 66. Proliferation assay of a monolayer of HaCaT cells stimulated continuously with a frequency of 80 Hz for 6 days using AlamarBlue (AB). The curves represent the values of the absorbances of the AB dye in the control (black line), static (green line), and dynamic (pink line) samples.

The analysis of the measured fluorescence intensities is depicted in Figure 67, which was calculated as described in Chapter III, section 3.2.2. The grouped analysis two-way ANOVA followed by a Bonferroni post-test showed no significances ($p > 0.05$) between the control culture (CC) and static control (SC) samples at any day. On the other hand, a significant

difference was detected between the control group (control culture and static control) and the stimulated group (FR (80Hz)) at days 1 ($p < 0.01$), 3 ($p < 0.001$) and 6 ($p < 0.05$), indicating that the stimulated samples had a lower proliferation, which is consistent with the results of Figure 66.

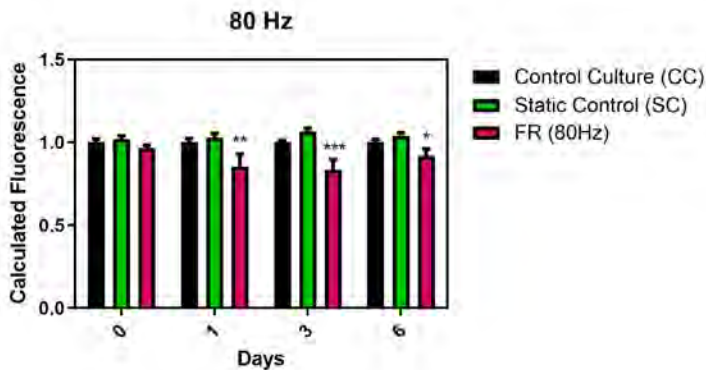


Figure 67. Proliferation assay of a monolayer of HaCaT keratinocytes cells stimulated continuously with a frequency of 80 Hz for 6 days using AlamarBlue (AB). The bars represent the values of the fluorescence of the AB dye in the control (black bars), static (green bars), and dynamic (pink bars) samples. Note that day 0 represent 24 h after seeding cells.

As with the set of experiments applying low-frequency excitation, photomicrographs of the cell cultures were taken using a fluorescence microscope at day 1 (images A, C,E at the left in Figure 68) and day 5 (images B,D,F at the right in Figure 68) for a visual inspection of cell proliferation. Qualitatively all samples show a similar number of cells at day 1 and a higher population of cells at day 5, demonstrating that the cell proliferation assay is evolving properly. Some differences are observed at day 5 in which samples stimulated at 80 Hz present a noticeably lower population of cells compared with the control cultures and the static controls. On the other hand, controls and static devices (CC and SC, respectively) reached the same

cell number at day 5. Qualitatively, these data support the conclusions from Figure 66 and Figure 67 calculated from the fluorescence and absorbance of the Alamar Blue dye.

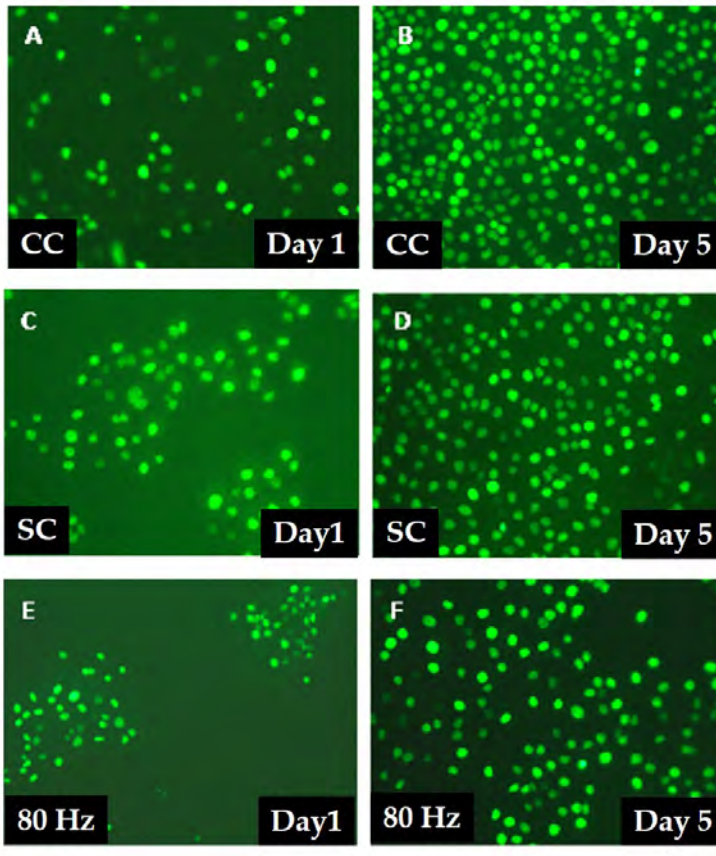


Figure 68. Visual inspection of the cell cultures of HaCaT keratinocytes cells expressing green fluorescent protein (GFP) in their nucleus was observed using a fluorescence microscope at day 1 and day 5 in the proliferation assay for the 80 Hz excitation frequency. A) Photomicrograph of one control culture (CC) sample at day 1. B) Photomicrograph of one CC sample taken at day 5. C) Image of one static control (SC) at day 1. D) Image of one SC device at day 5. E) Stimulated sample at 80-Hz frequency at day 1. F) Photomicrograph of one sample continuously stimulated with 80 Hz at day 5. (Scale bar: 100 μm).

This set of experiments allowed us, in the first place, to assess the cytocompatibility of the actuating devices proposed in the framework of this thesis. Secondly, the proliferation studies performed using the devices by mechanically actuating on the cell culture have shown a frequency-dependent behavior in which mechanical stimulations at low frequencies (1 Hz) enhanced the metabolic activity and proliferation of the cells (compared to the Controls) and the 80 Hz excitation frequency produced the contrary effect.

5.7.2. Second observation: Dynamic mechanical stimulation of low frequency enhances the cell migration rate in HaCaT cells

After this first study we proceed to study the effect of the dynamic-mechanical stimulation of cells in scenarios relevant to processes like wound healing. In this second set of experiments, HaCaT-GFP cells were seeded on collagen-coated actuating devices in an amount enough to ensure confluence the following day as it was described in Chapter III, section 3.3.3.2. 24 h after cell seeding the scratch assay was performed following the protocol described in ref. ³⁰⁹. A group of samples was stimulated continuously with a frequency of 1 Hz while another group was stimulated at 80 Hz. The cell migration process was tracked at 0, 9, 24 and 30 hours until the wound (scratch) was closed using fluorescence microscopy and the acquired images were processed using the algorithm described in Chapter III, section 3.3.3.3.

Figure 69 shows the scratch closing progression for the control groups (control cultures (upper part) and static control (lower part)). Confidence bands for each sample are shown with discontinuous lines, whereas the sampled data points of the distance calculated from processing the wound

progression are shown with inverted triangles and squares for the control cultures (CC) and static controls (SC) respectively. Note that from the curve of CC and SC it seems that the wounds closed completely at 30 h. This is because the images taken at 30 h shown a closed wound for those samples. To estimate the closing time (which is expected to be at any moment between 24 h and 30 h), it was used a linear regression fit (x-intercept of the curve). Using the linear regression, the wound (scratch) in the controls was completely closed after 27.9 hours while for the static samples that happened after 28.85 hours.

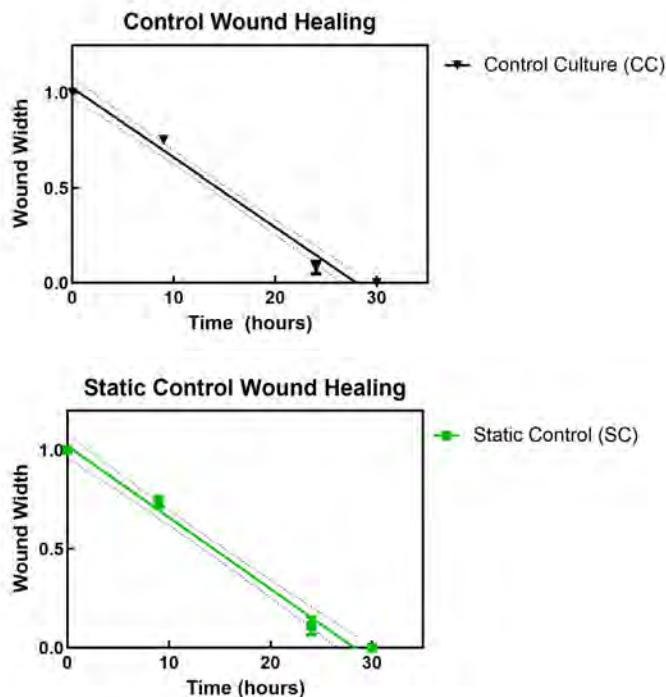


Figure 69. Wound healing progression in control cultures and static controls. The upper figure shows cell migration of cells in control-culture (CC) samples while the one in the bottom the cell migration of cells in static-control (SC) samples (i.e., cell seeded on static devices but without stimulation). The scratch is completely closed at 27.9 h in CC samples while it takes 28.8 h in SC samples. Total of samples: $n = 9$ CC, $n = 9$ SC in three experiments.

The results of the same experiment when the cellular substrate is excited with a frequency of 1 Hz are shown in Figure 70 (upper part) with the sampled data points represented as pink triangles. The healing process (scratch closure) is completed at 24.41 hours with a slope of $-0,04004 \pm 0,002576$. The curve represents the mean cell front progression in a total of $n = 9$ samples and the confidence intervals are depicted in blue. As mentioned, the acquired images were processed using the algorithm described in Chapter III, section 3.3.3.3.

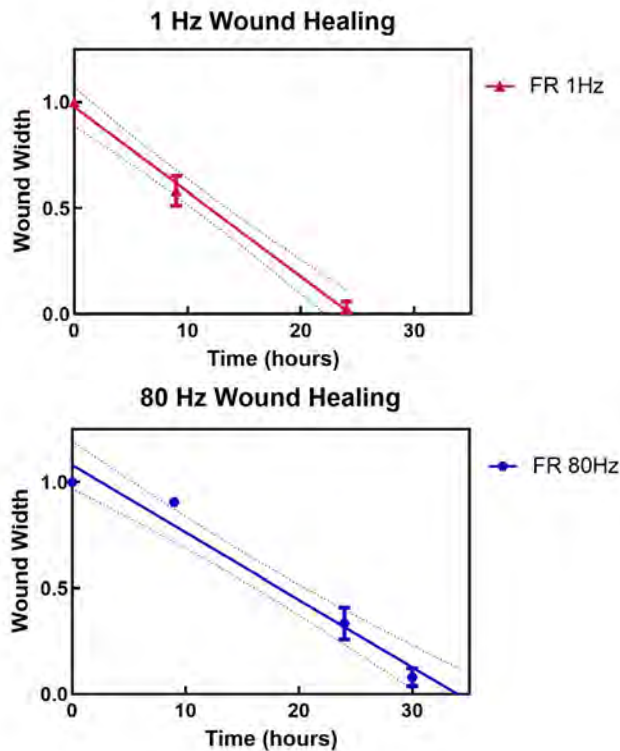


Figure 70. Wound closure progression in dynamic samples stimulated with 1 Hz (upper figure) and 80 Hz (lower figure). The scratch is completely closed after 24 h in 1-Hz samples and after 30 h in 80-Hz samples. Total of samples: $n = 9$ for 1Hz, $n = 9$ for 80Hz in three repetitions. The blue dashed lines in the curves show the confidence interval and the brackets the error bars which cannot be shown when the size is shorter than the size of the symbol (i.e., triangle for 1 Hz and circle for 80 Hz).

The bottom plot of Figure 70 shows the normalized values of the scratch closing for the piezoelectric devices stimulated at a frequency of 80 Hz (FR (80Hz)). As calculated by the curve regression the wound is closed after 33.97 hours with a slope of $-0,03183 \pm 0,002552$.

A summary of the results described above for the experimental samples can be found in Table 6. Statistical analysis of the results among all groups showed a clearly significant difference for the samples seeded on the actuating device stimulated at 1 Hz and at 80 Hz when compared with the control specimens ($p < 0.0001$).

Table 6. Summary of the results using plot regression with the values obtained from the processed images in the cell migration experiments.

Parameter	Control Culture	Static Control	1-Hz stimulation	80-Hz stimulation
Slope	$-0,03703 \pm 0,001502$	$-0,03614 \pm 0,001644$	$-0,04004 \pm 0,002576$	$-0,03183 \pm 0,002552$
Closing time (hours)	27,9	28,25	24,41	33,97

A representative example of the progression of the scratch in all the different experimental samples (i.e., control (C) and dynamic groups of 1 Hz and 80 Hz) at 0, 9 and 24 hours are depicted in Figure 71. Qualitatively, cell migration in the samples with dynamic vibration of the cellular substrate is different than that in the control groups. For example, at 24 h, the experimental group stimulated at 1 Hz showed a scratch completely closed, while the scratch progression in the experimental group stimulated at 80 Hz was still bigger than the control culture. The preliminary

conclusion we can extract from these results is thus that cell migration in the samples stimulated with 1 Hz dynamic frequency shows qualitatively a faster rate while the ones stimulated at 80 Hz significantly decreased this rate when compared to the controls.

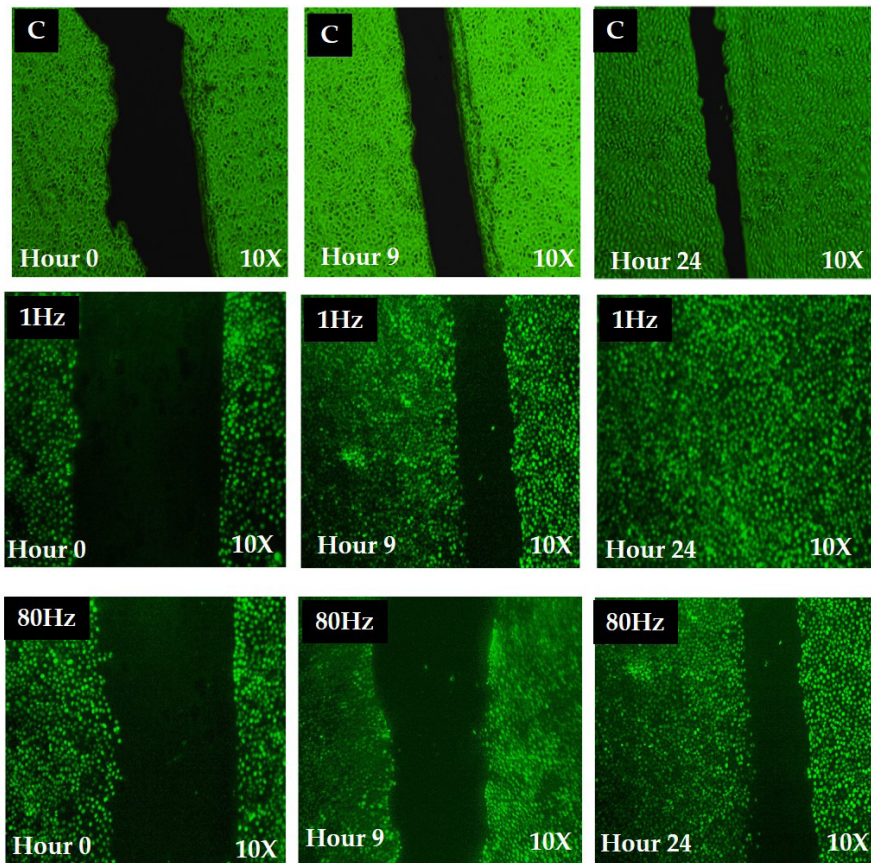


Figure 71. Fluorescence micrographs of the scratch progression in a control (C) and experimental groups seeded on the actuator-based device stimulated at 1 Hz and 80 Hz at different time points. Qualitatively, cell migration in the samples dynamically stimulated at 1 Hz shows a faster rate of the scratch closure.

This set of experiments demonstrated, in the first place, the potential use of the actuating device proposed in this thesis to study cellular migration relevant to wound healing processes. Second, cell migration rate seems to be frequency-dependent in which dynamic-mechanical stimulation at low frequency reduced the scratch closing time while excitation at 80 Hz significantly increased this rate. Cells grown onto the piezoelectric-based devices without stimulation (i.e., static condition) did not show any significant deviation compared with the control cultures (Petri dish control).

5.7.3. Third observation: Effect of dynamic mechanical stimulation on the morphology of cells

In this section a third set of experiments using the actuating device is described. The objective was to test the hypothesis that the frequency dependent changes observed in the cell proliferation and migration behaviors described above (section 5.7.1 and 5.7.2) could be related to morphological and structural changes in the cells. To that aim scanning electron microscopy (SEM) and immunostaining experiments were performed as described in Chapter III, section 3.2.

The morphology of the cells under different experimental conditions is shown in Figure 72. The SEM micrograph of a HaCaT cellular culture grown in a control Petri dish is shown in Figure 72A, where cells present a polygonal shape and a collective growth forming colonies. The diameter of these cells is about 35 μm . Cells seeded on the actuating device without being mechanically stimulated exhibit a similar topography (Figure 72B). In both cases epithelial cells formed colonies and were

well attached to the surface. The morphology is different in the samples under dynamic mechanical stimulation, i.e., cells seeded on devices driven at 1 Hz (Figure 72C) and 80 Hz (Figure 72D). Some observed areas of the group of 1 Hz showed cytoplasmic projections and a more prominent nucleus at 48 h of the experiment while the group subjected to 80 Hz excitation shows rounded cells with smaller size. This observation of a more extruded nucleus in the group stimulated at 1 Hz might indicate that the cells were observed just prior to cell division. More images from this set of experiments can be observed in Appendix VI.

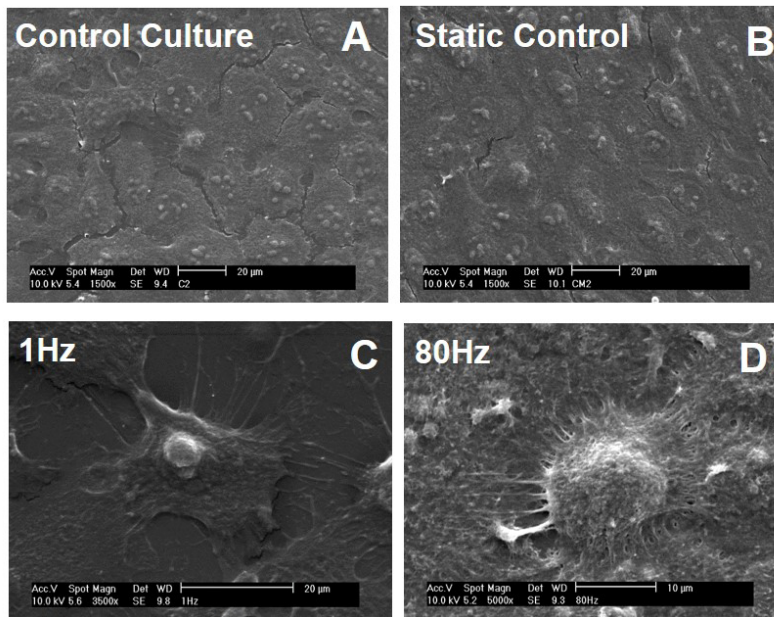


Figure 72. SEM images of control and experimental group samples. Differences in the area and projections in the dynamically excited samples compared to the static controls are observed. Non-significant differences are observed between samples of the control group, i.e., images A and B, at $t = 48$ h. However, cellular morphology is different between control group and the 1 Hz excited samples (image C) and 80Hz excited samples (image D). In the image C (1Hz) the cells show cytoplasmic projections and a more condensed nucleus at 48 h. On the other hand, the morphology of cells stimulated with 80Hz was rounded at 48 h. Length scale: 20 μm .

After these results obtained with the SEM, we moved on to immunostaining assays to better understand the identified changes in the cells' morphology. For this immunofluorescence study the cytoskeleton and the nucleus of the cells were stained using a red fluorescent phallotoxin (specifically labeling f-actin) and blue fluorescent DAPI (labeling the nucleus). Focal adhesions were stained using vinculin but unfortunately, the quality of those images was poor to determine changes among samples. Figure 73 shows the merged images of the control group (Figure 73A,B) and dynamic group (Figure 73C,D) showing the stained f-actin cytoskeleton and the stained nucleus. According to Figure 73C the experimental group stimulated at 1 Hz for 48 h showed larger and well-spread cells which show well delimited pericellular and intracellular f-actin fibers compared with the control samples (both control culture and static control). These cells under low-frequency (1 Hz) dynamic stimulation showed similar cytoplasmic projections (filopodia) observed using SEM. In the control groups (Figure 73A,B), f-actin showed fewer projections and was distributed perinuclearly in a homogenous manner in the cells, showing less organization. Finally, in the 80-Hz experimental samples no significant changes were observed both in cell shape and size and in f-actin structure and distribution compared with controls. In this case, using immunohistochemical staining with a magnification of 20x we were not able to observe the morphology noted at SEM in the 80-Hz group.

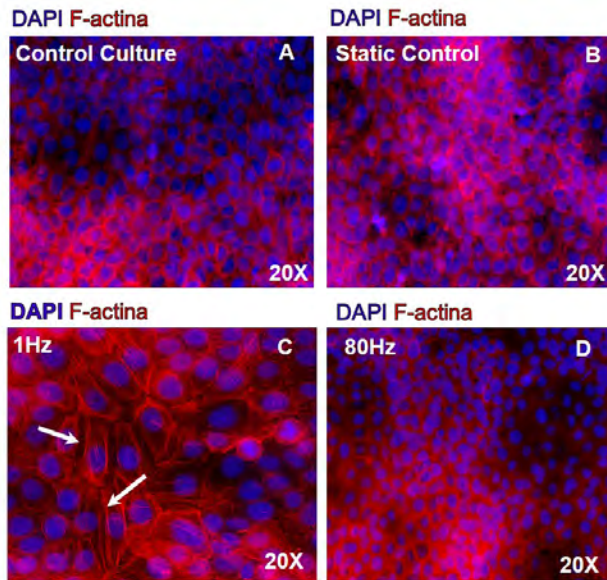


Figure 73. Immunostaining assay for the study of the effect of the dynamic mechanical stimulation on the cellular morphology. Merged images of f-actin stained with phalloidin Alexa Fluor® (red) and nuclei stained with DAPI (blue) at 48 h of treatment of dynamic mechanical stimulation. A) Control-culture samples seeded on Petri dishes. B) Static control of cells grown on the actuating device under static conditions (no excitation). C) 1-Hz excitation group. D) 80-Hz excitation group.

Qualitatively, it seems like in the samples stimulated with 1 Hz (Figure 73C) the nucleus showed a slight increment in size compared to the other samples and presented an oval and elongated shape consistent with the directions of the actin fibers. To gain more insight on whether the stimulation changed the nuclei size, DAPI images were analyzed as described in Chapter III, section 3.3.3.4. The result obtained from processing the DAPI staining images (nucleus) is depicted in Figure 74. This graph represents the average size of the nucleus in the experimental samples normalized to control cultures at 48 h with a total of $n > 300$, where n is the amount of nucleus analyzed. As we can see, the size of the nucleus in the 1-Hz excitation samples only varied 0.069 units compared

to the controls while in the 80-Hz excitation experimental group the size of the nucleus was 0.059 units greater than the controls, neither of them showing a significant statistically difference.

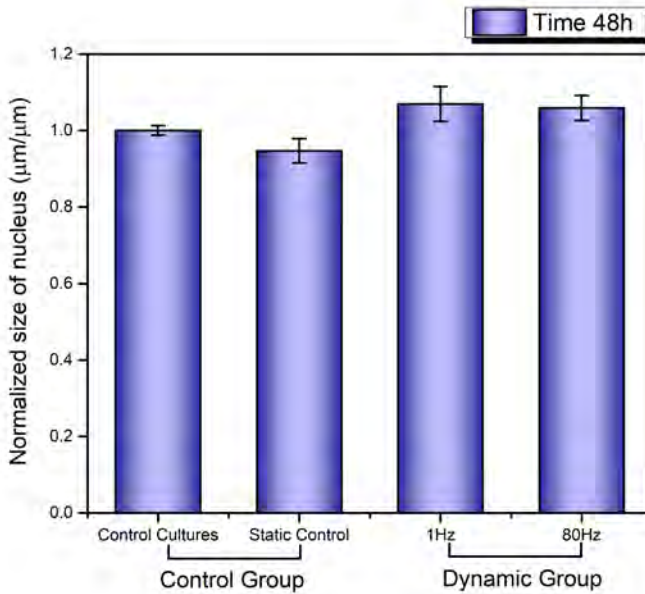


Figure 74. Nucleus' sizes normalized to control-culture samples at 48 h obtained through the processing of the DAPI images. (Number of nuclei, $n > 300$).

The study presented in this section shows that there is a difference in the morphology of the cells under dynamic-mechanical stimulation. These results support the initial hypothesis that the frequency-dependent responses observed in the cells in cell proliferation and migration experiments might be associated with changes in the cellular shape. Indeed, the changes observed at 48 h by SEM and immunostaining may support the following preliminary hypothesis to explain the results.

Dynamic-mechanical stimulation at low frequencies alters the cells at already early times of the experiment which may potentially promote the proliferation and migration rates during the whole periods of stimulation. Based on the observations presented above, we can think that f-actin fibers could promote and increase mechanical tension across the cell when low frequency is applied. Such tensions may cause downstream responses (mechanical stimulations lead to mechanotransduction events) increasing the metabolic activity and the increase in the cellular migration rate observed in sections 5.7.1 and 5.7.2. Due to this f-actin extension, cells might trigger an increase in their motility (1-Hz stimuli enhanced scratch closing and the cells showed more extended actin fibers). Interestingly this statement concurs with some correlations between actin re-arrangement and increased rates in motility observed by Artherton *et al.*, who have demonstrated that low-intensity ultrasound pulses generate a rapid reorganization of the actin cytoskeleton that led to an increase in cell velocity *via* activation of the Rac GTPase.^{378,379}

In addition, studies performed by Stefano Piccolo's group have proposed Yorkie-homologues YAP (Yes-associated protein) and TAZ (transcriptional coactivator with a PDZ-binding motif) as nuclear relays of mechanical signals exerted by cell shape.³⁴⁷⁻³⁴⁹ According to their studies, when YAP and TAZ are mechanically activated they translocate from the cytoplasm to the nucleus where they interact with TEAD factors to regulate gene expression. This mechanical activation is linked to the f-actin fibers in the cytoskeleton and they have observed that in distended cells (e.g., our 1-Hz samples) YAP and TAZ are localized at high levels in the nucleus. On the contrary, in compressed and rounded cells (e.g., our 80-Hz samples) YAP and TAZ are inhibited and have been

localized at higher levels in the cytoplasm. They have also shown a relationship between the level of YAP/TAZ in the nucleus of endothelial cells and cellular proliferation.

In conclusion, the proposed actuating device and these preliminary observations open an interesting route for future research. The mechanism by which the dynamic-mechanical stimulation promotes the rates in cell proliferation and migration of epithelial cells is an exciting, albeit enigmatic, research field.

5.8. DISCUSSION

In this chapter we have described the design, fabrication, and characterization of an actuating device that can act as a mechanically active substrate as well as its validation in 2D epithelial cell cultures. After cytocompatibility testing, we have demonstrated its use to study the effects of dynamic-mechanical stimulation on cells.

The proposed system permits the application of dynamic-mechanical stimulations to biological cultures *in vitro* in a wide range of frequencies. In this work we have selected a specific frequency (1 Hz) to study its effect on HaCaT cultures because such frequency has been previously identified as relevant for biological processes.^{377,380-382} However, there is no limitation in the use of this device with other excitation frequencies or mechanical conditions. For example, previous works have shown that

high frequencies (500 Hz and 1 kHz) applied to mesenchymal stem cells promote osteogenesis, which could be of a significant impact for bone grafts.³⁸³⁻³⁸⁵ Those frequencies can also be attained with this actuating bioelectronic device without compromising the setup nor the mechanical performance since the first vibrational mode of the system was calculated to be around 148 kHz. Therefore, this device could be used to explore intriguing biological responses of engineered-skin tissues or other biological tissues at different frequencies.

The estimated forces applied from the active substrate to cells was calculated to be in the order of pN. This magnitude is thought to be perceived by the cells as reported in the literature,^{375,386,387} without inducing cell detachment from the substrate. In addition, the cyclic movement of the piezoelectric device did not induce any fluidic stream in the culture medium which could have induced an additional stimulation to cells. This conclusion was established by assessing the absence of fluid streaming using sodium salt as a fluorescent tracer. Therefore, all cellular responses described above were attributed to the dynamic-mechanical stimuli.

To validate the device and explore its use in cellular mechanotransduction research some preliminary studies on the influence of the dynamic-mechanical stimulations entailing cell proliferation, migration and morphology were performed. These results have shown that dynamic mechanical vibrations of low amplitude (nanometer range), long duration (up to 8 days), and low frequency (1 Hz) enable *in vitro* increased rates of proliferation and motility of HaCaT cells, but compromised cell morphology. This is not totally new as some studies have shown that the application *in vitro* of frequencies that mimic physiological conditions (in the order of Hz) improves cellular proliferation and cell division.^{382,388} On

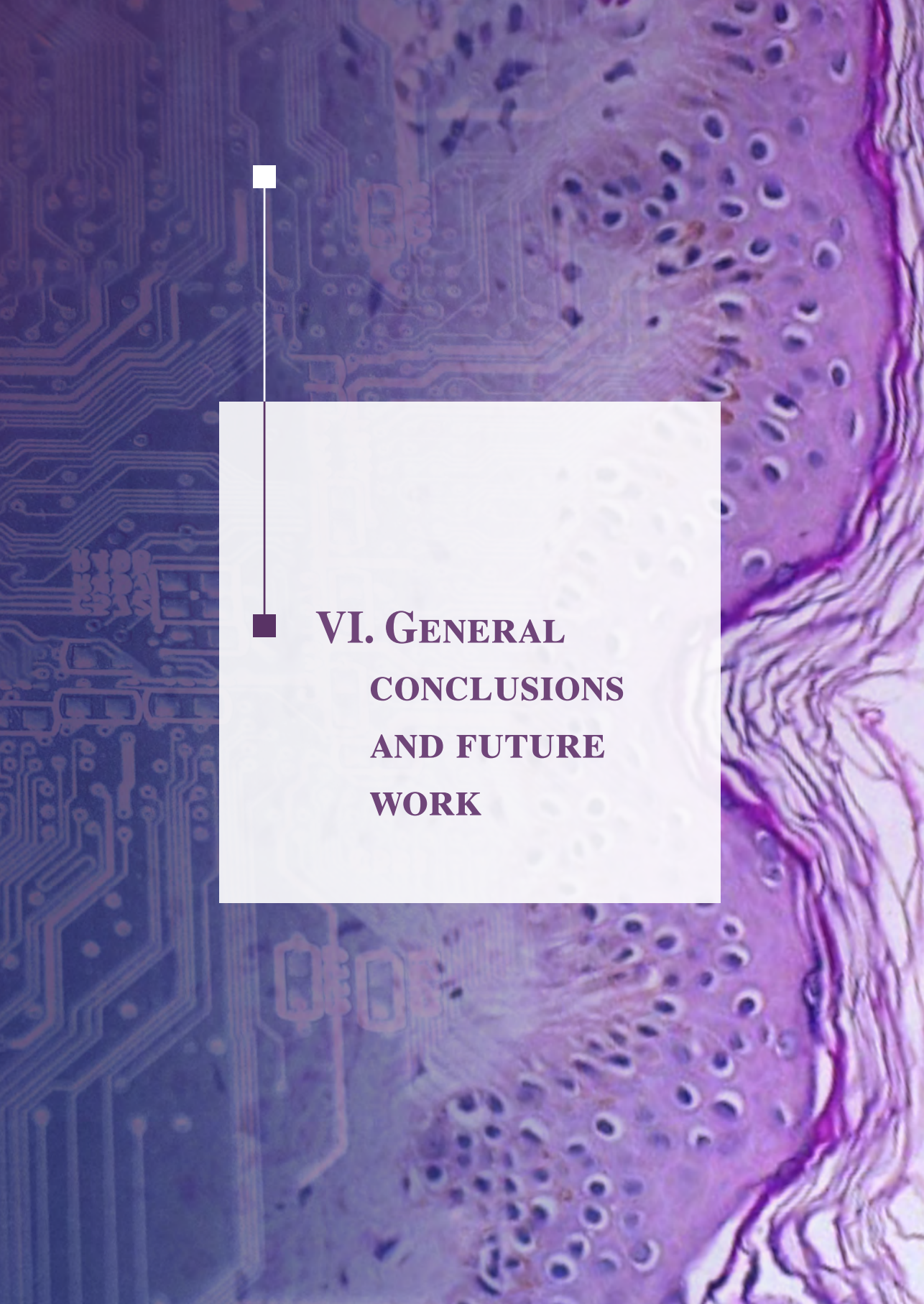
the other hand, mechanical stimulus at a frequency of 80 Hz produced the contrary effect: rates of cellular proliferation and migration decreased with a considerable impact on cell morphology. These results may indicate that the response of HaCaT cells, and eventually organotypic skin cultures, are frequency dependent. This hypothesis opens an interesting research line in cell biology.

Finally, immunostaining studies showed significant changes in actin organization depending on the stimulation frequency. In samples stimulated with 1 Hz, f-actin appeared stretched and more organized than that of the static controls in the observation performed at 48 h. In 80 Hz stimulated samples actin fibers were distributed perinuclear similar to the cells seeded on the controls and devices under static conditions.

The preliminary observations reported in this chapter have shown the potential importance of dynamic-mechanical stimulation in modulating keratinocyte —HaCaT— phenotype. Significant differences in HaCaT proliferation, migration, and morphology have been found depending on the excitation frequency and, consequently, the magnitude of the stimuli imposed on the cells from this movement of their substrate in the z-axis. Further research is necessary to determine whether this type of mechanical stimulation (direction, magnitude, frequency and duration of the stimuli) results in clinical benefits in the treatment of wounds, for example.

Finally, we must emphasize that the most relevant contribution of this work is the development of this entirely cytocompatible bioelectronic device (in form of a bioelectronic Petri dish) that depicts an easy

manipulation (highly desirable for testing cells *in vitro*), a scalable and cheap fabrication process, and a user-friendly and real-time configuration, opening new possibilities for the study of (dynamic) cellular mechanotransduction. This latter characteristic is new when compared to most of the current mechanical stimulation techniques (e.g., scaffolds, substrate patterning) where first, the cellular substrate's properties are fixed and constant (non-dynamic) during the duration of the experiment and, second, in order to vary those cellular substrate's properties the scaffold or substrate patterning must be fabricated from scratch (and eventually characterized). In other words, they are incapable of reconfiguring their mechanical properties in real-time.



VI. GENERAL
CONCLUSIONS
AND FUTURE
WORK

El fin justifica los miedos.

Ramón Eder

CHAPTER VI. General conclusions and future work

6.1. CONCLUSIONS

Integrating electronics into engineered-skin substitutes not only to continuously monitor the tissue (sensing) but also to actively intervene in the responses (actuating) of the engineered tissue without the need for direct medical supervision would be a great advance in reconstructive surgery and other clinical scenarios requiring skin grafts. In the framework of this vision, the aim of this thesis has been the development —using fabrication technologies compatible with bioprinting—, integration into cell cultures and validation of sensors and actuators mechanically soft that allow an intimate interface with epithelial cells and can properly operate embedded in a cell culture environment.

In this work, two different electronic devices have been proposed, fabricated and validated. The first one have allowed performing impedance spectroscopy across flexible printed sensors in real-time to assess cellular proliferation, migration, and cell-sensor adhesions of a cell line of keratinocytes. The second device have allowed actuating onto cells *via* dynamic variations of the cellular substrate. This actuating device was

exploited to study the effects of dynamic stimulations on cellular proliferation, migration and morphology of a cell line of keratinocytes.

Sensing system embedded into epithelial cell cultures

From micro- to macroscale, biology is three-dimensional, flexible and temperature sensitive. This renders manufacturing techniques classically optimized for electronics incompatible with biological fabrication. To overcome these dichotomies and promote the eventual fabrication of free-form blending of bio/electronics materials, we have proposed fabricating flexible biocompatible electronic sensors by inkjet printing technology. We have found this manufacturing process suitable for the fabrication of flexible sensors at temperatures much lower compared to those required in microfabrication methods. We have fabricated flexible inkjet-printed sensors at room temperature, in a cost-effective manner, and without the necessity of cleanroom facilities. We have used silver-nanoparticle-based inks as a conductive element for the sensors and found that printing three-layers of a non-conductive SU-8 based ink formulation efficiently passivated the conductive lines. The morphology of our passivated sensors simulated micro-grooves with features size of 300 μm and $\sim 4 \mu\text{m}$ in width and depth, respectively, which we have found suitable to promote tight adherences between cells and the surface of the sensors. The cytocompatibility of silver nanoparticles is still not thoroughly comprehend but we have demonstrated that the passivation used provided with a completely biocompatible sensor device while retaining good electrical performance (i.e., sensitivity to impedance changes under the presence of cells), which allowed to complete several sets of experiments with cell cultures. These sensors can also be used in microfluidic and/or lab-on-chip devices.

From the first results of the developed platform we have been able to monitor cell proliferation, but for the method to be used as an indicator of such cellular process (by determining cell densities) the number of cells initially seeded should be known and the type of cells (size) and the area available for cells to proliferate should be taken into account (i.e., the system should be calibrated). These additional considerations are required to gain confidence in any study because on one hand the behavior of cells is concentration/time-dependent, and on the other hand impedance-based measurements only represent the spatial average of individual events. Likewise, we must highlight that our developed platform is able to detect *confluence* non-invasively and remotely to the culture. Also, when using impedimetric sensors for monitoring cell cultures the obtained impedance can be influenced by both the electrical properties of the cellular membranes and the medium conductivity due to cellular metabolic wastes. To gain insight into this issue we have found that increasing the porosity in the cell membrane by adding Triton (i.e., hyper-permeabilization) correlates with impedance changes, which steered us to attribute that the main contribution to the measured impedance was the insulating electrical properties of the cellular membrane. By disrupting the integrity in the membrane's structures, the cell-medium/cell-cell ionic interchange was altered as well as the physical path for the electrical current. We have also found that the impedance measurement can detect the keratinocytes cell-sensor adhesions. We believe this type of measurement may be relevant for ascertaining/monitoring the adherence of tissues and cells on implanted electronics.

Finally, we have found that the impedance measured using the developed sensors was able to track cellular migration for at least 80 h in a cellular migration experiment. We have established this correlation

between cellular migration and measured impedance using image processing. Although the data have shown a very good linear correlation, we must be aware that the developed sensing system may lack specificity in measuring cellular migration over other factors such as cellular density, proliferation, and propagation of the electrical signal through the cell monolayer, which has been shown to play an important role during cellular migration. Albeit these preliminary results are promising, we conclude that to gain a fully electrical monitorization of biological-related events of engineered tissues/organotypic cell cultures multimodal sensing systems are desirable.

In any case, we consider that the results obtained with this first generation of inkjet printing sensors and the associated fabrication, design and strategies represent an initial step towards joining bioprinting of engineered-skin tissues with smart embedded sensors.

Actuating system embedded into epithelial cell cultures

The second device developed in the framework of this thesis was an actuating system based on an organic electroactive piezoelectric material. We have chosen the PVDF polymer as the most suitable for the fabrication of biocompatible, thin, and mechanically compliant actuating devices. We have thus designed and fabricated a novel electromechanical system as an experimental tool to perform dynamic-mechanical stimulation to cell cultures. The actuating devices allowed performing long-term cellular experiments, reconfiguring the mechanical parameters of the actuator in real-time, and applying forces in the range of the ones that appear at biological scales.

Bearing in mind that physical forces-based approaches would be a promising new way of controlling cellular behavior, and therefore, of new therapies, we have studied the effects of varying the magnitude, frequency, and duration of dynamic-mechanical stimuli on cellular behavior. We have found that a stimulus of low frequency (1 Hz), low magnitude (< 0.4 nm), and up to 6 days enhances proliferation and migration of a cell line of keratinocytes (HaCaT) with an apparent relation to the actin elongation and organization. A mechanical stimulus at higher frequencies (80 Hz) resulted in totally different outcomes: rates of cellular proliferation and migration decreased with a considerable impact on the cell morphology. Based on these results we can conclude that the cellular responses of a cell line of keratinocytes (HaCaT) upon dynamic-mechanical stimuli are frequency dependent. However, this preliminary result has to be supported by further research to determine whether this type of mechanical stimulation (direction, magnitude, frequency, and duration of the stimuli) results in a similar impact in 3D engineered-skin tissues and thus pushes the field of bio-integrated flexible actuators devices forward.

Finally, and although the validation of this ultrathin actuator embedded into cell cultures was demonstrated in a cell line of keratinocytes, the actuating system proposed seems to be cytocompatible, with a scalable and cheap fabrication, and it is easy to configure and manipulate, so we understand it can support the study of (dynamic) cellular mechanotransduction of other types of cells. This is a unique and advantageous feature compared with most of the current mechanical stimulation techniques used for the study of cellular mechanotransduction. Unlike the real-time reconfiguration of the mechanical properties offered by our device, most of those mechanical stimulation systems require fabricating/characterizing new devices from scratch in order to vary their mechanical properties

(e.g., new microfabrication pattern, new scaffold synthesis, etc. with their associated characterizations). Understating cellular mechanotransduction is not only crucial to gain far deeper insight into the function of cells, but it could also lead to new technologies and clinical applications. In this sense, we understand that the fabrication, design, strategies, and methods used in the developed actuating system represents an initial step towards engineered-skin substitutes with smart embedded actuators.

In summary, the objective of this Ph.D. work and its main contribution has been to pave exciting avenues towards this idea of **living smart bifunctional skin substitutes**. We believe in the potential of the 3D printing technique to guide yet another revolution in bioelectronics as it is the only electronic manufacturing technique compatible with current bioprinting. No other platform as 3D printing enables the deposition of a wide range of functional materials —from semiconductors to cell-laden hydrogels— on a large area of movable, curved and three-dimensional surfaces in a contactless fashion. This ability to directly interweave three-dimensional multi-materials from these two distant worlds (biology and electronics) is fueling the vision of engineering cyborg tissues with internally integrated electronic arrays that can ultimately be used on-demand as engineered transplants with augmented functionalities (biological, physical, electrical). This potential would add an elegant new dimension to 3D bioprinting —a fourth dimension— for the ability to create transformable and smart organotypic tissues. Such technology may facilitate the development of next-generation bioelectronic devices with a seamless level of integration, eventually blurring the lines between living and man-made smart systems.

6.2. FUTURE DIRECTIONS

In this thesis, we have developed (design, fabrication, and characterization) and validated biocompatible sensors and actuators, mechanically soft and compliant embedded into a cell culture environment. Future work may arise from the contributions presented in this thesis, providing a better fundamental understanding of the tissue-electronics interfaces and new applications for printable **sensing devices**:

- **Exploring organic printed materials for the fabrication of entirely biodegradable devices.** Entirely biodegradable materials and transient systems that disappear at the end of their using cycle together with innovative fabrication methods represent a promising approach for subcutaneous sensors. In this line, the use of hydrogels as substrates³⁸⁹ for the fabrication of sensors could provide an excellent platform with a twofold purpose: mechanical support for the electrodes and three-dimensional structure for the cells. This proposed future work may push forward three-dimensional electrical measurements.
- **Determine the concentration of the silver-nanoparticles electrodes to maintain viable cells and still ensure electrical performance.** The cytocompatibility of the silver nanoparticles (AgNP) is still not completely clear. However, relevant progress has been achieved in sintering-free silver-nanoparticle-based ink for printed electronics,^{202,295} which places AgNP-based formulation as a potential candidate to print concomitantly with

bio-inks materials and cells.²⁹³ Performing this study may help to assess the use of AgNP and the related concentrations to be printed with bio-based inks.

- **Evaluating organic-based conducting materials for the fabrication of the sensing devices instead of using metal-based electrodes (AgNP).** Metal-free electrodes represent an improvement in the compatibility between the tissue and the electronics interface. Conducting polymers such as PEDOT: PSS or carbon-based inks such as carbon flakes offer several advantages like commercial availability, more compliant interfaces to the tissues, and the support of not only electronic but also ionic charge transports. This future work opens the road toward organic printed flexible bioelectronics.
- **Compare the use of sensors based on interdigitated electrodes to monopolar electrodes for measuring the impedance in 3D organotypic skin cultures.** Scaling the size of the electrodes to the size of the cells may improve the specificity of the recording into the culture. Impedance-based recording can be performed using monopolar electrodes distributed in 3D scaffolds to create a map of impedance inside the tissue exploiting the technique named tomography impedance spectroscopy. This approach may help to increase both the sensitivity and the specificity in the impedance sensing.
- **Study the dual function of using electrodes to record and electrically stimulate the cultures.** Some groups are actively studying the role of the endogenous and applied (i.e., internal and external) electric fields to promote wound healing. With minor changes in

the instrumental system, external electric fields could be applied while the same system would monitor the state of the healing. This proposal would provide a platform for the understanding of the role of the electric fields in wound healing.

In parallel with the future work outlined above, the following areas will provide a step forward in the fundamentals of mechanical stimulation in biology and new applications for **actuating bioelectronic devices**:

- **Exploring organic printed electrodes in PVDF membranes for the fabrication of entirely metal-free bio-actuators.** All-organic based actuators with organic electrodes such as PEDOT:PSS or carbon-based conductive electrodes would produce a fully polymeric bioelectronic device with no metal components. The PDVF can be easily synthesized or even inkjet-printed³⁹⁰ as well as the organic electrodes. Performing this work may help to produce implantable, metal-free devices less susceptible to mechanical failure to be used as actuators in engineered hybrid tissues.
- **Study the cellular pathway of the frequency-dependent responses of the epithelial cells.** Some groups are actively studying the role of the YAP/TAZ molecules in mechanotransduction. With no changes in the instrumental system, deeper studies can be performed to understand the cellular pathways underneath the improved rates in the proliferation and migration observed in this thesis. This proposal would give insight into the understanding of the role of the frequency of stimulation for skin-related scenarios.

- **Integrate the proposed actuating device in 3D cell cultures.** Stimulation of 3D bioengineered skin tissues by the inverse piezoelectric effect has not been studied. The integrations of this actuating device, initially as substrate, and eventually into the 3D culture, is feasible since the mechanical stimulation could be propagated into the tissue. Performing this work may help to mimic a more realistic scenario and to study the potential use of the 3D dynamic-mechanical stimulation.
- **Expand the frequency range of stimulation to characterize the cellular responses of the epithelial cells to dynamic-mechanical stimulation.** Expanding the excitation frequency beyond the ones already studied (i.e., 1 Hz and 80 Hz) may help to better understand the cellular responses under different stimulation frequencies that might be relevant for skin-related issues.
- **Exploring novel devices to enable transversal stimuli in cell cultures.** A (dynamic) mechanical stimuli in uni- and/or biaxial fashion referenced to the axis of cells (i.e., X- and Y-axis) might be of more relevance for skin-related scenarios since the naturally elastic response of skin tissues is achieved in these directions. This proposal would bring out novel mechanical-based smart systems with yet another effective manner to stimulate the engineered-skin tissues.

Finally, the following studies will build on newly developed sensing and actuating system and continue to advance towards dermo-epidermal skin substitutes with actuators and sensors as non-biological components:

- **Combining the sensing and actuating systems in a multi-modal platform.** Bioelectronic interfaces combining arrays of sensors and actuators are promising tools for the study, monitoring and self-induced regenerations on engineered tissues. A technological challenge is the design and integration of soft and compliant bioelectronic devices into cell cultures, which has been one of the main contributions of this thesis. Thus, based on the work presented in this dissertation, it could be feasible to monitor the changes in the cellular responses observed in the cell cultures under dynamic stimulation using the sensing platform. The impedimetric sensor could then be used to monitor the proliferation, migration, and morphological changes induced by the actuator. This work would provide an autonomous electronic system to assess and induce cellular responses.
- **Integrating the sensing/actuating, and multimodal system into three-dimensional skin tissues.** Two-dimensional models of cell cultures do not mimic the conditions prevailing in human tissues in every respect. A key step for the development of truly living bionic skin tissues is to be able to integrate both sensors/actuators into organotypic cultures. To achieve this goal, testing the capacities of the sensing/actuating system proposed in this thesis could be a viable first step. This study would provide critical know-how about the requirements for scaling towards 3D sensing and actuating bioelectronics.

- **Bioprinting living cells on the inkjet-printed sensors.** We have studied the cell-sensors interface by seeding manually the cells. However, by bioprinting cells on our inkjet-printed devices new challenges can emerge. The contact angle between the deposited cells and the surface of the sensors, the wettability, and the tissue-electronics adhesions needs to be thoroughly comprehended to develop a hybrid platform that prints electronics and living matters concomitantly. This research would pave the way for the understanding of the printing challenges that may arise from this technology.

The background of the slide is a collage of two images. On the left, there is a close-up of a blue and purple printed circuit board (PCB) with intricate circuit traces. On the right, there is a histological micrograph showing a cross-section of tissue, likely skin, stained with hematoxylin and eosin (H&E), showing various cellular structures and layers.

VII. BIBLIOGRAPHY

CHAPTER VII. Bibliography

1. Myers, S., Navsaria, H. & Ojeh, N. Skin engineering and keratinocyte stem cell therapy. in *Tissue Engineering* (eds. Blitterswijk, C. van & Boer, J. De) 497-528 (Elsevier, 2015). doi:10.1016/B978-0-12-420145-3.00015-8.
2. Jones, I., Currie, L. & Martin, R. A guide to biological skin substitutes The function of normal skin. *Br. J. Plast. Surg. Br. Assoc. Plast. Surg.* 55, 185-193 (2002).
3. Jackson, D. M. G. The diagnosis of the depth of burning. *Br. J. Surg.* 40, 588-596 (1953).
4. Gómez, C. *et al.* Use of an autologous bioengineered composite skin in extensive burns: Clinical and functional outcomes. A multicentric study. *Burns* 37, 580-589 (2011).
5. Cubo, N., Garcia, M., Del Cañizo, J. F., Velasco, D. & Jorcano, J. L. 3D bioprinting of functional human skin: Production and in vivo analysis. *Biofabrication* 9, (2017).
6. Albanna, M. *et al.* In situ bioprinting of autologous skin cells accelerates wound healing of extensive excisional full-thickness wounds. *Sci. Rep.* 9, 1-15 (2019).
7. Dargaville, T. R. *et al.* Sensors and imaging for wound healing: A review. *Biosens. Bioelectron.* 41, 30-42 (2013).
8. Derakhshandeh, H., Kashaf, S. S., Aghabaglou, F., Ghanavati, I. O. & Tamayol, A. Smart bandages: The future of wound care. *Trends Biotechnol.* 36, 1259-1274 (2018).
9. Yoshiaki, H. *et al.* Multifunctional skin-like electronics for quantitative, clinical monitoring of cutaneous wound healing. *Adv. Healthc. Mater.* 3, 1597-1607 (2015).
10. Saghazadeh, S. *et al.* Drug delivery systems and materials for wound healing applications. *Adv. Drug Deliv. Rev.* 127, 138-166 (2018).
11. Derakhshandeh, H., Kashaf, S. S., Aghabaglou, F., Ghanavati, I. O. & Tamayol, A. Smart Bandages: The future of wound care. *Trends Biotechnol.* 36, 1259-1274 (2018).
12. Tatara, A. M., Kontoyiannis, D. P. & Mikos, A. G. Drug delivery and tissue engineering to promote wound healing in the immunocompromised host: Current challenges and future directions. *Adv. Drug Deliv. Rev.* 129, 319-329 (2018).
13. Mostafalu, P. *et al.* A textile dressing for temporal and dosage controlled drug delivery. *Adv. Funct. Mater.* 27, 1-10 (2017).
14. Bagherifard, S. *et al.* Dermal patch with integrated flexible heater for on demand drug delivery. *Adv. Healthc. Mater.* 5, 175-184 (2016).

15. Dai, X., Hong, G., Gao, T. & Lieber, C. M. Mesh nanoelectronics: Seamless integration of electronics with tissues. *Acc. Chem. Res.* 51, 309–318 (2018).
16. Zhao, Y. *et al.* Patch clamp technique: Review of the current state of the art and potential contributions from nanoengineering. *Proc. Inst. Mech. Eng. Part N J. Nanoeng. Nanosyst.* 222, 1–11 (2008).
17. Kang, H. & Nam, Y. In vitro neural recording by microelectrode arrays. in *Stretchable bioelectronics for medical devices and systems* (eds. Rogers, J. A., Ghaffari, R. & Kim, D.-H.) 275–291 (Springer, 2016).
18. Spira, M. E. & Hai, A. Microelectrodes get on your nerves Multi-electrode array technologies for neuroscience and cardiology. *Nat. Nanotechnol.* 8, 83–94 (2013).
19. Shmoel, N. *et al.* Multisite electrophysiological recordings by self-assembled loose-patch-like junctions between cultured hippocampal neurons and mushroom-shaped microelectrodes. *Sci. Rep.* 6, 27110 (2016).
20. Tian, B. & Lieber, C. M. Nanowired bioelectric interfaces. *Chem. Rev.* 119, 9136–9152 (2019).
21. Discher, D. E., Janmey, P. & Wang, Y.-L. Tissue cells feel and respond to the stiffness of their substrate. *Science* (80-.). 310, 1139–1143 (2005).
22. Wang, S. *et al.* Skin electronics from scalable fabrication of an intrinsically stretchable transistor array. *Nature* 555, 83–88 (2018).
23. Koh, A. *et al.* A soft, wearable microfluidic device for the capture, storage, and colorimetric sensing of sweat. *Sci. Transl. Med.* 8, (2016).
24. Lee, H. *et al.* Wearable/disposable sweat-based glucose monitoring device with multistage transdermal drug delivery module. *Sci. Adv.* 3, 1–9 (2017).
25. Baumgartner, M. *et al.* Resilient yet entirely degradable gelatin-based biogels for soft robots and electronics. *Nat. Mater.* (2020) doi:10.1038/s41563-020-0699-3.
26. Kim, D. H. *et al.* Materials for multifunctional balloon catheters with capabilities in cardiac electrophysiological mapping and ablation therapy. *Nat. Mater.* 10, 316–323 (2011).
27. Xu, L. *et al.* 3D multifunctional integumentary membranes for spatiotemporal cardiac measurements and stimulation across the entire epicardium. *Nat. Commun.* 5, (2014).
28. Kim, D. H. *et al.* Electronic sensor and actuator webs for large-area complex geometry cardiac mapping and therapy. *Proc. Natl. Acad. Sci. U. S. A.* 109, 19910–19915 (2012).
29. Liu, J. *et al.* Intrinsically stretchable electrode array enabled in vivo electrophysiological mapping of atrial fibrillation at cellular resolution. *Proc. Natl. Acad. Sci. U. S. A.* 117, 14769–14778 (2020).
30. Xie, C. *et al.* Three-dimensional macroporous nanoelectronic networks as minimally invasive brain probes. *Nat. Mater.* 14, 1286–1292 (2015).
31. Fu, T. M. *et al.* Stable long-term chronic brain mapping at the single-neuron level. *Nat. Methods* 13, 875–882 (2016).
32. Liu, Y. *et al.* Soft and elastic hydrogel-based microelectronics for localized low-voltage neuromodulation. *Nat. Biomed. Eng.* 3, 58–68 (2019).
33. Boutry, C. M. *et al.* A stretchable and biodegradable strain and pressure sensor for orthopaedic application. *Nat. Electron.* 1, 314–321 (2018).
34. Bai, W. *et al.* Bioresorbable photonic devices for the spectroscopic characterization of physiological status and neural activity. *Nat. Biomed. Eng.* 3, 644–654 (2019).

35. Mickle, A. D. *et al.* A wireless closed loop system for optogenetic peripheral neuro-modulation. *Nature* 565, 361–365 (2019).
36. Lacour, S. P., Courtine, G. & Guck, J. Materials and technologies for soft implantable neuroprostheses. *Nat. Rev. Mater.* 1, (2016).
37. Feiner, R. & Dvir, T. Tissue-electronics interfaces: From implantable devices to engineered tissues. *Nat. Rev. Mater.* 3, (2017).
38. Tian, B. *et al.* Macroporous nanowire nanoelectronic scaffolds for synthetic tissues. *Nat. Mater.* 11, 986–994 (2012).
39. Feiner, R. *et al.* Engineered hybrid cardiac patches with multifunctional electronics for online monitoring and regulation of tissue function. *Nat. Mater.* 15, 679–685 (2016).
40. Dai, X., Zhou, W., Gao, T., Liu, J. & Lieber, C. M. Three-dimensional mapping and regulation of action potential propagation in nanoelectronics-innervated tissues. *Nat. Nanotechnol.* 11, 776–782 (2016).
41. Lee, S. *et al.* Ultrasoft electronics to monitor dynamically pulsing cardiomyocytes. *Nat. Nanotechnol.* 14, 156–160 (2019).
42. Feiner, R., Fleischer, S., Shapira, A., Kalish, O. & Dvir, T. Multifunctional degradable electronic scaffolds for cardiac tissue engineering. *J. Control. Release* 281, 189–195 (2018).
43. Wang, X. *et al.* Three-dimensional electronic scaffolds for monitoring and regulation of multifunctional hybrid tissues. *Extrem. Mech. Lett.* 35, (2020).
44. Schuhmann, T. G., Yao, J., Hong, G., Fu, T. M. & Lieber, C. M. Syringe-Injectable Electronics with a Plug-and-Play Input/Output Interface. *Nano Lett.* 17, 5836–5842 (2017).
45. Liu, J. *et al.* Syringe-injectable electronics. *Nat. Nanotechnol.* 10, 629–635 (2015).
46. Koh, A. *et al.* Ultrathin injectable sensors of temperature, thermal, conductivity, and heat capacity for cardiac ablation monitoring. *Adv. Healthc. Mater.* 5, 373–381 (2016).
47. Rehfeldt, F., Engler, A. J., Eckhardt, A., Ahmed, F. & Discher, D. E. Cell responses to the mechanochemical microenvironment—Implications for regenerative medicine and drug delivery. *Adv. Drug Deliv. Rev.* 59, 1329–1339 (2007).
48. Plotczyk, M. & Higgins, C. A. Skin biology. in *Biomaterials for Skin Repair and Regeneration* vol. 1 3–25 (Elsevier Ltd, 2019).
49. Kim, D. H. *et al.* Epidermal electronics. *Science* (80-.). 333, 838–843 (2011).
50. Chortos, A., Liu, J. & Bao, Z. Pursuing prosthetic electronic skin. *Nat. Mater.* 15, 937–950 (2016).
51. Argumugan, V., Naresh, M. D. & Sanjeevi, R. Effects of strain rate on the fracture behaviour of skin. *J. Biosci.* 19, 307–313 (1994).
52. Venus, M., Waterman, J. & McNab, I. Basic physiology of the skin. *Surgery* 28, 469–472 (2010).
53. Zhang, B., Korolj, A., Lai, B. F. L. & Radisic, M. Advances in organ-on-a-chip engineering. *Nat. Rev. Mater.* 3, 257–278 (2018).
54. Rogers, J. A. *et al.* Paper-like electronic displays: Large-area rubber-stamped plastic sheets of electronics and microencapsulated electrophoretic inks. *Proc. Natl. Acad. Sci. U. S. A.* 98, 4835–4840 (2001).
55. Someya, T. *et al.* A large-area, flexible pressure sensor matrix with organic field-effect transistors for artificial skin applications. *Proc. Natl. Acad. Sci. U. S. A.* 101, 9966–9970 (2004).

56. Kaltenbrunner, M. *et al.* An ultra-lightweight design for imperceptible plastic electronics. *Nature* 499, 458-463 (2013).
57. Miyamoto, A. *et al.* Inflammation-free, gas-permeable, lightweight, stretchable on-skin electronics with nanomeshes. *Nat. Nanotechnol.* 12, 907-913 (2017).
58. Kaltenbrunner, M. *et al.* Ultrathin and lightweight organic solar cells with high flexibility. *Nat. Commun.* 3, (2012).
59. Irimia-Vladu, M. 'Green'electronics: biodegradable and biocompatible materials and devices for a sustainable future. *Chem. Soc. Rev.* 43, 588-610 (2014).
60. Tao, H. *et al.* Silk-based conformal, adhesive, edible food sensors. *Adv. Mater.* 24, 1067-1072 (2012).
61. Kim, T. II *et al.* Injectable, cellular-scale optoelectronics with applications for wireless optogenetics. *Science (80-.)*. 340, 211-216 (2013).
62. Gutruf, P. & Rogers, J. A. Implantable, wireless device platforms for neuroscience research. *Curr. Opin. Neurobiol.* 50, 42-49 (2018).
63. Rogers, J. A., Someya, T. & Huang, Y. Materials and mechanics for stretchable electronics. *Science (80-.)*. 327, 1603-1607 (2010).
64. Wagner, S. & Bauer, S. Materials for stretchable electronics. *MRS Bull.* 37, 207-213 (2012).
65. Someya, T., Kaltenbrunner, M. & Yokota, T. Ultraflexible organic electronics. *MRS Bull.* 40, 1130-1137 (2015).
66. Someya, T., Bauer, S. & Kaltenbrunner, M. Imperceptible organic electronics. *MRS Bull.* 42, 124-130 (2017).
67. Hammock, M. L., Chortos, A., Tee, B. C. K., Tok, J. B. H. & Bao, Z. 25th anniversary article: The evolution of electronic skin (e-skin): a brief history, design considerations, and recent progress. *Adv. Mater.* 25, 5997-6038 (2013).
68. Lipomi, D. J. & Bao, Z. Stretchable and ultraflexible organic electronics. *MRS Bull.* 42, 93-97 (2017).
69. Tee, B. C. K., Wang, C., Allen, R. & Bao, Z. An electrically and mechanically self-healing composite with pressure- and flexion-sensitive properties for electronic skin applications. *Nat. Nanotechnol.* 7, 825-832 (2012).
70. Oh, J. Y. *et al.* Intrinsically stretchable and healable semiconducting polymer for organic transistors. *Nature* 539, 411-415 (2016).
71. Bettinger, C. J. & Bao, Z. Organic thin film transistor fabricated on reabsorbable bio-material substrates. *Adv. Mater.* 22, 651-655 (2010).
72. Hwang, S. W. *et al.* A physically transient form of silicon electronics. *Science (80-.)*. 337, 1640-1644 (2012).
73. Weimer, P. K. The TFT- a new thin-film transistor. *Proc. Inst. Radio Eng.* 50, 1462 (1962).
74. Ray, K. A. Flexible solar cell arrays for increased space power. *IEEE Trans. Aerosp. Electron. Syst.* 3, 107 (1967).
75. Brody, T. P. The birth and early childhood of active matrix – a personal memoir. *Journal of the Society for Information Display* vol. 4 113 (1996).
76. Ma, E. Y. & Wagner, S. Amorphous silicon transistors on ultrathin steel foil substrates. *Appl. Phys. Lett.* 74, 2661-2662 (1999).
77. Suo, Z., Ma, E. Y., Gleskova, H. & Wagner, S. Mechanics of rollable and foldable film-on-foil electronics. *Appl. Phys. Lett.* 74, 1177-1179 (1999).

78. Song, J. Mechanics of stretchable electronics. *Curr. Opin. Solid State Mater. Sci.* 19, 160–170 (2015).
79. Harris, K. D., Elias, A. L. & Chung, H.-J. Flexible electronics under strain: a review of mechanical characterization and durability enhancement strategies. *J. Mater. Sci.* 51, 2771–2805 (2016).
80. Schomburg, W. K. *Introduction to microsystem design*. vol. Membranes (Springer, Berlin, Heidelberg, 2011).
81. Song, J., Jiang, H., Huang, Y. & Rogers, J. A. Mechanics of stretchable inorganic electronic materials. *J. Vac. Sci. Technol. A Vacuum, Surfaces, Film.* 27, 1107–1125 (2009).
82. Jiang, H. *et al.* Finite deformation mechanics in buckled thin films on compliant supports. *Proc. Natl. Acad. Sci. U. S. A.* 104, 15607–15612 (2007).
83. Song, J. *et al.* An analytical study of two-dimensional buckling of thin films on compliant substrates. *J. Appl. Phys.* 103, (2008).
84. Wang, S. *et al.* Mechanics of epidermal electronics. *J. Appl. Mech.* 79, 1–7 (2012).
85. Mengüç, Y. *et al.* Wearable soft sensing suit for human gait measurement. *Int. J. Rob. Res.* 33, 1748–1764 (2014).
86. Webb, R. C. *et al.* Ultrathin conformal devices for precise and continuous thermal characterization of human skin. *Nat. Mater.* 12, 938–944 (2013).
87. Zaidi, Z. & Lanigan, S. W. Skin: structure and function. in *Dermatology in Clinical Practice* 1–15 (Springer London, 2010). doi:10.1007/978-1-84882-862-9_1.
88. Lacour, S. P., Wagner, S., Huang, Z. & Suo, Z. Stretchable gold conductors on elastomeric substrates. *Appl. Phys. Lett.* 82, 2404–2406 (2003).
89. Ko, H. C. *et al.* A hemispherical electronic eye camera based on compressible silicon optoelectronics. *Nature* 454, 748–753 (2008).
90. Drack, M. *et al.* An imperceptible plastic electronic wrap. *Adv. Mater.* 27, 34–40 (2014).
91. Yokota, T. *et al.* Ultraflexible organic photonic skin. *Sci. Adv.* 2, 1–9 (2016).
92. Reeder, J. *et al.* Mechanically adaptive organic transistors for implantable electronics. *Adv. Mater.* 26, 4967–4973 (2014).
93. Kim, D. H. & Rogers, J. A. Stretchable electronics: materials strategies and devices. *Adv. Mater.* 20, 4887–4892 (2008).
94. Kim, D. H., Xiao, J., Song, J., Huang, Y. & Rogers, J. A. Stretchable, curvilinear electronics based on inorganic materials. *Adv. Mater.* 22, 2108–2124 (2010).
95. Sun, Y., Choi, W. M., Jiang, H., Huang, Y. Y. & Rogers, J. A. Controlled buckling of semiconductor nanoribbons for stretchable electronics. *Nat. Nanotechnol.* 1, 201–207 (2006).
96. Xu, F. & Potier-Ferry, M. Quantitative predictions of diverse wrinkling patterns in film/substrate systems. *Sci. Rep.* 7, 1–10 (2017).
97. Sekitani, T. & Someya, T. Stretchable, large-area organic electronics. *Adv. Mater.* 22, 2228–2246 (2010).
98. Choi, W. M. *et al.* Biaxially stretchable ‘wavy’ silicon nanomembranes. *Nano Lett.* 7, 1655–1663 (2007).
99. Kim, D. H. *et al.* Materials and noncoplanar mesh designs for integrated circuits with linear elastic responses to extreme mechanical deformations. *Proc. Natl. Acad. Sci. U. S. A.* 105, 18675–18680 (2008).

100. Yamamoto, Y. *et al.* Printed multifunctional flexible device with an integrated motion sensor for health care monitoring. *Sci. Adv.* 2, (2016).
101. Shyu, T. C. *et al.* A kirigami approach to engineering elasticity in nanocomposites through patterned defects. *Nat. Mater.* 14, 785–789 (2015).
102. Kim, D. H., Lu, N., Huang, Y. & Rogers, J. A. Materials for stretchable electronics in bioinspired and biointegrated devices. *MRS Bull.* 37, 226–235 (2012).
103. Xu, S. *et al.* Assembly of micro/nanomaterials into complex, three-dimensional architectures by compressive buckling. *Science* (80-.). 347, 154–159 (2015).
104. Fan, J. A. *et al.* Fractal design concepts for stretchable electronics. *Nat. Commun.* 5, 1–8 (2014).
105. Xu, S. *et al.* Soft microfluidic assemblies of sensors, circuits, and radios for the skin. *Science* (80-.). 344, 70–74 (2014).
106. Krishnan, S. R. *et al.* Wireless, battery-free epidermal electronics for continuous, quantitative, multimodal thermal characterization of skin. *Small* 14, 1–13 (2018).
107. Kim, J. *et al.* Epidermal electronics with advanced capabilities in near-field communication. *Small* 11, 906–912 (2015).
108. Kim, J. *et al.* Stretchable silicon nanoribbon electronics for skin prosthesis. *Nat. Commun.* 5, (2014).
109. Moore, G. E. Cramming more components onto integrated circuits. *Electronics* 38, 114 (1965).
110. Lochner, C. M., Khan, Y., Pierre, A. & Arias, A. C. All-organic optoelectronic sensor for pulse oximetry. *Nat. Commun.* 5, 1–7 (2014).
111. Xu, B. *et al.* An epidermal stimulation and sensing platform for sensorimotor prosthetic control, management of lower back exertion, and electrical muscle activation. *Adv. Mater.* 28, 4462–4471 (2016).
112. Chung, H. U. *et al.* Skin-interfaced biosensors for advanced wireless physiological monitoring in neonatal and pediatric intensive-care units. *Nat. Med.* 26, 418–429 (2020).
113. Lee, K. *et al.* Mechano-acoustic sensing of physiological processes and body motions via a soft wireless device placed at the suprasternal notch. *Nat. Biomed. Eng.* 4, 148–158 (2020).
114. Bauer, S. *et al.* 25th anniversary article: A soft future: from robots and sensor skin to energy harvesters. *Adv. Mater.* 26, 149–162 (2014).
115. Liu, Y., Pharr, M. & Salvatore, G. A. Lab-on-skin: A Review of flexible and stretchable electronics for wearable health monitoring. *ACS Nano* 11, 9614–9635 (2017).
116. Choi, S., Lee, H., Ghaffari, R., Hyeon, T. & Kim, D. H. Recent advances in flexible and stretchable bio-electronic devices integrated with nanomaterials. *Adv. Mater.* 28, 4203–4218 (2016).
117. Wu, H., Huang, Y. A., Xu, F., Duan, Y. & Yin, Z. Energy harvesters for wearable and stretchable electronics: from flexibility to stretchability. *Adv. Mater.* 28, 9881–9919 (2016).
118. Nathan, A. *et al.* Flexible electronics: the next ubiquitous platform. *Proc. IEEE* 100, 1486–1517 (2012).
119. Chen, Y. *et al.* Flexible inorganic bioelectronics. *npj Flex. Electron.* 4, 1–20 (2020).
120. Rogers, J. A., Ghaffari, R. & Kim, D.-H. *Stretchable bioelectronics for medical devices and systems. Microsystems and Nanosystems series* (Springer International Publishing Switzerland, 2016). doi:10.1007/978-3-319-28694-5.

121. Materials, A. Special issue: Flexible hybrid electronics. Vol. 32. No.15 (2020).
122. Heeger, A. J. Semiconducting and metallic polymers: the fourth generation of polymeric materials. Nobel Lecture. *Angew. Chemie Int. Ed.* 40, 2591-2611 (2001).
123. Savagatrup, S., Printz, A. D., Rodriguez, D. & Lipomi, D. J. Best of both worlds: conjugated polymers exhibiting good photovoltaic behavior and high tensile elasticity. *Macromolecules* 47, 1981-1992 (2014).
124. Burroughes, J. H. *et al.* Light-emitting diodes based on conjugated polymers. *Nature* 347, 539-541 (1990).
125. Sun, Y. & Rogers, J. A. Inorganic semiconductors for flexible electronics. *Adv. Mater.* 19, 1897-1916 (2007).
126. Choi, S., Han, S. I., Kim, D., Hyeon, T. & Kim, D. H. High-performance stretchable conductive nanocomposites: Materials, processes, and device applications. *Chem. Soc. Rev.* 48, 1566-1595 (2019).
127. Savagatrup, S., Printz, A. D., O'Connor, T. F., Zaretski, A. V. & Lipomi, D. J. Molecularly stretchable electronics. *Chem. Mater.* 26, 3028-3041 (2014).
128. Park, S. *et al.* Soft, stretchable, fully implantable miniaturized optoelectronic systems for wireless optogenetics. *Nat. Biotechnol.* 33, 1280-1286 (2015).
129. Someya, T. *et al.* Conformable, flexible, large-area networks of pressure and thermal sensors with organic transistor active matrixes. *Proc. Natl. Acad. Sci. U. S. A.* 102, 12321-12325 (2005).
130. Wirthl, D. *et al.* Instant tough bonding of hydrogels for soft machines and electronics. *Sci. Adv.* 3, 1-10 (2017).
131. Danninger, D. *et al.* Stretchable polymerized high internal phase emulsion separators for high performance soft batteries. *Adv. Energy Mater.* 2000467, 1-8 (2020).
132. Yu, K. J., Yan, Z., Han, M. & Rogers, J. A. Inorganic semiconducting materials for flexible and stretchable electronics. *npj Flex. Electron.* 1, 1-13 (2017).
133. O'Connor, T. F., Rajan, K. M., Printz, A. D. & Lipomi, D. J. Toward organic electronics with properties inspired by biological tissue. *J. Mater. Chem. B* 3, 4947-4952 (2015).
134. Kim, D. C., Shim, H. J., Lee, W., Koo, J. H. & Kim, D. H. Material-based approaches for the fabrication of stretchable electronics. *Adv. Mater.* 32, 1-29 (2020).
135. Lipomi, D. J. *et al.* Skin-like pressure and strain sensors based on transparent elastic films of carbon nanotubes. *Nat. Nanotechnol.* 6, 788-792 (2011).
136. Lee, P. *et al.* Highly stretchable and highly conductive metal electrode by very long metal nanowire percolation network. *Adv. Mater.* 24, 3326-3332 (2012).
137. Xu, J. *et al.* Highly stretchable polymer semiconductor films through the nanoconfinement effect. *Science* (80-.). 355, 59-64 (2017).
138. Cai, G. *et al.* Extremely stretchable strain sensors based on conductive self-healing dynamic cross-links hydrogels for human-motion detection. *Adv. Sci.* 4, (2017).
139. Lin, Y., Fang, Y., Yue, J. & Tian, B. Soft-hard composites for bioelectric interfaces. *Trends Chem.* 1-16 (2020) doi:10.1016/j.trechm.2020.03.005.
140. Tee, B. C.-K. *et al.* A skin-inspired organic digital mechanoreceptor. *Science* (80-.). 350, 313-316 (2015).
141. Choi, S. *et al.* Stretchable heater using ligand-exchanged silver nanowire nanocomposite for wearable articular thermotherapy. *ACS Nano* 9, 6626-6633 (2015).
142. Zhou, R., Li, P., Fan, Z., Du, D. & Ouyang, J. Stretchable heaters with composites of an intrinsically conductive polymer, reduced graphene oxide and an elastomer for wearable thermotherapy. *J. Mater. Chem. C* 5, 1544-1551 (2017).

143. Kim, J. *et al.* Ultrathin quantum dot display integrated with wearable electronics. *Adv. Mater.* 29, 1–6 (2017).
144. Jung, S. *et al.* Wearable fall detector using integrated sensors and energy devices. *Sci. Rep.* 5, 1–9 (2015).
145. Park, J. *et al.* Electromechanical cardioplasty using a wrapped elasto-conductive epicardial mesh. *Sci. Transl. Med.* 8, 1–12 (2016).
146. Bhagavatheswaran, E. S. *et al.* Construction of an interconnected nanostructured carbon black network: Development of highly stretchable and robust elastomeric conductors. *J. Phys. Chem. C* 119, 21723–21731 (2015).
147. Kim, Y. *et al.* Stretchable nanoparticle conductors with self-organized conductive pathways. *Nature* 500, 59–63 (2013).
148. Zhu, Y., Xu, F., Wang, X. & Zhu, Y. Wavy ribbons of carbon nanotubes for stretchable conductors. *Adv. Funct. Mater.* 22, 1279–1283 (2012).
149. Chen, Z. *et al.* Three-dimensional flexible and conductive interconnected graphene networks grown by chemical vapour deposition. *Nat. Mater.* 10, 424–428 (2011).
150. Matsuhisa, N. *et al.* Printable elastic conductors with a high conductivity for electronic textile applications. *Nat. Commun.* 6, (2015).
151. Yu, Z., Niu, X., Liu, Z. & Pei, Q. Intrinsically stretchable polymer light-emitting devices using carbon nanotube-polymer composite electrodes. *Adv. Mater.* 23, 3989–3994 (2011).
152. Liang, J., Li, L., Niu, X., Yu, Z. & Pei, Q. Elastomeric polymer light-emitting devices and displays. *Nat. Photonics* 7, 817–824 (2013).
153. Printz, A. D. & Lipomi, D. J. Competition between deformability and charge transport in semiconducting polymers for flexible and stretchable electronics. *Appl. Phys. Rev.* 3, (2016).
154. Jeong, Y. R. *et al.* A skin-attachable, stretchable integrated system based on liquid GalnSn for wireless human motion monitoring with multi-site sensing capabilities. *NPG Asia Mater.* 9, 1–8 (2017).
155. Lee, Y., Cha, S. H., Kim, Y. W., Choi, D. & Sun, J. Y. Transparent and attachable ionic communicators based on self-cleanable triboelectric nanogenerators. *Nat. Commun.* 9, (2018).
156. Kang, J. *et al.* Tough and water-insensitive self-healing elastomer for robust electronic skin. *Adv. Mater.* 30, 1–8 (2018).
157. Son, D. *et al.* An integrated self-healable electronic skin system fabricated via dynamic reconstruction of a nanostructured conducting network. *Nat. Nanotechnol.* 13, 1057–1065 (2018).
158. Yao, S. *et al.* Nanomaterial-enabled flexible and stretchable sensing systems: Processing, integration, and Applications. *Adv. Mater.* 32, 1–31 (2020).
159. Lee, K. J. *et al.* Large-area, selective transfer of microstructured silicon: A printing-based approach to high-performance thin-film transistors supported on flexible substrates. *Adv. Mater.* 17, 2332–2336 (2005).
160. MacK, S., Meitl, M. A., Baca, A. J., Zhu, Z. T. & Rogers, J. A. Mechanically flexible thin-film transistors that use ultrathin ribbons of silicon derived from bulk wafers. *Appl. Phys. Lett.* 88, 2004–2007 (2006).
161. Carlson, A., Bowen, A. M., Huang, Y., Nuzzo, R. G. & Rogers, J. A. Transfer printing techniques for materials assembly and micro/nanodevice fabrication. *Adv. Mater.* 24, 5284–5318 (2012).

162. Stauth, S. A. & Parvis, B. A. Self-assembled single-crystal silicon circuits on plastic. *Proc. Natl. Acad. Sci. U. S. A.* 103, 13922–13927 (2006).
163. Kim, D. H. *et al.* Stretchable and foldable silicon integrated circuits. *Science* (80-.). 320, 507–511 (2008).
164. He, J., Nuzzo, R. G. & Rogers, J. A. Inorganic materials and assembly techniques for flexible and stretchable electronics. *Proc. IEEE* 103, 619–632 (2015).
165. Menard, E., Lee, K. J., Khang, D. Y., Nuzzo, R. G. & Rogers, J. A. A printable form of silicon for high performance thin film transistors on plastic substrates. *Appl. Phys. Lett.* 84, 5398–5400 (2004).
166. Shin, J. *et al.* Bioresorbable pressure sensors protected with thermally grown silicon dioxide for the monitoring of chronic diseases and healing processes. *Nat. Biomed. Eng.* 3, 37–46 (2019).
167. Suikkola, J. *et al.* Screen-printing fabrication and characterization of stretchable electronics. *Sci. Rep.* 6, 1–8 (2016).
168. Sekitani, T. *et al.* Stretchable active-matrix organic light-emitting diode display using printable elastic conductors. *Nat. Mater.* 8, 494–499 (2009).
169. Chou, N., Kim, Y. & Kim, S. A method to pattern silver nanowires directly on wafer-scale PDMS substrate and its applications. *ACS Appl. Mater. Interfaces* 8, 6269–6276 (2016).
170. Ge, J. *et al.* Stretchable conductors based on silver nanowires: Improved performance through a binary network design. *Angew. Chemie - Int. Ed.* 52, 1654–1659 (2013).
171. Das, R., He, X. & Ghaffarzadeh, K. Printed, organic and flexible electronics 2020–2030: Forecasts, players & opportunities. *IDTEchEX Reserach* (2020).
172. Alamán, J., Alicante, R., Peña, J. I. & Sánchez-Somolinos, C. Inkjet printing of functional materials for optical and photonic applications. *Materials (Basel)*. 9, (2016).
173. Schiaffino, S. & Sonin, A. A. Molten droplet deposition and solidification at low Weber numbers. *Phys. Fluids* 9, 3172–3187 (1997).
174. Yarin, A. L. Drop impact dynamics: Splashing, spreading, receding, bouncing.... *Annu. Rev. Fluid Mech.* 38, 159–192 (2006).
175. Dijkman, J. F. *et al.* Precision ink jet printing of polymer light emitting displays. *J. Mater. Chem.* 17, 511–522 (2007).
176. Zhang, Z. *et al.* Synthesis of monodisperse silver nanoparticles for ink-jet printed flexible electronics. *Nanotechnology* 22, 425601 (2011).
177. Whittow, W. G. *et al.* Inkjet-printed microstrip patch antennas realized on textile for wearable applications. *IEEE Antennas Wirel. Propag. Lett.* 13, 71–74 (2014).
178. Bihar, E. *et al.* A fully inkjet-printed disposable glucose sensor on paper. *npj Flex. Electron.* 2, 1–8 (2018).
179. Swisher, S. L. *et al.* Impedance sensing device enables early detection of pressure ulcers in vivo. *Nat. Commun.* 6, 1–10 (2015).
180. Khan, Y. *et al.* Inkjet-printed flexible gold electrode arrays for bioelectronic interfaces. *Adv. Funct. Mater.* 26, 1004–1013 (2016).
181. Yuan, Y. *et al.* Layer-by-layer inkjet printing SPS:PEDOT NP/RGO composite film for flexible humidity sensors. *RSC Adv.* 6, 113298–113306 (2016).
182. Derby, B. Inkjet printing of functional and structural materials: Fluid property requirements, feature stability, and resolution. *Annu. Rev. Mater. Res.* 40, 395–414 (2010).

183. Park, J. U. *et al.* High-resolution electrohydrodynamic jet printing. *Nat. Mater.* 6, 782–789 (2007).
184. Wijshoff, H. The dynamics of the piezo inkjet printhead operation. *Phys. Rep.* 491, 77–177 (2010).
185. Khan, Y. *et al.* A new frontier of printed electronics: Flexible hybrid electronics. *Adv. Mater.* 32, 1–29 (2020).
186. Feng, Z. *et al.* Paper-based printed impedance sensors for water sorption and humidity analysis. *Flex. Print. Electron.* (2017).
187. Stempien, Z., Rybicki, E., Rybicki, T. & Lesnikowski, J. Inkjet-printing deposition of silver electro-conductive layers on textile substrates at low sintering temperature by using an aqueous silver ions-containing ink for textronic applications. *Sensors Actuators B Chem.* 224, 714–725 (2016).
188. Mikkonen, R., Puistola, P., Jönkkäri, I. & Mäntysalo, M. Inkjet printable polydimethylsiloxane for all-inkjet-printed multilayered soft electrical applications. *ACS Appl. Mater. Interfaces* 12, 11990–11997 (2020).
189. Adly, N. *et al.* Printed microelectrode arrays on soft materials: from PDMS to hydrogels. *npj Flex. Electron.* 2, 1–9 (2018).
190. Qin, Y., Alam, A. U., Howlader, M. M. R., Hu, N. X. & Deen, M. J. Inkjet printing of a highly loaded palladium ink for integrated, low-cost pH sensors. *Adv. Funct. Mater.* 26, 4923–4933 (2016).
191. Haque, R. I., Ogam, E., Loussert, C., Benaben, P. & Boddart, X. Fabrication of capacitive acoustic resonators combining 3D printing and 2D inkjet printing techniques. *Sensors* 15, 26018–26038 (2015).
192. Suganuma, K. *Introduction to printed electronics.* (Springer Science and Business Media, 2014).
193. Gao, M., Li, L. & Song, Y. Inkjet printing wearable electronic devices. *J. Mater. Chem. C* 5, 2971–2993 (2017).
194. Wu, L. *et al.* Printing patterned fine 3D structures by manipulating the three phase contact line. *Adv. Funct. Mater.* 25, 2237–2242 (2015).
195. Alizadeh, A. *et al.* Influence of substrate elasticity on droplet impact dynamics. *Langmuir* 29, 4520–4524 (2013).
196. Wang, L. *et al.* Interface manipulation for printing three-dimensional microstructures under magnetic guiding. *Small* 11, 1900–1904 (2015).
197. Bao, B. *et al.* Fabrication of patterned concave microstructures by inkjet imprinting. *Adv. Funct. Mater.* 25, 3286–3294 (2015).
198. Guo, Y., Li, L., Li, F., Zhou, H. & Song, Y. Inkjet print microchannels based on a liquid template. *Lab Chip* 15, 1759–1764 (2015).
199. Chung, S. *et al.* Inkjet-printed stretchable silver electrode on wave structured elastomeric substrate. *Appl. Phys. Lett.* 98, 2011–2014 (2011).
200. Lee, J., Chung, S., Song, H., Kim, S. & Hong, Y. Lateral-crack-free, buckled, inkjet-printed silver electrodes on highly pre-stretched elastomeric substrates. *J. Phys. D: Appl. Phys.* 46, 105305 (2013).
201. Garma, L. D., Ferrari, L. M., Scognamiglio, P., Greco, F. & Santoro, F. Inkjet-printed PEDOT:PSS multi-electrode arrays for low-cost: In vitro electrophysiology. *Lab Chip* 19, 3776–3786 (2019).
202. Grouchko, M., Kamyshny, A., Mihailescu, C. F., Anghel, D. F. & Magdassi, S. Conductive inks with a 'built-in' mechanism that enables sintering at room temperature. *ACS Nano* 5, 3354–3359 (2011).

203. Deegan, R. D. *et al.* Capillary flow as the cause of ring stains from dried liquid drops. *Nature* 389, 827–829 (1997).
204. Oh, Y. *et al.* Inkjet printing of Al₂O₃ dots, lines, and films: From uniform dots to uniform films. *Curr. Appl. Phys.* 11, 359–363 (2011).
205. Soltman, D. & Subramanian, V. Inkjet-printed line morphologies and temperature control of the coffee ring effect. *Langmuir* 24, 2224–2231 (2008).
206. Zhang, Z. *et al.* Controlled inkjetting of a conductive pattern of silver nanoparticles based on the coffee-ring effect. *Adv. Mater.* 25, 6714–6718 (2013).
207. Gorter, H. *et al.* Toward inkjet printing of small molecule organic light emitting diodes. *Thin Solid Films* 532, 11–15 (2013).
208. Wood, V. *et al.* Inkjet-printed quantum dot-polymer composites for full-color AC-driven displays. *Adv. Mater.* 21, 2151–2155 (2009).
209. Lee, J. *et al.* Reliable and uniform thin-film transistor arrays based on inkjet-printed polymer semiconductors for full color reflective displays. *Adv. Mater.* 25, 5886–5892 (2013).
210. Choi, K.-H., Yoo, J., Lee, C. K. & Lee, S.-Y. All-inkjet-printed solid-state flexible supercapacitors on paper. *Energy Environ. Sci.* 9, 2812–2821 (2016).
211. Wang, S. *et al.* Inkjet printing of conductive patterns and supercapacitors using a multi-walled carbon nanotube/Ag nanoparticle based ink. *J. Mater. Chem. A* 3, 2407–2413 (2015).
212. Angmo, D., Larsen-Olsen, T. T., Jørgensen, M., Søndergaard, R. R. & Krebs, F. C. Roll-to-roll inkjet printing and photonic sintering of electrodes for ITO free polymer solar cell modules and facile product integration. *Adv. Energy Mater.* 3, 172–175 (2013).
213. Doodoo Arhin, D. *et al.* Inkjet-printed graphene electrodes for dye-sensitized solar cells. *Carbon N. Y.* 105, (2016).
214. Li, S.-G. *et al.* Inkjet printing of CH₃NH₃PbI₃ on a mesoscopic TiO₂ film for highly efficient perovskite solar cells. *J. Mater. Chem. A* 3, 9092–9097 (2015).
215. Besganz, A. *et al.* Inkjet printing as a flexible technology for the deposition of thermoelectric composite structures. *Procedia Technol.* 15, 99–106 (2014).
216. Kang, M., Baeg, K. J., Khim, D., Noh, Y. Y. & Kim, D. Y. Printed, flexible, organic nano-floating-gate memory: Effects of metal nanoparticles and blocking dielectrics on memory characteristics. *Adv. Funct. Mater.* 23, 3503–3512 (2013).
217. Salim, A. & Lim, S. Review of recent inkjet-printed capacitive tactile sensors. *Sensors* 17, (2017).
218. Moya, A., Gabriel, G., Villa, R. & Javier del Campo, F. Inkjet-printed electrochemical sensors. *Curr. Opin. Electrochem.* 3, 29–39 (2017).
219. Delaney, J. T., Smith, P. J. & Schubert, U. S. Inkjet printing of proteins. *Soft Matter* 5, 4866–4877 (2009).
220. Komuro, N., Takaki, S., Suzuki, K. & Citterio, D. Inkjet printed (bio)chemical sensing devices. *Anal. Bioanal. Chem.* 405, 5785–5805 (2013).
221. Boudouris, B. W. & Yee, S. Structure, properties and applications of thermoelectric polymers. *J. Appl. Polym. Sci.* 134, (2017).
222. Ferrari, L. M. *et al.* Ultraconformable temporary tattoo electrodes for electrophysiology. *Adv. Sci.* 5, 1–11 (2018).
223. Ferrari, L. M., Ismailov, U., Badier, J.-M., Greco, F. & Ismailova, E. Conducting polymer tattoo electrodes in clinical electro- and magneto-encephalography. *npj Flex. Electron.* 4, 1–9 (2020).

224. Bachmann, B. *et al.* All-inkjet-printed gold microelectrode arrays for extracellular recording of action potentials. *Flex. Print. Electron.* 2, (2017).
225. *Cell and organ printing.* (Springer, Netherlands, 2010).
226. Derby, B. Bioprinting: Inkjet printing proteins and hybrid cell-containing materials and structures. *J. Mater. Chem.* 18, 5717-5721 (2008).
227. Boukamp, P. *et al.* Normal keratinization in a spontaneously immortalized aneuploid human keratinocyte cell line. *J. Cell Biol.* 106, 761-771 (1988).
228. Lai-Cheong, J. E. & McGrath, J. A. Structure and function of skin, hair and nails. *Medicine (Baltimore).* 45, 347-351 (2017).
229. Article 16(1) of Directive 89/391/EEC. *Directive 2000/54/EC of the European Parliament and of the Council of 18 September 2000 on the protection of workers from risks related to exposure to biological agents at work.* (2000).
230. Rampersad, S. N. Multiple applications of Alamar blue as an indicator of metabolic function and cellular health in cell viability bioassays. *Sensors (Switzerland)* 12, 12347-12360 (2012).
231. Lancaster, M. V. & Fields, R. D. Antibiotic and cytotoxic drug susceptibility assays using resazurin and poisoning agents. (1995).
232. Invitrogen. alamarBlue® Assay. *US Pat. No 5501959* 1-27 (2007) doi:U.S. Patent No. 5,501,959.
233. Vedula, S. R. K., Ravasio, A., Lim, C. T. & Ladou, B. Collective cell migration: A mechanistic perspective. *Physiology* 28, 370-379 (2013).
234. Armstrong, R. A. When to use the Bonferroni correction. *Ophthalmic Physiol. Opt.* 34, 502-508 (2014).
235. Johnston, I. D., McCluskey, D. K., Tan, C. K. L. & Tracey, M. C. Mechanical characterization of bulk Sylgard 184 for microfluidics and microengineering. *J. Micromechanics Microengineering* 24, (2014).
236. Molina-Lopez, F., Quintero, A. V., Mattana, G., Briand, D. & De Rooij, N. F. Large-area compatible fabrication and encapsulation of inkjet-printed humidity sensors on flexible foils with integrated thermal compensation. *J. Micromechanics Microengineering* 23, (2013).
237. Altenberend, U. *et al.* Inkjet printed capacitive transducers on flexible plastic substrates with increase stability: Ag on PET. *IMCS 2012, 14th Int. Meet. Chem. sensors* 527-530 (2012) doi:10.5162/IMCS2012/6.2.1.
238. Solly, K., Wang, X., Xu, X., Strulovici, B. & Zheng, W. Application of real-time cell electronic sensing (RT-CES) technology to cell-based assays. *Assay Drug Dev. Technol.* 2, 363-372 (2004).
239. Ueberschlag, P. PVDF piezoelectric polymer. *Sens. Rev.* 21, 118-126 (2001).
240. Gao, W. *et al.* Fully integrated wearable sensor arrays for multiplexed in situ perspiration analysis. *Nature* 529, 509-514 (2016).
241. Zhu, C. *et al.* Stretchable temperature-sensing circuits with strain suppression based on carbon nanotube transistors. *Nat. Electron.* 1, 183-190 (2018).
242. Hua, Q. *et al.* Skin-inspired highly stretchable and conformable matrix networks for multifunctional sensing. *Nat. Commun.* 9, 1-11 (2018).
243. Jeong, J. W. *et al.* Capacitive epidermal electronics for electrically safe, long-term electrophysiological measurements. *Adv. Healthc. Mater.* 3, 642-648 (2014).
244. Yeo, W. H. *et al.* Multifunctional epidermal electronics printed directly onto the skin. *Adv. Mater.* 25, 2773-2778 (2013).

245. Li, S. *et al.* Physical sensors for skin-inspired electronics. 1–28 (2019) doi:10.1002/inf2.12060.
246. Zhu, Z., Park, H. S. & McAlpine, M. C. 3D printed deformable sensors. *Sci. Adv.* 6, 1–11 (2020).
247. Farooqui, M. F. & Shamim, A. Low Cost Inkjet Printed Smart Bandage for Wireless Monitoring of Chronic Wounds. *Sci. Rep.* 6, 1–13 (2016).
248. Saunders, R., Gough, J. & Derby, B. Piezoelectric inkjet printing of cells and biomaterials. in *Cell and Organ printing* (eds. Ringeisen, B., Spargo, B. & Wu, P.) 35–50 (Springer Netherlands, 2010).
249. Feiner, R. & Dvir, T. Engineering Smart Hybrid Tissues with Built-In Electronics. *iScience* 23, 100833 (2020).
250. Grimenes, S. & Martinsen, Ø. G. *Bioimpedance and Bioelectricity basics*. (Elsevier, 2015).
251. Xu, Y. *et al.* A review of impedance measurements of whole cells. *Biosens. Bioelectron.* 77, 824–836 (2016).
252. Patel, P. & Markx, G. H. Dielectric measurement of cell death. *Enzyme Microb. Technol.* 43, 463–470 (2008).
253. Schwan, H. P. Electric Characteristics of Tissues. in *Biophysik 1* 198–208 (1963).
254. Schwan, H. P. *Electrical properties of tissue and cell suspensions. Advances in Biological and Medical physics* vol. 5 (Academic Press Inc., 1957).
255. Nasir, N. & Al Ahmad, M. Cells electrical characterization: dielectric properties, mixture, and modeling theories. *J. Eng.* 2020, (2020).
256. Al Ahmad, M., Al Natour, Z., Mustafa, F. & Rizvi, T. A. Electrical Characterization of Normal and Cancer Cells. *IEEE Access* 6, 25979–25986 (2018).
257. Lukaski, H. C. & Moore, M. Bioelectrical impedance: Assessment of wound healing. 6, 209–212 (2012).
258. Lo, C. M., Keese, C. R. & Giaever, I. Impedance analysis of MDCK cells measured by electric cell-substrate impedance sensing. *Biophys. J.* 69, 2800–2807 (1995).
259. Ehret, R. *et al.* Monitoring of cellular behaviour by impedance measurements on interdigitated electrode structures. *Biosens. Bioelectron.* 12, 29–41 (1997).
260. Ehret, R., Baumann, W., Brischwein, M., Schwinde, A. & Wolf, B. On-line control of cellular adhesion with impedance measurements using interdigitated electrode structures. *Med. Biol. Eng. Comput.* 36, 365–370 (1998).
261. Bhansali, S., Chornokur, G., Arya, S. K., Phelan, C. & Tanner, R. Impedance-based miniaturized biosensor for ultrasensitive and fast prostate-specific antigen detection. *J. Sensors* 2011, (2011).
262. Caviglia, C. *et al.* Interdependence of initial cell density, drug concentration and exposure time revealed by real-time impedance spectroscopic cytotoxicity assay. *Analyst* 140, 3623–3629 (2015).
263. Xie, F. *et al.* Use of cellular electrical impedance sensing to assess in vitro cytotoxicity of anticancer drugs in a human kidney cell nephrotoxicity model. *Analyst* 137, 1343–1350 (2012).
264. Henderson, R. O. & Webster, J. G. An impedance camera for spatially specific measurements of the thorax. *IEEE Trans. Biomed. Eng.* BME-25, 250–254 (1978).
265. *Electrical impedance tomography: Methods, history and applications*. (Institution of Physics Publishing, 2005).

266. Warren Spence, D. & Pomeranz, B. Surgical wound healing monitored repeatedly in vivo using electrical resistance of the epidermis. *Physiol. Meas.* 17, 57-69 (1996).
267. Lukaski, H. C. & Moore, M. Bioelectrical impedance assessment of wound healing. *J. Diabetes Sci. Technol.* 6, 209-212 (2012).
268. Huang, X., Yeo, W. H., Liu, Y. & Rogers, J. A. Epidermal differential impedance sensor for conformal skin hydration monitoring. *Biointerphases* 7, 1-9 (2012).
269. ACEA Biosciences, Inc. <https://www.aceabio.com/>.
270. Drinan, D. D. & Edman, C. F. US 2010/02681 11 A1. vol. Patent App 1-16 (2010).
271. Giaever, I. & Keese, C. R. Micromotion of mammalian cells measured electrically. *Proc. Natl. Acad. Sci.* 88, 7896-7900 (1991).
272. Wang, J. *et al.* Review. Microfabricated electrochemical cell-based biosensors for analysis of living cells in vitro. *Biosensors* 2, 127-170 (2012).
273. Deblois, R. W. & Bean, C. P. Counting and sizing of submicron particles by the resistive pulse technique. *Rev. Sci. Instrum.* 41, 909-916 (1970).
274. Grossi, M. & Riccò, B. Electrical impedance spectroscopy for biological analysis and food characterization: a review. *J. Sensors Sens. Syst.* 6, 303-325 (2017).
275. Yang, L. & Bashir, R. Electrical/electrochemical impedance for rapid detection of foodborne pathogenic bacteria. *Biotechnol. Adv.* 26, 135-150 (2008).
276. Krinke, D., Jahnke, H., Pänke, O. & Robitzki, A. A. A microelectrode-based sensor for label-free in vitro detection of ischemic effects on cardiomyocytes. *Biosens. Bioelectron.* 24, 2798-2803 (2009).
277. Mamouni, J. & Yang, L. Interdigitated microelectrode-based microchip for electrical impedance spectroscopic study of oral cancer cells. *Biomed. Microdevices* 13, 1075-1088 (2011).
278. Cho, S. & Thielecke, H. Electrical characterization of human mesenchymal stem cell growth on microelectrode. *Microelectron. Eng.* 85, 1272-1274 (2008).
279. Turner, A. P. F. Biosensors: sense and sensitivity. *Chem. Soc. Rev.* 42, 3184-3196 (2013).
280. Daniels, J. S. & Porumand, N. Label-free impedance biosensors : Opportunities and challenges. *Electroanalysis* 19, 1239-1257 (2007).
281. Owino, I. O. K. & Sadik, O. A. Impedance spectroscopy : A powerful tool for rapid biomolecular screening and cell culture monitoring. *Electroanalysis* 17, 2101-2113 (2005).
282. Wang, Y., Ye, Z. & Ying, Y. New trends in impedimetric biosensors for the detection of foodborne pathogenic bacteria. *Sensors* 12, 3449-3471 (2012).
283. Bourjilat, A., Sarry, F., Kourtiche, D. & Nadi, M. Modelization of interdigitated electrode sensor for impedance spectroscopy measurement. *Elev. Int. Conf. Sens. Technol.* (2017) doi:10.1109/ICSensT.2017.8304461.
284. Blume, S. O. P., Ben-mrad, R. & Sullivan, P. E. Modelling the capacitance of multi-layer conductor-facing interdigitated electrode structures. *Sensors Actuators B. Chem.* 213, 423-433 (2015).
285. Starzyk, F. Parametrisation of interdigit comb capacitor for dielectric impedance spectroscopy. *Arch. Mater. Sci. Eng.* 34, 31-34 (2008).
286. Van Gerwen, P. *et al.* Nanoscaled interdigitated electrode arrays for biochemical sensors. *Sensors Actuators, B Chem.* 49, 73-80 (1998).
287. Rivadeneyra, A. *et al.* A novel electrode structure compared with interdigitated electrodes as capacitive sensor. *Sensors Actuators B. Chem.* 204, 552-560 (2014).

288. Molina-López, F., Briand, D. & de Rooij, N. F. Decreasing the size of printed comb electrodes by the introduction of a dielectric interlayer for capacitive gas sensors on polymeric foil: Modeling and fabrication. *Sensors Actuators B. Chem.* 189, 89–96 (2013).
289. Jackson, W. F. & Duling, B. R. Toxic effects of silver-silver chloride electrodes on vascular smooth muscle. *Circ. Res.* 53, 105–109 (1983).
290. Han, D.-W. *et al.* In-vivo and in-vitro biocompatibility evaluations of silver nanoparticles with antimicrobial activity. *J. Nanosci. Nanotechnol.* 12, 5205–5209 (2012).
291. Greulich, C., Kittler, S., Epple, M., Muhr, G. & Köller, M. Studies on the biocompatibility and the interaction of silver nanoparticles with human mesenchymal stem cells (hMSCs). *Langenbeck's Arch. Surg.* 394, 495–502 (2009).
292. Pauksch, L. *et al.* Biocompatibility of silver nanoparticles and silver ions in primary human mesenchymal stem cells and osteoblasts. *Acta Biomater.* 10, 439–449 (2014).
293. Agarwala, S., Min, J., Long, W., Layani, M. & Yee, W. A novel 3D bioprinted flexible and biocompatible hydrogel bioelectronic platform. *Biosens. Bioelectron.* 102, 365–371 (2018).
294. Agarwala, S., Lee, J. M., Yeong, W. Y., Layani, M. & Magdassi, S. 3D printed bioelectronic platform with embedded electronics. *MRS Adv.* 3, 3011–3017 (2018).
295. Magdassi, S., Grouchko, M., Berezin, O. & Kamysny, A. Triggering the sintering of silver nanoparticles at room temperature. *ACS Nano* 4, 1943–1948 (2010).
296. Vert, M. *et al.* Terminology for biorelated polymers and applications (IUPAC Recommendations 2012). *Pure Appl. Chem.* 84, 377–410 (2012).
297. Nemani, K. V., Moodie, K. L., Brennick, J. B., Su, A. & Gimi, B. In vitro and in vivo evaluation of SU-8 biocompatibility. *Mater Sci Eng C Mater Biol Appl.* 71, 233–236 (2013).
298. Teixeira, A. I., Abrams, G. A., Bertics, P. J., Murphy, C. J. & Nealey, P. F. Epithelial contact guidance on well-defined micro- and nanostructured substrates. *J. Cell Sci.* 116, 1881–1892 (2003).
299. Pennacchio, F. A., Garma, L. D., Matino, L. & Santoro, F. Bioelectronics goes 3D: New trends in cell-chip interface engineering. *J. Mater. Chem. B* 6, 7096–7101 (2018).
300. Xu, Y. *et al.* A review of impedance measurements of whole cells. *Biosens. Bioelectron.* 77, 824–836 (2016).
301. Martin, P. Wound healing - Aiming for perfect skin regeneration. *Science (80-).* 276, 75–81 (1997).
302. de Araujo, A. L. A., Claudel, J., Kourtiche, D. & Nadi, M. Use of an insulation layer on the connection tracks of a biosensor with coplanar electrodes to increase the normalized impedance variation. *Biosensors* 9, (2019).
303. Cui, Y., An, Y., Jin, T., Zhang, F. & He, P. Real-time monitoring of skin wound healing on nano-grooves topography using electric cell-substrate impedance sensing (ECIS). *Sensors Actuators, B Chem.* 250, 461–468 (2017).
304. Koley, D. & Bard, A. J. Triton X-100 concentration effects on membrane permeability of a single HeLa cell by scanning electrochemical microscopy (SECM). *Proc. Natl. Acad. Sci.* 107, 16783 LP - 16787 (2010).
305. Mazlan, N. S. *et al.* Interdigitated electrodes as impedance and capacitance biosensors: A review. *AIP Conf. Proc.* 1885, (2017).
306. Abercrombie, M. Contact inhibition in tissue culture. *In Vitro* 6, 128–142 (1970).

307. Curtis, A. S. G. & Varde, M. Control of cell behavior: Topological factors. *J. Natl. Cancer Inst.* 33, 15–26 (1964).
308. Liang, C. C., Park, A. Y. & Guan, J. L. In vitro scratch assay: A convenient and inexpensive method for analysis of cell migration in vitro. *Nat. Protoc.* 2, 329–333 (2007).
309. Riahi, R., Yang, Y., Zhang, D. D. & Wong, P. K. Advances in wound-healing assays for probing collective cell migration. *J. Lab. Autom.* 17, 59–65 (2012).
310. Tonello, S. *et al.* Impedance-based monitoring of mesenchymal stromal cell three-dimensional proliferation using aerosol jet printed sensors: A tissue engineering application. *Materials (Basel)*. 13, (2020).
311. Marziano, M. *et al.* Monitoring Caco-2 to enterocyte-like cells differentiation by means of electric impedance analysis on printed sensors. *Biochim. Biophys. Acta - Gen. Subj.* 1863, 893–902 (2019).
312. Kim, Y., Kim, J. W., Kim, J. & Noh, M. A novel fabrication method of Parylene-based microelectrodes utilizing inkjet printing. *Sensors Actuators, B Chem.* 238, 862–870 (2017).
313. Blaschke, B. M. *et al.* Flexible graphene transistors for recording cell action potentials. *2D Mater.* 3, 0 (2016).
314. Brischwein, M. *et al.* Electric cell-substrate impedance sensing with screen printed electrode structures. *Lab Chip* 6, 819–822 (2006).
315. Pejcic, B. & De Marco, R. Impedance spectroscopy: Over 35 years of electrochemical sensor optimization. *Electrochim. Acta* 51, 6217–6229 (2006).
316. Sandison, M. E., Anicet, N., Glidle, A. & Cooper, J. M. Optimization of the geometry and porosity of microelectrode arrays for sensor design. *Anal. Chem.* 74, 5717–5725 (2002).
317. Min, J. & Baeumner, A. J. Characterization and optimization of interdigitated ultra-microelectrode arrays as electrochemical biosensor transducers. *Electroanalysis* 16, 724–729 (2004).
318. Price, D. T., Rahman, A. R. A. & Bhansali, S. Design rule for optimization of microelectrodes used in electric cell-substrate impedance sensing (ECIS). *Biosens. Bioelectron.* 24, 2071–2076 (2009).
319. Radke, S. M. & Alcocilja, E. C. Design and fabrication of a microimpedance biosensor for bacterial detection. *IEEE Sens. J.* 4, 434–440 (2004).
320. Koley, D. & Bard, A. J. Triton X-100 concentration effects on membrane permeability of a single HeLa cell by scanning electrochemical microscopy (SECM). *Proc. Natl. Acad. Sci. U. S. A.* 107, 16783–16787 (2010).
321. Yokus, M. A., Songkakul, T., Pozdin, V. A., Bozkurt, A. & Michael, A. Wearable multiplexed biosensor system toward continuous monitoring of metabolites. *Biosens. Bioelectron.* 112038 (2020) doi:10.1016/j.bios.2020.112038.
322. Hahn, C. & Schwartz, M. A. Mechanotransduction in vascular physiology and atherogenesis. *Nat. Rev. Mol. Cell Biol.* 10, 53–62 (2009).
323. Wolff, J. *The law of bone remodelling.* (Springer, 1986).
324. Alonso, J. L. & Goldmann, W. H. Cellular mechanotransduction. *AIMS Biophys.* 3, 50–62 (2016).
325. Ingber, D. E. Cellular mechanotransduction: putting all pieces together again. *FASEB J.* 20, 811–827 (2006).

326. Mofrad, M. R. K. & Kamm, R. D. *Cellular mechanotransduction: Diverse perspectives from molecules to tissues*. (Cambridge University Press, 2009). doi:10.1017/CBO9781139195874.
327. Petridou, N. I., Spiró, Z. & Heisenberg, C. P. Multiscale force sensing in development. *Nat. Cell Biol.* 19, 581–588 (2017).
328. Paszek, M. J. *et al.* Tensional homeostasis and the malignant phenotype. *Cancer Cell* 8, 241–254 (2005).
329. Glenister, F. K., Coppel, R. L., Cowman, A. F., Mohandas, N. & Cooke, B. M. Contribution of parasite proteins to altered mechanical properties of malaria-infected red blood cells. *Blood* 99, 1060–1063 (2002).
330. Vinay, S. *et al.* Mechanical stiffness grades metastatic potential. *Cancer Res.* 71, 5075–5080 (2012).
331. Paluch, E. K. *et al.* Mechanotransduction: Use the force(s). *BMC Biol.* 13, 1–14 (2015).
332. Chen, C. S., Mrksich, M., Huang, S., Whitesides, G. M. & Ingber, D. E. Geometric control of cell life and death. *Science* (80-.). 276, 1425–1428 (1997).
333. Watt, F. M., Jordan, P. W. & O'Neill, C. H. Cell shape controls terminal differentiation of human epidermal keratinocytes. *Proc. Natl. Acad. Sci. U. S. A.* 85, 5576–5580 (1988).
334. Curtis, A. . & Seehar, G. . The control of cell division by tension or diffusion. *Nature* 274, 52–53 (1978).
335. Vogel, V. & Sheetz, M. Local force and geometry sensing regulate cell functions. *Nat. Rev. Mol. Cell Biol.* 7, 265–275 (2006).
336. Moeendarbary, E. *et al.* The cytoplasm of living cells behaves as a poroelastic material. *Nat. Mater.* 12, 253–261 (2013).
337. Pontes, B. *et al.* Membrane elastic properties and cell function. *PLoS One* 8, 1–10 (2013).
338. Roca-Cusachs, P., Conte, V. & Trepát, X. Quantifying forces in cell biology. *Nat. Cell Biol.* 19, 742–751 (2017).
339. Muhamed, I., Chowdhury, F. & Maruthamuthu, V. Biophysical tools to study cellular mechanotransduction. *Bioengineering* 4, 1–27 (2017).
340. Weinheimer-Haus, E. M., Judex, S., Ennis, W. J. & Koh, T. J. Low-intensity vibration improves angiogenesis and wound healing in diabetic mice. *PLoS One* 9, 3–10 (2014).
341. d'Agostino, M. C., Craig, K., Tibalt, E. & Respizzi, S. Shock wave as biological therapeutic tool: From mechanical stimulation to recovery and healing, through mechanotransduction. *Int. J. Surg.* 24, 147–153 (2015).
342. Sari, Y. *et al.* Vibration inhibits deterioration in rat deep-tissue injury through HIF1-MMP axis. *Wound Repair Regen.* 23, 386–393 (2015).
343. Arashi, M. *et al.* Vibration therapy accelerates healing of stage I pressure ulcers in older adult patients. *Adv. Skin Wound Care* 23, 321–327 (2010).
344. Abraira, V. E. & Ginty, D. D. The sensory neurons of touch. *Neuron* 79, 618–639 (2013).
345. Johansson, R. S. & Flanagan, J. R. Coding and use of tactile signals from the fingertips in object manipulation tasks. *Nat. Rev. Neurosci.* 10, 345–359 (2009).
346. Wang, N., Tytell, J. D. & Ingber, D. E. Mechanotransduction at a distance: Mechanically coupling the extracellular matrix with the nucleus. *Nat. Rev. Mol. Cell Biol.* 10, 75–82 (2009).

347. Panciera, T., Azzolin, L., Cordenonsi, M. & Piccolo, S. Mechanobiology of YAP and TAZ in physiology and disease. *Nat. Rev. Mol. Cell Biol.* 18, 758-770 (2017).
348. Totaro, A. *et al.* YAP/TAZ link cell mechanics to Notch signalling to control epidermal stem cell fate. *Nat. Commun.* 8, 1-13 (2017).
349. Dupont, S. *et al.* Role of YAP/TAZ in mechanotransduction. *Nature* 474, 179-184 (2011).
350. Brown, T. D. Techniques for mechanical stimulation of cells in vitro: a review. *J. Biomech.* 33, (2000).
351. Tan, J. L. *et al.* Cells lying on a bed of microneedles: An approach to isolate mechanical force. *Proc. Natl. Acad. Sci.* 100, 1484-1489 (2003).
352. Tajik, A. *et al.* Transcription upregulation via force-induced direct stretching of chromatin. *Nat. Mater.* 15, 1287-1296 (2016).
353. Du, V. *et al.* A 3D magnetic tissue stretcher for remote mechanical control of embryonic stem cell differentiation. *Nat. Commun.* 8, (2017).
354. Nikukar, H. *et al.* Production of nanoscale vibration for stimulation of human mesenchymal stem cells. *J. Biomed. Nanotechnol.* 12, 1478-1488 (2016).
355. Tsimbouri, P. M. *et al.* Stimulation of 3D osteogenesis by mesenchymal stem cells using a nanovibrational bioreactor. *Nat. Biomed. Eng.* 1, 758-770 (2017).
356. Robertson, S. N. *et al.* Control of cell behaviour through nanovibrational stimulation: Nanokicking. *Philos. Trans. R. Soc. A Math. Phys. Eng. Sci.* 376, (2018).
357. Childs, P. G. *et al.* Use of nanoscale mechanical stimulation for control and manipulation of cell behaviour. *Acta Biomater.* 34, 159-168 (2016).
358. Wehner, R. *et al.* Collective cell durotaxis emerges from long-range intercellular force transmission. *Science (80-)*. 353, 1157-1161 (2016).
359. Gilbert, P. *et al.* Substrate elasticity regulates skeletal muscle stem cell self-renewal in culture. *Science (80-)*. 27, 1078-1081 (2010).
360. Huaga, H. S., Choub, S. H., Don, T. M., Lai, W. C. & Cheng, L. P. Formation of microporous poly(hydroxybutyric acid) membranes for culture of osteoblast and fibroblast. *Polym. Adv. Technol.* 20, 1082-1090 (2009).
361. Engler, A. J., Sen, S., Sweeney, H. L. & Discher, D. E. Matrix elasticity directs stem cell lineage specification. *Cell* 126, 677-689 (2006).
362. du Roure, O. *et al.* Force mapping in epithelial cell migration. *Proc. Natl. Acad. Sci. U. S. A.* 102, 2390-2395 (2005).
363. Tanaka, S. M. *et al.* Effects of broad frequency vibration on cultured osteoblasts. *J. Biomech.* 36, 73-80 (2003).
364. Wang, L., Hsu, H. Y., Li, X. & Xian, C. J. Effects of frequency and acceleration amplitude on osteoblast mechanical vibration responses: A finite element study. *Biomed Res. Int.* 2016, (2016).
365. Ito, Y., Kimura, T., Nam, K., Katoh, A. & Masuzawa, T. Effects of vibration on differentiation of cultured PC12 cells. *Biotechnol. Bioeng.* 108, 592-599 (2011).
366. Nishimura, K., Blume, P., Ohgi, S. & Sumpio, B. E. The effect of different frequencies of stretch on human dermal keratinocyte proliferation and survival. *J. Surg. Res.* 155, 125-131 (2009).
367. Cui, Y. *et al.* Cyclic stretching of soft substrates induces spreading and growth. *Nat. Commun.* 6, 1-8 (2015).
368. Hoffman, B. D., Grashoff, C. & Schwartz, M. A. Dynamic molecular processes mediate cellular mechanotransduction. *Nature* 475, 316 (2011).

369. Syahir, M. *et al.* A Brief Review on Prospective of Polyvinylidene Fluoride as a Tissue Engineered Scaffold Material. *J. Adv. Ind. Technol. Appl.* 2, 12-22 (2020).
370. Sakiyama, T. & Huang, M. Free vibration analysis of rectangular plates with variable thickness. *J. Sound Vib.* 216, 379-397 (1998).
371. *Piezo Film Sensors. Technical Manual. Measurement Specialities, Inc.* (1999) doi:10.1148/100.2.415.
372. Liu, K., Zhang, S., Xu, M., Wu, T. & Shen, S. The research of effective flexoelectric coefficient along 1123 direction in polyvinylidene fluoride. *J. Appl. Phys.* 121, (2017).
373. Chang Liu. *Foundations of MEMS.* (Prentice Hall, 2012).
374. Posada-Roman, J. E., Jackson, D. A. & Garcia-Souto, J. A. Variable configuration fiber optic laser doppler vibrometer system. *Photonic Sensors* 6, 97-106 (2016).
375. Yusko, E. C. & Asbury, C. L. Force is a signal that cells cannot ignore. *Mol. Biol. Cell* 25, 3717-3725 (2014).
376. Riley, N. Steady Streaming. *Annu. Rev. Fluid Mech.* 33, 43-65 (2001).
377. Chou, K. C. & Kiang, Y. S. The biological functions of low-frequency vibrations. *Bio-phys. Chem.* 22, 219-235 (1985).
378. Atherton, P. *et al.* Vinculin controls talin engagement with the actomyosin machinery. *Nat. Commun.* 6, 1-12 (2015).
379. Atherton, P., Stutchbury, B., Jethwa, D. & Ballestrem, C. Mechanosensitive components of integrin adhesions: Role of vinculin. *Exp. Cell Res.* 343, 21-27 (2016).
380. Tsimbouri, P. Adult Stem Cell Responses to Nanostimuli. *J. Funct. Biomater.* 6, 598-622 (2015).
381. Lee, D. A. & Bader, D. L. Compressive strains at physiological frequencies influence the metabolism of chondrocytes seeded in agarose. *J. Orthop. Res.* 15, 181-188 (1997).
382. Kaspar, D., Seidl, W., Ignatius, A. & Claes, L. Dynamic cell stretching increases human osteoblast proliferation and C1CP synthesis but decreases osteocalcin synthesis and alkaline phosphatase activity. *J. Biomech.* 33, 45-51 (2000).
383. Tsimbouri, P. M. *et al.* Stimulation of 3D osteogenesis by mesenchymal stem cells using a nanovibrational bioreactor. *Nat. Biomed. Eng.* 1, 758-770 (2017).
384. Pemberton, G. D. *et al.* Nanoscale stimulation of osteoblastogenesis from mesenchymal stem cells: nanotopography and nanokicking. *Nanomedicine* 10, 547-560 (2015).
385. Pemberton, G. D. *et al.* Nanoscale stimulation of osteoblastogenesis from mesenchymal stem cells: nanotopography and nanokicking. *Nanomedicine* 10, 547-560 (2015).
386. Hoffman, B. D., Grashoff, C. & Schwartz, M. A. Dynamic molecular processes mediate cellular mechanotransduction. *Nature* 475, (2011).
387. Na, S. *et al.* Rapid signal transduction in living cells is a unique feature of mechanotransduction. *Proc. Natl. Acad. Sci.* 105, 6626-6631 (2008).
388. Kaspar, D. *et al.* Proliferation of human-derived osteoblast-like cells depends on the cycle number and frequency of uniaxial strain. *Journal of Biomechanics* vol. 35 873-880 (2002).
389. Baumgartner, M. *et al.* Resilient yet entirely degradable gelatin-based biogels for soft robots and electronics. *Nat. Mater.* doi:10.1038/s41563-020-0699-3.
390. Abdolmaleki, H. & Agarwala, S. PVDF-batio₃ nanocomposite inkjet inks with enhanced β -phase crystallinity for printed electronics. *Polymers (Basel)*. 12, 1-12 (2020).

The background of the page is a collage of two images. On the left, there is a close-up of a blue and purple printed circuit board (PCB) with intricate circuit traces. On the right, there is a histological slide showing a cross-section of tissue, likely skin, stained with hematoxylin and eosin (H&E), showing various cellular structures and layers.

VIII. APPENDIX

Appendix I. Materials List for the fabrication of the sensors

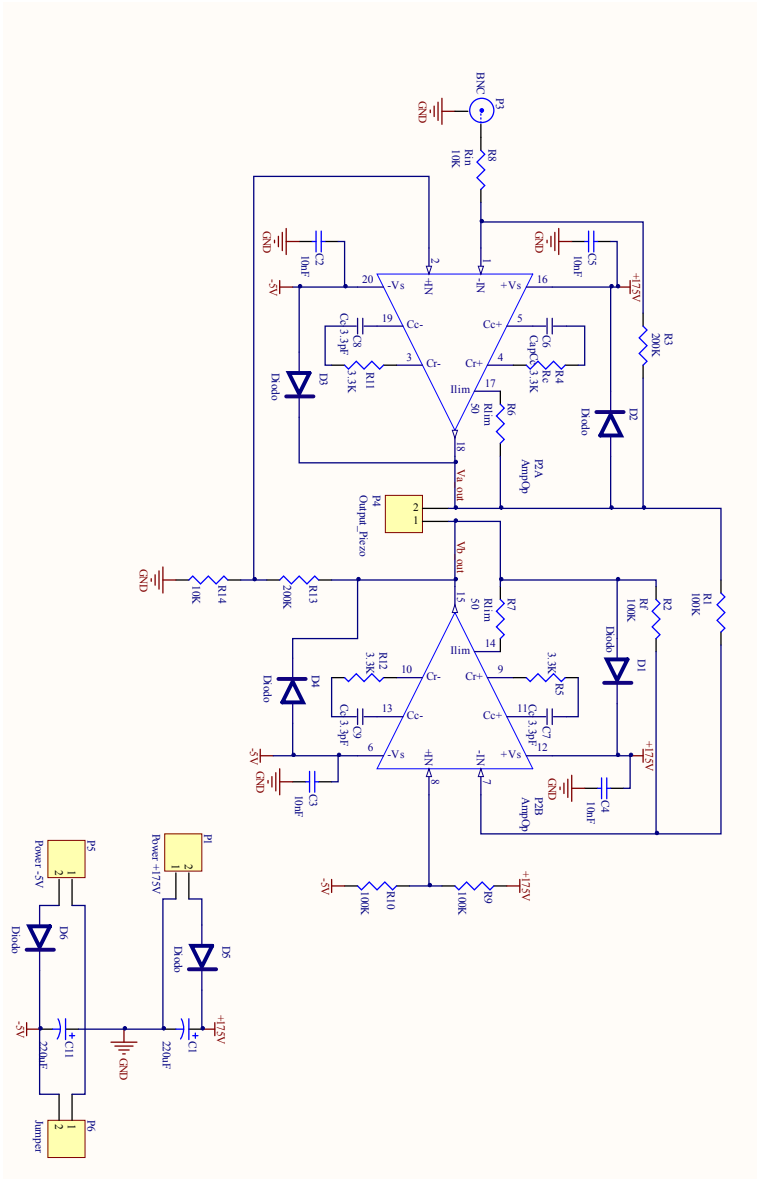
Material	Specification	Supplier
Silver Nanoparticle	15% Ag, Ethylene glycol 15-25%, ethanol 1-2% and water 50-70	Sigma Aldric
SU-8 formulation		MicroChem PriElex®
PET foils	100 µm	Mitsubishi Paper Mills
EPO-TEK®H20E		Epoxy Technology, Inc.
PDMS	Sylgard® 184	Sigma Aldrich
Adhesive Kapton® films		Sigma Aldrich
Dow Corning™ High-Vacuum Grease		Fisher Scientific

Appendix II. Materials List for the fabrication of the actuators

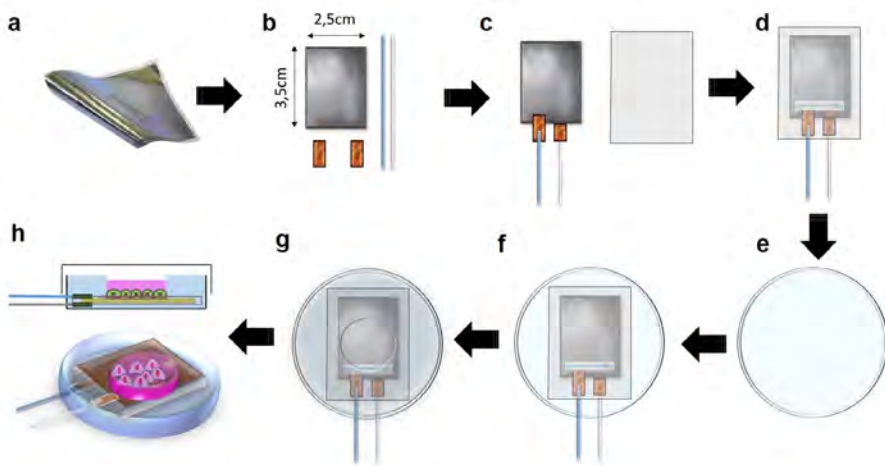
Material	Specification	Supplier
PVDF	18 μm thickness	PiezoTech
Adhesive Copper tape	RF EMI Shielding Tape 1181 Copper Foil Conductive, Single Sided 0.250" (6.35mm) X 54.000' (16.50m) X 0.003" (0.07mm)	3M Authorized Distributor
Adhesive Polymer Film		
Apex PA79DK	Apex Microtechnology	Digi-Key
Power Supply IHB200-0.12		RS Component

Comment	Description	Designator	Footprint	Footprint Description	Lib Ref	Quantity
Cap Pol1	Polarized Capacitor (Radial)	C1, C11	ECA2EM221	Cap	Cap Pol1	2
100nF	Capacitor (Semiconductor SIM Model), Polarized Capacitor (Radial)	C2, C3	C1808V104K-BRACTU	Cap_Bypass	Cap Pol1, Cap Semi	2
Cap Semi	Capacitor (Semiconductor SIM Model)	C4, C5	C1206	Chip Capacitor; Body 3.2 x 1.6 mm (LxW typ)	Cap Semi	2
Cc 3.3pF		C6, C8, C7, C9	MC0805N-3R3C501CT		Cap	4
Diodo		D1, D2, D3, D4, D5, D6	AU1PJM384A		Diode	6
Power +175V	Header, 2-Pin	P1, P4, P5, P6	B2B-XH-2		Header 2	4
AmpOp		P2	PA79SOP20		PA79	1
	BNC Elbow Connector	P3	BNC_RA CON	Connector; BNC Elbow	BNC	1
RinB	Resistor	R1, R2, R9, R10	5025[2010]	Chip Resistor; Body 5.0 x 2.5 mm (LxW typ)	Res3	4
Rf	Resistor	R3, R13	5025[2010]	Chip Resistor; Body 5.0 x 2.5 mm (LxW typ)	Res3	2
Rc	Resistor	R4, R5, R11, R12	6332[2512]	Chip Resistor; Body 6.3 x 3.2 mm (LxW typ)	Res3	4
Rlim	Resistor	R6, R7	6332[2512]	Chip Resistor; Body 6.3 x 3.2 mm (LxW typ)	Res3	2
Rin	Resistor	R8, R14	3225[1210]	Chip Resistor; Body 3.2 x 2.5 mm (LxW typ)	Res3	2

Appendix III. Board Circuit Schematic for the driver of the actuator device

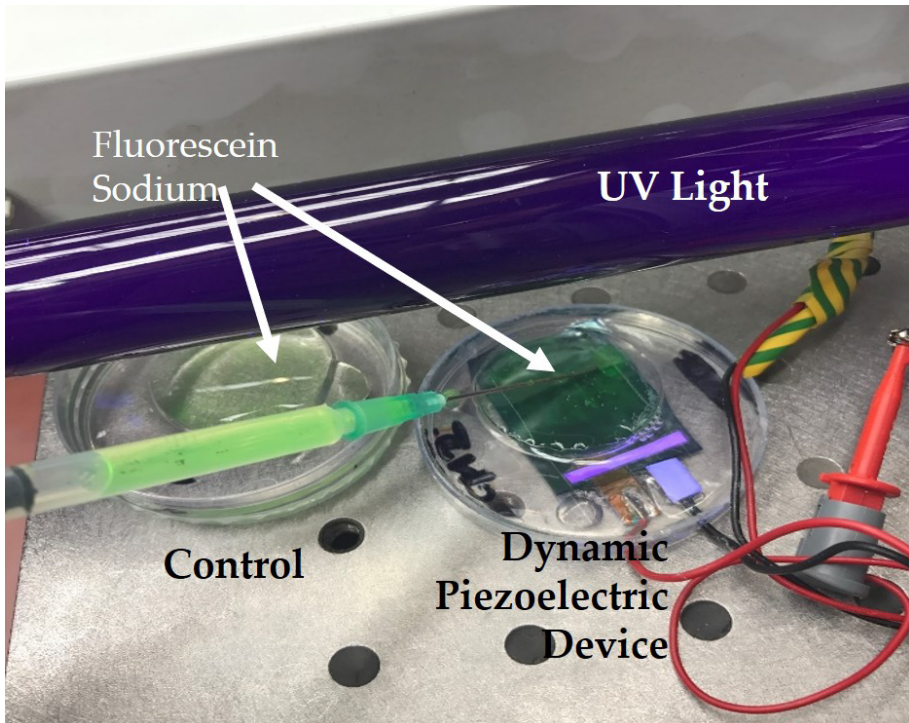


Appendix IV. Flow chart in the assembly of the experimental stage of the actuator devices



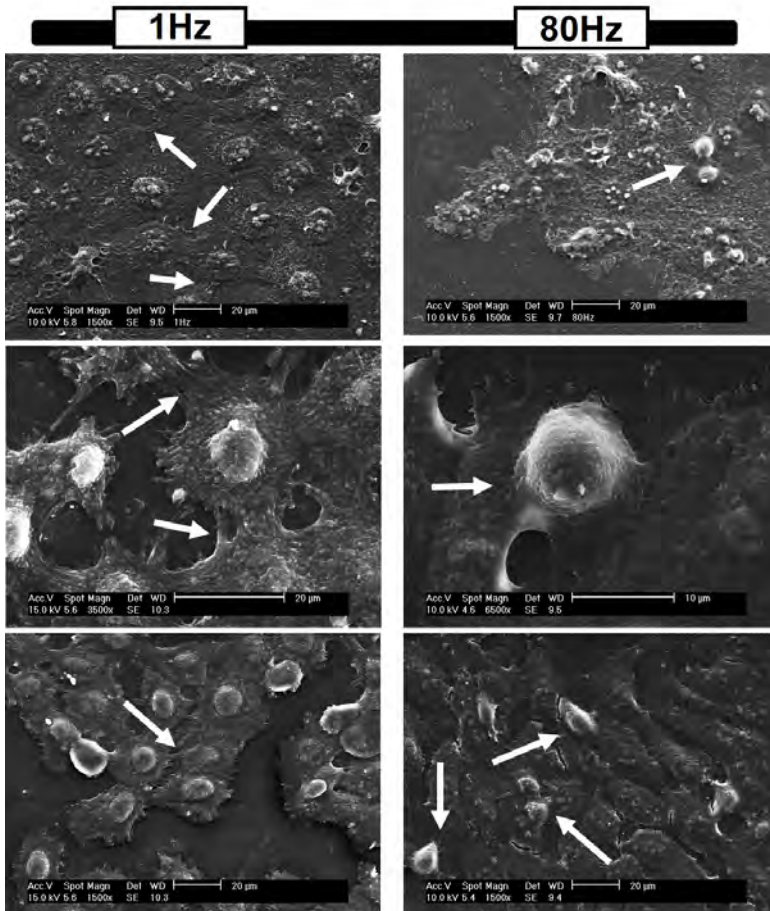
The PVDF film as received (a) is split into small pieces of 2.5 cm × 3.5 cm (b) as well as two copper adhesive tapes and the external cables. (c) The external cables are soldered to the copper adhesive tapes and attached to each side of the PVDF piezoelectric and pieces of the non-conductive polymer are adhered to each side of the film (d) to avoid electrical stimulation to the cell cultures. A paper label is included just before sticking the non-conductive polymer on top of the flexible copper electrodes. (e) Petri dishes with lateral wholes are conditioned to hold the organic piezoelectric in their bottom (f). A ring made with PDMS is cured on top of the assembled actuator leaving a well to culture cells (g). Finally, the schematic in (h) shows the actuator device holding a long-lasting cell culture.

Appendix V. Experimental setup for the analysis of fluid streaming within the actuating device



Fluorescein Sodium is added dropwise under blue light into the devices filled with water. Devices were dynamically stimulated with a frequency of 80 Hz while the tracks in the fluxes were monitored. No fluxes were observed in the dye.

Appendix VI. Additional scanning electron microscopy images of cell cultures seeded on the actuators



Changes in the cell morphology in samples stimulated at 1 Hz and 80 Hz for 48 h using the designed actuating device. In samples stimulated at 1-Hz frequency the cell-cell union and the structure of cells appear elongated and stressed while in cell cultures stimulated at 80 Hz, some cells presented a rounded and compacted shape. While the rounded morphology observed at 80 Hz could be representative of cells that are going to divide (the upper and lower micrographs in the 80 Hz column shows two cells tightly gripped to each other), it might be also an effect of the dynamic mechanical stimulation since this characteristic was observed more significant in this group.

Appendix VII. Fitting values of the electrical circuit model for detachment experiments

Impedance spectrum Time	Chi-Sqr	Sum-Sqr	Rs(\pm)	Rs (Error)	Rs (Error%)	Cide(\pm)	Cide (Error)	Cide (Error%)
Time 15h	0,0065041	23,369	29,18	0,34127	1,1695	9,81E-12	1,29E-10	1,3162
Time 23h	0,0066099	23,749	30,41	0,31985	1,0518	1,11E-11	1,52E-10	1,3616
Time 36h	0,006949	24,968	30,26	0,3366	1,1124	1,18E-11	1,88E-10	1,5983
Time 48h	0,0073915	22,123	30,01	0,36434	1,2141	1,32E-11	2,59E-10	1,9604
Time 56h	0,0074047	17,719	28,87	0,40276	1,3951	1,48E-11	3,82E-10	2,5775
Time 80h	0,0085544	17,049	26,05	0,45779	1,7574	1,83E-11	7,42E-10	4,0561

Rinterfaz(\pm)	Rinterfaz (Error)	Rinterfaz (Error%)	CPE_interfaz-T(\pm)	CPE_interfaz-T (Error)	CPE_interfaz-T (Error%)	CPE_interfaz-P(\pm)	CPE_interfaz-P (Error)	CPE_interfaz-P (Error%)
57,53	0,31508	0,54768	0,00015605	2,17E-06	1,3913	0,47377	0,0018875	0,3984
52,66	0,28887	0,54856	0,00011929	1,62E-06	1,3596	0,51319	1,82E-03	0,35439
46,67	0,28938	0,62006	8,58E-05	1,12E-06	1,3076	0,5486	0,0017197	0,31347
41,12	0,30924	0,75204	7,87E-05	1,13E-06	1,4346	0,55469	1,87E-03	0,33756
34,17	0,32916	0,9633	7,70E-05	1,20E-06	1,5528	0,55196	2,01E-03	0,36387
24,15	0,34761	1,4394	7,46E-05	1,30E-06	1,7454	0,5534	2,22E-03	0,40183

Appendix VIII. Materials List for the cell biology experiments and Solutions

A. Material Lists for Cell Biology Experiments

Material	Specification	Supplier
Trypsin EDTA	0.05 % and 0.025 %	Life Technologies
Glutaraldehyde	25% in water 50ml	Sigma Aldrich
Paraformaldehyde	Powder, 95%	Sigma Aldrich
Virkon 5g		
Dimethyl Sulfoxide		
Antibiotic/Antimicotic	105 U·ml-1 /104 µg·ml-1	Thermo Scientific HyClone
FBS Qualite Recherche Us	500ml	
DMEM High w/Glutamax	500ml	Invitrogen Gibco
DMEM w/o phenol red		Invitrogen Gibco
Alamar Blue Cell Viability	25ml	Bio-Rad AbD Se- rotec
Collagen from Calf Skin	0.1% Solution In 0.1 M Acetic Acid	Sigma Aldrich
Serological pipet	5 mL, 10 mL	
P60 culture dish	60x15mm	
P100 culture dish	100x20mm	
Corning 96-Well Multiwells		
Parafilm 38mx100mm		
Syringe	3p ste 60ml luer-lock x25	

Material	Specification	Supplier
Filters paradisc	25 AS PS 0,2 μ 25MM X50	
Count. Chamber		Neubauer
Filtration units	250ML 0,1 μ M X12	
Micropipette tips	100 - 1000 μ l / 2 - 200 μ l / 0,5 - 10 μ	
Graduated centrifuge tube with screw cap (falcon)	15 mL, 50 mL	
Cryotubes cryovial	2 mL sterile nalgene	

B. A.5.2 Phosphate Buffer Saline Solution (PBS)

In 1 liter of distilled water, NaCl, KCl and Na₂HPO₄, KH₂PO₄ are dissolved to a final concentration of 137 mM, 2.7 mM, 8 mM and 1.8 mM, respectively. The solution is then diluted in a final concentration of 1:10 in distilled water.

C. A.5.3 Blocking Solution (BS)

In 50 mL of PBS solution, it is dissolved 0.5 g of Bovine Serum and 1 mL of Goat Serum.

